On the Trail of the Unseen: Probing Exotic Physics at Colliders

PhD Thesis

Emanuela Musumeci

IFIC - Universitat de València - CSIC

Programa de Doctorat en Física - 3126

Supervisor:

Vasiliki Mitsou

Tutor:

Óscar Vives García

Valencia, March 2025

"Per chi viaggia in direzione ostinata e contraria."
Fabrizio De André, *Smisurata preghiera*

Preface

The goal of this doctoral thesis is to investigate the potential existence of new physics (NP) within collider experiments, both at the Large Hadron Collider (LHC) and future colliders.

The Standard Model (SM), briefly outlined in Section 1.1, provides a robust framework for particle physics; however, it presents some limitations that require extensions. The search for NP beyond the SM (BSM) has been a longstanding endeavour in particle physics, fuelled by theoretical predictions and experimental discrepancies, as discussed in Section 1.2. An overview of collider physics, which provides the experimental framework to explore BSM phenomena, is presented in Chapter 2.

This dissertation explores various aspects of this quest, focusing on highly ionising particles (HIPs) — namely Magnetic Monopoles (MMs) and High-Electric-Charge Objects (HECOs) — and examining their production mechanisms and phenomenology at the LHC, which are discussed in detail in Chapter 3.

A major component of this research is the development and implementation of a non-perturbative resummation technique to improve theoretical predictions for HECO production. Chapter 4 presents a detailed discussion of the Dyson–Schwinger approach applied to both spin-1/2 and spin-0 HECOs, addressing the breakdown of perturbative Quantum Electrodynamics (QED) in scenarios involving large electric charges. Unlike traditional tree-level calculations—typically used to derive mass bounds from Drell–Yan and photon-fusion processes—this framework ensures reliable cross-section computations in the strongly coupled regime.

The resummation procedure involves determining non-trivial ultraviolet

(UV) fixed points, whose origin differs depending on the HECO spin, leading to robust predictions crucial for collider phenomenology. Theoretical results are embedded into Monte Carlo event generators via Universal FeynRules Output (UFO) models, facilitating realistic simulations at the LHC. This combined framework of improved UFO models and Monte Carlo simulations enables the extraction of more reliable mass bounds, offering significant improvements over conventional tree-level analyses performed by ATLAS and MoEDAL.

Additionally, this work examines the role of magnetic monopoles in light-by-light (LbL) scattering processes. Effective field theory (EFT) interpretations and Born-Infeld (BI) modifications of electrodynamics are explored as alternative methods to constrain monopole masses using photon-photon interactions. Chapter 5 details these approaches, highlighting their impact on experimental constraints from diphoton searches.

The final part of this thesis explores two-particle angular correlations as a tool to probe Hidden Valley (HV) scenarios, offering a promising avenue for discovering NP at future e^+e^- colliders. Chapter 6 presents a detailed study of a Quantum Chromodynamics (QCD)-like HV model with relatively light v-quarks — hypothetical fermions confined under a new strong force in a hidden sector —- which perturbs the QCD partonic cascade and modifies the azimuthal and (pseudo)rapidity correlations of final-state SM hadrons. These angular correlations are investigated as a novel probe of such effects, with a focus on event-level analyses at high-energy lepton colliders. The study, performed using Pythia8 and fast detector simulation tools, examines unexpected structures in the angular correlation function while considering selection cuts and detector effects.

Chapter 7 contains a short conclusion and outlook. A detailed summary in Valencian of the motivations, methodology and results of this thesis are given in Chapter 8.

Contents

Preface 2

List of Figures 9

List of Tables 13

1 The Standard Model and Beyond 17

1.1 The Standard Model of particle physics 18

1.1.1 The SM Lagrangian and Particle Content 19

1.1.2 Achievements of the Standard Model 22

1.2 Beyond the Standard Model 24

1.2.1 Observational Evidence for BSM Physics 24

1.2.2 Theoretical Puzzles Motivating BSM Physics 27

1.2.3 Frameworks for New Physics 29

1.2.3.1 Effective Field Theories 29

1.2.3.2 Supersymmetry (SUSY) 30

1.2.3.3 Grand Unified Theories (GUTs) 31

1.2.3.4 Extra dimensions 33

2 Collider Physics 35

2.1 General Features 35

2.1.1 Events, cross sections and luminosity 37

2.2 Detector Measurements and Event Kinematics 39

2.3 Types of Colliders 42

2.3.1 e^+e^- colliders 43

2.3.2 Hadron Colliders 50

3 Highly Ionising Particles **55**

3.1 Searches for HIPs at colliders 57

3.1.1 HIP Searches in ATLAS and CMS 57

3.1.2 The MoEDAL Experiment 58

3.2 Magnetic Monopoles 60

3.3 Highly Electrically Charged Objects 62

3.4 HIPs Production Mechanisms and searches 65

4 Dyson-Schwinger Resummation for HECOs **71**

4.1 Introduction 71

4.2 Resummation for spin-$^1/_2$ HECOs 72

4.2.1 Coupled Quantum Corrections 73

4.2.2 Fixed-Point Solution 75

4.2.2.1 Effective Running Coupling 77

4.2.3 Application to HECOs 79

4.2.3.1 Running Mass 79

4.2.3.2 Effective Feynman Rules 80

4.2.3.3 Incorporating the Z^0 Boson Contribution . 81

4.2.4 HECO Self-Energy and Analytical Considerations . . 85

4.2.5 Implementation in MadGraph and Cross section Analysis 89

4.3 Resummation for scalar HECOs 98

4.3.1 Non-Perturbative Resummation Approach to Scalar HECOs 98

4.3.1.1 Overview of Scalar Quantum Electrodynamics 98

4.3.2 Resummation 99

4.3.3 Fixed point and dressed HECO mass 102

4.3.4 MADGRAPH Implementation - Effective Feynman Rules 106

4.3.5 Cross Sections for Scalar HECO Production at Colliders 108

4.4 Re-evaluated Mass Limits 115

4.5 Conclusions 120

5 Constraining Magnetic Monopoles via $\gamma\gamma$ Events 123

5.1 Light-by-Light Scattering 123

5.1.1 Central Exclusive Processes 124

5.2 EFT Interpretation 126

5.3 Born-Infeld Scenario 130

5.4 Conclusions 133

6 Angular Correlations as Probes for New Physics 135

6.1 Two-particle angular correlations 136

6.2 Hidden Valley Phenomenology 139

6.2.1 QCD-like scenario 141

6.3 Analysis at detector level 142

6.4 Prospects on the Experimental Sensitivity 149

6.5 Different energies and colliders 152

6.6 Conclusions 153

7 Conclusions and Outlook 155

8 Resum de la tesi 157

8.1 Introducció 157

8.1.1 El Model Estàndard de la Física de Partícules 157

8.1.2 Motivacions per a Nova Física 158

8.1.3 Física de Col·lisionadors 158

8.1.4 Partícules Altament Ionitzants 159

8.2 Objectius 160

8.3 Metodologias 162

8.3.1 Metodologia per a la resummació DS i la implementació en models UFO per a HECOs de spin-$\frac{1}{2}$ i spin-0 162

8.3.1.1 Cas Spin-$\frac{1}{2}$ 163

8.3.1.2 Cas Spin-0 165

8.3.2 Restriccions per a Monopols Magnètics mitjançant Esdeveniments $\gamma\gamma$ 167

8.3.3 Estudi de correlacions angulars i la recerca de senyals Hidden Valley . . . 169
8.4 Resultats . . . 171
8.4.1 Resultats per als HECOs . . . 171
8.4.2 Exploració de Monopols amb Esdeveniments de Difotons . . . 172
8.4.3 Sensibilitat a sectors ocults mitjançant correlacions angulares de dues partícules . . . 176
8.5 Conclusions . . . 177

A Scalar self-energy and self-interaction 179
A.1 Loop integrals . . . 179
A.2 Polarization tensor of gauge bosons . . . 181
A.3 Scalar self energy . . . 181
A.4 Scalar self-interaction . . . 183

B UFO model validation 187
B.1 Validation at Tree Level . . . 187
B.2 Validation with Resummation Effects . . . 189

Acknowledgements 195

Bibliography 197

List of Figures

2.1 A schematic layout of the International Linear Collider. . . . 45

2.2 Overview of the CLIC layout at $\sqrt{s} = 380$ GeV. 46

2.3 A schematic map showing where the Future Circular Collider tunnel is proposed to be located. 49

2.4 A schematic depiction of the LHC. 51

3.1 A schematic view of the MoEDAL detector deployed in the VELO cavern at IP8 59

3.2 Monopole M pair production diagrams in hadron colliders: Drell-Yan and via Photon Fusion 66

4.1 Wave-function renormalisation $\mathcal{Z}$ as a function of k/m for $g^2 = 8\pi^2$. The value of $\mathcal{Z}$ asymptotically approaches $\mathcal{Z}^\star \equiv \mathcal{Z}_+$ as $k \to \infty$. 77

4.2 The ratio $\mathcal{M}(\Lambda)/\Lambda$ as a function of n, calculated using Eq. (4.24). The ratio approaches unity as $n \to \infty$. 80

4.3 Processes contributing to the production of spin–$1/2$ HECO particle-antiparticle ($\mathcal{H}\overline{\mathcal{H}}$) pairs at hadron colliders: Drell-Yan via γ exchange; Drell-Yan including γ/Z^0 exchange; and photon-fusion processes. 82

4.4 Comparison of cross section values obtained after (solid line) and before (dashed-line) resummation as a function of the HECO mass M. 94

4.5 Cross section values for spin-$1/2$ HECO pair production via DY (top) and PF (bottom) after resummation as a function of mass M for various charge values. 95

4.6 Cross section values for spin-1/2 HECO pair production via DY (top) and PF (bottom) after resummation as a function of charge Q for different cutoff Λ values. 96
4.7 Cross section values for spin-1/2 HECO pair production via DY (top) and PF (bottom) after resummation as a function of the cutoff Λ for various Q. 97
4.8 Comparison of cross section values obtained after (solid line) and before (dashed line) resummation as a function of the scalar HECO mass M 111
4.9 Scalar HECO pair production cross section at $\sqrt{s} = 13$ TeV as a function of mass M for various charge values. 112
4.10 Scalar HECO pair production cross section at $\sqrt{s} = 13$ TeV as a function of charge Q for different cutoff Λ values. 113
4.11 Scalar HECO pair production cross section at $\sqrt{s} = 13$ TeV as a function of the cutoff Λ for different Q. 114
4.12 Excluded lower mass limits for spin-0 HECOs at $\sqrt{s} = 13$ TeV at leading order (dashed lines) and re-calculated with resummation (solid lines). 119
4.13 Excluded lower mass limits for spin-1/2 HECOs at $\sqrt{s} = 13$ TeV at leading order (dashed lines) and re-calculated with resummation (solid lines). 120

5.1 Monopole contribution to light-by-light scattering. 124
5.2 Exclusion lower mass limits for spin-0, spin-1/2 and spin-1 MMs as a function of Q in Dirac charge g_D units. 130

6.1 Leading diagrams of production in e^+e^- collisions for a) HV, and b) SM light quarks including bottom. 144
6.2 3D plots of the two-particle angular correlation function in the thrust frame, $C^{(2)}(\Delta y, \Delta\phi)$, at detector level, separately for the pure HV signal and the SM background in e^+e^- collisions at $\sqrt{s} = 250$ GeV. 147

6.3 Yield $Y(\Delta\phi)$ for both HV signal *combined* with SM and for pure SM background (red line) for the $0 < |\Delta y| < 1.6$ (left) and $1.6 < |\Delta y| < 5$ (right) intervals. 148
6.4 Expected sensitivity for HV models alongside the SM background after collecting 100 fb^{-1} of integrated luminosity. . . 151

8.1 Comparació entre les seccions eficaces abans i després de la ressumació per a HECOs d'espín 0 i 1/2 en els processos Drell–Yan i fusió de fotons a $\sqrt{s} = 13$ TeV. 173
8.2 Comparació dels límits inferiors d'exclusió per a HECOs d'espín 0 i 1/2 a $\sqrt{s} = 13$ TeV, destacant els efectes de la ressumació en els processos DY i PF. 174
8.3 Límits inferiors d'exclusió per a la massa dels monopols magnètics en funció de la càrrega en unitats de g_D. 175
8.4 Distribució del rendiment angular $Y(\Delta\phi)$ després de talls de selecció per a $0 < |\Delta y| \leq 1.6$. El pic a $\Delta\phi \sim \pi$ suggereix la presència d'un sector ocult. 177

A.1 One-loop self-energy diagrams for the photon and the scalar field. 180
A.2 One-loop corrections to the scalar self-coupling. 180

List of Tables

4.1 Cross section comparison for HECO production in pp collisions at $\sqrt{s} = 13$ TeV via the Drell-Yan ($\gamma-$only) process between tree level and after resummation with $\Lambda = 2$ TeV. The HECO mass is also listed. The `NNPDF23` PDF is used. . 91

4.2 Cross section comparison for HECO production in pp collisions at $\sqrt{s} = 13$ TeV via the Drell-Yan (including Z^0) process at tree level and after resummation with $\Lambda = 2$ TeV. The HECO mass is also listed. The `NNPDF23` PDF is used. . 91

4.3 Cross section comparison for HECO production in pp collisions at $\sqrt{s} = 13$ TeV via the PF process at tree level and after resummation with $\Lambda = 2$ TeV. The HECO mass is also listed. The PDF `LUXqed17` is used. 92

4.4 Cross section comparison for scalar HECO production in pp collisions at $\sqrt{s} = 13$ TeV via the Drell-Yan process between tree level and after resummation with $\Lambda = 2$ TeV. 110

4.5 Cross section comparison for scalar HECO production in pp collisions at $\sqrt{s} = 13$ TeV via Photon-Fusion process between tree level and after resummation with $\Lambda = 2$ TeV. 110

4.6 95% CL experimental mass limits for spin-0 HECOs with (RES) and without (LO) resummation techniques to calculate production cross sections. Reported bounds are not necessarily extracted from the same dataset size. 116

4.7 95% CL experimental mass limits for spin-1/2 HECOs with (RES) and without (LO) resummation techniques to calculate production cross sections. Reported bounds are not necessarily extracted from the same dataset size. 117

6.1 Inclusive cross sections for $e^+e^- \to D_v\bar{D}_v$, $e^+e^- \to q\bar{q}$ and $WW \to 4q$ processes at $\sqrt{s} = 250$ GeV, with different assignments for the m_{D_v} and m_{q_v} masses. 145

6.2 Breakdown of efficiencies of the selection criteria described in the main text. For simplicity, only one HV model is shown, since results are very similar for the rest: $e^+e^- \to D_v\bar{D}_v$ with $m_{D_v} = 125$ GeV and $m_{q_v} = 100$ GeV. The two SM processes described in the text and in Table 6.1 are also shown. . . . 146

6.3 Inclusive cross sections of the HV signal and SM background at $\sqrt{s} = 500$ GeV and $\sqrt{s} = 1$ TeV. 153

B.1 Cross section of spin-1/2 HECO production of mass $M = 1$ TeV via the DY $u\bar{u} \to \mathcal{H}\overline{\mathcal{H}}$ process at $\sqrt{s} = 13$ TeV obtained with MadGraph and with theoretical calculations at tree level. The simulation/theory ratio is also listed. . . . 188

B.2 Cross section of spin-1/2 HECO production of mass $M = 1$ TeV via the PF $\gamma\gamma \to \mathcal{H}\overline{\mathcal{H}}$ process at $\sqrt{s} = 13$ TeV obtained with MadGraph and with theoretical calculations at tree level. The simulation/theory ratio is also listed. 188

B.3 Cross section of scalar HECO production at tree level via the DY $u\bar{u} \to \mathcal{H}\overline{\mathcal{H}}$ process at $\sqrt{s} = 13$ TeV obtained with MadGraph by importing the related UFO model and with theoretical calculations. The simulation/theory ratio is also listed. 188

B.4 Cross section of spin-0 HECO production at tree level via the PF $\gamma\gamma \to \mathcal{H}\overline{\mathcal{H}}$ process at $\sqrt{s} = 13$ TeV obtained with MadGraph by importing the related UFO model and with theoretical calculations. A HECO mass $M = 1$ TeV is assumed. The simulation/theory ratio is also listed. 189

B.5 Cross section of spin-1/2 HECO production via the DY $u\bar{u} \to \mathcal{H}\overline{\mathcal{H}}$ process at $\sqrt{s} = 13$ TeV obtained with MadGraph by importing the relevant UFO models and with theoretical calculations. Resummation with $\Lambda = 2$ TeV is assumed. The simulation/theory ratio is also listed. 189
B.6 Cross section of spin-1/2 HECO production via the PF $\gamma\gamma \to \mathcal{H}\overline{\mathcal{H}}$ process at $\sqrt{s} = 13$ TeV obtained with MadGraph by importing the relevant UFO models and with theoretical calculations. Resummation with $\Lambda = 2$ TeV is assumed. The simulation/theory ratio is also listed. 190
B.7 Cross section of spin-0 HECO production via the DY $u\bar{u} \to \mathcal{H}\overline{\mathcal{H}}$ process at $\sqrt{s} = 13$ TeV obtained with MadGraph by importing the related UFO model and with theoretical calculations. Resummation with $\Lambda = 2$ TeV is assumed. The simulation/theory ratio is also listed. No PDF is considered. 190
B.8 Cross section of spin-0 HECO production via the PF $\gamma\gamma \to \mathcal{H}\overline{\mathcal{H}}$ process at $\sqrt{s} = 13$ TeV obtained with MadGraph by importing the related UFO model and with theoretical calculations. Resummation with $\Lambda = 2$ TeV is assumed. The simulation/theory ratio is also listed. No PDF has been used. 191

Chapter 1

The Standard Model and Beyond

The SM of particle physics is our foundational framework for understanding the fundamental interactions among elementary particles. It describes how these constituents interact through gauge fields, mediated by force-carrying particles known as bosons. In nature, four fundamental interactions exist: weak, electromagnetic (EM), strong, and gravitational. The latter, however, is not accounted for within the SM.

Elementary fermions are divided into leptons and quarks. Leptons interact via the EM force (if electrically charged) and the weak force, whereas quarks participate in EM, weak and strong interactions [1]. The interplay between EM and weak forces is elegantly described by the Glashow-Weinberg-Salam theory [2–4], formulated in the 1960s, which unified these interactions into what is known as the electroweak theory.

The strong interaction, which is described by QCD, is responsible for binding quarks together to form hadrons, such as protons and neutrons. QCD describes the unique properties of the strong force, such as *colour confinement*, which ensures that quarks are never found in isolation, but always in bound states. Moreover, unlike other forces, the strong interaction grows stronger as the distance between quarks increases. More details are provided in Section 1.1.

The SM has undergone extensive experimental testing and has emerged as an exceptionally successful theory for describing elementary particles. It is grounded in fundamental principles like Lorentz invariance and unitarity, and it incorporates renormalizability and specific particle content—all of which are supported by experimental evidence, as described in Section 1.1.2.

Despite its success, the SM does not provide a complete description of all observed phenomena, suggesting the need for an extension into what is known as BSM physics, which will be discussed in Section 1.2. The SM faces both theoretical challenges — there are hints that it may be a low-energy approximation of a more fundamental theory — and experimental challenges, such as phenomena that remain unverified or unexplained (e.g., dark matter, neutrino masses, or the matter–antimatter asymmetry) [5].

1.1 The Standard Model of particle physics

The SM relies on a local gauge symmetry represented by the group structure $\mathrm{SU}(3)_C \times \mathrm{SU}(2)_L \times \mathrm{U}(1)_Y$. The $\mathrm{SU}(3)_C$ group is associated with QCD, governing the strong force [6, 7], while the electroweak sector is defined by the $\mathrm{SU}(2)_L \times \mathrm{U}(1)_Y$ symmetry [2–4]. The strong, weak and EM interactions within the SM arise from the exchange of spin-one gauge bosons among spin-half matter particles.

The $\mathrm{SU}(3)_C$ group, associated with colour charge, has eight massless gauge bosons called *gluons* (G^α_μ), which mediate the strong interaction. Particles that interact with gluons are referred to as "coloured" and participate in strong interactions.

The $\mathrm{SU}(2)_L$ group contributes with three gauge bosons, W^a_μ, while the $\mathrm{U}(1)_Y$ factor provides a single gauge boson, B_μ. The subscript L indicates that only left-handed fermions couple to the $\mathrm{SU}(2)_L$ group, and Y denotes the weak hypercharge. The four spin-one fields of the $\mathrm{SU}(2)_L \times \mathrm{U}(1)_Y$ symmetry mix to produce the physical gauge bosons $W^\pm$, Z^0 and the photon (γ), which mediate the weak ($W^\pm$, Z^0) and EM (γ) interactions.

In addition to spin-one particles, the SM includes fundamental spin-half fermions and a single spin-zero particle, the Higgs boson. The fermions are organised into three generations that share identical gauge interactions, but differ in mass due to their distinct Yukawa couplings to the Higgs field. Leptons are defined as spin-half particles that do not participate in the strong interactions. The six known leptons—e, μ, τ, ν_e, ν_μ, and ν_τ—are categorised as charged leptons (e, μ, τ) — with e and μ denoted by ℓ — and neutrinos (ν_e, ν_μ, ν_τ), collectively denoted by ν. On the other hand, quarks are particles that participate in strong interactions. The hadron spectrum can be understood as bound states of the six known quarks: u, d, s, c, b and t, collectively denoted by q [5].

1.1.1 The SM Lagrangian and Particle Content

The Lagrangian describing the kinetic terms and self-interactions of the gauge bosons is given by:

$$\mathcal{L}_{\text{gauge}} = -\frac{1}{4} G^A_{\mu\nu} G^{\mu\nu}_A - \frac{1}{4} W^a_{\mu\nu} W^{\mu\nu}_a - \frac{1}{4} B_{\mu\nu} B^{\mu\nu}, \tag{1.1}$$

where:

- $G^A_{\mu\nu}$ is the field strength tensor for the gluon fields associated with the $\mathrm{SU}(3)_C$ group;
- $W^a_{\mu\nu}$ is the field strength tensor for the weak boson fields associated with the $\mathrm{SU}(2)_L$ group; and
- $B_{\mu\nu}$ is the field strength tensor for the hypercharge gauge field associated with the $\mathrm{U}(1)_Y$ group.

These terms represent the dynamics and self-interactions of the gauge bosons in the SM. The fermionic matter content of the SM is organised according to their quantum numbers under the gauge group $SU(3)_C \times SU(2)_L \times U(1)_Y$, where:

- $SU(3)_C$ corresponds to the strong interaction (colour charge). Fermions can be in triplet (3) or singlet (1) representations, indicating whether they interact via the strong force.

- $SU(2)_L$ corresponds to the weak interaction. Fermions transform either as doublets (2) or singlets (1) under this group, with doublets interacting via the weak force.

- $U(1)_Y$ is associated with the hypercharge Y, which determines the electric charge Q of the particle through the relation $Q = T_3 + \frac{Y}{2}$, where T_3 is the third component of weak isospin.

The fermionic matter content in the SM can be categorised based on their representations under the gauge group $SU(3)_C \times SU(2)_L \times U(1)_Y$. The fields are organised as follows:

- **Left-handed quark doublets:**

$$Q_L^i = \left\{ \begin{pmatrix} u_L \\ d_L \end{pmatrix}, \begin{pmatrix} c_L \\ s_L \end{pmatrix}, \begin{pmatrix} t_L \\ b_L \end{pmatrix} \right\}, \quad \left(\mathbf{3}, \mathbf{2}, \frac{1}{6}\right) \tag{1.2}$$

  These are weak isospin doublets (2) under $SU(2)_L$, transforming as triplets (3) under $SU(3)_C$, and have hypercharge $Y = \frac{1}{6}$.

- **Right-handed up-type quark singlets:**

$$u_R^i = \{u_R, c_R, t_R\}, \quad \left(\bar{\mathbf{3}}, \mathbf{1}, \frac{2}{3}\right) \tag{1.3}$$

  These are singlets (1) under $SU(2)_L$, anti-triplets ($\bar{3}$) under $SU(3)_C$, with hypercharge $Y = \frac{2}{3}$.

- **Right-handed down-type quark singlets:**

$$d_R^i = \{d_R, s_R, b_R\} \quad \left(\bar{\mathbf{3}}, \mathbf{1}, -\frac{1}{3}\right) \tag{1.4}$$

  Similar to the up-type quarks, these also transform as singlets under $SU(2)_L$ and anti-triplets under $SU(3)_C$ but have hypercharge $Y = -\frac{1}{3}$.

- **Lepton doublets:**

$$L_L^i = \left\{ \begin{pmatrix} \nu_L \\ e_L \end{pmatrix}, \begin{pmatrix} \nu_\mu \\ \mu_L \end{pmatrix}, \begin{pmatrix} \nu_\tau \\ \tau_L \end{pmatrix} \right\}, \quad \left(\mathbf{1}, \mathbf{2}, -\frac{1}{2}\right) \tag{1.5}$$

Lepton doublets are singlets under $SU(3)_C$, weak isospin doublets under $SU(2)_L$ and have hypercharge $Y = -\frac{1}{2}$.

- **Right-handed charged leptons:**

$$e_R^i = \{e_R, \mu_R, \tau_R\}, \quad (\mathbf{1},\ \mathbf{1}, -1) \tag{1.6}$$

The right-handed charged leptons are singlets under both $SU(2)_L$ and $SU(3)_C$ with hypercharge $Y = -1$.

The Lagrangian for fermions can be expressed as the sum of two components:

$$\mathcal{L}_F = \mathcal{L}^F_{\text{kinetic}} + \mathcal{L}^F_{\text{Yukawa}}, \tag{1.7}$$

where the kinetic term for the fermions takes the form:

$$\mathcal{L}^F_{\text{kinetic}} = i\overline{L}^i_L \gamma^\mu D_\mu L^i_L + i\overline{Q}^i_L \gamma^\mu D_\mu Q^i_L + i\overline{e}^i_R D_\mu e^i_R + i\overline{u}^i_R D_\mu u^i_R + i\overline{d}^i_R D_\mu d^i_R. \tag{1.8}$$

The covariant derivative is defined as:

$$D_\mu = \partial_\mu - ig_s G^A_\mu T^A - igW^a_\mu T^a - ig' Y B_\mu. \tag{1.9}$$

The Yukawa couplings are given by:

$$\mathcal{L}^F_{\text{Yukawa}} = -y^d_{ij}\overline{Q}^i_L H d^j_R - y^u_{ij}\overline{Q}^i_L \tilde{H} u^j_R + y^e_{ij}\overline{L}^i_L H e^j_R + \text{h.c.} \tag{1.10}$$

Here, *h.c.* denotes the Hermitian conjugate of the preceding terms. For example, the Hermitian conjugate of $y^d_{ij}\overline{Q}^i_L H d^j_R$ is $(y^d_{ij}\overline{Q}^i_L H d^j_R)^\dagger$, which involves taking the complex conjugate and transposing the term.

The Higgs field is represented as a complex scalar doublet:

$$H = \begin{pmatrix} H^+ \\ H^0 \end{pmatrix}, \quad \left(\mathbf{1}, \mathbf{2}, \frac{1}{2}\right) \tag{1.11}$$

with its corresponding Lagrangian given by:

$$\mathcal{L}_{\text{Higgs}} = D_\mu H (D^\mu H)^\dagger + V(H), \quad V(H) = m^2|H|^2 - \lambda|H|^4. \tag{1.12}$$

Thus, the complete SM Lagrangian can be writtene as

$$\mathcal{L}_{\text{SM}} = \mathcal{L}_{\text{gauge}} + \mathcal{L}^{F}_{\text{kinetic}} + \mathcal{L}^{F}_{\text{Yukawa}} + \mathcal{L}_{\text{Higgs}}. \tag{1.13}$$

This Lagrangian describes the dynamics of the gauge bosons, fermions and the Higgs field, encapsulating the interactions and mass generation mechanisms of the SM [8].

1.1.2 Achievements of the Standard Model

Many experimental results have confirmed the validity of the SM. One of its major achievements was the unification of EM and weak interactions into the electroweak theory, which led to the prediction and subsequent discovery of the $W^{\pm}$ and Z bosons at CERN in the 1980s [4, 9, 10]. These discoveries were crucial in establishing the SM as the correct theory of electroweak interactions. Precision measurements at the Large Electron-Positron Collider (LEP) further confirmed the properties of the Z boson, with results consistent with electroweak theory predictions [11]. Additionally, experiments such as those at the Tevatron and LHC have continued to provide crucial experimental confirmation of the SM.

The discovery of the *top quark* at Fermilab in 1995 by the CDF and D0 collaborations [12, 13] was another major success. This quark, the heaviest elementary particle observed so far, has a mass that aligns with theoretical predictions derived from electroweak radiative corrections. Its detection completed the third generation of quarks, confirming the quark structure of matter and reinforcing the SM as a robust theory of fundamental particles and interactions. Due to its large Yukawa coupling to the Higgs field, the top quark plays a key role in electroweak symmetry breaking and contributions to precision electroweak tests have since been essential for further experimental confirmations of the SM.

The discovery of the Higgs boson at CERN's LHC by the ATLAS and CMS collaborations in 2012 [14, 15], represented a crucial moment in particle physics, providing direct evidence for the mechanism of electroweak symmetry breaking within the SM. The existence of the Higgs boson had been theoretically predicted to explain how elementary particles acquire mass through interactions with the Higgs field [9, 16], but its detection had eluded experimental efforts for nearly five decades. The ATLAS [17] and CMS [18] collaborations observed a new particle with a mass ∼125 GeV, consistent with the properties expected of the SM Higgs boson. This discovery confirmed the last missing component of the SM and established the theoretical framework for describing fundamental interactions. In recognition of this profound contribution to physics, François Englert and Peter Higgs were awarded the Nobel Prize in Physics in 2013 [19].

1.2 Beyond the Standard Model

As mentioned, the SM of particle physics has been incredibly successful in explaining a wide range of experimental phenomena and making accurate predictions for particle interactions. However, despite its triumphs, the SM is incomplete. Several experimental observations and theoretical inconsistencies indicate the need for new physics BSM.

1.2.1 Observational Evidence for BSM Physics

- **Neutrino Masses and Mixings** In the SM, neutrinos are massless. However, experiments such as those studying neutrino oscillations have clearly demonstrated that neutrinos have small, non-zero masses and can change flavors as they propagate [20–24]. These phenomena are not explained by the SM. The lack of a neutrino mass term in the SM Lagrangian implies that NP is required [25]. Among the various scenarios for neutrino mass generation that continue to hold relevance today, the seesaw mechanism is among the most popular frameworks for model building. Various forms of the see-saw mechanism have been proposed, including Type I [26–28], Type II [29, 30], and Type III [31]. These mechanisms extend the SM by introducing different particles: the Type I see-saw introduces singlet right-handed neutrinos N_R, the Type II see-saw involves an $SU(2)_L$ scalar triplet Δ and the Type III see-saw incorporates an $SU(2)_L$ fermionic triplet. For comprehensive reviews on neutrino physics, see Refs. [32, 33]

- **Dark Matter** Since the 1930s, evidence from various scales has revealed the existence of an additional component of matter that interacts only gravitationally, without engaging through other forces. Like neutrinos, this matter does not carry EM charge and is referred to as *dark matter*. It constitutes about 25% of the universe's content, with observations from galaxy rotation curves [34], gravitational lensing [35] and the cosmic microwave background (CMB) [36] pointing to the presence of a cold, non-baryonic, neutral and massive form of matter. The SM does not account for dark matter, as neutrinos are too light to explain cold dark matter. To address this gap, theorists have proposed several dark matter candidates, ranging from weakly interacting massive particles (WIMPs) [37] and axions [38] to sterile neutrinos [39] and even primordial black holes [40–44]. Despite decades of experimental searches, these candidates have yet to be detected directly. Nonetheless, ongoing efforts have significantly constrained the parameter space for these particles, narrowing the field of possibilities [45]. The quest to uncover the nature and origin of dark matter remains a high-priority challenge in cosmology and particle physics.

- **Dark Energy** In addition to dark matter, observations of the universe's accelerated expansion indicate the existence of another unknown component, referred to as *dark energy*. This phenomenon was first inferred from measurements of distant Type Ia supernovae [46, 47] and has since been confirmed through observations of the CMB [36] and large-scale structure [48]. Dark energy constitutes approximately 70% of the total energy density of the universe and is believed to drive its accelerated expansion. Within the framework of general relativity, dark energy can be described by a cosmological constant Λ, representing a uniform energy density with a negative pressure [49]. However, the observed small value of Λ compared to theoretical expectations has led to the so-called *cosmological constant problem* [50], which will be discussed in more detail in the next section. Alternative models have been proposed to explain dark energy, including dynamic scalar fields such as quintessence [51, 52] and modifications of gravity [53, 54]. Despite significant progress in observations and theory, the true nature of dark energy remains elusive and represents one of the most profound challenges in modern physics and cosmology.

- **Inflation and Density Perturbations** The large-scale structure of the universe, as observed today, is consistent with the presence of scale-invariant, Gaussian and apparently acausal density perturbations. These perturbations, which serve as the seeds for the formation of galaxies and large-scale structures, likely arose during a period of rapid expansion known as cosmic inflation. This inflationary epoch is believed to have occurred in the very early universe, approximately 10^{-36} to 10^{-32} seconds after the Big Bang and is characterised by an exponential expansion that smoothed out any initial inhomogeneities, leading to the uniformity observed in the CMB radiation today [55, 56]. Theories of cosmic inflation predict that quantum fluctuations during this rapid expansion would produce the observed density perturbations, which can be described by a nearly scale-invariant power spectrum. This power spectrum aligns well with the measurements from the CMB [36], confirming the inflationary model's validity.

However, the SM of particle physics does not contain a mechanism for inflation or for generating these perturbations, highlighting the need for NP. To explain the origin of these early-universe features, various BSM frameworks have been proposed. Central to many of these models is the introduction of new fields, such as the inflaton—a hypothetical scalar field responsible for driving inflation [57].

- **Matter-Antimatter Asymmetry** One of the biggest mysteries in cosmology is the observed predominance of matter over antimatter in the universe, a phenomenon known as *baryon asymmetry*. This asymmetry is crucial for the formation of the structures we observe today, including galaxies and stars. The SM of particle physics permits some violation of charge-parity (CP) symmetry, which is necessary for explaining this asymmetry. However, the amount of CP violation predicted by the SM is insufficient to account for the observed abundance of matter compared to antimatter [58].

  To reconcile this discrepancy, additional sources of CP violation are required, potentially arising from new BSM particles or interactions. Various mechanisms have been proposed to generate the observed baryon asymmetry, among which *leptogenesis* and *baryogenesis* are often proposed. Leptogenesis suggests that an asymmetry in lepton number can lead to a baryon asymmetry through sphaleron processes, which are non-perturbative interactions that can convert lepton number into baryon number [59]. On the other hand, baryogenesis mechanisms directly generate a baryon asymmetry during the early universe's evolution [60]. Both leptogenesis and baryogenesis require physics BSM, highlighting the necessity of extending our current theoretical frameworks to fully understand the origins of the universe's matter-antimatter imbalance.

1.2.2 Theoretical Puzzles Motivating BSM Physics

In addition to observational evidences, several theoretical inconsistencies within the SM suggest the need for NP. These theoretical challenges include:

- **The Hierarchy Problem:** A major unresolved issue in particle physics is the hierarchy problem, which refers to the vast difference between the weak scale ($\sim$ 100 GeV) and the Planck scale ($\sim 10^{19}$ GeV) [61, 62]. The Higgs boson mass is extremely sensitive to quantum corrections from higher energy scales, which should drive it up to the Planck scale. However, the observed Higgs mass ($\sim$ 125 GeV [63]) is much smaller [14, 15]. This raises the question of why the weak scale is so much lower than the Planck scale, a discrepancy of many orders of magnitude. Solutions to this problem include new symmetries, such as supersymmetry (SUSY) [64, 65] or extra dimensions [66, 67], both discussed below, that could protect the Higgs mass from large quantum corrections.

- **Strong CP problem:** The strong CP problem, arising from the potential violation of CP symmetry in QCD, is another significant question within the SM. This framework allows for a CP-violating term in the QCD Lagrangian, parametrised by the angle θ. Experimentally, however, CP violation in strong interactions is extremely small, with the neutron electric dipole moment providing an upper limit on the value of θ at around 10^{-10} [68]. This discrepancy remains unexplained within the SM. One solution to this problem is the introduction of a hypothetical particle called the *axion*, which arises naturally from the Peccei-Quinn mechanism [69–72]. The axion dynamically cancels the θ term, thus providing a natural resolution to the strong CP problem.

- **Cosmological Constant Problem:** Another challenge lies in the Cosmological Constant Problem. Quantum field theory predicts that the energy density of the vacuum should be enormous—many orders of magnitude larger than what is observed through the cosmological constant in Einstein's equations. Observationally, the cosmological constant (or vacuum energy density) is extremely small, leading to a discrepancy of 120 orders of magnitude between theoretical expectations and experimental reality [49, 73, 74]. This mismatch is one of the greatest fine-tuning problems in theoretical physics, and it remains a driving motivation for new physics BSM. Proposed solutions often involve new symmetries, extra dimensions or modifications of gravity to address this problem, though no conclusive solution has been found [75, 76].

- **Quantisation of Electric Charge:** In the SM, the electric charges of particles are quantised in integer multiples of a fundamental unit (e.g., 1/3 for quarks, 1 for electrons). However, the SM does not provide an explanation for this quantisation. The existence of magnetic monopoles in certain BSM frameworks could offer a solution to this puzzle through a mechanism known as the Dirac quantisation condition. This concept will be explored further in Chapter 5.

- **The Fermion Mass Hierarchy:** The masses and mixing angles of the SM fermions exhibit a hierarchical structure, with no apparent explanation within the SM. The masses of these particles span many orders of magnitude, from the electron (0.511 MeV [63]) to the top quark ($\sim$ 173 GeV [63]). In the SM, these masses and mixing parameters are free parameters, set by Yukawa couplings to the Higgs field. The origin of this hierarchy is unknown and addressing it may require new symmetries or BSM dynamics.

- **Number of Fermion Families:** The SM contains three generations of fermions, but it offers no explanation for why there are exactly three. The existence of additional generations or a deeper reason behind this structure remain open questions in particle physics.

- **Inclusion of gravity:** Another limitation of the SM is its inability to incorporate gravity, which remains fundamentally described by General Relativity [3]. This absence leads to a disconnect between the descriptions of quantum field theories governing the EM, weak and strong forces, and the classical framework that describes gravitational interactions. The quest for a quantum theory of gravity, such as string theory [77, 78] or loop quantum gravity [79], seeks to unify these disparate frameworks.

1.2.3 Frameworks for New Physics

In what follows, some of the most well-known theoretical frameworks to address these open questions of the SM will be explored.

1.2.3.1 Effective Field Theories

Effective Field Theories (EFTs) provide a systematic framework for describing physical phenomena at a given energy scale. The essential idea behind EFTs is to separate the degrees of freedom associated with low-energy processes from those of high-energy processes. By *integrating out* the high-energy degrees of freedom, EFTs allow to make predictions for low-energy observables using a well-defined expansion in terms of higher-dimensional operators [80].

In the context of the SM, the *Standard Model Effective Field Theory* (SMEFT) extends the SM by introducing a series of higher-dimensional operators that are suppressed by powers of an energy scale Λ, which represents the scale of NP [81]. These higher-dimensional operators respect the gauge symmetries of the SM, but account for potential new interactions or particles that manifest at energy scales higher than those directly probed in current experiments, such as the LHC or future high-energy colliders [82].

A general expression for the SMEFT Lagrangian is given by:

$$\mathcal{L}_{\text{SMEFT}} = \mathcal{L}_{\text{SM}} + \sum_i \frac{c_i}{\Lambda^2} O_i + \mathcal{O}\left(\frac{1}{\Lambda^4}\right).$$

Here, $\mathcal{L}_{\text{SM}}$ represents the SM Lagrangian and the sum runs over all possible dimension-six operators O_i, each with a coefficient c_i that reflects the strength of the interaction. These operators are constructed to be gauge-invariant under the SM gauge group $SU(3)_C \times SU(2)_L \times U(1)_Y$ [83]. Examples of such operators include modifications to the Higgs couplings, additional four-fermion interactions and corrections to electroweak precision observables [84].

Since the SMEFT introduces corrections to the SM predictions at high energies, it can be used to search for signs of NP in precision measurements. Deviations from SM predictions can be captured by the higher-dimensional operators, providing indirect evidence of new particles or interactions at energies beyond the reach of current experiments. The framework of EFTs allows for a systematic exploration of new physics BSM, introducing higher-dimensional operators suppressed by a new energy scale [80–83].

EFTs also played a historical role in particle physics, with Fermi's theory of weak interactions providing a successful description of beta decay before the discovery of the W boson [85].

1.2.3.2 Supersymmetry (SUSY)

SUSY represents a theoretical extension of the space-time symmetry of quantum field theory. It postulates a fundamental symmetry between fermions and bosons, hypothesising that each particle in the SM is associated with a superpartner differing by half a unit of spin [86]. This theoretical framework has received significant attention due to its potential to address several outstanding issues in the field. One of the primary motivations for SUSY is its capacity to provide a natural solution to the hierarchy problem. SUSY elegantly resolves this issue through the introduction of superpartners, whose contributions to quantum corrections naturally cancel the quadratic divergences, thereby stabilizing the Higgs mass [87]. Moreover, SUSY offers a framework for the unification of fundamental forces. In the context of renormalization group (RG) evolution, SUSY models facilitate the convergence of gauge coupling constants at high energies, a prerequisite for Grand Unified Theories [88]. Another notable aspect of SUSY is its potential to provide a candidate for dark matter. Many SUSY models incorporate R-parity conservation, which implies the stability of the Lightest Supersymmetric Particle (LSP). If the LSP is electrically neutral and only weakly interacting, it becomes a promising candidate for cold dark matter, addressing one of the most significant open questions in cosmology [89]. Despite its theoretical appeal, high-energy collider experiments, particularly those conducted at the LHC, have yet to observe any supersymmetric particles. These null results have imposed increasingly stringent constraints on the parameter space of SUSY models, necessitating ongoing refinement of theoretical predictions and experimental search strategies [90–96].

1.2.3.3 Grand Unified Theories (GUTs)

GUTs represent a class of models that aim to unify three of the four fundamental forces: the strong nuclear force, the weak nuclear force and electromagnetism [97]. These theories proposed that at extremely high energies, typically around 10^{16} GeV, these three forces merge into a single, fundamental interaction governed by a larger gauge symmetry group [98].

There are several motivations for GUTs. Firstly, they offer the possibility of simplifying the SM by reducing the number of fundamental forces, a goal that aligns with the historical trend of unification in physics [97]. Secondly, GUTs provide an elegant explanation for charge quantisation, addressing a long-standing puzzle in particle physics [99]. Another intriguing aspect of GUTs is their prediction of proton decay, although this phenomenon has not yet been observed experimentally [100]. Furthermore, some GUT models offer potential resolutions to the hierarchy problem [88]. An additional fascinating prediction of GUTs is the existence of magnetic monopoles, as independently proposed by 't Hooft and Polyakov [101, 102].

The landscape of GUT models is rich and diverse, with each proposal offering unique insights and challenges. One of the earliest and most influential GUT models is the Georgi-Glashow model, based on the $SU(5)$ gauge group [97]. This model successfully unifies the SM $U(1)$, $SU(2)$ and $SU(3)$ gauge groups into a single $SU(5)$ group. However, it faces significant challenges, particularly its prediction of rapid proton decay, which conflicts with current experimental bounds [103].

Building upon the foundation laid by the $SU(5)$ model, more sophisticated GUT frameworks have been developed. The $SO(10)$ models have been promising due to their ability to accommodate right-handed neutrinos naturally, providing a framework for understanding neutrino masses [104]. This feature is particularly appealing in light of the experimental confirmation of neutrino oscillations [105]. Another interesting class of GUTs are the $E6$ models, which have connections to string theory [106]. These models emerge from certain string theory compactifications and offer a rich phenomenology, including the possibility of exotic particles that could be discovered at high-energy colliders [107].

In response to some of the shortcomings of the original $SU(5)$ theory, variants such as the flipped $SU(5)$ models were developed [108]. These models address issues like the proton decay prediction while keeping many of the attractive features of $SU(5)$ unification.

Despite their theoretical appeal, GUTs face significant challenges that have thus far prevented their confirmation. The primary obstacle is the lack of experimental evidence, particularly the non-observation of proton decay [103]. Additionally, the extreme energy scales involved in these theories make direct testing currently impossible with existing particle accelerators.

Recent developments in GUT research have focused on several promising directions. Supersymmetric extensions of GUTs have been explored as a way to address some of the theoretical and phenomenological challenges. The interplay between GUTs and string theory continues to be a fertile area of research, with the ultimate goal of incorporating gravity and achieving a true *Theory of Everything.*

1.2.3.4 Extra dimensions

Extra dimensions have emerged as a intriguing idea in theoretical physics, particularly in string theory and various models of BSM physics. The notion of additional spatial dimensions beyond the familiar three is motivated by the need to unify the fundamental forces of nature and to provide a framework for addressing some of the open questions in particle physics, such as the hierarchy problem and dark matter. In conventional four-dimensional spacetime, the gravitational force is significantly weaker than the other fundamental forces, leading to the question of why gravity is so relatively weak. One proposed solution involves the existence of extra dimensions, where gravity can propagate. In higher-dimensional theories, the gravitational field can spread out into these additional dimensions, effectively diluting its strength in our observable three-dimensional universe. This idea is often encapsulated in models such as the Randall-Sundrum scenario, which postulates a five-dimensional spacetime with warped geometry [61]. Another prominent framework incorporating extra dimensions is string theory, which posits that fundamental particles are not point-like, but rather one-dimensional "strings." These strings can vibrate in multiple dimensions, leading to a rich variety of particle properties. String theory typically requires at least ten dimensions for mathematical consistency, with six of these dimensions compactified on small scales that are not directly observable at current energy levels [109]. The implications of extra dimensions extend to the search for NP. For example, if extra dimensions exist, they could provide new mechanisms for particle interactions and contribute to phenomena such as the production of Kaluza-Klein (KK) states at colliders. These KK states are higher-mass states arising from the compactification of extra dimensions and their presence could manifest as deviations in particle behaviour from the predictions of the SM [110]. Furthermore, extra dimensions can lead to modifications of gravitational interactions at short distances, potentially providing observable effects in high-energy physics experiments. For instance, experiments at the LHC could probe scenarios where extra dimensions change the cross sections for certain processes, offering a way to test these theories against experimental data [111].

One of the most promising approaches for exploring BSM scenarios is through collider experiments, the general features of which will be discussed in the following chapter.

Chapter 2

Collider Physics

2.1 General Features

Our understanding of sub-nuclear physics primarily stems from the analysis of outcomes resulting from high-energy collisions of elementary particles [112]. A collider is a facility that enables such collisions by requiring one or more particle accelerators to increase the kinetic energy of charged particles before bringing them into collision. To achieve this, particle accelerators meticulously employ a combination of electric and magnetic fields, generating tightly focused beams of energetic particles—commonly electrons, protons and their antiparticles [113].

There are two primary types of experiments conducted in colliders. In a *fixed-target* experiment, a beam of particles is directed at a stationary target, resulting in collisions where only a portion of the beam's energy is available in the centre-of-mass frame due to the asymmetry of the system. These experiments, which utilise particle beams rather than colliders, were historically more common due to their simpler setup. However, they are limited by the energy available for the creation of new particles. By contrast, in a *colliding beam* experiment, two beams of particles are brought into motion towards each other, typically with momenta equal in magnitude and opposite in direction. This configuration maximises the energy available for particle production by aligning the laboratory frame with the centre-of-mass frame. The collision occurs at a designated *interaction point*, which is surrounded by particle detectors designed to identify particles produced in the collision and their decay products, and measure their energies and momenta [114]. Although technically more challenging, colliding beam experiments have become the standard for exploring high-energy physics due to their greater potential for discovering new particles. Modern collider experiments gather and analyse large datasets from vast numbers of collisions. The probability of a particular collision outcome, known as *cross section*, provides a link between theoretical predictions and experimental observations [112].

Colliders can be either *linear* or *circular*. Linear colliders, like Stanford Linear Accelerator Center (SLAC), accelerate particles along a straight path, whereas circular colliders, such as the Hadron–Electron Ring Accelerator (HERA) [115], the Tevatron [116], the Large Electron Positron (LEP) [117] collider and the LHC [118], accelerate particles in a ring. In circular colliders, strong dipole magnets — such as those in the LHC — deflect the particle beams, keeping them in a circular orbit. This allows particles to pass through the accelerating electric fields multiple times, gradually gaining energy with each revolution. As a result, circular designs require less powerful electric fields than linear colliders, where particles are accelerated in a single pass. However, one of the main disadvantages of circular colliders is *synchrotron radiation (SR)*, which causes energy loss as particles travel along curved paths. This energy loss is proportional to

$$\left|\frac{dE}{dt}\right| \propto m^{-4} r^{-2}, \tag{2.1}$$

where m is the mass of the particle, and r is the radius of the collider. As a result, this effect is more pronounced for lighter particles, such as electrons and positrons.

For future electron–positron colliders, both linear and circular designs are being considered. Linear proposals include the International Linear Collider (ILC) [119], the Compact Linear Collider (CLIC) [120] and the Cool Copper Collider (C^3) [121]. Circular colliders with large radii, such as the Future Circular Collider-ee [122], are active investigation. To mitigate

SR, larger radii are beneficial, which is one reason why LEP was built with a 27 km circumference, and its tunnel was later repurposed for the LHC [113].

2.1.1 Events, cross sections and luminosity

In a collider experiment, the main focus is on the interactions between beam particles that could result in the production of something remarkable, such as particles predicted in BSM theories or interesting SM particles that enable precision measurements. Each occurrence of such an interaction is referred to as a scattering *event*, or simply an *event*.

The *rate of events*, expressed as the number of events of a particular type per unit time, depends on two main factors:

i) The interactions between individual beam particles.

ii) The properties of the beams themselves, such as the number of particles per beam and their spatial characteristics.

When a particle enters a particular region of space, it interacts with a target particle, potentially resulting in scattering or deflection. These interactions occur via the exchange of force-carrying particles and can result in elastic collisions, where the particles remain intact, or inelastic collisions, where they may fragment or annihilate each other. However, for any interaction to take place, the incident particle must approach within a certain region surrounding the target particle. Thus, every target particle has an effective cross sectional area for interaction, known as the *scattering cross section* (σ), with dimensions of area (or energy^{-2} in natural units). The cross section depends on the properties of the colliding particles, such as their charges and masses.

Let N denote the total number of scattering events, excluding those where no interaction occurs. The *event rate*, directly related to the probability of interaction, satisfies the equation:

$$\frac{dN}{dt} = \sigma L(t), \tag{2.2}$$

where $L(t)$ is the *instantaneous luminosity*, which depends on the beam parameters and may vary over time. Since N is dimensionless, the luminosity (L) has units of $(\text{area})^{-1}(\text{time})^{-1}$. Increasing the luminosity corresponds to a higher event rate, making it a measure of the "brightness" of the beams. Luminosity is proportional to the number of particles in each beam and inversely proportional to the beam area, aligning with the idea that brighter beams contain more particles or have smaller cross sectional areas.

Using Eq. (2.2), we define the total number of events as:

$$N = \sigma \mathcal{L}, \tag{2.3}$$

where

$$\mathcal{L} = \int_0^T L(t)dt \tag{2.4}$$

is the *integrated luminosity* over a time period T.

Luminosity is conventionally expressed in units of inverse barns (b^{-1}) and prefixes, a unit chosen because it conveniently aligns with cross sections measured in barns and prefixes, simplifying data analysis and interpretation.

The cross section is a single value representing the likelihood of a given process occurring. However, in many cases, we may require more detailed information beyond this simple probability. The differential cross section for an observable $\mathcal{O}$, denoted as

$$\frac{d\sigma_i}{d\mathcal{O}}, \tag{2.5}$$

describes the distribution of $\mathcal{O}$ and can be computed within a theoretical framework to compare with experimental data. Differential cross sections provide insight into the kinematics of particle production, which is crucial for testing theories BSM. Experimental results are often presented in terms of normalised differential cross sections:

$$\frac{1}{\sigma_i}\frac{d\sigma_i}{d\mathcal{O}}, \tag{2.6}$$

which is advantageous because the ratio cancels many experimental and theoretical uncertainties. The total cross section is recovered by integrating over the observable:

$$\int d\mathcal{O} \frac{1}{\sigma_i} \frac{d\sigma_i}{d\mathcal{O}} = 1. \tag{2.7}$$

This normalisation is widely used because it facilitates comparison between different experiments and theoretical predictions [113].

2.2 Detector Measurements and Event Kinematics

Events are recorded by particle detectors, which in colliding beam experiments are typically cylindrical and surround the beam pipe. These detectors are designed to capture the properties of particles produced during collisions, allowing for the reconstruction and analysis of the events. The measurable parameters include the energy of stable particles on detector timescales, identified through deposits in various calorimeters. Typically, the innermost tracking system —constructed with numerous silicon pixels and strips and/or gaseous detectors—captures the momentum of charged particles. This detector reconstructs the paths of charged particles through a distinctive pattern of dots (hits) that can be connected to form a track. By applying a magnetic field, the curvature of each particle's track is used to estimate its momentum. The *electromagnetic calorimeter* (ECAL) is adept at identifying photons and electrons/positrons, while the *hadronic calorimeter* specialises in detecting hadrons by measuring the deposited energy. [113].

Muons exhibit a unique behaviour as they traverse the detector, comparable to tiny cannonballs penetrating through before expending all their energy. Measuring the momentum of muons involves utilising the curvature of their trajectories as they pass through the muon spectrometer. This process necessitates powerful magnetic fields to alter the muons' paths and/or ample space to discern the subtle curvature of their energetic tracks. Track curvature is also exploited in the inner detector to differentiate between charged particles such as electrons, positrons, and pions, aiding in the precise measurement of their momentum. Exceptions to this detection pattern exist, notably with (anti)-neutrinos, which interact so weakly that they pass through the detector without leaving a trace. This results in an imbalance in the sum of the four-momentum of all particles in the transverse plane, the so-called *missing transverse momentum* or *missing transverse energy*. Additionally, the detector may miss particles passing through the beam pipe or slipping through cracks/gaps in its structure [114].

It is customary to adopt a specific coordinate system where the incoming beams are aligned along the $+z$ and $-z$ directions. This choice provides a convenient reference frame for analysis. Within this framework, assuming that the (x, y) plane lies perpendicular to the beam axis, it becomes advantageous to decompose the three-momentum of a particle, denoted as $\mathbf{p} = (p_x, p_y, p_z)$, into two-dimensional momentum transverse to the beam axis:

$$p_T \equiv (p_x, p_y), \qquad |p_T| = \sqrt{p_x^2 + p_y^2}, \tag{2.8}$$

and the longitudinal component p_z. It is convenient to work with variables that have the same values in the laboratory and partonic centre-of-mass frame. Such variables are longitudinally Lorentz *boost invariant*. Since the x and y components of momentum, p_x and p_y, remain invariant under boosts, the transverse momentum p_T also exhibits this boost invariance.

The azimuthal angle

$$\phi \equiv \tan^{-1}\left(\frac{p_x}{p_y}\right) \tag{2.9}$$

is also boost invariant. However, the longitudinal component p_z does undergo changes, as it becomes mixed with the energy E. Therefore, it is advantageous to introduce another variable to replace it. To this end, it is customary to define the *rapidity*

$$y = \frac{1}{2}\ln\left(\frac{E + p_z}{E - p_z}\right). \tag{2.10}$$

The difference of rapidities y_1 and y_2 for two momenta q_1 and q_2 is boost invariant. Therefore, we define the angular separation as follows:

$$\Delta R = \sqrt{(\Delta\phi)^2 + (\Delta y)^2}, \tag{2.11}$$

which is also boost invariant. Rapidity essentially quantifies the degree to which a particle is moving forwards or backwards, with "forwards" indicating proximity to the $+z$ direction. In this context, the $+z$ axis corresponds to infinite rapidity, while a particle produced centrally has a rapidity of zero.

To refine this concept for highly energetic particles, i.e. when $E \gg m$, such that $E \simeq |\mathbf{p}|$, one can express the momentum component as

$$p_z \simeq E\cos\theta, \tag{2.12}$$

where θ represents the angle between the particle's direction and the beam axis. Then we can rewrite Eq. (2.10) as

$$y \simeq \frac{1}{2}\ln\left(\frac{E(1+\cos\theta)}{E(1-\cos\theta)}\right) = \frac{1}{2}\ln\left(\frac{1+\cos\theta}{1-\cos\theta}\right), \tag{2.13}$$

which can be rewritten as

$$\eta = -\ln\tan\left(\frac{\theta}{2}\right), \tag{2.14}$$

where η is called *pseudorapidity*, which is equal to rapidity only for massless particles. Experimentalists often prefer this formulation as it is based on the polar angle θ, which can be precisely measured. Additionally, it provides a more intuitive visualisation of rapidity, reinforcing the notion that higher $|\eta|$ values correspond to particles that are less centrally produced. Thus, there is a simple mapping between rapidity and angle for massless particles. Pseudorapidity is a *geometric* quantity, but for massive particles, differences in pseudorapidities are not boost invariant [113].

2.3 Types of Colliders

Particle colliders are broadly categorised into two main types: *hadronic* and *leptonic*, each with distinct characteristics and capabilities.

Hadron colliders, utilising proton-proton (pp) or proton-antiproton ($p\bar{p}$) collisions, have historically served as discovery machines at the energy frontier: from the Super Proton-Antiproton Synchrotron ($Sp\bar{p}S$) [123] to the Tevatron [116] and now the LHC [118]. As discussed in Section 1.1.2, these machines have played a crucial role in the discovery of massive gauge bosons, the top quark and the Higgs boson. Their ability to reach the highest centre-of-mass (c.o.m.) energies — denoted as $\sqrt{s}$ — rises from reduced energy losses through SR, owing to the larger mass of protons compared to electrons. In addition to pp collisions, hadron colliders also support heavy-ion collisions, such as lead-lead ($PbPb$) or proton-lead (pPb) interactions, enabling the study of strongly interacting matter under extreme conditions. These experiments are crucial for exploring the quark-gluon plasma (QGP), a state of matter that existed shortly after the Big Bang [124]. The LHC, with its heavy-ion programme, has provided unprecedented insights into the properties of the QGP and the dynamics of high-energy nuclear interactions.

Lepton colliders, particularly electron-positron (e^+e^-) machines, offer complementary advantages through their precision measurement capabilities. These colliders benefit from the point-like nature of leptons. The clean experimental environment and precisely known collision energies make them ideal for detailed studies of particle properties and coupling measurements.

An emerging class of lepton colliders involves muon-antimuon ($\mu^+\mu^-$) collisions. These machines combine the precision of lepton colliders with the ability to reach higher c.o.m. energies, thanks to the larger mass of muons, which reduces SR losses [125]. $\mu^+\mu^-$ colliders hold promise for exploring the Higgs sector and potential NP at multi-TeV scales.

The kinematics and analysis of collision events differ significantly between these collider types. In e^+e^- collisions, the c.o.m. frame coincides with the laboratory frame, simplifying reconstruction. For hadron colliders, the interacting partons (quarks and gluons) carry varying fractions of the proton momentum, resulting in a boosted c.o.m. frame along the beam axis. In both cases, the masses of the colliding particles can typically be neglected at high energies, as they are substantially smaller than the operational energy scales of interest [112].

Both leptonic and hadronic collisions are considered within the scope of this thesis. The following sections examine in detail the specific characteristics, technological challenges and physics capabilities of hadronic and leptonic colliders.

2.3.1 e^+e^- colliders

High-energy e^+e^- colliders have played a crucial role as indispensable tools in the quest to uncover the fundamental building blocks of matter and the forces that govern their interactions. Complemented by experimental findings from hadron accelerators, such colliders have contributed to the development of a coherent understanding of matter's structure, encapsulated within the framework of the SM [126].

The discovery of the Higgs boson reinforced the need for a high-energy e^+e^- collider to achieve precision measurements surpassing those of LEP, thereby constituting a *Higgs factory*. In addition to the high priority of Higgs boson studies, a future e^+e^- collider promises a rich physics programme for testing the SM and exploring physics beyond it.

In 2000, the LEP [117] concluded its operations, reaching a maximum centre-of-mass energy of 208 GeV. Further escalation of beam energies proved to be significantly inefficient due to SR effects, which induce an energy loss per turn proportional to $\frac{E^4}{r}$, where r denotes the effective bending radius of the collider.

Extremely large radii are required to run e^+e^- circular colliders at high energies. In addition to power consumption, the tunnel length is a critical cost factor. Linear colliders offer an alternative: with high accelerating gradients, the required energy can be achieved with a more manageable tunnel length. However, luminosity is equally important for physics measurements. In circular colliders, beams can be reused, whereas in linear colliders, the beams are discarded after each collision. To reach high luminosities, very small beam sizes are necessary. Therefore, the choice of future e^+e^- collider projects will depend on the machine's performance, energy range and physics potential [127].

The primary advantages of a linear collider lie in the ability to polarise beams and the potential for future energy upgrades to meet evolving physics requirements. Conversely, circular colliders offer the advantage of accommodating multiple collision points, high luminosities at energies below 250 GeV (such as at the Z pole) and the potential reuse of the same circular tunnel for a proton-proton collider in the future. Currently, the main projects under discussion are: the ILC [119], the CLIC [120], the C^3 [121], the FCC-ee [122] and the CEPC [128]. In what follows, their principal characteristics will be discussed.

The International Linear Collider Proposed to be located in Japan, the ILC [119] represents a proposed state-of-the-art electron-positron collider, commencing operations at $\sqrt{s} = 250$ GeV, primarily serving as a Higgs factory. The precise investigation of the Higgs boson is regarded as a crucial objective in the context of collider physics; the ILC is expected to achieve significant milestones in measuring the couplings of the Higgs boson. These high-precision measurements will guide the choice of energy scales for subsequent facilities. The layout of the proposed ILC is depicted in Fig. 2.1.

Designed to achieve a luminosity of more than $10^{34}\,\mathrm{cm}^{-2}\,\mathrm{s}^{-1}$, the ILC aims to provide an integrated luminosity $\mathcal{L}$ of 400 fb^{-1} during its first four years of operation. The electron beam will be polarised to 80%, while positrons will have a 30% polarisation, contingent upon the implementation of the undulator-based positron source concept.

In addition to its primary mission, the ILC offers a platform for various searches for NP phenomena, including monophoton or invisible and exotic Higgs decays, such as those leading to a light dark sector. The collider is designed to accommodate auxiliary experiments, featuring beam dump systems and/or detectors situated near the interaction point, to investigate

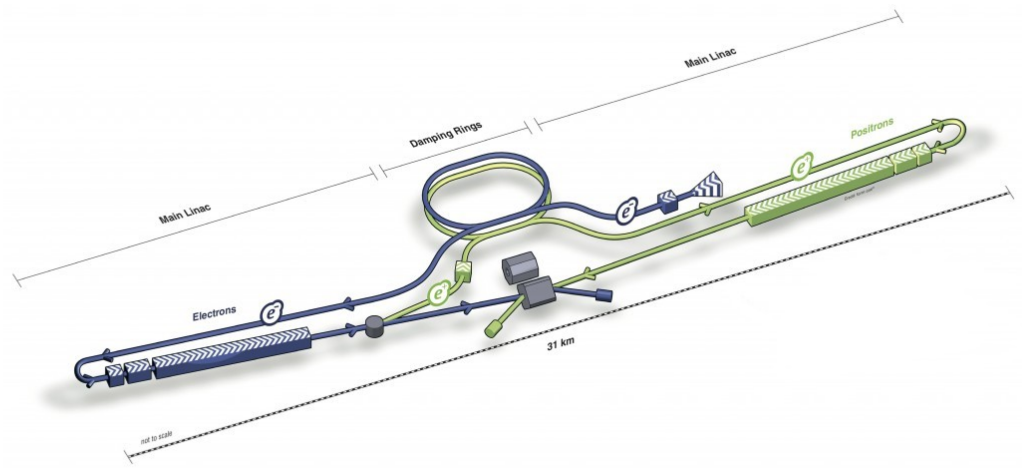

Figure 2.1: A schematic layout of the International Linear Collider. Image credit: ILC Technical Design Report [119].

long-lived and elusive particles.

Its technology is well established, with a comprehensively understood cost structure comparable to that of the LHC. The linear configuration permits the possibility of future phases at both higher and lower energy levels. The ILC can conduct dedicated runs at the Z resonance, significantly enhancing the precision of electroweak observables by an order of magnitude. The facility's design allows for an extension to reach the top quark-antiquark threshold, enabling the production of both $t\bar{t}$ and $t\bar{t}H$ at energy levels of 500–550 GeV.

The chosen location is specifically selected to facilitate upgrades up to 1 TeV, utilising the same technological framework, which will enable precise measurements of Higgs self-coupling alongside numerous searches for NP. Furthermore, superconducting radio-frequency cavity technology possesses substantial potential for improvements, possibly facilitating a collider with energies in the range of 3–4 TeV within the same tunnel. Emerging technologies, such as plasma wakefield and dielectric laser accelerators, have the potential to achieve energy levels in the tens of TeV range [129].

The Compact Linear Collider The Compact Linear Collider (CLIC) [120], proposed to be built at CERN, is a multi-TeV high-luminosity linear electron-positron collider under development by the CLIC accelerator

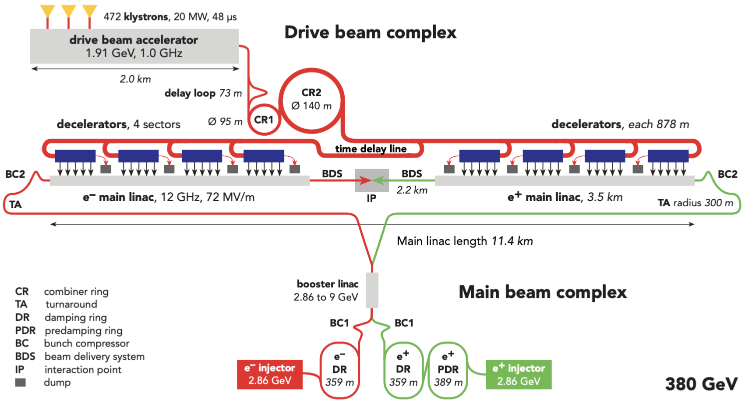

Figure 2.2: Overview of the CLIC layout at $\sqrt{s} = 380$ GeV. Image from Ref. [120].

collaboration. It utilises an innovative two-beam acceleration technique with normal conducting structures operating at 70–100 MV/m.

The Conceptual Design Report (CDR) [120], published in 2012, established the feasibility of CLIC at high energies (3 TeV) and its capability for enablingprecision measurements, despite challenges from luminosity spectrum and background particles.

Following the CDR, extensive studies focused on Higgs and top-quark physics determined that the optimal centre-of-mass energy for the initial energy stage of CLIC is 380 GeV. Consequently, an optimisation study was conducted, evaluating CLIC's performance, costs and energy consumption for 380 GeV and 3 TeV, leading to refined design parameters for a proposed staged operation at 380 GeV, 1.5 TeV and 3 TeV. The layout of the proposed CLIC at $\sqrt{s} = 380$ GeV is illustrated in Fig. 2.2.

CLIC's broad energy range allows for unprecedented precision in studying the properties and interactions of the Higgs boson, top quark and electroweak gauge bosons. The collider could uncover new states inaccessible at other facilities, potentially providing insights into dark matter and significant cosmological questions, such as vacuum stability and baryon asymmetry. Its scientific programme includes precision studies of the SM and searches for prospective NP by aiming at directly producing new states or novel interactions.

Each stage of the CLIC programme is expected to last seven to eight years, with around two years between stages, leading to a total duration of approximately 25 to 30 years. The initial stage at $\sqrt{s} = 380\,\text{GeV}$ focuses on SM Higgs and top-quark physics, including top-quark pair production threshold scans.

The second stage at 1.5 TeV enables additional Higgs production channels, such as $t\bar{t}H$ and double-Higgs production, while the final stage at 3 TeV enhances sensitivity to Higgs self-coupling and BSM physics.

CLIC proposes ±80% electron polarisation, with the initial stage employing equal amounts of -80% and +80% polarisation. For higher-energy stages, an 80:20 ratio between -80% and +80% polarisation is suggested to balance SM and BSM physics goals. The –80% polarisation significantly enhances single and double Higgs production via WW fusion, while the +80% polarisation improves sensitivity to certain BSM effects that may couple preferentially to right-handed electrons [130].

The Cool Copper Collider The Cool Copper Collider (C^3) is a proposed next-generation linear electron-positron collider that seeks to provide a cost-effective and compact alternative to traditional designs [121]. Unlike conventional superconducting technologies, C^3 utilises advanced room-temperature copper radiofrequency cavities, enabling high accelerating gradients of up to 120 MV/m while reducing infrastructure demands and construction costs. This innovative approach significantly shortens the facility footprint and allows for scalable energy upgrades.

C^3 is designed to operate at c.o.m. energies of up to 3 TeV, making it ideal for precision measurements of the Higgs boson and top-quark physics. Additionally, the collider offers unique opportunities to explore BSM scenarios [131]. Its modular design supports incremental energy increases, adapting to the evolving needs of the particle physics community. By combining high precision and a reduced cost structure, the C^3 proposal aims to contribute significantly to advancing high-energy physics research and fostering international collaboration [121].

The Circular Electron Positron Collider The Circular Electron Positron Collider (CEPC) [128] is a large scientific initiative started and hosted by China, developed through extensive collaboration with international partners. This ambitious project comprises four accelerators: a 30 GeV Linac, a 1.1 GeV Damping Ring, a Booster capable of achieving energies up to 180 GeV, and a Collider operating in various energy modes (W, Z, H and $t\bar{t}$). The Linac and Damping Ring are located on the surface, while the Booster and Collider are housed in a $\sim$ 100 km circumference underground tunnel, strategically designed to accommodate future expansions, including provisions for a Super Proton-Proton Collider (SPPC).

The CEPC primarily serves as a Higgs factory. In its baseline design, with a SR power of 30 MW per beam, it can achieve a luminosity of $5 \times 10^{34}\,\mathrm{cm}^{-2}\,\mathrm{s}^{-1}$, resulting in an integrated luminosity of 13 ab^{-1} for two interaction points over a decade, which corresponds to the production of 2.6 million Higgs bosons. By increasing the SR power to 50 MW per beam, the CEPC's capacity for Higgs boson generation expands to 4.3 million, enabling precise measurements of Higgs couplings at sub-percent levels. The construction of the CEPC is expected to take approximately eight years, with experiments projected to begin in the mid-2030s. The facility would play a pivotal role in advancing Higgs boson research and exploring BSM physics, serving as a cornerstone for the future of high-energy physics and international collaboration [132].

Future Circular Collider (FCC-ee) The e^+e^- option of the Future Circular Collider (FCC) — proposed at CERN as shown in Fig. 2.3 — allows operation at several energy levels, including the Z-boson resonance, the WW threshold at 160 GeV, 240 GeV for Higgs boson production via the Higgsstrahlung process and at 350 GeV and 365 GeV for producing top-quark pairs. The technological foundation for the FCC-ee is already established and closely resembles that of the LEP, providing confidence in its feasibility and performance.

One of the key challenges associated with running at energies beyond

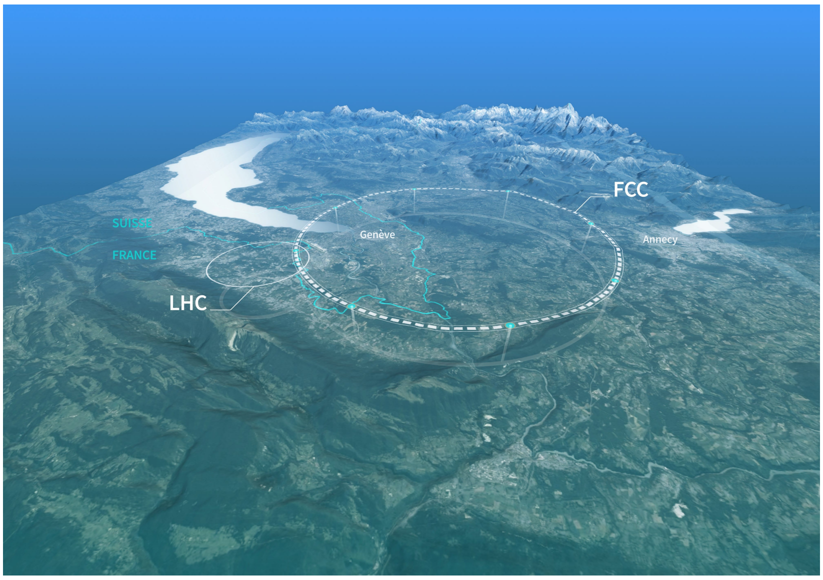

Figure 2.3: A schematic map showing where the Future Circular Collider tunnel is proposed to be located. Image: CERN

300 GeV is the increase in SR, which surpasses the levels experienced at LEP. To maintain power consumption within acceptable limits, the SR power should not exceed 50 MW per beam across the various operating energies. This constraint is critical for ensuring the collider's sustainability and efficiency.

The FCC-ee features a sophisticated double-ring design for the electron and positron beams. This configuration is complemented by a booster synchrotron, which facilitates top-up injection, allowing the beam current and luminosity to be consistently maintained throughout the operational period. While two collision points are planned for initial operations, the design also accommodates the potential for up to four collision points, enhancing its experimental versatility.

The interaction region of the FCC-ee is designed to mitigate SR effects, ensuring cleaner collision events and accurate measurements. The implementation of the innovative "crab-waist" mode significantly enhances luminosity, achieving approximately $1.5 \times 10^{36}\,\mathrm{cm}^{-2}\,\mathrm{s}^{-1}$ at the Z pole, enabling unprecedented precision.

To achieve this, the FCC-ee utilises a large number of bunches per beam and a reduced beam size. Accurate energy calibration, essential for precision measurements, will be performed using resonant depolarisation.

2.3.2 Hadron Colliders

Hadron colliders require particle accelerators in which hadrons, typically protons, are accelerated and brought into collision at high energies. These machines provide a unique environment for probing the fundamental constituents of matter and exploring high-energy physics phenomena BSM.

The most notable existing hadron collider is the LHC at CERN, while future projects such as the Future Circular Collider (FCC-hh) aim to extend the reach of hadron colliders to unprecedented energy scales.

The Large Hadron Collider (LHC) The LHC is currently the world's most powerful particle accelerator, with a circumference of 27 km. Located at CERN, it accelerates protons to nearly the speed of light, achieving collision energies up to 13.6 TeV in its current configuration [118]. Since its commissioning, the LHC has been a critical tool in high-energy physics, particularly due to its high collision luminosity and energy. The collider's most significant achievement to date has been the discovery of the Higgs boson in 2012 by the ATLAS and CMS experiments [14, 15], confirming the mechanism of electroweak symmetry breaking as predicted by the SM.

The LHC is a state-of-the-art facility, employing superconducting magnets cooled to below 2 K to facilitate proton circulation in the collider's beam pipe with minimal energy loss. This sophisticated infrastructure enables the LHC to operate at high luminosity, making it ideal for observing rare processes and testing theories of BSM physics. The ongoing High-Luminosity LHC (HL-LHC) upgrade, scheduled for completion in the early 2030s, is expected to increase the collider's luminosity by a factor of ten, allowing for more precise measurements and access to even rarer physics events [133].

The LHC hosts several major experiments, each designed to explore different aspects of particle physics:

- **ATLAS (A Toroidal LHC ApparatuS)**: A general-purpose detector that employs a sophisticated layered structure to measure a wide

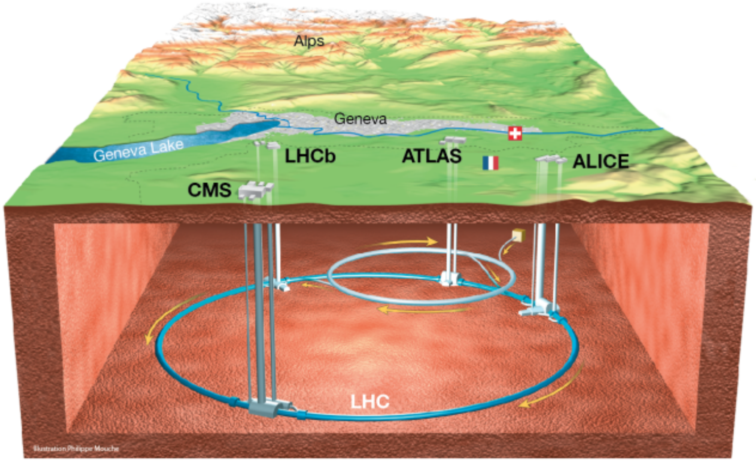

Figure 2.4: A schematic depiction of the LHC. Source: CERN.

range of particle interactions and is particularly adept at searching for BSM phenomena [17].

- **CMS (Compact Muon Solenoid)**: Another general-purpose detector, CMS is known for its robust design and high precision in measuring particles. Like ATLAS, CMS was crucial to the Higgs boson discovery and continues to investigate various aspects of particle physics, including searches for supersymmetry and extra dimensions [18].

- **LHCb (LHC Beauty)**: This experiment focuses on the study of B mesons, particularly in the search for CP violation and its implications for the matter-antimatter asymmetry in the universe. LHCb has provided significant insights into rare decay processes and flavour physics [134].

- **ALICE (A Large Ion Collider Experiment)**: Specialised in heavy-ion collisions, ALICE studies QGP, a state of matter thought to have existed shortly after the Big Bang. This experiment aims to understand the properties of strong interactions and the behaviour of nuclear matter under extreme conditions [135].

In addition to the four main experiments, the LHC is home to several smaller, yet highly specialised experiments that target more specific aspects of particle physics, often serving complementary research or investigating niche areas of high-energy physics:

- **TOTEM (TOTal Elastic and diffractive cross section Measurement)**: Located near CMS, TOTEM investigates protons scattered at small angles to measure the total proton-proton cross section and understand elastic and diffractive scattering processes. Although data taking concluded in 2023, analysis of the TOTEM data is ongoing and continues within the CMS–TOTEM Precision Proton Spectrometer (PPS) framework, with results published by the TOTEM or CMS–TOTEM collaborations. These measurements provide valuable insights into the structure of the proton and the nature of the strong interaction [136].

- **LHCf (LHC-forward)**: Positioned to capture particles emitted in the forward direction, LHCf studies high-energy cosmic-ray interactions by observing forward-emitted neutrons and photons. This experiment is critical for calibrating cosmic-ray shower models, essential for high-energy astrophysics [137].

- **MoEDAL (Monopole and Exotics Detector At the LHC)**: MoEDAL aims to search for magnetic monopoles and other highly ionising particles, which could provide evidence for BSM physics [138]. Due to its relevance to this thesis — where the study of highly ionising particles plays a central role — MoEDAL will be discussed in more detail in Section 3.

- **FASER (ForwArd Search ExpeRiment)**: Positioned far downstream from ATLAS, FASER is sensitive to long-lived particles such as dark photons that travel far from the collision point before decaying. By focusing on light dark matter, FASER extends the LHC's reach in exploring BSM scenarios [139].

- **SND@LHC (Scattering and Neutrino Detector)**: Dedicated to detecting high-energy neutrinos from LHC collisions, SND@LHC focuses on tau neutrino interactions, contributing to our understanding of particle physics and astrophysics [140].

Together, these smaller experiments enhance the LHC's ability to explore a wide range of phenomena, complementing the main LHC detectors in the search for NP.

Future Circular Collider (FCC-hh) The Future Circular Collider (FCC-hh) is a proposed next-generation hadron collider, conceptualised as a successor to the LHC. With a planned circumference of approximately 90 kilometres, the FCC-hh aims to reach collision energies of 100 TeV [141]. Such energy levels would allow for direct access to heavy particles beyond the reach of the LHC, providing unique opportunities for precision measurements and discovery [142].

The FCC-hh design requires advancements in superconducting magnet technology, mainly the development of high-field magnets that can sustain fields of up to 16 T. This technological leap is essential for bending the paths of protons along the collider's vast circumference, making the FCC-hh a significant engineering challenge. If constructed, the FCC-hh would expand our discovery reach by several orders of magnitude. Its unprecedented energy range is expected to facilitate studies of phenomena involving possible BSM particles, such as dark matter candidates,and high-precision measurements of the Higgs boson. The impact of the FCC-hh on particle physics would be transformative, allowing for exploration into energy regimes previously inaccessible and addressing long-standing questions in both particle physics and cosmology [143].

Chapter 3

Highly Ionising Particles

The search for Highly Ionising Particles (HIPs) as potential indicators of physics BSM has long been a significant focus of research at accelerator facilities. HIPs are hypothetical particles predicted by various theories extending the SM, including GUTs, SUSY and models with extra dimensions [144]. These particles are characterised by their exceptional ability to ionise detector materials due to high electric or magnetic charges, or their low velocities due to large masses.

To detect a HIP, it must interact with the detector material and lose energy mainly through the process of ionisation. Charged particles interact with atomic electrons in the detector medium, resulting in an energy loss that depends on the particle's mass, charge and velocity. The mean energy loss per unit path length, or stopping power (denoted $\frac{dE}{dx}$), is a critical parameter for particle detection and identification.

For charged particles heavier than electrons, the energy loss can be accurately described by the Bethe-Bloch formula [145]. This equation quantifies the energy loss due to ionisation and excitation of atoms by a passing particle and is given by:

$$-\frac{dE}{dx} = \frac{4\pi N_A r_e^2 m_e c^2}{A} \frac{Z}{\beta^2} z^2 \left[\ln\left(\frac{2m_e c^2 \beta^2 \gamma^2}{I} \right) - \beta^2 \right], \tag{3.1}$$

where:

- $-\frac{dE}{dx}$ is the mean energy loss per unit distance,

- z is the electric charge number of the incident particle,
- Z and A are the atomic number and mass number of the absorber material,
- N_A is Avogadro's number,
- r_e is the classical electron radius,
- m_e is the electron mass,
- c is the speed of light in vacuum,
- $\beta = \frac{v}{c}$ is the particle's velocity,
- $\gamma = \frac{1}{\sqrt{1-\beta^2}}$ is the Lorentz factor,
- I is the mean excitation potential of the material.

HIPs, due to their high charge or low velocity, experience significantly greater energy loss compared to minimally ionising particles. For instance, a particle with charge $z = 2$ loses four times the energy per unit distance as a singly charged particle at the same velocity. This distinctive ionising behaviour makes HIPs readily identifiable in tracking detectors and ionisation chambers.

In proton-proton collisions at the LHC, electrically charged particles can only cause significant ionisation if they are either very massive and moving slowly, with $\beta\gamma < 1$, or if they carry multiple charges. For a SM particle to exhibit strong ionisation, it must be decelerating as it approaches rest. Therefore, the detection of massive, stable, or quasi-stable HIPs would serve as a clear signal of NP, with no obvious background within the SM.

Among the exotic HIP candidates are magnetic monopoles, HECOs and particles carrying both magnetic and electric charges (dyons). These candidates will be discussed in subsequent sections, including their theoretical foundations, potential production mechanisms and experimental search strategies.

3.1 Searches for HIPs at colliders

The search for HIPs at the LHC involves specialised detection techniques that exploit the unique signatures these particles would produce in detectors. HIPs are expected to create highly ionising tracks due to their large charge or low velocity, and potentially long lifetimes, which differentiate them from SM particles. Major LHC experiments, including ATLAS, CMS and MoEDAL, have developed specific strategies to detect such particles.

3.1.1 HIP Searches in ATLAS and CMS

The ATLAS and CMS detectors, primarily designed for general-purpose particle detection, incorporate several features that enable HIP searches. Both experiments rely on ionisation measurements and time-of-flight (ToF) techniques to identify anomalously slow or highly charged particles:

- **Transition Radiation Tracker (TRT)**: In ATLAS, the TRT plays a crucial role in HIP searches due to its dual capability of tracking charged particles and detecting transition radiation [146]. The TRT is composed of a series of straw tubes filled with a xenon-based gas mixture, surrounded by radiative material. When a particle with a high Lorentz factor γ traverses these boundaries, it emits transition radiation, which the TRT detects. Although primarily used to differentiate high-energy electrons from other particles, the TRT also provides essential $\frac{dE}{dx}$ measurements. These measurements help identify particles with abnormally high ionization energy loss, characteristic of HIPs. By enhancing the ionization data obtained from silicon detectors, the TRT significantly improves the robustness of HIP identification [147].

- **Other Ionisation Measurements ($\frac{dE}{dx}$)**: HIPs are characterised by high $\frac{dE}{dx}$ as they traverse the detector. ATLAS and CMS utilise their tracking detectors, including silicon pixels and strips, to measure $\frac{dE}{dx}$. Particles with higher-than-expected ionization levels for a given momentum are flagged as HIP candidates. This technique is particularly effective for identifying particles with charges significantly exceeding e [148, 149].

- **Time-of-Flight (ToF) Systems**: Both ATLAS and CMS employ ToF systems, including their calorimeters and dedicated timing detectors, to estimate the velocities of particles. HIPs, due to their high mass or low velocities, are expected to move slower than SM particles. By measuring the delay in arrival time relative to SM expectations, ATLAS and CMS can identify slow-moving HIPs, providing a secondary confirmation alongside $\frac{dE}{dx}$ measurements [148, 150].

Despite these capabilities, ATLAS and CMS are general-purpose detectors, and thus, HIP searches are often constrained by detector saturation and limitations in dynamic range. This has led to the development of dedicated experiments, such as MoEDAL [138, 151–153], which is optimised for HIP searches.

3.1.2 The MoEDAL Experiment

The Monopole and Exotics Detector at the LHC (MoEDAL) [138] is uniquely designed to search for manifestations of NP through HIPs, complementing the searches conducted by ATLAS and CMS. MoEDAL is optimised for the detection of magnetic monopoles and massive, long-lived, and slow-moving particles with single or multiple electric charges, as predicted in various BSM scenarios.

MoEDAL is located around the intersection region at Point 8 of the LHC, within the LHCb experiment Vertex Locator (VELO) cavern. Its largely passive design consists of three subdetector systems, as illustrated in Fig. 3.1, tailored for HIPsearches [154]. These subdetectors are:

- **Nuclear Track Detectors (NTDs)**: The main detection system of MoEDAL consists of NTDs, made of CR-39, Makrofol®, and Lexan™ plastic sheets, surrounding the intersection area. These detectors are sensitive to ionising particles with a charge-to-velocity threshold of $z/\beta \sim 5$. The Very High Charge Catcher (VHCC), a high-threshold

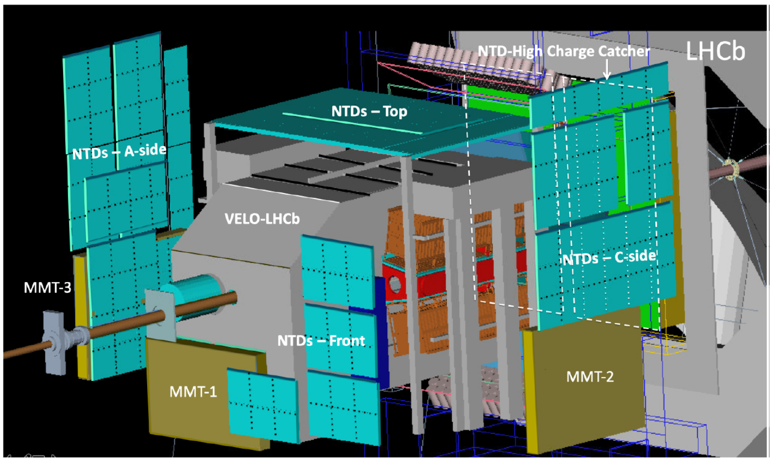

Figure 3.1: A schematic view of the MoEDAL detector deployed in the VELO cavern at IP8. Source: Ref. [157]

NTD with $z/\beta \sim 50$, covers part of the forward region in the LHCb acceptance, enhancing MoEDAL's geometrical coverage for detecting highly charged particles.

- **Magnetic Monopole Trapping Volumes (MMTs)**: MoEDAL also employs MMTs, consisting of aluminium absorbers designed to capture magnetically charged particles, like monopoles or dyons. The MMTs are periodically removed and analysed at the Superconducting Quantum Interference Device (SQUID) magnetometer facility at ETH Zurich, where they are scanned for monopoles through an induction technique [155]. This method provides a rapid, non-destructive analysis that enables multiple measurements on potential monopole signals.

- **TimePix Radiation Monitors**: MoEDAL's only active detection system is an array of MediPix TimePix pixel detectors [156]. These devices monitor the radiation environment in real-time, providing a 3D mapping of the charge deposition, distinguishing between particle species from mixed radiation fields, and measuring their energy deposition profiles. This system enhances MoEDAL's background understanding and contributes to beam-related event monitoring.

MoEDAL's design offers several unique advantages for HIP searches:

- **Background-Free Detection**: The NTDs provide a background-free environment, as SM particles do not typically produce latent tracks, making MoEDAL highly sensitive to HIPs.

- **High Charge Sensitivity**: With NTDs and VHCCs, MoEDAL is capable of detecting particles with charges several times that of the elementary charge e, which general-purpose detectors like ATLAS and CMS may miss due to saturation issues.

- **Dedicated Magnetic Monopole Detection**: The MMTs are optimised to capture monopoles directly, offering a capability unique to MoEDAL, as neither ATLAS nor CMS has dedicated systems for magnetic charge detection [154].

MoEDAL's specialised focus on HIPs makes it a key experiment in the quest for NP at the LHC. Recent results have set stringent limits on the production cross sections for monopoles and other HIPs, enhancing MoEDAL's sensitivity with each LHC luminosity upgrade [158–166]. Moreover, prospects for discovering singly charged particles arising in various extensions of the SM, such as supersymmetric long-lived partners [167–169] and other exotic scenarios such as D-matter [170–176] look promising.

3.2 Magnetic Monopoles

A prominent example of a HIP arising from BSM theories is the magnetic monopole. Numerous searches for MMs have been conducted since Paul Dirac predicted their existence in 1931 [177]. Dirac demonstrated that MMs could account for the discrete nature of electric charge through the Dirac Quantization Condition (DQC), given by:

$$\alpha g = \frac{N}{2}e, \quad N \in \mathbb{N}, \tag{3.2}$$

where $\alpha = \frac{e^2}{4\pi\epsilon_0}$ is the fine structure constant, e is the elementary electric charge and g represents the magnetic monopole charge in natural units. According to Dirac's formulation, monopoles are point-like particles, and quantum mechanical consistency conditions lead to Eq. (3.2), which determines the value of their magnetic charge. The mass m and spin s of monopoles remain free parameters in the theory. An intriguing aspect of Dirac's work is the symmetry in Maxwell's equations between magnetic and electric fields, leading to the concept of *electric-magnetic duality* [178].

Since Dirac's proposal, various theoretical frameworks have predicted the existence of magnetic monopoles, including GUTs, electroweak symmetry models and cosmological models. Each predicts monopoles with unique properties and masses, influencing the nature of experimental searches. Below are some of the major theoretical predictions for monopoles:

- **GUT Monopoles:** Magnetic monopoles were first predicted by GUTs, which attempt to merge the strong and electroweak interactions into a unified framework [97]. In 1974, 't Hooft [101] and Polyakov [102] independently showed that in a unified gauge theory involving a semi-simple group such as $SU(5)$, spontaneous symmetry breaking generates monopoles as solitonic solutions. These GUT monopoles are predicted to be extremely massive, with estimated masses of $O(10^{15})$ GeV, far beyond the reach of current or near-future particle colliders [179]. The expected mass and rarity of GUT monopoles have led to searches focusing on cosmic monopoles [154, 180], where they could theoretically be produced in the early universe and persist to the present day.

- **Electroweak Monopoles:** In addition to GUT monopoles, electroweak models predict monopoles with magnetic charges arising from the structure of the electroweak gauge group. Cho and Maison proposed an electroweak monopole as a hybrid of Dirac and 't Hooft–Polyakov monopoles, carrying a magnetic charge twice that of a Dirac monopole [181]. This charge emerges from the quotient group $SU(2) \times U_Y(1)/U_{em}(1)$, with $U_{em}(1)$ being the EM subgroup of the electroweak theory. Recent estimates suggest that the electroweak monopole could be light enough to be detectable at the LHC [182], making it a primary candidate for collider-based monopole searches.

- **Global Monopoles:** Proposed within cosmological models, global monopoles arise as topological defects when internal global symmetries, such as the global $SO(3)$ symmetry, break spontaneously in non-gauged versions of the Georgi–Glashow model [183, 184]. Unlike electroweak monopoles, global monopoles carry no magnetic charge but can affect the space-time around them by introducing a deficit angle. This feature creates gravitational effects that could be detected indirectly, either through gravitational lensing or scattering effects of SM particles [184]. Experimental searches for global monopoles at colliders could exploit such scattering signatures to detect these particles indirectly.

- **Monopolium:** One of the challenges in detecting Dirac monopoles directly may arise from their tendency to form bound states called *monopolium* [185, 186]. Monopolium consists of a monopole-antimonopole pair in a bound, electrically neutral state, which makes direct detection difficult. However, if monopolium decays into photons, this could provide a detectable signature at the LHC [187], particularly in experiments like ATLAS, CMS and the CMS-TOTEM Precision Proton Spectrometer (CT-PPS) [188]. This kind of signature will be further explored in Section 5. Monopolium searches offer a complementary approach to traditional monopole searches by targeting the unique decay products of these bound states.

3.3 Highly Electrically Charged Objects

HECOs are defined by their unique experimental signatures, including high mass, long lifetimes and a high electric charge, often measured in multiples of the elementary charge e. These characteristics set HECOs apart from other particles typically studied in high-energy physics, as they have the potential to create highly ionising tracks when passing through detector materials. HECOs are particularly intriguing in the search for physics BSM, as they provide a possible pathway to discovering exotic, long-lived particles with properties that challenge current theoretical frameworks.

A notable aspect of HECO searches is their model-independent approach. Unlike conventional particle searches, which often target particles predicted by specific theoretical models, HECOs are investigated as a broad category of hypothetical particles with minimal assumptions about their origins or interactions [189]. By focusing on observable properties such as mass, lifetime and electric charge, HECO searches aim to detect anomalous signals that could indicate NP without being restricted by particular theoretical constructs. This approach allows experiments to remain open to a wide variety of potential signals, enhancing the likelihood of discovering unexpected or previously unconsidered phenomena [190].

Despite the model-agnostic nature of HECO searches, the literature provides several theoretical examples of particles that could display HECO-like properties. These theoretical candidates stem from diverse BSM frameworks and are summarised below:

- **Q-balls**: Q-balls are non-topological solitons predicted in certain supersymmetric theories, arising from scalar fields with conserved charges. These stable or long-lived objects can carry high electric charge and mass, making them prime candidates for HECOs [191, 192]. In some scenarios, Q-balls are proposed as dark matter candidates, as they could have formed in the early universe and may remain undetectable today. Their high charge-to-mass ratio and unique stability properties make Q-balls an intriguing example of HECOs in theoretical physics.

- **Strangelets**: Strangelets are hypothetical particles composed of strange quark matter — a form of dense matter consisting of up, down, and strange quarks — predicted in certain theoretical models [193]. Depending on their size and composition, strangelets could carry large masses and electric charges. These particles are conjectured to arise in extreme environments, such as heavy-ion collisions or astrophysical events like neutron star mergers. In such scenarios, strangelets could manifest as HECOs, potentially leaving highly ionising tracks in detectors.

- **Micro-Black Hole Remnants**: Theoretical models involving extra spatial dimensions and quantum gravity predict the possible formation of microscopic black holes in high-energy collisions [194]. While these black holes would typically evaporate through Hawking radiation, certain models propose that stable, electrically charged remnants could survive the evaporation process. Such remnants could exhibit properties characteristic of HECOs, with substantial mass and electric charge, and their detection would have profound implications for quantum gravity and extra-dimensional theories.

- **Schwinger Dyons**: Schwinger dyons are hypothetical particles that possess both electric and magnetic charges. These particles arise in specific extensions of QED and in some BSM frameworks that incorporate dual symmetries [195]. Dyons' dual charge property would make them exceptionally ionising, with both electric and magnetic interactions with detector materials, producing unique signatures that distinguish them from ordinary charged particles.

- **Doubly Charged Particles**: Certain BSM theories predict the existence of particles with doubly or even multiply charged states. For example, extensions of the SM involving additional Higgs fields can lead to the formation of doubly charged Higgs bosons, which would act as HECOs if they were stable or long-lived [196]. These doubly charged particles would ionise detector materials at rates far exceeding those of singly charged particles, making them a distinctive target in HECO searches.

- **Radiative Neutrino Mass Models**: Radiative neutrino mass models, which generate neutrino masses through loop-level interactions, often predict the existence of scalar or fermionic particles with high electric charge [197]. These particles participate in loop processes and are promising HECO candidates. For example:

  - **The Zee Model** introduces a charged scalar in one-loop neutrino mass generation, predicting doubly charged particles as HECO candidates [198].

- **The Zee-Babu Model** includes a doubly charged scalar (k^{++}) as part of the two-loop mass generation process, which could be detectable in collider searches [199].
- **The Scotogenic Model** incorporates multiply charged scalars in one-loop processes, providing candidates with high ionisation signatures [200].

In this thesis, a model-independent approach is adopted to search for HECOs. By prioritising observable characteristics such as mass and high electric charge, this approach maximises the sensitivity of the search to NP, regardless of the specific theoretical model. The examples above illustrate the wide variety of BSM theories that predict particles with HECO-like properties, highlighting the potential diversity of particles that could be discovered through this method.

3.4 HIPs Production Mechanisms and searches

HECOs and MMs share similar production mechanisms in high-energy collisions.

For the *direct* mechanisms, we consider two primary processes: the Drell-Yan (DY) process—occurring via the s-channel— and Photon Fusion (PF)—taking place via the t-channel [201–204]. In both cases, the production dynamics vary based on the properties of HECOs and monopoles.

- HECOs are produced through interactions involving photons, with a coupling strength of $g = ne$, where e is the elementary electric charge and n is an integer. For spin-$\frac{1}{2}$ HECOs, there is an additional coupling to the Z^0 boson, which influences production in the DY process. Spin-0 and spin-1 HECOs couple directly to photons. Scalar HECOs involve both three-point and four-point photon interactions, while

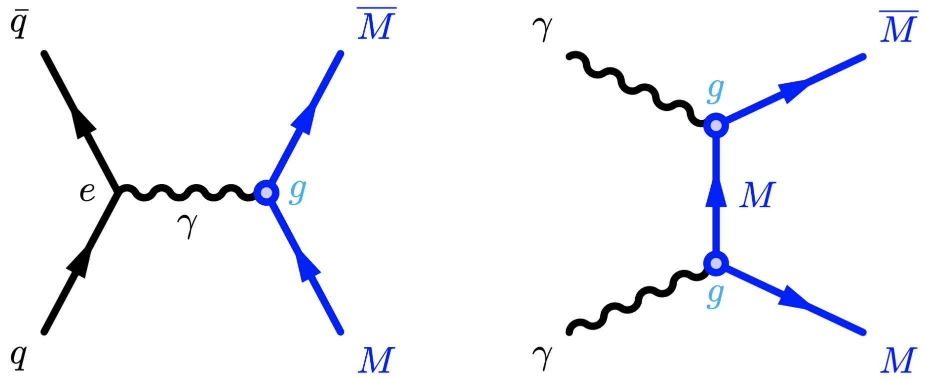

Figure 3.2: Monopole M pair production diagrams in hadron colliders: Drell-Yan (left) and via Photon Fusion (right). Image from Ref. [154]

spin-1 HECOs couple to photons only through three-point vertices. Spin-$\frac{1}{2}$ HECOs couple to both photons (with $g = ne$) and the Z^0 boson. In the DY process, a quark-antiquark annihilation can produce a Z^0 boson that decays into a pair of spin-$\frac{1}{2}$ HECOs.

- MMs couple exclusively to photons and possess a magnetic charge, g_D, which determines their coupling strength to the photon. In both the DY and PF processes, illustrated in Fig. 3.2, the monopole-photon interaction is governed by this magnetic charge. One can assume that the monopole–photon coupling may additionally be β-dependent, where $\beta = \sqrt{1 - \frac{4M^2}{s}}$, with M the monopole mass and s the Mandelstam variable [154, 203, 204].

For *indirect* mechanisms, virtual HIPs have been proposed to mediate processes that result in multi-photon final states, often illustrated by a *box diagram* [154]. This process is expanded upon in Section 5 as it is crucial for this thesis work.

A promising approach for the monopole indirect detection is through the search for monopolium [185, 205]. As discussed in Section 5, monopolium can be produced via PF, in processes such as electron-positron annihilation and high-energy proton- (anti)proton collisions. This indirect approach offers a complementary avenue for detecting monopoles, particularly in cases where direct detection might be challenging due to their strong interactions with photons and large masses. Similar to monopolium, HECOs can form bound states and can be detected via a two-photon final states [189].

To address the issue of non-perturbativity in monopole production, an improved resummation approach has been proposed [206]. This method aims to describe the dynamics of MMs, which are inherently non-perturbative field-theoretic objects due to their large magnetic charge, as dictated by the Dirac quantisation condition. However, for MMs with internal structure, such as those predicted by GUTs that extend the SM [154], there is significant suppression of the associated production cross section at colliders. This suppression arises from the underlying structure of these monopoles [207]. Therefore, the resummation scheme described is more suitable for point-like Dirac monopoles [206, 208], where the perturbative approach is more applicable.

The challenge of non-perturbativity and the suppression of monopole production cross sections at colliders can be addressed by considering the thermal Schwinger production mechanism in heavy-ion collisions [178, 209–211]. This process is particularly relevant in the presence of strong EM fields, such as those generated in high-energy heavy-ion collisions. Thermal Schwinger production involves the creation of particle-antiparticle pairs from the vacuum due to intense electric fields [212]. In the context of monopole production, this mechanism can lead to the formation of monopole-antimonopole pairs when the EM fields reach a sufficiently strong intensity. Thermal Schwinger production is a non-perturbative process that does not rely on perturbation theory. The effectiveness of this process depends on the strength of the EM fields and the temperature of the system. Heavy-ion collisions at high energies produce sufficiently strong EM fields, making thermal Schwinger production a viable mechanism for monopole creation.

A notable search for the Schwinger mechanism was conducted by the MoEDAL collaboration, focusing on MM production in heavy-ion collisions. This search was performed at the LHC, where the collisions of lead ions produce some of the strongest magnetic fields known in the current Universe [213]. The MoEDAL experiment was exposed to approximately

0.235 nb^{-1} of Pb–Pb collisions with a centre-of-mass energy $\sqrt{s} = 5.02$ TeV in November 2018. This exposure allowed the collaboration to search for magnetic monopoles potentially produced via the Schwinger mechanism in these high-energy collisions. A SQUID magnetometer was employed to scan the trapping detectors for the presence of magnetic charge. Such a charge would induce a persistent current in the SQUID, allowing for the detection of monopoles. The analysis excluded magnetic monopoles with integer Dirac charges $1g_D \leq g \leq 3g_D$ and masses up to 75 GeV at the 95% confidence level.

Additionally, the ATLAS experiment conducted a search for MMs using Pb–Pb collisions, focusing on Schwinger production [214]. Using 0.16 nb^{-1} of Pb–Pb collision data at $\sqrt{s} = 5.02$ TeV per nucleon pair, ATLAS aimed to detect HIPs by identifying their unique energy depositions in the detector's calorimeters. The strong fields in these heavy-ion collisions provided ideal conditions for Schwinger production of monopoles, allowing ATLAS to place constraints on monopole properties across a range of masses and magnetic charges. Specifically, the ATLAS search set limits on monopole production for magnetic charges up to $5g_D$ and masses up to approximately 150 GeV, extending the exclusion range of previous experiments and complementing MoEDAL's findings.

Another MoEDAL search for magnetic monopoles was carried out in ultraperipheral Pb–Pb collisions during Run 1 of the LHC [215]. In this study, the beam pipe surrounding the interaction region of the CMS experiment was exposed to 184.07 μb^{-1} of Pb–Pb collisions at a centre-of-mass energy of 2.76 TeV in December 2011. After the collisions, the beam pipe was removed in 2013 and scanned by the MoEDAL experiment using a SQUID magnetometer, with the aim of detecting any trapped magnetic monopoles. Although no monopole signal was observed, this search had two distinct advantages that made it particularly noteworthy. First, the trapping volume was located very close to the collision point, which increased the likelihood of capturing any monopoles produced in the collisions. Second, the ultrahigh magnetic fields generated during the heavy-ion run provided the ideal conditions for monopole production via the Schwinger mechanism. The search set the most stringent limits on monopoles with charges between 2 and 45 g_D, excluding those with masses of up to 80 GeV at a 95% confidence level. This marked a significant step forward in constraining the possible properties of monopoles and expanded the mass bounds established by previous searches.

Chapter 4

Dyson-Schwinger Resummation for HECOs

4.1 Introduction

This chapter builds upon previous research, detailed in Refs. [216–219], where the PhD candidate contributed as one of the authors.

As explored in Chapter 3, HECOs present unique challenges in theoretical and experimental particle physics due to their strong EM interactions. The coupling strength for HECOs, characterised by $\alpha = \frac{n^2 e^2}{4\pi}$, grows significantly with the charge $Q = ne$, invalidating the applicability of perturbative QED. Addressing these challenges requires the use of non-perturbative techniques, such as Dyson-Schwinger (DS) resummation, to obtain reliable predictions for physical observables.

The DS equations form a set of integral equations that describe the behaviour of propagators and vertices in quantum field theory. By resumming all orders of perturbative corrections, they provide a non-perturbative approach to describe the effects of strong coupling. For HECOs, where $\alpha \gg 1$, this method accounts for self-energy corrections and vertex functions, yielding resummed propagators that enable meaningful predictions of physical observables.

This chapter focuses on the application of DS resummation techniques to HECOs, with an emphasis on spin-$1/2$ and spin-0 cases. The differences in the theoretical framework and phenomenological implications for these spins are discussed in dedicated subchapters.

In conventional QED, the perturbative approach relies on the smallness of the coupling constant, which ensures the convergence of the series expansion in powers of α. However, for HECOs, the effective coupling constant increases dramatically due to their large charge Q.

For $Q \gg 1$, α_{eff} approaches or exceeds unity, causing the perturbative expansion to diverge. This behaviour indicates the dominance of higher-order terms, which can no longer be truncated as negligible corrections. As a result, traditional perturbative methods fail to provide reliable predictions for cross sections and other observables [220]. Consequently, studying HECOs requires fully non-perturbative methods, such as strongly coupled lattice QED or continuous DS resummation techniques. The DS approach provides exact relations between fully dressed propagators and vertices in gauge theories, formulated as integral equations. By employing an ansatz for the functional form of the effective action (consistent with Ward identities), these equations enable the inclusion of non-perturbative effects.

Throughout this thesis, the focus is on HECOs with charges $Q \gtrsim 11e$. To establish mass bounds for HECOs based on experimental upper limits on HECO pair-production cross sections, tree-level processes, such as DY and PF, are commonly considered. However, for HECOs with large charges, this approach becomes invalid due to the breakdown of perturbative methods caused by the strong coupling associated with large electric charges.

4.2 Resummation for spin-1/2 HECOs

In this section, the DS resummation scheme for spin-1/2 HECOs is outlined, which incorporates specific approximations explicitly stated throughout the analysis. This approach provides a significant improvement in deriving mass bounds for HECOs. These bounds are obtained by comparing the predictions of our effective Lagrangian with experimentally established upper limits on HECO production cross sections at current colliders. This methodology offers a substantial enhancement over previous interpretations based on tree-level processes, such as DY and PF.

The DS resummation focuses on the effective HECO mass and coupling, which evolve with the renormalisation group momentum scale. At the ultraviolet (UV) fixed-point solution, these parameters define the effective Lagrangian used in subsequent cross section calculations. This framework is particularly relevant for HECOs carrying large electric charge, typically $|n| \geq 11$, where the effective electromagnetic coupling becomes strong enough to render perturbative QED inapplicable. For smaller charges, standard QED results are recovered.

4.2.1 Coupled Quantum Corrections

Let us consider the EM interactions of a HECO, which, for concreteness, is assumed to be a spin-1/2 Dirac fermion, $\psi(x)$. This fermion couples to a massless photon $A_\mu(x)$ with a bare charge:

$$g = ne, \quad n \in \mathbb{Z}^+ \quad \text{(a positive integer)}, \tag{4.1}$$

where e represents the elementary electron charge. The bare Lagrangian is given by the standard QED formulation:

$$\mathcal{L}_{\text{bare}} = -\frac{1}{4}F_{\mu\nu}F^{\mu\nu} + \frac{\lambda}{2}(\partial_\mu A^\mu)^2 + \overline{\psi}\Big(i\not{\partial} + g\not{A} - m\Big)\psi, \tag{4.2}$$

where m is the bare HECO mass and $\lambda \in \mathbb{R}$ is a gauge-fixing parameter.

The dressed propagators and vertex corrections are described by:

$$\begin{aligned} G &= i\frac{\mathcal{Z}\not{p} + M}{\mathcal{Z}^2 p^2 - M^2}, \\ \Delta_{\mu\nu} &= \frac{-i}{(1+\omega)q^2}\left(\eta_{\mu\nu} + \frac{1+\omega-\lambda}{\lambda}\frac{q_\mu q_\nu}{q^2}\right), \\ \Gamma_\mu &= g\mathcal{Z}\gamma_\mu, \end{aligned} \tag{4.3}$$

where the quantum corrections $\mathcal{Z}$, ω, and M — representing, respectively, the wavefunction renormalisations of the fermionic HECO and the photon, and the renormalised HECO mass — are considered independent of the momentum.* The coupled DS equations for the photon and fermion self-energies are considered in $4-\epsilon$ dimensions. By adopting the momentum-independent ansatz introduced in Eq. (4.3), and following the procedure outlined in Ref. [206], the resulting equations take the form:

$$\begin{aligned}
\mathcal{Z} &= 1 + \frac{g^2}{8\pi^2\lambda}\frac{1}{\epsilon}\left(\frac{\mathcal{Z}k}{M}\right)^{\epsilon} + \text{finite}, \\
\omega &= \frac{g^2}{6\pi^2\mathcal{Z}}\frac{1}{\epsilon}\left(\frac{\mathcal{Z}k}{M}\right)^{\epsilon} + \text{finite}, \\
1 - \frac{m}{M} &= \frac{g^2}{8\pi^2\lambda\mathcal{Z}}\frac{1+3\lambda+\omega}{1+\omega}\frac{1}{\epsilon}\left(\frac{\mathcal{Z}k}{M}\right)^{\epsilon} + \text{finite},
\end{aligned} \tag{4.4}$$

where m denotes the bare HECO mass and k is an energy scale introduced by dimensional regularisation.
The goal is to solve the full set of equations without assuming a perturbative regime ($g^2 \ll 1$), allowing for large corrections in $(\mathcal{Z}-1)$, ω, and $(M-m)$.

In the following, it is assumed that g and m are independent of the scale k. The equations in Eq. (4.4) are then differentiated with respect to k to eliminate the explicit ϵ-dependence, and subsequently integrated back with respect to k, thereby introducing constants of integration. This procedure, together with the boundary conditions

$$(\mathcal{Z}, \omega, M) = (1, 0, m), \quad \text{when} \quad k = m, \tag{4.5}$$

leads directly to the following relations:

$$\begin{aligned}
\mathcal{Z} &= 1 + \frac{g^2}{8\pi^2\lambda}\ln\left(\frac{\mathcal{Z}k}{M}\right), \\
\mathcal{Z}\omega &= \frac{g^2}{6\pi^2}\ln\left(\frac{\mathcal{Z}k}{M}\right), \\
\mathcal{Z}\left(1 - \frac{m}{M}\right) &= \frac{g^2}{8\pi^2\lambda}\frac{1+3\lambda+\omega}{1+\omega}\ln\left(\frac{\mathcal{Z}k}{M}\right).
\end{aligned} \tag{4.6}$$

These equations recover the familiar one-loop perturbative results when

*This work adopts the Minkowski spacetime metric $\eta^{\mu\nu}$ with signature $(+,-,-,-)$.

$g^2 \ll 1$:

$$\mathcal{Z} = 1 + \frac{g^2}{8\pi^2\lambda} \ln\left(\frac{k}{m}\right) + \mathcal{O}(g^4),$$
$$\omega = \frac{g^2}{6\pi^2} \ln\left(\frac{k}{m}\right) + \mathcal{O}(g^4),$$
$$M = m + \frac{g^2 m}{8\pi^2\lambda}(1+3\lambda) \ln\left(\frac{k}{m}\right) + \mathcal{O}(mg^4). \tag{4.7}$$

4.2.2 Fixed-Point Solution

In this section, the focus is on the analysis within the Feynman gauge:

$$\lambda = 1, \tag{4.8}$$

which is often referred to as a *physical* gauge in the context of scattering calculations. This gauge choice can be justified within perturbation theory by resumming specific classes of Feynman diagrams, where the gauge dependence cancels, resulting in outcomes equivalent to those obtained using the Feynman gauge (see "pinched technique" [221, 222]).

Due to the resummation inherent in the DS framework, the equations described in Eq. (4.6) remain valid even for strong coupling g. In such cases, both $\mathcal{Z}$ and M must be retained inside the logarithmic arguments in Eq. (4.6), leading to modifications to the naive logarithmic running behaviour seen in Eq. (4.7). It can be shown that these equations admit an UV fixed-point solution, where the running mass ratio $M/\mathcal{Z}$ diverges as $k \to \infty$, but in such a way that:

$$\lim_{k\to\infty} \frac{k\,\mathcal{Z}}{M} = \text{finite}, \tag{4.9}$$

with $\mathcal{Z}$ and ω stabilising at finite values.

Rewriting the equations in Eq. (4.6), one obtains:

$$\begin{aligned}
\mathcal{Z} &= 1 + \frac{g^2}{8\pi^2} \ln\left(\frac{\mathcal{Z}k}{M}\right), \\
\omega &= \frac{4}{3}\left(1 - \frac{1}{\mathcal{Z}}\right), \\
1 - \frac{m}{M} &= 4\frac{4\mathcal{Z} - 1}{7\mathcal{Z} - 4}\left(1 - \frac{1}{\mathcal{Z}}\right).
\end{aligned} \tag{4.10}$$

The scale k can then be expressed in terms of $\mathcal{Z}$ as:

$$\frac{k}{m} = \frac{7\mathcal{Z} - 4}{9(\mathcal{Z}_+ - \mathcal{Z})(\mathcal{Z} - \mathcal{Z}_-)} \exp\left(\frac{8\pi^2}{g^2}(\mathcal{Z} - 1)\right), \tag{4.11}$$

where the values of $\mathcal{Z}_\pm$ are given by:

$$\mathcal{Z}_\pm = \frac{8}{9}\left(1 \pm \frac{\sqrt{7}}{4}\right) \simeq \begin{cases} 1.477 = \mathcal{Z}^\star \\ 0.301. \end{cases} \tag{4.12}$$

From Eq. (4.11), it is evident that $k > 0$ only if $\mathcal{Z}_- < \mathcal{Z} < \mathcal{Z}_+$, with $k \to \infty$ as $\mathcal{Z} \to \mathcal{Z}_\pm$. A consistent solution satisfying unitarity ($\mathcal{Z} > 1$) is achieved for:

- $\mathcal{Z} = 1$ at $k = m$ (the boundary condition),
- $\mathcal{Z} \to \mathcal{Z}^\star$ as $k \to \infty$, as illustrated in Figure 4.1.

In the limit $k \to \infty$, the following fixed-point values are obtained:

$$\begin{aligned}
\omega \to \omega^\star &= \frac{4}{3}\left(1 - \frac{1}{\mathcal{Z}^\star}\right) \simeq 0.431, \\
\tilde{M} \equiv \frac{M}{k} &\to \mathcal{Z}^\star \exp\left(-\frac{8\pi^2}{g^2}(\mathcal{Z}^\star - 1)\right),
\end{aligned} \tag{4.13}$$

where $\tilde{M}$ corresponds to the dimensionless running mass parameter. The UV fixed point is therefore defined as:

$$\lim_{k\to\infty} (\mathcal{Z}, \omega, \tilde{M}) = (\mathcal{Z}^\star, \omega^\star, \tilde{M}^\star). \tag{4.14}$$

This novel UV fixed point pertains to scenarios where the mass $M \to \infty$ as

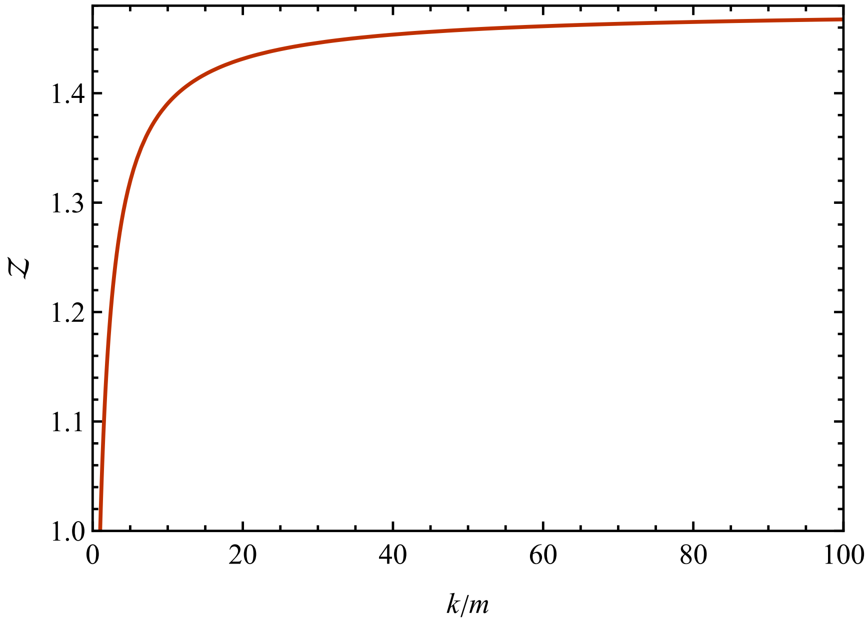

Figure 4.1: Wave-function renormalisation $\mathcal{Z}$ as a function of k/m for $g^2 = 8\pi^2$. The value of $\mathcal{Z}$ asymptotically approaches $\mathcal{Z}^\star \equiv \mathcal{Z}_+$ as $k \to \infty$.

$k \to \infty$, while maintaining a finite value for M/k.

It is worth noting that the condition $\mathcal{Z} \geq 1$, consistent with unitarity, allows in principle the HECO to be a fundamental particle. Indeed, in quantum field theory, $\mathcal{Z}$ represents the wavefunction renormalisation factor, which quantifies the quantum corrections to the particle propagator. A value of $\mathcal{Z} \geq 1$ implies that the renormalised propagator respects unitarity and ensures that the particle's wavefunction is well-defined.

4.2.2.1 Effective Running Coupling

The effective Lagrangian, incorporating the renormalisation group running parameters, can be expressed as:

$$\mathcal{L}_{\text{eff}} = \frac{1}{2} A_\mu \Big((1+\omega)\eta^{\mu\nu}\Box - \omega\partial^\mu\partial^\nu \Big) A_\nu + \overline{\psi}\Big(\mathcal{Z} i\partial\!\!\!/ + \mathcal{Z} g A\!\!\!/ - M \Big)\psi. \tag{4.15}$$

To achieve a canonically normalised form, simultaneous field rescalings are applied:

$$A_\mu \to \frac{A_\mu}{\sqrt{1+\omega}}, \quad \psi \to \frac{\psi}{\sqrt{\mathcal{Z}}}. \tag{4.16}$$

After performing these transformations, the Lagrangian is rewritten as:

$$\mathcal{L}_{\text{eff}} \to \frac{1}{2} A_\mu \left(\eta^{\mu\nu} \Box - \frac{\omega}{1+\omega} \partial^\mu \partial^\nu \right) A_\nu + \overline{\psi} \left(i\partial\!\!\!/ + \frac{g}{\sqrt{1+\omega}} A\!\!\!/ - \frac{M}{\mathcal{Z}} \right) \psi. \tag{4.17}$$

This formulation reveals that the effective Lagrangian Eq. (4.17), which emerges from the DS resummation approach, corresponds to a modified QED Lagrangian. The modifications include a "shifted" covariant gauge parameter:

$$\lambda_{\text{eff}} = \frac{1}{1+\omega} = 1 - \frac{\omega}{1+\omega}, \tag{4.18}$$

and the introduction of scale-dependent quantities, such as the running mass $\mathcal{M}(k)$ and coupling $g(k)$:

$$\mathcal{M}(k) = \frac{M(k)}{\mathcal{Z}(k)}, \quad \alpha(k) = \frac{g^2/(4\pi)}{1+\omega(k)}. \tag{4.19}$$

Here, $\alpha(k)$ denotes the effective fine-structure constant at the energy scale k. As a result, physical observables, such as decay rates and cross sections, are shown to remain unaffected by the choice of either a one-loop-resummed or bare photon propagator. This invariance will be explicitly demonstrated in Section 4.2.5.

In conventional perturbative treatments, the coupling α is typically fixed at a reference scale k_0 as $\alpha \equiv \alpha_0$, and the evolution of the bare coupling $g_b(k)$ is then derived. For small values of $\omega(k)$, this leads to:

$$\frac{g_b^2(k)}{4\pi} = \big(1+\omega(k)\big)\alpha_0 \simeq \frac{\alpha_0}{1-\omega(k)}, \tag{4.20}$$

reproducing the well-known Landau pole singularity when $\omega(k)$ is described by its perturbative expression, as in Eq. (4.7). However, the approach discussed here diverges from this standard method by employing a different boundary condition and incorporating non-perturbative resummation effects.

The DS resummation method, as implemented here, begins with a fixed bare coupling g. Non-perturbative quantum corrections then lead to a finite, well-defined dressed coupling $\alpha(k)$ across all scales k, effectively avoiding the Landau pole singularity. This behaviour mirrors that found in alternative non-perturbative approaches, such as the one presented in Ref. [223], which utilises a differential functional equation to describe the evolution of the dressed coupling with the bare mass. Similar to the DS formalism, this approach circumvents the Landau pole by capturing the non-trivial quantum corrections within the coupling's evolution.

4.2.3 Application to HECOs

This section applies the previous theoretical developments to define the *running mass* of a HECO, denoted by $\mathcal{H}$, as a function of the renormalisation group momentum scale k. Based on these results, one can derive the appropriate Feynman rules describing the effective (resummed) non-chiral interactions of a spin-1/2 HECO, first with photons and then with a mixture of photons and Z^0-bosons in the SM sector. Here, the scale k serves as the UV cutoff, which acts as the energy threshold where NP phenomena become relevant. In the context of collider experiments, k can be associated with the centre-of-mass energy $\sqrt{s}$.

4.2.3.1 Running Mass

Using the previously established formalism, one can write the flow equation for the mass scale as:

$$\mathcal{M}(k) = k \exp\left(-\frac{2\pi}{\alpha(k)}(\mathcal{Z}(k) - 1)\right), \tag{4.21}$$

where the mass evolves from its bare value, $\mathcal{M}(m) = m$ at $k = m$, to an asymptotic value at the UV cutoff:

$$\lim_{k\to\Lambda} \mathcal{M}(k) \equiv \mathcal{M}(\Lambda) = \Lambda \exp\left(-\frac{2\pi}{\alpha^\star}(\mathcal{Z}^\star - 1)\right), \tag{4.22}$$

where $\Lambda \gg m$ is the natural UV cutoff in this context. The boundary conditions in Eq. (4.5) provide a smooth interpolation between the bare mass at low scales (infrared) and the renormalised mass at the UV fixed

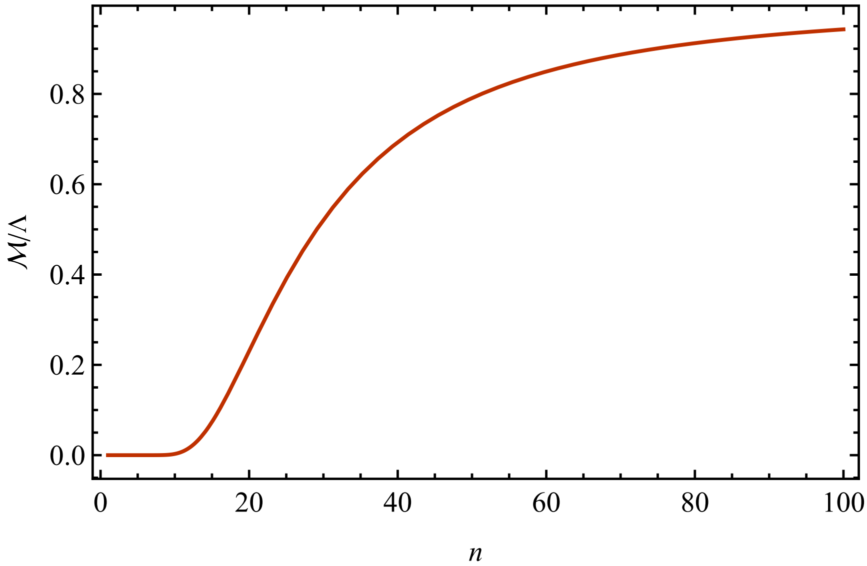

Figure 4.2: The ratio $\mathcal{M}(\Lambda)/\Lambda$ as a function of n, calculated using Eq. (4.24). The ratio approaches unity as $n \to \infty$.

point.

For a HECO with the same charge as an electron, the low-energy regime corresponds to a perturbative QED scenario. For a HECO with an electric charge defined in Eq. (4.1), the relationship is given by:

$$\frac{2\pi}{\alpha^\star}(\mathcal{Z}^\star - 1) \simeq \frac{2\pi \times 137 \times (1 + 0.431) \times (1.477 - 1)}{n^2}, \tag{4.23}$$

which leads to the expression:

$$\frac{\mathcal{M}(\Lambda)}{\Lambda} \simeq \exp\left(-\frac{587}{n^2}\right). \tag{4.24}$$

Figure 4.2 illustrates this relationship, showing that the "resummed" mass $\mathcal{M}(\Lambda)$ is determined by the cutoff Λ, which is linked to the NP scale within an EFT for HECOs. For production cross section calculations, Λ spans the range of parton collision energies, approximately 1–10 TeV at the LHC.

4.2.3.2 Effective Feynman Rules

At the UV fixed point, the HECO production cross sections at colliders can be computed using Feynman rules derived from the effective Lagrangian in Eq. (4.17). The relevant expressions include:

$$
\begin{aligned}
G^{\text{eff}} &= i\,\frac{\not{p} + \mathcal{M}(\Lambda)}{p^2 - \mathcal{M}(\Lambda)^2},\\
\Delta^{\text{eff}}_{\mu\nu} &= \frac{-i}{q^2}\left(\eta_{\mu\nu} + \omega^\star \frac{q_\mu q_\nu}{q^2}\right),\\
\Gamma^{\text{eff}}_{\mu} &= g\,\mathcal{Z}^\star \gamma_\mu. \qquad (4.25)
\end{aligned}
$$

To prevent overcounting of resummed loops, the calculations focus on tree-level DY and PF processes, described in Refs. [164, 204, 224], as depicted in Figure 4.3. Importantly, the tree-level Feynman rules are replaced with their effective, resummed counterparts from Eq. (4.25). The magnitude of these resummed diagrams is comparable to that of naive tree-level processes discussed in Refs. [164, 204, 224].

The effective $\mathcal{H} - \overline{\mathcal{H}} - \gamma$ vertex in Eq. (4.25) introduces a subtle modification. While the tree-level vertex rule is expected to be $\Gamma_\mu = \frac{g}{\sqrt{1+\omega^\star}}\gamma_\mu$, this neglects the gauge fixing introduced by the $\omega^\star$-dependent longitudinal terms in the gauge sector. Consequently, the Ward identity, which ensures the equality of wavefunction renormalisations for HECOs ($\mathcal{Z}$) and vertices ($\mathcal{Z}_V$), is not directly applicable in this resummed scenario.

Instead, the renormalised HECO coupling g_R at the UV fixed point is defined by:

$$
g \to g_R \sqrt{1+\omega^\star}\,\frac{\mathcal{Z}^\star}{\mathcal{Z}_V^\star}. \qquad (4.26)
$$

By applying appropriate field rescalings to achieve canonical normalisation, one arrives at the generalised vertex rule in Eq. (4.25), assuming $\mathcal{Z}_V^\star \sim \mathcal{Z}^\star \sim 1$.

4.2.3.3 Incorporating the Z^0 Boson Contribution

In contrast to magnetic monopoles, which interact solely through photons via the EM neutral current, HECOs are expected to interact through the weak neutral current as well. This introduces a non-trivial coupling between HECOs and the SM Z^0 boson.

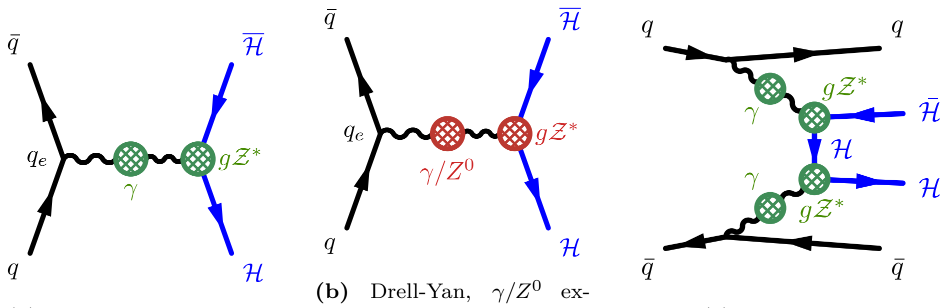

(a) Drell-Yan, γ exchange

(b) Drell-Yan, γ/Z^0 exchange

(c) Photon fusion

Figure 4.3: Processes contributing to the production of spin–1/2 HECO particle-antiparticle ($\mathcal{H}\overline{\mathcal{H}}$) pairs at hadron colliders: (a) Drell-Yan via γ exchange; (b) Drell-Yan including γ/Z^0 exchange; and (c) photon-fusion processes. Resummed propagators and vertices are denoted by green (photon) and red (γ/Z^0) blobs, as described by Eq. (4.25). Image from [216].

The nature of this interaction depends on the transformation properties of HECOs under the SM weak-isospin group $SU(2)$. As described in Ref. [204], this coupling requires assumptions about how HECOs transform under $SU(2) \times U(1)_Y$. The coupling can be introduced through a covariant derivative acting on the spin-1/2 HECO field in a Dirac-like Lagrangian. However, the chiral nature of the $SU(2)$ group—acting only on left-handed fermions—results in potentially asymmetric couplings for the left-handed (L) and right-handed (R) components. The general form of the interaction Lagrangian for $\mathcal{H}$–$\overline{\mathcal{H}}$–Z^0 couplings is given as [204]:

$$\begin{aligned}\mathcal{L}_{\text{int}} &= -\frac{e}{\sin(2\theta_W)}\overline{\mathcal{H}}\gamma^\mu Z^0_\mu \left(c_L\frac{1}{2}(1-\gamma^5) + c_R\frac{1}{2}(1+\gamma^5)\right)\mathcal{H} \\ &= -\frac{e}{\sin(2\theta_W)}\overline{\mathcal{H}}\gamma^\mu Z^0_\mu \left[\frac{1}{2}(c_L+c_R) - \frac{1}{2}(c_L-c_R)\gamma^5\right]\mathcal{H}. \end{aligned} \tag{4.27}$$

Here, the left (c_L) and right (c_R) couplings are expressed as:

$$c_L = t^3 - |n|\sin^2\theta_W, \quad c_R = -|n|\sin^2\theta_W, \tag{4.28}$$

where $|n|$ is the HECO charge multiplicity, θ_W represents the weak mixing angle, and t^3 denotes the weak isospin's third component. A common assumption is that HECOs are singlets under the $SU(2)$ transformation, corresponding to $t^3 = 0$. Under this condition, the interaction simplifies to a purely vector form:

$$\mathcal{L}_{\text{int}} = \frac{1}{2} e|n| \tan\theta_W \overline{\mathcal{H}} \gamma^\mu Z^0_\mu \mathcal{H}. \tag{4.29}$$

To estimate the Z^0 boson's contribution to non-perturbative processes, Eq. (4.29) is considered. The DS equation for the HECO self-energy incorporates one-loop corrections where the propagators and vertices are dressed. The Z^0 boson's contribution to these corrections is additive, resembling a one-loop diagram but using the resummed parameters.

The Z^0 propagator, influenced by $\mathcal{H}$–$\overline{\mathcal{H}}$–Z^0 interactions, requires resummation over HECO loops, similar to the photon case. However, this inclusion significantly complicates the analysis and prevents an analytical solution for the fixed-point parameters. Nonetheless, the relatively weak coupling of HECOs to Z^0, governed by $\sin^2\theta_W \simeq 0.23$ [63], ensures that the one-loop DS resummation leads to a negligible correction, approximately an order of magnitude smaller than the corresponding photon contribution.

In high-momentum scenarios, such as those encountered in DY processes, the Z^0 bosons produced predominantly exhibit large momenta. This allows them to be approximated as massless in the relevant diagrams. Consequently, their dressed propagator closely resembles that of the photon, with minor differences in fixed-point parameters.

The bare Z^0 Lagrangian under R_ξ gauge-fixing conditions is given by:

$$\mathcal{L}_{Z^0} = -\frac{1}{2}\partial_\mu Z^0_\nu(\partial^\mu Z^{0\nu} - \partial^\nu Z^{0\mu}) + \frac{1}{2} M_Z^2 Z^0_\mu Z^{0\mu} - \frac{1}{2\xi_V}(\partial_\mu Z^{0\mu})^2, \tag{4.30}$$

where ξ_V is the gauge-fixing parameter. The corresponding propagator in momentum space reads:

$$\Delta^{Z^0}_{\mu\nu} = -\frac{i}{p^2 - M_Z^2 + i\epsilon}\left(\eta_{\mu\nu} - (1-\xi_V)\frac{p_\mu p_\nu}{p^2 - \xi_V M_Z^2}\right), \quad \epsilon \to 0^+. \tag{4.31}$$

For the massive gauge boson at high energies, which is the case of interest in this work, given that the kinematic distribution in the production of the internal Z^0-bosons is such that the latter carry mostly high energies and momenta, it is convenient to use the $R_{\xi=0}$ (i.e. $\xi_V \to 0$) Landau gauge, which leads to an approximately massless Z^0-propagator before resummation, similar in form to that of photon:

$$\Delta_{\mu\nu}^{Z^0\,\text{high energy}} \simeq -\frac{i}{p^2 - M_Z^2 + i\epsilon}\left(\eta_{\mu\nu} - \frac{p_\mu p_\nu}{p^2}\right), \quad \epsilon \to 0^+ \,. \tag{4.32}$$

In the high-energy and large-momentum regime, where $M_Z \ll E, |\vec{p}|$, the mass term M_Z becomes negligible in the propagator denominator. This approximation results in a propagator that resembles that of a photon in Landau gauge, corresponding to the limit $\lambda_V \to +\infty$. Under this condition, the one-loop resummed Dyson–Schwinger dressing induced by HECO loops follows the same structure as in the photon case, leading to the propagator form given in Eq. (4.3), now evaluated in the limit $\lambda_V \to +\infty$, which coincides with the bare propagator defined in Eq. (4.32).

In the Feynman gauge, defined by $\xi_V = 1/\lambda_V = 1$, and still within the high-energy limit, the Z^0-boson effectively behaves as a second photon. The dressing of its propagator is then expected to yield a transverse tensor structure similar to that shown in Eq. (4.25), though multiplied by a distinct wavefunction renormalisation factor ω_{Z^0}. While this factor differs from the corresponding photon parameter, it is anticipated to be of the same order of magnitude. The resulting resummed Z^0 propagator in this limit takes the form:

$$\Delta_{\mu\nu}^{Z^0\,\text{high energy}}\Big|_{\lambda_V=1}^{\text{resum}} \simeq -\frac{i}{p^2 - M_Z^2 + i\epsilon}\left(\eta_{\mu\nu} + \omega_{Z^0}\frac{p_\mu p_\nu}{p^2}\right), \quad \epsilon \to 0^+. \tag{4.33}$$

Although $M_Z^2 \ll p^2$ in the high-energy limit and may be neglected, it is retained here for completeness. These fixed-point expressions, once incorporated into the previous photon-based framework, obstruct the derivation of an analytic solution for the coupled fixed-point system, as noted earlier.

Finally, in the unitary gauge, corresponding to $\xi_V \to +\infty$, the Z^0-boson—being massive—admits a standard Proca-type propagator given by:

$$\Delta_{\mu\nu}^{Z^0} = -\frac{i}{p^2 - M_Z^2 + i\epsilon}\left(\eta_{\mu\nu} - \frac{p_\mu p_\nu}{M_Z^2}\right), \quad \epsilon \to 0^+. \tag{4.34}$$

The unitary gauge corresponds to the absence of a gauge-fixing term, as such terms are not required in the case of massive vector bosons.

For collider processes, the approximation of neglecting resummation effects in the Z^0 propagator is adopted, while fully incorporating HECO-resummed effects in the photon-HECO vertex and propagator. This approach balances analytical tractability and physical accuracy. Consequently, Z^0 contributions to HECO production cross sections are minimal at current LHC energies, where electroweak contributions to proton content are suppressed. These contributions could become significant at future colliders operating at higher energies, such as ~ 100 TeV, where electroweak effects grow in importance [225].

For the scope of this thesis, the focus is on dominant photon-mediated processes, leaving the exploration of electroweak contributions to future investigations.

4.2.4 HECO Self-Energy and Analytical Considerations

This section outlines the analytical evaluation of the HECO self-energy, incorporating resummed corrections, with an emphasis on high-energy exchanges involving the Z^0-boson. These calculations are integral to deriving the effective theory's Feynman rules for HECO production, particularly in the context of implementing resummation effects in UFO models and MadGraph simulations, as discussed in Section 4.2.5.

When the photon is the only gauge boson mediating interactions, the HECO fermion self-energy at zero external momentum, accounting for resummation effects (*cf.* Eqs. (4.17) and (4.18)), is expressed as:

$$\begin{aligned}\Sigma_1(0) &= \frac{ig^2}{1+\omega}\int \frac{d^4p}{(2\pi)^4}\gamma^\mu \frac{M+\not{p}}{p^2-M^2}\gamma^\nu \frac{\eta_{\mu\nu}+\omega\, p_\mu p_\nu/p^2}{p^2} \\ &= \frac{4+\omega}{1+\omega}\frac{g^2 M}{16\pi^2}\ln\left(\frac{\Lambda^2+M^2}{M^2}\right). \end{aligned} \tag{4.35}$$

To obtain the final expression, the calculation is first performed in Euclidean momentum space, which is appropriate for introducing an UV momentum cutoff Λ in the momentum integrals. The Feynman gauge is adopted for the photon propagator. The aim here is to compare the respective contributions of the photon and the Z^0 boson to the HECO fermion self-energy. The relation between these contributions is independent of the specific regularisation scheme for the UV divergencies, as will be explicitly demonstrated later (see Eq.(4.37)). In this context, the introduction of an UV momentum cutoff Λ is for the sake of simplicity and concreteness only. It is noted that, in the expression for the photon propagator in Eq. (4.35), the corrections $Z-1$ are neglected, as they are of order $Z^\star \sim 1$ and do not play a significant role in the present context It will be shown that the effects of photon polarisation corrections are effectively cancelled by the corresponding contributions from the Z^0 boson. Thus, only the dressed fermion mass M should be considered in the "one-loop-like" diagram associated with the self-energy in Eq. (4.35), which suffices for the present purpose. This approximation enables an analytic expression for the modified fixed-point solution when the Z^0-boson corrections are included.

If the HECO fermion also couples to a Z^0 boson with mass M_Z, the DS equation for the fermion self-energy acquires an additional term, denoted Σ_2, in which the dressed fermion propagator is inserted inside the loop. The one-loop resummed Z^0-boson propagator, given in Eq. (4.33), is considered in the high-energy limit and in Feynman gauge. To obtain the corresponding contribution to the HECO fermion self-energy, it is understood that both the integration momenta and the gauge boson propagators are analytically continued to Euclidean momentum space, with a UV momentum cutoff Λ applied to regulate the integrals. This leads to the expression:

$$\begin{aligned}\Sigma_2(0) &= \frac{ig'^2}{1+\omega_{Z^0}} \int \frac{d^4p}{(2\pi)^4} \gamma^\mu \frac{M+\not{p}}{p^2-M^2} \gamma^\nu \frac{\eta_{\mu\nu}+\omega_{Z^0} p_\mu p_\nu/p^2}{p^2-M_Z^2} \\ &= \frac{4+\omega_{Z^0}}{(1+\omega_{Z^0})16\pi^2} \frac{g'^2 M}{M^2-M_Z^2} \times \left(M^2 \ln\left(\frac{\Lambda^2+M^2}{M^2}\right) - M_Z^2 \ln\left(\frac{\Lambda^2+M_Z^2}{M_Z^2}\right)\right) ,\end{aligned} \tag{4.36}$$

where g' denotes the relevant coupling determined from Eq. (4.29). In the high-energy limit, where $M_Z \ll M < \Lambda$, the Z^0-boson contribution is found to be approximately proportional to the photon contribution:

$$\Sigma_2(0) \simeq \frac{(4+\omega_{Z^0})\,(1+\omega)}{(1+\omega_{Z^0})\,(4+\omega)}\frac{g'^2}{g^2}\Sigma_1(0) \equiv \mathcal{A}\,\frac{g'^2}{g^2}\Sigma_1(0)\ . \tag{4.37}$$

This suggests that the calculation of the fermion self-energy, initially performed under the assumption of photon exchange only, can be generalised to incorporate contributions from the Z^0-boson by employing an effective replacement:

$$g^2 \to \hat{g}^2 \equiv g^2 + \mathcal{A}\,g'^2\ . \tag{4.38}$$

Considering the processes under investigation and the structural similarity between the propagators of the high-energy Z^0-boson and the photon, the numerical analysis adopts the approximation $\mathcal{A} \sim 1$. Specifically, in the subsequent analysis presented in Section 4.2.5, the following value is used for concreteness:

$$\mathcal{A} = \frac{3}{4}\ . \tag{4.39}$$

This substitution modifies the self-energy flow equations to include the combined effects of the photon and Z^0-boson interactions:

$$\begin{aligned}
\mathcal{Z} &= 1 + \frac{\hat{g}^2}{8\pi^2}\ln\left(\frac{\mathcal{Z}k}{M}\right), \\
\mathcal{Z}\omega &= \frac{g^2}{6\pi^2}\ln\left(\frac{\mathcal{Z}k}{M}\right), \\
\mathcal{Z}\left(1-\frac{m}{M}\right) &= \frac{\hat{g}^2}{8\pi^2}\frac{4+\omega}{1+\omega}\ln\left(\frac{\mathcal{Z}k}{M}\right).
\end{aligned} \tag{4.40}$$

As a result, the expression for k/m is modified in this scenario, replacing Eq. (4.11) with the following:

$$\frac{k}{m} = \frac{(3+4\eta)\mathcal{Z} - 4\eta}{9(\hat{\mathcal{Z}}_+ - \mathcal{Z})(\mathcal{Z} - \hat{\mathcal{Z}}_-)}\exp\left(\frac{8\pi^2}{\hat{g}^2}(\mathcal{Z}-1)\right), \tag{4.41}$$

where $\eta \equiv g^2/\hat{g}^2 < 1$, and the parameters $\hat{\mathcal{Z}}_\pm$ are defined as:

$$\hat{\mathcal{Z}}_\pm = \frac{2}{9}(3+\eta)\left(1 \pm \sqrt{1 - \frac{9\eta}{(3+\eta)^2}}\right). \tag{4.42}$$

Both $\hat{\mathcal{Z}}_+$ and $\hat{\mathcal{Z}}_-$ are real for any value of η, with $\hat{\mathcal{Z}}_+ > 1$. Within the range $0 < \eta < 1$, $\hat{\mathcal{Z}}_- < 1$, which constrains the regime of interest to $1 \leq \mathcal{Z} \leq \hat{\mathcal{Z}}_+$, ensuring $k > 0$. This behaviour is analogous to the scenario involving only photon exchange, albeit with modified UV fixed-point parameters.

The UV fixed point for this case is characterised by:

$$\begin{aligned}
\hat{\mathcal{Z}}^\star &= \hat{\mathcal{Z}}_+, \\
\hat{\omega}^\star &= \frac{4}{3}\eta\left(1 - \frac{1}{\hat{\mathcal{Z}}^\star}\right), \\
\left(\frac{M}{k}\right)^\star &= \hat{\mathcal{Z}}^\star \exp\left(-\frac{2\pi}{\hat{\alpha}^\star}(\hat{\mathcal{Z}}^\star - 1)\right),
\end{aligned} \tag{4.43}$$

where $\hat{\alpha}^\star = \frac{g^2}{4\pi\eta} = \frac{\hat{g}^2}{4\pi}$. As in the photon-only case, discussed in Sections 4.2.2.1 and 4.2.3.1, the effective coupling in tree-level DY or PF processes is rescaled by a factor $1/\sqrt{1+\omega}$.

Consequently, the effective fine-structure parameter at the fixed point, incorporating Z^0-boson effects, is given by:

$$\hat{\alpha}^\star_{\text{eff}} = \frac{\hat{g}^2/4\pi}{1+\hat{\omega}^\star}. \tag{4.44}$$

Numerical analysis reveals that, for a fixed scale k, the physical mass $M(k)/Z(k)$ increases as g' increases (or equivalently as η decreases). This is consistent with the expectation that stronger interactions induce larger corrections to the mass.

If the UV fixed-point scale is identified with the UV cutoff Λ, which in this framework represents the scale of NP accessible to collider experiments, the fixed-point value of the physical mass in the presence of Z^0-mediated interactions, denoted as:

$$\hat{\mathcal{M}}^\star \equiv \mathcal{M}(k = \Lambda), \tag{4.45}$$

differs from the corresponding value obtained for photon-only interactions, as discussed in Section 4.2.3.1, Eq. (4.13). This distinction arises from the differences in the UV fixed-point parameters, Eqs. (4.43) and (4.44), compared to those derived in the photon-only case, Eqs. (4.13) and (4.14). The hat notation is used to indicate the modified fixed-point mass. This difference is of physical significance and should be accounted for when deriving mass bounds for HECOs from collider experiments using the resummation scheme.

4.2.5 Implementation in MadGraph and Cross section Analysis

The implementation of the resummation effects described above has been carried out specifically for Universal Feynrules Output (UFO) models [226, 227]. These models are designed to be compatible with Monte Carlo event generators such as MadGraph5_aMC@NLO 3.5.1 [228], which is the tool employed in this study.

The primary goal is to simulate the production mechanisms of DY and PF involving spin-1/2 HECOs at the LHC using the resummation scheme described in the previous section. For the case of DY production, both γ-only and γ/Z^0 exchanges have been considered in the implementation.

Two distinct models have been developed:

- **γ exchange UFO model**: It takes into account the sole contribution from γ exchange, which is suitable for simulating both DY and PF processes. It uses the Feynman rules from Eq. (4.25), stemming from the effective Lagrangian in Eq. (4.17), at the UV fixed point in Eqs. (4.13), (4.23) and (4.24).

- **γ/Z^0 exchange UFO model**: This model includes the additional exchange of the Z^0 boson in DY production. It makes use of the pertinent Feynman rules at the UV fixed point in Eqs. (4.38), (4.39), (4.43) and (4.44), in the non-chiral vector case described in Eq. (4.29), which is the focus here.

By incorporating the resummation effects into the UFO models, reliable predictions for the production mechanisms under study are provided. The simulations using the implemented models allow for the study of various observables related to DY and PF processes involving spin-$1/2$ HECOs at the LHC and the effects of the resummation on the predicted outcomes. These UFO models are meant to become a tool for comparison of experimental results with theoretical benchmarks. A summary of the Feynmam rules used and the validation procedure and results are given in Appendices A and B, respectively. The UFO models are validated by comparing the simulation-estimated cross section values against the outcome of analytical calculations using MATHEMATICA.

In addition to the standard input parameters such as centre-of-mass energy and parton distribution functions (PDFs), the UFO models introduced in this study incorporate two new parameters:

- The multiplicity of the charge, denoted by n, which appears in the coupling definition $g = ne$, where e is the elementary electric charge. The HECO charge is also denoted by $Q = ne$.
- The cutoff energy scale parameter, denoted by Λ, defined in Eq. (4.24).

Both the multiplicity and the cutoff parameter have a direct impact on the HECO mass and, consequently, affect the calculated cross section value. Furthermore, for the specific centre-of-mass energies considered in this study, i.e., those at the LHC, the fine-structure constant is set $\alpha_{\text{EM}} = 1/127.94$, i.e. to the value pertinent for the Z^0-boson mass scale. It is worth stressing here that the choice of this value affects significantly the cross section values.

Tables 4.1, 4.2 and 4.3 provide a comparison between the cross section values obtained at the tree level and after incorporating the resummation effects for both the DY and PF processes. The calculations are performed considering pp collisions at $\sqrt{s} = 13$ TeV.

For the DY process, the `NNPDF23` [229] PDF is utilised, while for the PF process, the `LUXqed17` [230] PDF is employed. These PDF choices are used in conjunction with the UFO model to calculate the cross section values. Upon comparing the cross section values before and after including resummation effects, one can see that for the same mass — bare for tree level and $\mathcal{M}(\Lambda)$ for the resummation scheme — the cross sections remain of the same order of magnitude. However, the DS resummation leads to a noticeable increase, highlighting its impact and validating the UFO models and underlying calculations.

In addition, the cross section values related to the PF process turn out to be higher than those of the DY process at the LHC energies and for this range of HECO masses. This behaviour arises from the cross section dependence which is $\propto n^2$ for DY, whereas it is $\propto n^4$ for PF.

Table 4.1: Cross section comparison for HECO production in pp collisions at $\sqrt{s}$ = 13 TeV via the Drell-Yan (γ−only) process between tree level and after resummation with $\Lambda = 2$ TeV. The HECO mass is also listed. The `NNPDF23` PDF is used.

DY $pp \to \gamma \to \mathcal{H}\overline{\mathcal{H}}$ @ $\sqrt{s} = 13$ TeV, $\Lambda = 2$ TeV			
Q (e)	$\sigma_{\text{tree-level}}$ (fb)	σ_{resum} (fb)	M (TeV)
20	775	1692	0.507
60	4.959	10.79	1.717
100	5.949	12.95	1.893
140	9.134	19.86	1.945
180	13.67	29.71	1.966
220	19.31	42.08	1.977

Table 4.2: Cross section comparison for HECO production in pp collisions at $\sqrt{s}$ = 13 TeV via the Drell-Yan (including Z^0) process at tree level and after resummation with $\Lambda = 2$ TeV. The HECO mass is also listed. The `NNPDF23` PDF is used.

DY $pp \to \gamma/Z^0 \to \mathcal{H}\overline{\mathcal{H}}$ @ $\sqrt{s} = 13$ TeV, $\Lambda = 2$ TeV			
Q (e)	$\sigma_{\text{tree-level}}$ (fb)	σ_{resum} (fb)	M (TeV)
20	101.4	211.8	0.758
60	3.125	6.527	1.796
100	4.722	9.835	1.924
140	7.752	16.25	1.961
180	11.95	24.92	1.976
220	17.22	35.94	1.984

Another interesting point, seen when comparing the Tables 4.1 and 4.3 with Table 4.2, is that the HECO mass for a specific value of charge and cutoff scale depends on the inclusion of the Z^0 in the vertex. As discussed

Table 4.3: Cross section comparison for HECO production in pp collisions at $\sqrt{s} = 13$ TeV via the PF process at tree level and after resummation with $\Lambda = 2$ TeV. The HECO mass is also listed. The PDF `LUXqed17` is used.

PF $pp \to \mathcal{H}\overline{\mathcal{H}}$ @ $\sqrt{s} = 13$ TeV, $\Lambda = 2$ TeV			
Q (e)	$\sigma_{\text{tree-level}}$ (fb)	σ_{resum} (fb)	M (TeV)
20	1.321×10^4	6.271×10^4	0.507
60	8.466×10^2	4.025×10^3	1.717
100	2.895×10^3	1.372×10^4	1.893
140	8.753×10^3	4.170×10^4	1.945
180	2.175×10^4	1.030×10^5	1.966
220	4.612×10^4	2.184×10^5	1.977

in Section 4.2.3.3 (*cf.* Eqs. (4.43), (4.45)), the inclusion of Z^0 in the vertex leads to a higher HECO mass M compared to the case where only $\mathcal{H}$–$\overline{\mathcal{H}}$–γ interactions are considered. It is worth reiterating here that the UFO model with $\mathcal{H}$–$\overline{\mathcal{H}}$–γ is used for resummation in DY process with γ-only (Table 4.1) and in PF (Table 4.3), whereas the $\mathcal{H}$–$\overline{\mathcal{H}}$–γ/Z^0 UFO model is deployed for the DY with γ/Z^0 exchange (Table 4.2).

The aforementioned points are also demonstrated in Figure 4.4 where the cross section versus the HECO mass M is drawn before and after resummation at $\sqrt{s} = 13$ TeV for various charge values. One observes that the production becomes more abundant with resummation by a factor of ~ 2.1 and ~ 4.75 for DY and PF, respectively. The stronger impact of the resummation on the PF cross section when compared with the DY process is due to the presence of two vertices involving a HECO in the former as opposed to one vertex in the latter, as shown in the related diagrams in Figure 4.3.

Figures 4.5, 4.6, and 4.7 show the cross section values for DY and PF processes for fermionic HECOs as a function of mass M, charge Q, and cutoff Λ, respectively. As expected, the cross section consistently increases as Q becomes larger for the same HECO mass M, due to the stronger electromagnetic coupling. However, when varying Q at fixed Λ, the behaviour becomes non-monotonic: the cross section initially drops with increasing Q, then slightly rises beyond a certain charge value. This trend reflects the highly non-linear dependence of the resummed HECO mass on charge, described analytically in Eq. (4.24). As n, i.e. Q, increases, the mass grows rapidly, eventually approaching the cutoff Λ, which suppresses the production rate and offsets the gain from stronger coupling. This explains the observed behaviour for lower charges, such as the $Q = 20e$ case in Fig. 4.7, where the cross section remains higher than for larger charges across the full Λ range. For smaller n, the resummed mass stays below Λ, resulting in a much lighter HECO that is more abundantly produced.

One can note again here the consistently more abundant production characterising PF when compared to the DY process at the considered collision energy of 13 TeV.

While here the main focus is on pp collisions, motivated by the recent searches conducted by LHC experiments such as ATLAS [148] and MoEDAL [164, 165], it is possible to extend the analysis to other colliding particles. By changing the type of collisions to e^+e^- or $\mu^+\mu^-$, for instance, the potential for discovering HECOs at future lepton colliders can be explored using this model. This flexibility allows for a broader investigation of HECOs and their detection prospects in various collider environments.

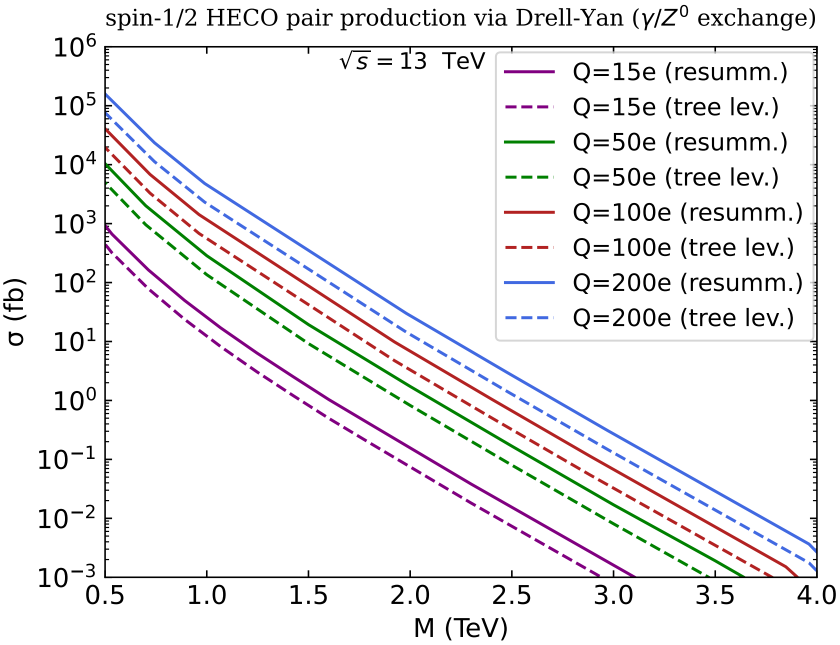

(a) DY cross section vs mass M

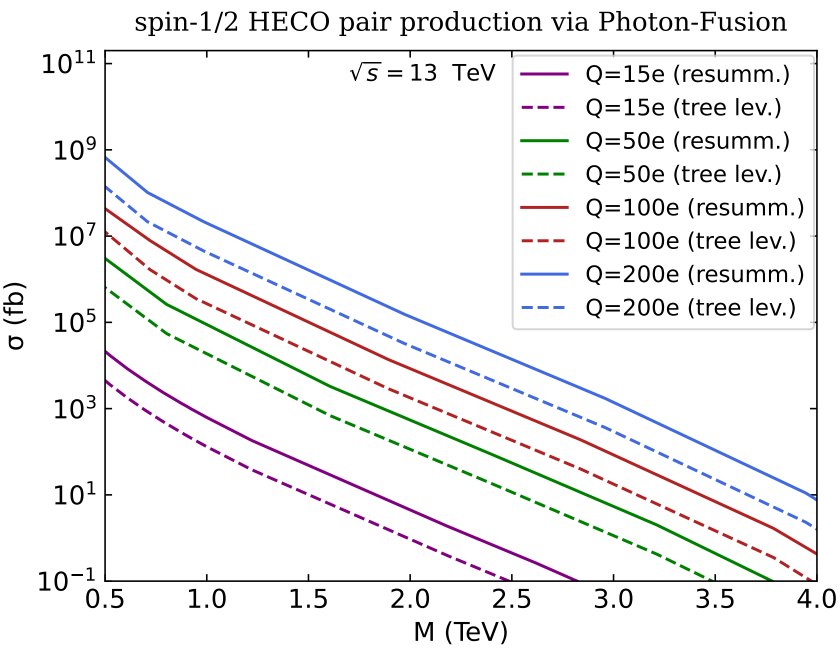

(b) PF cross section vs mass M

Figure 4.4: Comparison of cross section values obtained after (solid line) and before (dashed-line) resummation as a function of the HECO mass M for electric charges $Q = 15e$, $50e$, $100e$ and $200e$, demonstrating the significant effect of the resummation in the increase of the corresponding cross sections.

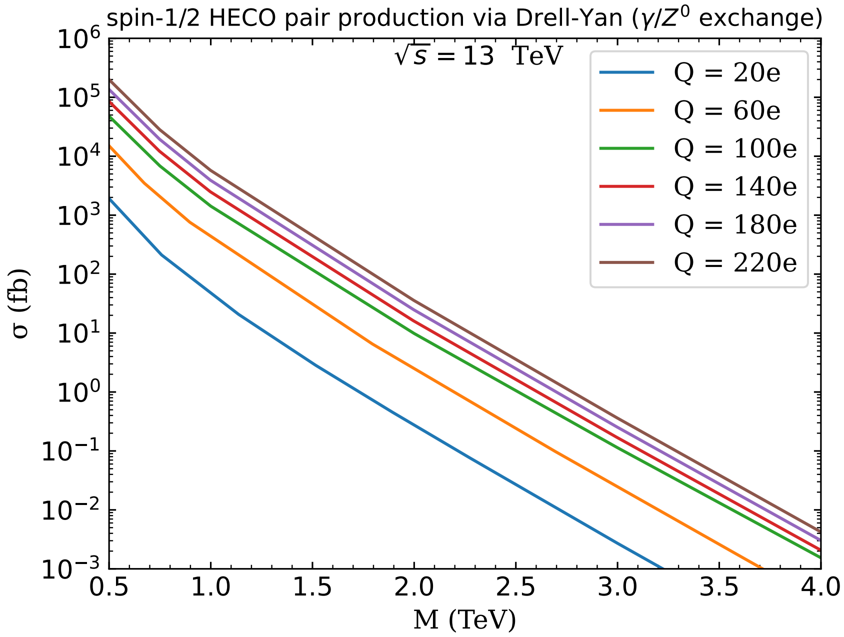

(a) DY cross section vs mass M

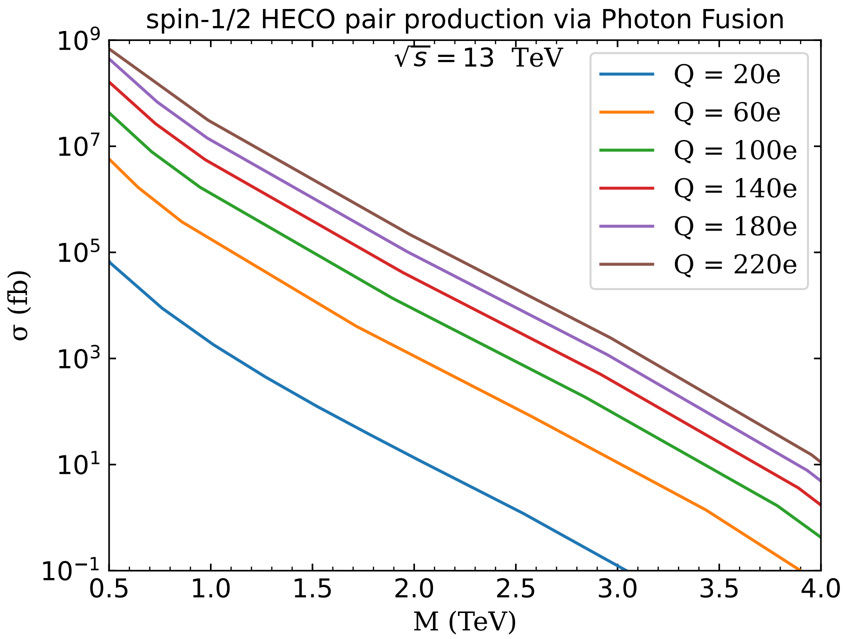

(b) PF cross section vs mass M

Figure 4.5: Cross section values for spin-1/2 HECO pair production via DY (top) and PF (bottom) after resummation as a function of mass M for various charge values.

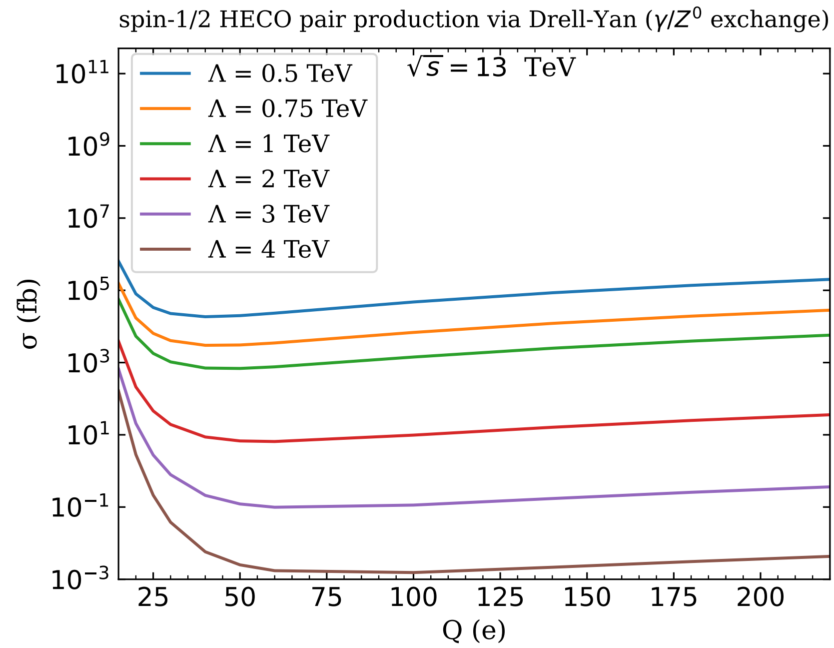

(a) DY cross section vs charge Q

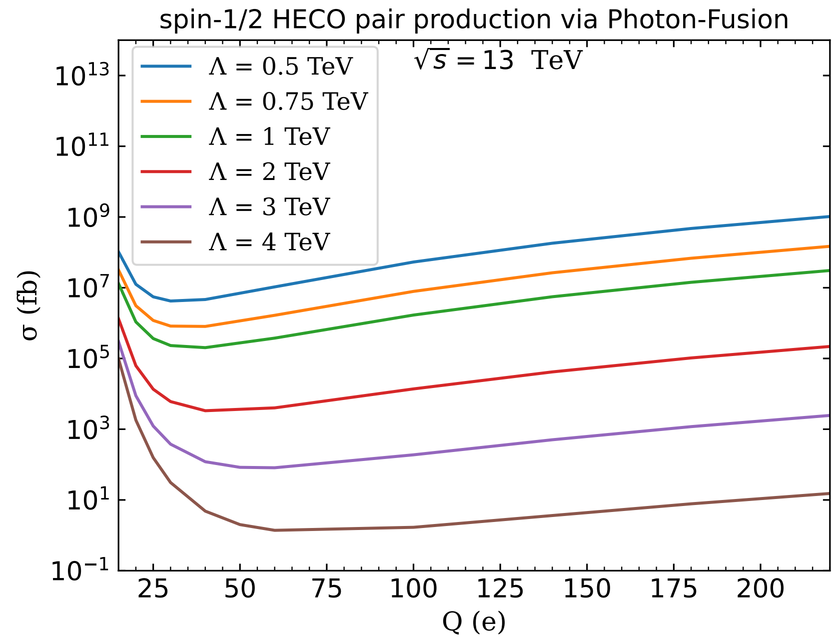

(b) PF cross section vs charge Q

Figure 4.6: Cross section values for spin-1/2 HECO pair production via DY (top) and PF (bottom) after resummation as a function of charge Q for different cutoff Λ values.

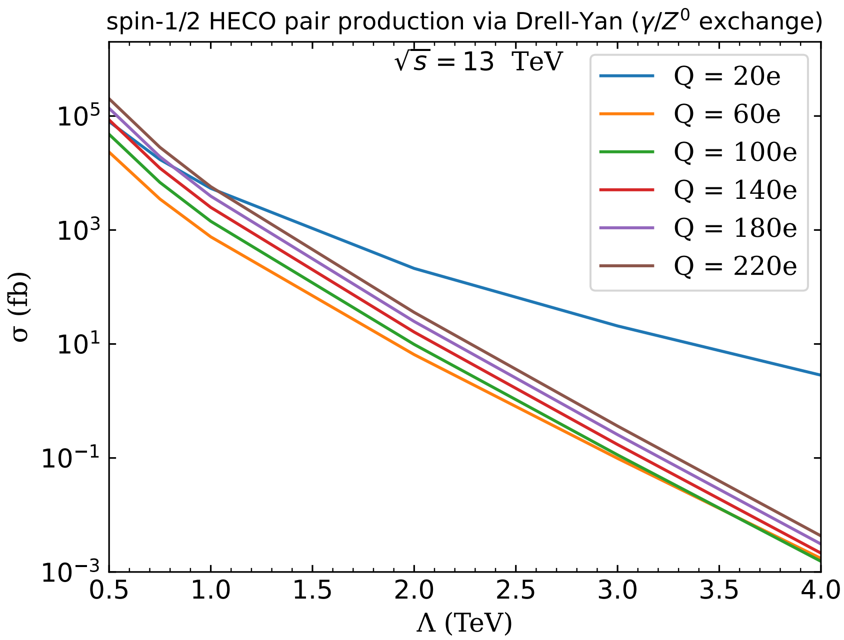

(a) DY cross section vs cutoff Λ

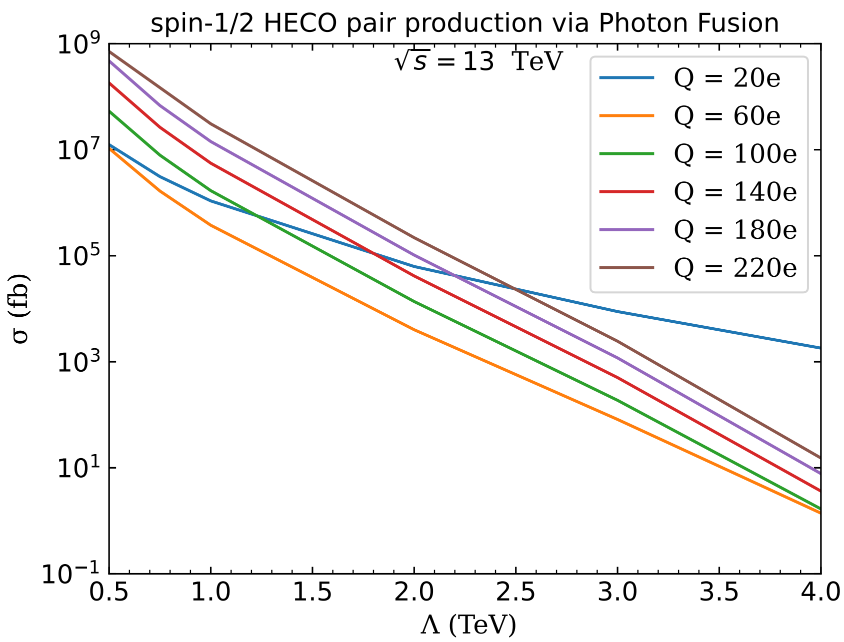

(b) PF cross section vs cutoff Λ

Figure 4.7: Cross section values for spin-$1/2$ HECO pair production via DY (top) and PF (bottom) after resummation as a function of the cutoff Λ for various Q.

4.3 Resummation for scalar HECOs

In the previous section, the DS resummation scheme for quantum corrections in strongly coupled QED was applied to spin-1/2 HECOs.

In this section, the resummation formalism is extended to scalar HECOs. Scalar HECOs, as hypothesised spin-0 particles with large electric charge, present distinct challenges compared to their fermionic counterparts. Unlike the fermionic case, the stability of a UV fixed point for scalar HECOs necessitates sufficiently strong self-interactions, where the scalar self-coupling must significantly exceed the squared gauge coupling. Once a UV fixed point is established, the dressed mass of the scalar HECO can be determined by solving the associated resummation equations. These results can then be employed to extract reliable mass limits using current collider data.

The implementation of the resummation framework for scalar HECOs is discussed in the following subsections.

4.3.1 Non-Perturbative Resummation Approach to Scalar HECOs

4.3.1.1 Overview of Scalar Quantum Electrodynamics

The formulation begins with the bare Lagrangian, expressed as:

$$\mathcal{L}_{\text{bare}} = \frac{1}{2}A^{\mu}\left[\eta_{\mu\nu}\Box - (1-\lambda)\partial_{\mu}\partial_{\nu}\right]A^{\nu} + D_{\mu}\phi(D^{\mu}\phi)^{*} - m^{2}\phi\phi^{*} - \frac{h}{4}(\phi\phi^{*})^{2} \ , \tag{4.46}$$

where $D_{\mu} = \partial_{\mu} + igA_{\mu}$, and λ represents the gauge-fixing parameter.

To account for quantum corrections, a dressed Lagrangian is considered, taking the form [231]:

$$\begin{aligned}\mathcal{L}_{\text{eff}} = &\frac{1}{2}A^{\mu}\left[\eta_{\mu\nu}\Box - (1-\lambda)\partial_{\mu}\partial_{\nu}\right]A^{\nu} \\ &+ \frac{\omega}{2}A^{\mu}\left[\eta_{\mu\nu}\Box - \partial_{\mu}\partial_{\nu}\right]A^{\nu} + \mathcal{Z}^{2}D_{\mu}\phi(D^{\mu}\phi)^{*} - M^{2}\phi\phi^{*} - \frac{H}{4}(\phi\phi^{*})^{2} \ .\end{aligned} \tag{4.47}$$

In this formulation, only the transverse part of the gauge field receives quantum corrections, and the scalar kinetic term remains consistent with gauge invariance.

The resulting dressed propagators for the scalar and gauge bosons are:

$$G(p) = \frac{i}{\mathcal{Z}^2 p^2 - M^2} , \tag{4.48}$$

$$D_{\mu\nu}(q) = \frac{-i}{(1+\omega)q^2}\left(\eta_{\mu\nu} + \frac{1+\omega-\lambda}{\lambda}\frac{q_\mu q_\nu}{q^2}\right) , \tag{4.49}$$

respectively. The corresponding gauge interaction vertices are given by:

$$\begin{aligned} &\text{3-point:} \qquad ig\mathcal{Z}(p^1_\mu \pm p^2_\mu) , \\ &\text{4-point:} \qquad 2ig^2\mathcal{Z}^2\eta_{\mu\nu} . \end{aligned} \tag{4.50}$$

By rescaling the fields as $A_\mu \to A_\mu/\sqrt{1+\omega}$ and $\phi \to \phi/\mathcal{Z}$, the Lagrangian can be rewritten in a canonically normalised form:

$$\begin{aligned} \tilde{\mathcal{L}}_{\text{eff}} = &\frac{1}{2}A^\mu\left[\eta_{\mu\nu}\Box - \frac{1-\lambda+\omega}{1+\omega}\partial_\mu\partial_\nu\right]A^\nu \\ &+ (\partial_\mu\phi + i\tilde{g}A_\mu\phi)(\partial^\mu\phi^* - i\tilde{g}A^\mu\phi^*) - \tilde{M}^2\phi\phi^* - \frac{\tilde{H}}{4}(\phi\phi^*)^2 . \end{aligned} \tag{4.51}$$

where the effective parameters are:

$$\tilde{g} \equiv \frac{g}{\sqrt{1+\omega}} \quad , \quad \tilde{H} \equiv \frac{H}{\mathcal{Z}^4} \quad , \quad \tilde{M}^2 \equiv \frac{M^2}{\mathcal{Z}^2} . \tag{4.52}$$

This rescaling assumes the validity of the Ward identities, ensuring consistency between the wavefunction renormalisations of the fields and vertices. However, this assumption is questioned later, where the effective theory is analysed as a bare theory in a specific gauge framework (see Section 4.3.4).

4.3.2 Resummation

The quantum corrections $M^2 - m^2, \mathcal{Z} - 1, \omega, H$ are assumed to be momentum-independent. However, these quantities generally depend on the scale k introduced by dimensional regularisation. The consistency of scale-independent corrections is assessed via the fixed points in the flow equations for k.

The resummation scheme employed considers one-loop-like Feynman diagrams for quantum corrections to scalar and gauge propagators, as well as the scalar self-coupling. In this approach, the bare propagators and vertices are replaced by their dressed counterparts. While this method bears similarity to the DS non-perturbative approach, it excludes two-loop-like graphs. This feature allows the couplings h and g^2 to take large values, motivating this study.

The self-consistent equations derived in $d = 4 - \epsilon$ dimensions (details in Appendix A) are expressed as:

$$\begin{aligned}
1 - \frac{m^2}{M^2} &= \frac{1}{8\pi^2 \mathcal{Z}^2}\left(\frac{g^2}{\lambda} + \frac{H}{\mathcal{Z}^2}\right)\frac{1}{\epsilon}\left(\frac{k\mathcal{Z}}{M}\right)^{\epsilon}, \\
\mathcal{Z}^2 &= 1 + \frac{g^2}{8\pi^2}\frac{1}{\epsilon}\left(\frac{k\mathcal{Z}}{M}\right)^{\epsilon}\left(\frac{3}{1+\omega} - \frac{1}{\lambda}\right), \\
\omega &= \frac{g^2}{24\pi^2 \mathcal{Z}^2}\frac{1}{\epsilon}\left(\frac{k\mathcal{Z}}{M}\right)^{\epsilon}, \\
H &= h + \frac{3}{8\pi^2}\left(-\frac{H^2}{\mathcal{Z}^4} + \frac{g^4}{\lambda}(2\mathcal{Z}^2 - \lambda^{-1}) + \frac{Hg^2}{\mathcal{Z}^2\lambda}\right)\frac{1}{\epsilon}\left(\frac{k\mathcal{Z}}{M}\right)^{\epsilon}.
\end{aligned} \tag{4.53}$$

Given that the couplings g and h remain constant with respect to the renormalization scale k, we derive the RG flow equations for the dressed parameters M, $\mathcal{Z}$, ω, and H. These equations emerge from the scale dependence of the renormalised quantities within the dimensional regularization framework. Specifically, the scale derivatives are expressed as:

$$\frac{\partial}{\partial k}\left[\mathcal{Z}^2\left(\frac{g^2}{\lambda}+\frac{H}{\mathcal{Z}^2}\right)^{-1}\left(1-\frac{m^2}{M^2}\right)\right]=\frac{1}{8\pi^2}\left(\frac{k\mathcal{Z}}{M}\right)^{-1}\frac{\partial}{\partial k}\left(\frac{k\mathcal{Z}}{M}\right),$$

$$\frac{\partial}{\partial k}\left[\frac{\lambda(1+\omega)}{3\lambda-1-\omega}(\mathcal{Z}^2-1)\right]=\frac{g^2}{8\pi^2}\left(\frac{k\mathcal{Z}}{M}\right)^{-1}\frac{\partial}{\partial k}\left(\frac{k\mathcal{Z}}{M}\right),$$

$$\frac{\partial}{\partial k}(\mathcal{Z}^2\omega)=\frac{g^2}{24\pi^2}\left(\frac{k\mathcal{Z}}{M}\right)^{-1}\frac{\partial}{\partial k}\left(\frac{k\mathcal{Z}}{M}\right),$$

$$\frac{\partial}{\partial k}\left[\left(-\frac{H^2}{\mathcal{Z}^4}+\frac{g^4}{\lambda^2}(2\mathcal{Z}^2-1)+\frac{Hg^2}{\mathcal{Z}^2\lambda}\right)^{-1}(H-h)\right]=\frac{3}{8\pi^2}\left(\frac{k\mathcal{Z}}{M}\right)^{-1}\frac{\partial}{\partial k}\left(\frac{k\mathcal{Z}}{M}\right). \tag{4.54}$$

To solve these flow equations, we impose the following boundary conditions at the reference scale $k = m$:

$$M(m)=m\ ,\quad \mathcal{Z}(m)=1\ ,\quad \omega(m)=0\ ,\quad H(m)=h\ . \tag{4.55}$$

Integrating these relations, we obtain the set of self-consistent RG equations that describe how the dressed quantities M, $\mathcal{Z}$, ω, and H evolve with the scale k:

$$\begin{aligned}
1-\frac{m^2}{M^2} &= \frac{g^2}{8\pi^2\mathcal{Z}^2}\left(\frac{1}{\lambda}+\frac{H}{g^2\mathcal{Z}^2}\right)\ln\left(\frac{k\mathcal{Z}}{M}\right)\ , \\
\mathcal{Z}^2 &= 1+\frac{g^2}{8\pi^2}\frac{3\lambda-1-\omega}{\lambda(1+\omega)}\ln\left(\frac{k\mathcal{Z}}{M}\right)\ , \\
\omega &= \frac{g^2}{24\pi^2\mathcal{Z}^2}\ln\left(\frac{k\mathcal{Z}}{M}\right)\ , \\
H &= h+\frac{3}{8\pi^2}\left(-\frac{H^2}{\mathcal{Z}^4}+\frac{g^4}{\lambda^2}(2\mathcal{Z}^2-1)+\frac{Hg^2}{\mathcal{Z}^2\lambda}\right)\ln\left(\frac{k\mathcal{Z}}{M}\right)\ .
\end{aligned} \tag{4.56}$$

These equations encapsulate the non-perturbative effects on the dressed parameters, showing their logarithmic dependence on the scale k. In the next section, we will investigate the UV limit $k \to \infty$ to analyse the existence and properties of the corresponding fixed points.

4.3.3 Fixed point and dressed HECO mass

Our goal is to identify a fixed-point solution $(\omega^\star, \mathcal{Z}^\star, H^\star)$ of Eqs. (4.56) in the limit $k \to \infty$, while keeping the ratio k/M constant to ensure that the logarithmic terms remain finite. The existence of such a fixed point would validate the assumption that the quantum corrections under consideration are momentum-independent.

By appropriately rearranging Eqs. (4.56), it is possible to eliminate the logarithmic terms. Taking the limit $M \to \infty$ (with m held finite), we arrive at the following set of equations:

$$\begin{aligned} (\mathcal{Z}^\star)^2 &= \frac{\lambda(1+\omega^\star)}{\lambda + (3-8\lambda)\omega^\star + 3(\omega^\star)^2} , \\ 1 &= 3\omega^\star \left(\frac{1}{\lambda} + \frac{H^\star}{g^2(\mathcal{Z}^\star)^2} \right) , \\ H^\star &= h + 9\omega^\star \left(-\frac{(H^\star)^2}{g^2(\mathcal{Z}^\star)^2} + \frac{g^2}{\lambda^2}(\mathcal{Z}^\star)^2 \left(2(\mathcal{Z}^\star)^2 - 1 \right) + \frac{H^\star}{\lambda} \right) . \end{aligned} \tag{4.57}$$

Assuming a solution exists in the regime where $g^2 \ll h$ and the gauge parameter λ is finite, we can approximate the solution as:

$$\omega^\star \simeq \frac{4g^2}{3h} , \quad (\mathcal{Z}^\star)^2 \simeq 1 + \frac{4g^2}{h}\left(3 - \frac{1}{\lambda}\right) , \quad H^\star \simeq \frac{h}{4} , \tag{4.58}$$

where higher-order terms in g^2/h, as well as additional λ-dependent corrections, are neglected.

Therefore, to first order in the limit $g^2/h \ll 1$, both $\omega^\star$ and $H^\star$ exhibit gauge independence. In contrast, the gauge dependence of $\mathcal{Z}^\star$ is relatively weak (a mild gauge dependence is expected in truncated DS systems, such as the one considered here). It is worth noting that the correction $H^\star - h \simeq -\frac{3h}{4}$ is not necessarily perturbative, which remains consistent with the framework adopted in this study.

The requirement for $\mathcal{Z}$ to be real, i.e., $(\mathcal{Z}^\star)^2 > 0$, imposes constraints on the allowed values of the gauge parameter λ, as inferred from Eq. (4.58). Additionally, unitarity of the S-matrix demands that $\mathcal{Z}^\star \geq 1$ [231]. In the limit case $\lambda \to \infty$, the unitarity condition leads to:

$$g^2/h > 0\,. \tag{4.59}$$

Given the requirement of gauge invariance for physically relevant observables, the above condition must hold for all permissible values of λ. Consequently, the following constraint on the gauge parameter is obtained:

$$\lambda > \frac{1}{3}\,, \tag{4.60}$$

thereby excluding the $\lambda \to 0$ gauge from the considered truncation scheme.

The positivity condition for $(\mathcal{Z}^\star)^2$ in a general gauge, subject to the constraint in Eq. (4.60) and the requirement $\omega^\star > 0$ (as indicated by Eq. (4.59)), necessitates that the denominator in the first equation of Eq. (4.58) be positive. This leads to the following condition on $\omega^\star$:

$$\begin{aligned} \text{either} \quad 0 \leq \omega^\star < \frac{8\lambda - 3 - \sqrt{64\lambda^2 - 60\lambda + 9}}{6} \\ \text{or} \quad \omega^\star > \frac{8\lambda - 3 + \sqrt{64\lambda^2 - 60\lambda + 9}}{6} \;. \end{aligned} \tag{4.61}$$

Furthermore, the unitarity requirement $\mathcal{Z}^\star > 1$ implies the condition:

$$0 < \omega^\star < 3\lambda - 1 \;. \tag{4.62}$$

Utilising the third equation of the RG flow system in Eq. (4.56), the effective (physical) mass of the scalar HECO in the UV limit, as defined by Eq. (4.72), is given by:

$$\tilde{M} = \Lambda \, \exp\left[-\frac{32\pi^2}{h}\left(1 + \frac{4g^2}{h}\left(3 - \frac{1}{\lambda}\right)\right)\right] \;. \tag{4.63}$$

Any residual gauge dependence, arising from the inherent limitations of the resummation scheme (specifically due to the partial selection of diagrams), can be absorbed into the definition of the cutoff scale Λ. This redefinition ensures that the resulting physical mass remains gauge invariant. Accordingly, the scalar HECO mass is expressed as:

$$\tilde{M} = \Lambda \exp\left(-\frac{32\pi^2}{h}\right) . \tag{4.64}$$

The approximate gauge invariance enables the selection of a convenient gauge for the analysis of the relevant HECO production cross sections.

The choice of gauge is guided by the Pinch Technique (PT) [221, 222, 232, 233], a method originally developed for non-Abelian gauge theories. The PT demonstrates that the gauge independence of scattering amplitudes can be achieved by isolating a specific subset of diagrams computed in the Feynman gauge, $\lambda = 1$. This correspondence arises from a subtle connection between the PT and the background field method, a gauge-fixing procedure that preserves gauge invariance at the level of the effective action. The PT ensures that, at all orders in perturbation theory, the gauge-invariant effective n-point correlation functions derived using this method coincide with the background field n-point functions evaluated at the background Feynman gauge ($\lambda = 1$).

Since the interactions under consideration are EM (Abelian) in nature, it is important to note that the validity of the Pinch Technique (PT) has also been established for Abelian gauge theories [234]. In particular, the PT has been successfully applied in the context of scalar electrodynamics (see also the Appendix of Ref. [235] for an analysis within a version of QED). Exploiting the previously discussed approximate gauge independence of the fixed-point structure described by Eq. (4.58), the gauge is fixed to the Feynman gauge ($\lambda = 1$) in the following analysis. This choice is motivated by the PT framework, wherein the Feynman gauge is regarded as the physical gauge.

For the specific choice of the Feynman gauge ($\lambda = 1$), the requirement that $(\mathcal{Z}^\star)^2$ remains positive imposes the following conditions for the existence of a consistent fixed-point solution:

$$\text{either} \quad 0 \le \omega^\star < \frac{5-\sqrt{13}}{6} \simeq 0.23 \quad \text{or} \quad \omega^\star > \frac{5+\sqrt{13}}{6} \simeq 1.43 . \tag{4.65}$$

Additionally, the unitarity condition of the S-matrix, which requires $\mathcal{Z}^\star \geq 1$ [231], leads to the constraint:

$$\omega^\star \leq 2 \ . \tag{4.66}$$

Combining these constraints, a consistent fixed point must lie within the following ranges:

$$\text{either} \quad 0 \leq \omega^\star \lesssim 0.23 \quad \text{or} \quad 1.43 \lesssim \omega^\star \leq 2 \ . \tag{4.67}$$

By expressing the ratios g^2/h and $H^\star/h$ as functions of $\omega^\star$, the following relations are obtained:

$$\begin{aligned}\frac{g^2}{h} &= \frac{3\,\omega^\star\Big(1 - 5\omega^\star + 3(\omega^\star)^2\Big)^2}{(1+\omega^\star)\Big(4 - 50\omega^\star + 189(\omega^\star)^2 - 549(\omega^\star)^3 + 243(\omega^\star)^4\Big)} \ , \\ \frac{H^\star}{h} &= \frac{(1-3\omega^\star)\Big(1 - 5\omega^\star + 3\omega^\star\Big)}{4 - 50\omega^\star + 189(\omega^\star)^2 - 549(\omega^\star)^3 + 243(\omega^\star)^4} \ .\end{aligned} \tag{4.68}$$

A numerical analysis reveals that the only range of $\omega^\star$ satisfying the conditions in Eq. (4.67), while ensuring both $\frac{g^2}{h} > 0$ and $\frac{H^\star}{h} > 0$, is:

$$0 \leq \omega^\star \lesssim 0.11 \ . \tag{4.69}$$

Under the Feynman gauge choice ($\lambda = 1$), the approximate solutions from Eq. (4.58) simplify to:

$$\omega^\star \simeq \frac{4g^2}{3h} \ , \quad (\mathcal{Z}^\star)^2 \simeq 1 + \frac{8g^2}{h} \ , \quad H^\star \simeq \frac{h}{4} \ , \tag{4.70}$$

with these approximations holding in the regime where $g^2 \ll h$.

Combining Eqs. (4.69) and (4.70) yields the following upper bound:

$$\frac{g^2}{h} \lesssim 0.0825 \quad \Rightarrow \quad h \gtrsim 12.12\, g^2 \ . \tag{4.71}$$

The inequalities presented above are to be regarded as gauge independent. Consequently, the existence of a consistent fixed-point solution necessitates sufficiently strong self-interactions among the scalar HECOs in this model. This requirement contrasts with the case of spin-$1/2$ HECOs [216], where fermion-HECO self-interactions are not required for the formation of a fixed point.

The UV limit $k \to \infty$ is regularised by introducing a large but finite UV cutoff $\Lambda > 0$, which defines the energy scale below which the effective field theory remains valid. In this context, the UV fixed point is defined as the limit of the running scale:

$$k \to k_{\mathrm{UV}} = \Lambda\,. \tag{4.72}$$

In this limit, the effective (physical) gauge-invariant mass of the scalar HECO is given by Eq. (4.64). The analysis that follows assumes the saturation of the constraint on the interaction couplings, as expressed in Eq. (4.71) and discussed in Ref. [218]. Under this assumption, the scalar HECO mass takes the form:

$$\tilde{M} \simeq \Lambda \, \exp\left(-\frac{2.64\,\pi^2}{g^2}\right)\,, \tag{4.73}$$

which serves as the basis for the subsequent analysis of the relevant experimental searches.

4.3.4 MADGRAPH Implementation - Effective Feynman Rules

The photon propagator in Eq. (4.48) for $\lambda = 1$ suggests that the fixed point discussed earlier corresponds to a bare theory with an effective gauge choice:

$$\lambda_{\mathrm{eff}} = \frac{1}{1+\omega^\star}\,, \tag{4.74}$$

arising from the partial resummation introduced in the non-perturbative framework. This prescription defines a "preferred gauge", influencing physical predictions and precluding the derivation of Ward identities. Consequently, the field rescaling $\phi \to \phi/\mathcal{Z}$ does not necessarily nullify the charge correction $g \to g\mathcal{Z}^\star$, diverging from conventional QED. As in the spin-$\frac{1}{2}$ HECO case [216], this vertex correction is retained for the scalar HECO charge, defined as:

$$\frac{g_{\text{HECO}}}{\sqrt{1+\omega^\star}} \equiv (\tilde{g}\mathcal{Z})^\star \to g_{\text{HECO}} = g\mathcal{Z}^\star \ . \tag{4.75}$$

Similar to the fermionic HECO case [216], the EM coupling g of the scalar HECO can be expressed in terms of the electron charge e as:

$$g = ne, \quad n \in \mathbb{Z}, \quad |n| \geq 11 \ [216]. \tag{4.76}$$

This condition reflects the breakdown of perturbation theory in QED for particles carrying sufficiently large electric charge, where the electromagnetic interaction enters a non-perturbative regime. For smaller charges, standard perturbative QED results are recovered.

The Feynman rules corresponding to the UV fixed point Eq. (4.58), under the condition $g^2/h \lesssim 0.0825$, are summarised as:

$$\begin{aligned}
&\textit{Scalar-photon vertex:} && -ig\mathcal{Z}^\star \simeq -ig\sqrt{1+\frac{8g^2}{h}}, \qquad (4.77)\\
&\textit{Scalar self-interaction vertex:} && -i\frac{H^\star}{(\mathcal{Z}^\star)^4} \simeq -i\frac{h}{4}\left(1+\frac{8g^2}{h}\right)^{-2},\\
&\textit{Gauge boson propagator:} && \frac{-i}{p^2-i\epsilon}\left(\eta_{\mu\nu}+\frac{4g^2}{3h}\frac{p_\mu p_\nu}{p^2}\right), \quad \epsilon \to 0^+,\\
&\textit{Charged scalar propagator:} && \frac{i}{p^2-\tilde{M}^2+i\epsilon}, \quad \epsilon \to 0^+,
\end{aligned}$$

where the scalar HECO mass $\tilde{M}$ is defined in Eq. (4.73).

In an experimental context, simplifying assumptions are adopted as outlined in [204]. Specifically, in DY processes, scalar HECOs are assumed to interact exclusively with photons, excluding interactions with the SM Z^0-boson. While scalar HECOs can be produced via Z^0-boson fusion through quartic interactions, such processes are suppressed at the LHC. Hence, the focus is limited to EM interactions, assuming scalar HECOs possess zero weak hypercharge.

The resummation effects described are implemented using UFO models [226, 227], as in the case of spin-1/2 HECOs. These models are compatible with Monte Carlo event generators, such as MadGraph5_aMC@NLO 3.5.4 [228], used in this study. The primary objective is to simulate DY and PF processes involving spin-0 HECOs at the LHC, considering the resummation scheme outlined in the previous section.

The developed UFO model incorporates the Feynman rules in Eq. (4.77), derived from the effective Lagrangian in Eq. (4.52), at the UV fixed point Eq. (4.58). This implementation serves as a bridge between experimental results and theoretical benchmarks. Details of the validation process are summarised in Appendix B, where simulated cross sections are compared against analytical calculations performed using Mathematica 13.0.1.

As in the spin-1/2 case, the UFO model for spin-0 HECOs introduces two additional parameters:

- The charge multiplicity n, appearing in the coupling definition $g = ne$, where e is the electron electric charge.
- The cutoff energy scale Λ, defined in Eq. (4.72).

Both parameters directly influence the HECO mass and, consequently, the computed cross section values. Also in this case, for the centre-of-mass energies relevant to LHC experiments, the fine-structure constant is set to $\alpha_{\rm EM} = 1/127.94$, corresponding to the energy scale of the Z^0-boson mass.

4.3.5 Cross Sections for Scalar HECO Production at Colliders

The cross sections for scalar HECO pair production at colliders are evaluated at tree level and after incorporating the DS resummation effects. Table 4.4 summarises the results for DY production, while Table 4.5 provides the corresponding values for PF. The calculations are performed for pp collisions at $\sqrt{s} = 13$ TeV, using the `NNPDF23` PDF [229] for DY processes and the `LUXqed17` PDF [230] for PF.

The comparison reveals that, for a given mass—bare at tree level and $\mathcal{M}(\Lambda)$ after resummation—the cross sections remain within the same order of magnitude. Notably, the DS resummation results in a significant enhancement in the cross section values. For DY processes, the cross section increases by a factor of approximately 1.66, proportional to $(\mathcal{Z}^{\star})^2$, due to the dependence on the square of the coupling $(g\mathcal{Z}^{\star})^2$. In the case of PF, the increase is more pronounced, by a factor of approximately 2.76, corresponding to $(\mathcal{Z}^{\star})^4$, as the cross section depends on g^4. These effects are visualised in Figure 4.8, where cross sections are plotted as a function of the HECO mass M for various charge values before and after resummation at $\sqrt{s} = 13$ TeV.

The observed enhancement in the scalar HECO cross sections, relative to the tree-level predictions, aligns with the findings for the spin-1/2 case. However, as expected, the cross section values for scalar HECO pair production are generally lower than those for spin-1/2 HECOs.

Figures 4.9, 4.10, and 4.11 illustrate cross sections for DY and PF production mechanisms as a function of different parameters: mass M, charge Q, and cutoff Λ, respectively..

Similar to the spin-1/2 case, cross section values increase with Q for a fixed HECO mass M. However, the production rate decreases for higher Q values until a threshold determined by Λ is reached, after which a slight increase is observed. This behaviour underscores the non-linear relationship between Λ and Q, as described in Eq. (4.73).

For smaller Q values, HECO masses contribute significantly, leading to reduced production rates. This explains why cross sections for $Q = 20e$ exceed those for higher charges when Λ surpasses a critical value. Notably, PF consistently exhibits higher production rates compared to DY at $\sqrt{s} = 13$ TeV.

Table 4.4: Cross section comparison for scalar HECO production in pp collisions at $\sqrt{s} = 13$ TeV via the Drell-Yan process between tree level and after resummation with $\Lambda = 2$ TeV. The ratio $\sigma_{\text{resum}}/\sigma_{\text{tree}}$ and the HECO mass are listed. The `NNPDF23` PDF [229] is used.

DY $pp \to \mathcal{H}\overline{\mathcal{H}}$ @ $\sqrt{s} = 13$ TeV, $\Lambda = 2$ TeV				
Q (e)	$\sigma_{\text{tree-level}}$ (fb)	σ_{resum} (fb)	$\sigma_{\text{resum}}/\sigma_{\text{tree}}$	M (TeV)
20	1.173	1.943	1.66	1.030
60	0.110	0.182	1.65	1.857
100	0.192	0.320	1.67	1.948
140	0.332	0.551	1.66	1.973
180	0.519	0.863	1.66	1.984
220	0.756	1.254	1.66	1.989

Table 4.5: Cross section comparison for scalar HECO production in pp collisions at $\sqrt{s} = 13$ TeV via Photon-Fusion process between tree level and after resummation with $\Lambda = 2$ TeV. The ratio $\sigma_{\text{resum}}/\sigma_{\text{tree}}$ and the HECO mass are shown. The `LUXqed17` PDF [230] is used for this process.

PF $\gamma\gamma \to \mathcal{H}\overline{\mathcal{H}}$ @ $\sqrt{s} = 13$ TeV, $\Lambda = 2$ TeV				
Q (e)	$\sigma_{\text{tree-level}}$ (fb)	σ_{resum} (fb)	$\sigma_{\text{resum}}/\sigma_{\text{tree}}$	M (TeV)
20	0.748×10^2	2.056×10^2	2.75	1.030
60	0.111×10^3	0.306×10^3	2.76	1.857
100	0.576×10^3	1.591×10^3	2.76	1.948
140	1.987×10^3	5.476×10^3	2.76	1.973
180	5.18×10^3	$14.\ 30 \times 10^3$	2.76	1.984
220	11.31×10^3	31.16×10^3	2.76	1.989

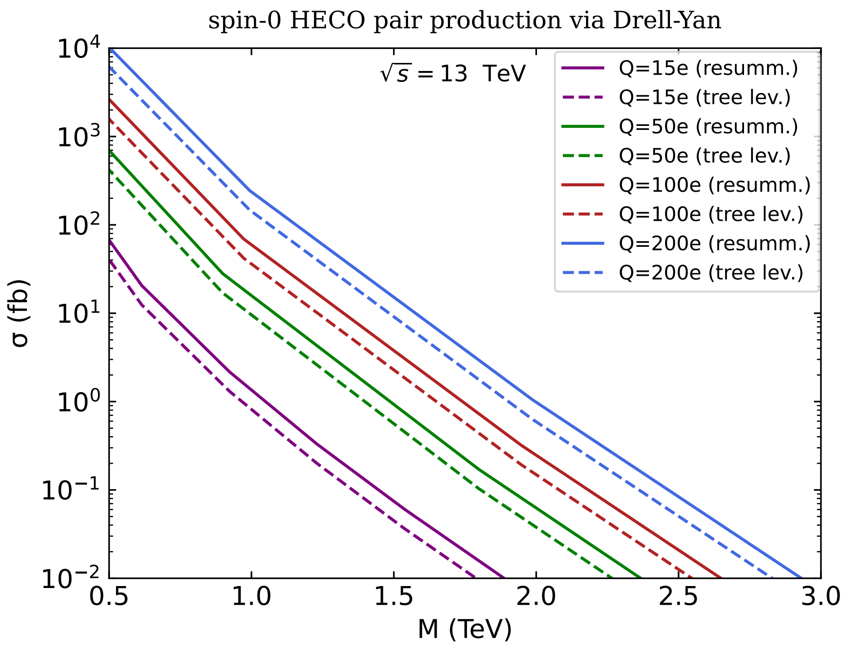

(a) DY cross section vs mass M

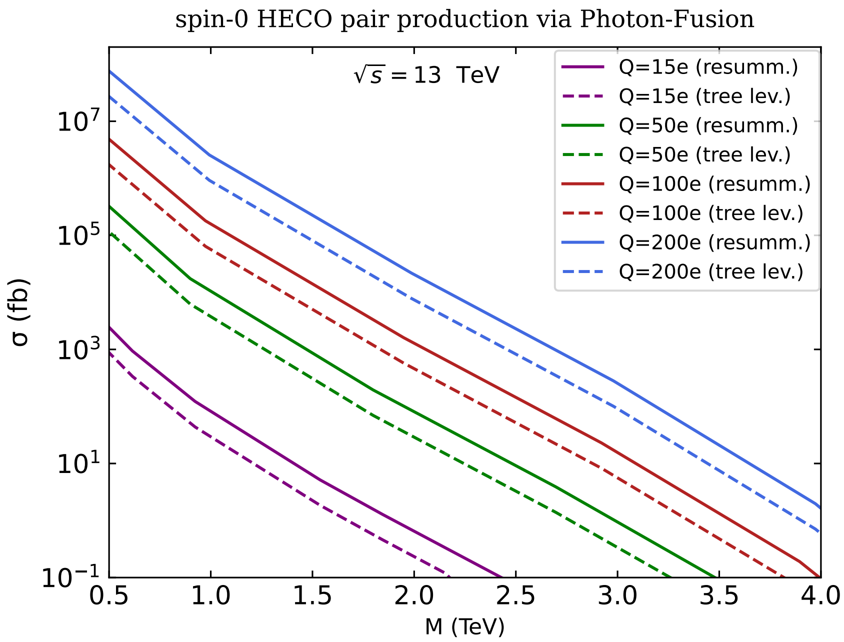

(b) PF cross section vs mass M

Figure 4.8: Comparison of cross section values obtained after (solid line) and before (dashed line) resummation as a function of the scalar HECO mass M for electric charges $Q = 15e$, $50e$, $100e$, and $200e$.

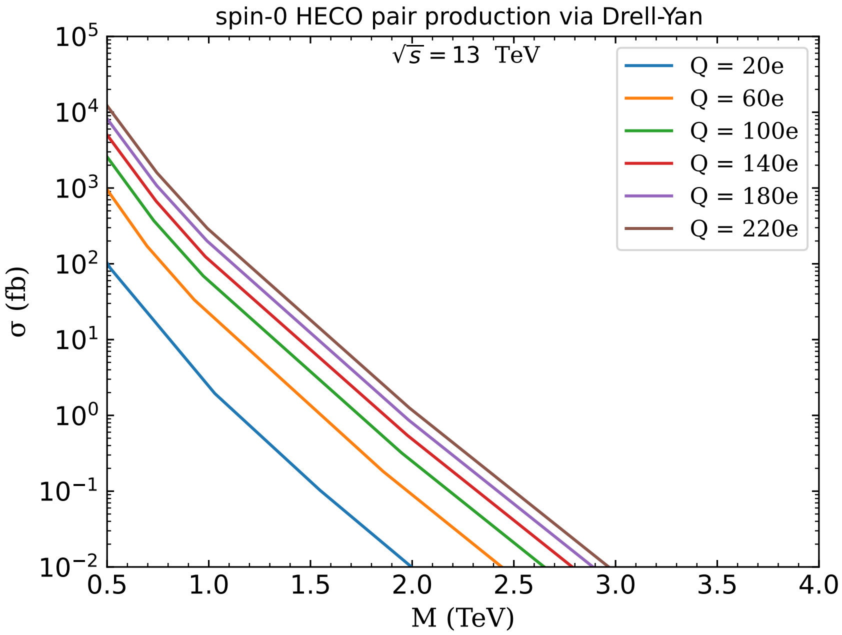

(a) DY cross section vs mass M

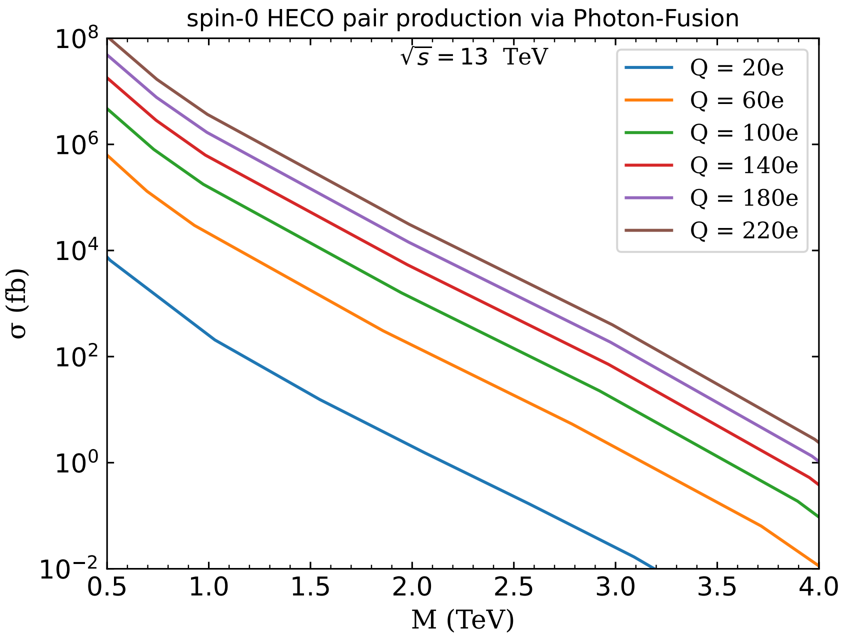

(b) PF cross section vs mass M

Figure 4.9: Scalar HECO pair production cross section at $\sqrt{s} = 13$ TeV as a function of mass M for various charge values.

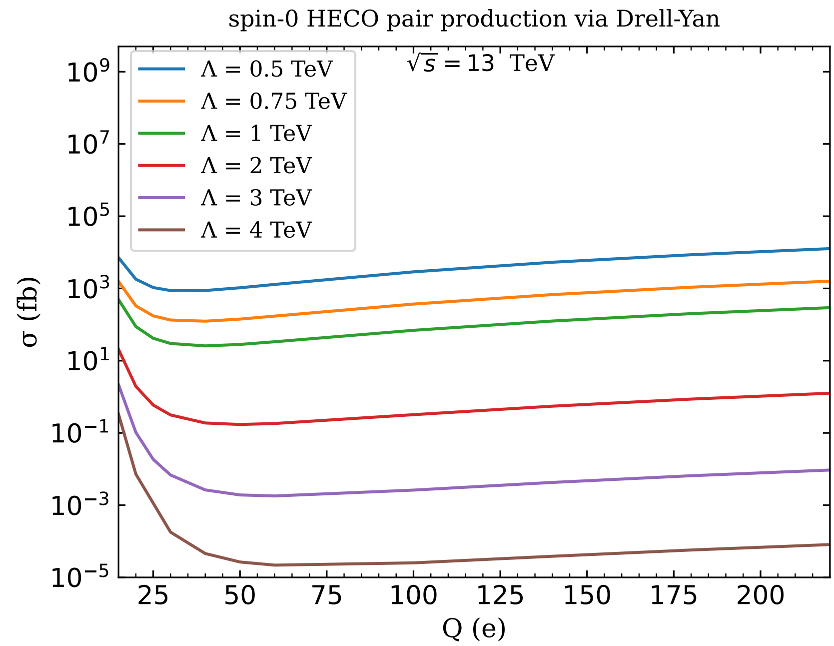

(a) DY cross section vs charge Q

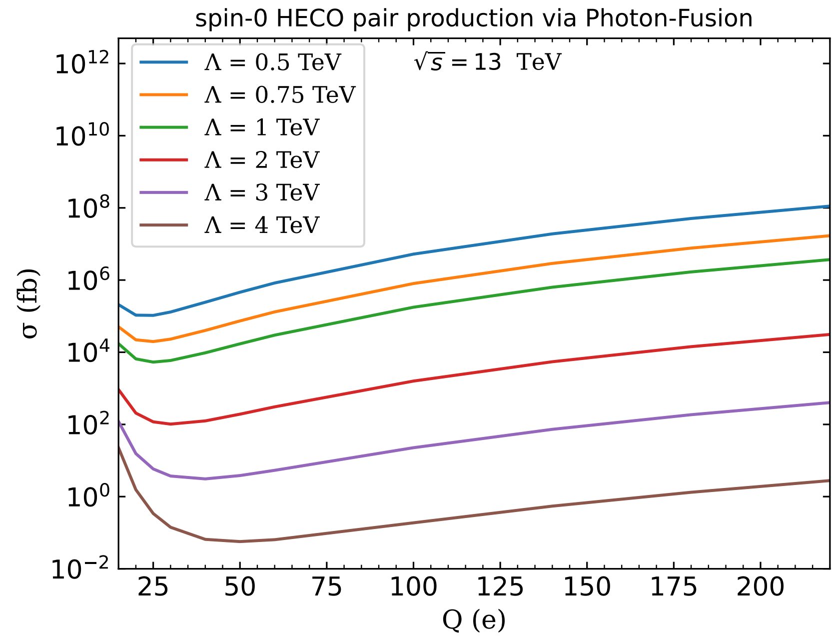

(b) PF cross section vs charge Q

Figure 4.10: Scalar HECO pair production cross section at $\sqrt{s} = 13$ TeV as a function of charge Q for different cutoff Λ values.

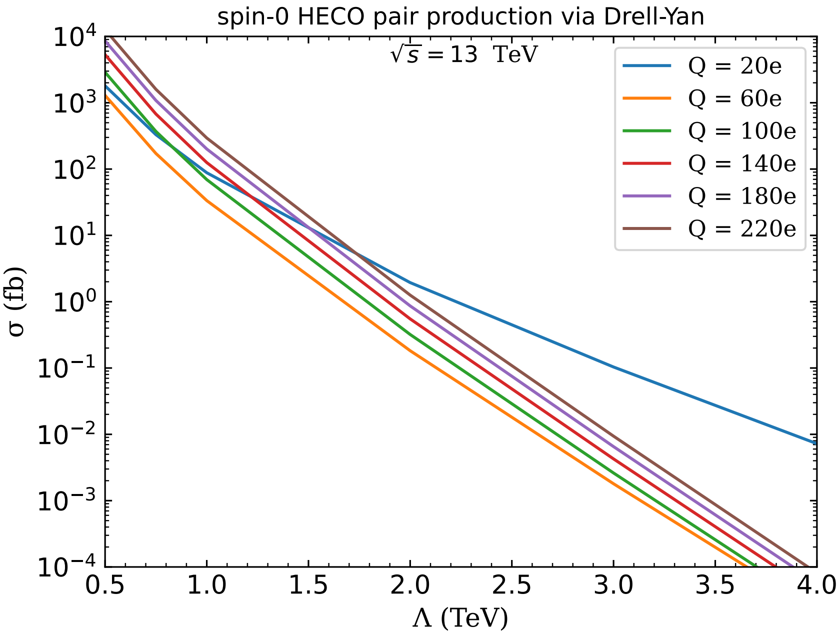

(a) DY cross section vs cutoff Λ

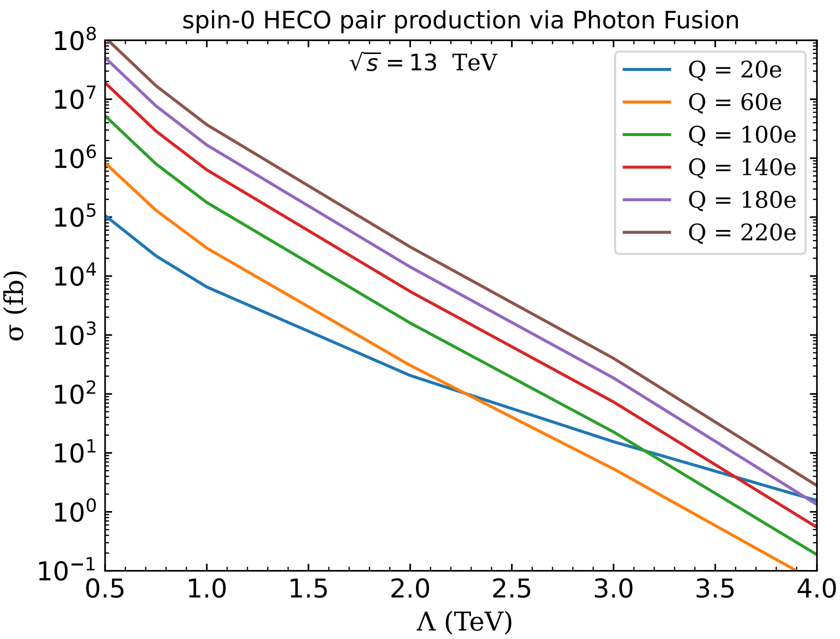

(b) PF cross section vs cutoff Λ

Figure 4.11: Scalar HECO pair production cross section at $\sqrt{s} = 13$ TeV as a function of the cutoff Λ for different Q.

4.4 Re-evaluated Mass Limits

In this section, new reliable mass limits for spin-0 and spin-$1/2$ HECOs are established based on searches conducted by the ATLAS [17] and MoEDAL [138] collaborations at the LHC. These limits incorporate the production cross section predictions presented in the previous section, which include resummation effects. The analysis considers results obtained at $\sqrt{s} = 13$ TeV [165, 224], where both DY and PF processes were examined. Additionally, earlier searches conducted at $\sqrt{s} = 8$ TeV [164, 236], focusing on DY processes, are also included.

The improved mass limits — derived using the DS resummation approach discussed in this chapter — are reported in Table 4.6 and Table 4.7 for scalar and fermion HECOs respectively. These updated limits are summarised in the "RES" columns, covering both DY and PF production processes, while the columns "LO" represent the mass limits at tree level as determined by the experimental searches conducted by ATLAS and MoEDAL.

The updated mass limits are consistently more stringent than those initially reported by the experimental collaborations, reflecting the enhanced cross sections obtained when resummation effects are included compared to tree-level production rates. The improvement spans a wide range, with increases of up to 30%, depending on the HECO mass and the specific experimental dataset.

A summary of the spin-0 and spin-$1/2$ HECO mass limits obtained in this work as a function of the HECO charge is presented in Figure 4.12 and Figure 4.13. These results incorporate the effects of DS resummation and are derived from the reinterpretation of HECO production-rate constraints reported by the ATLAS and MoEDAL collaborations, demonstrating that the resummation technique consistently leads to more stringent mass limits.

It is important to note that the results for the same experiment and centre-of-mass energy $\sqrt{s}$ may not necessarily correspond to the same dataset size. Consequently, direct comparisons between such results should be made with caution.

Table 4.6: 95% CL experimental mass limits for spin-0 HECOs with (RES) and without (LO) resummation techniques to calculate production cross sections. Reported bounds are not necessarily extracted from the same dataset size.

Experimental lower limits at 95% CL on spin-0 HECO mass (TeV)					
Experiment/ energy	Q (e)	DY γ exchange		PF	
		LO	RES	LO	RES
MoEDAL [165]	10	0.08	0.08*	0.30	0.30*
$\sqrt{s}=$	15	0.22	0.25	0.74	0.88
13 TeV	20	0.40	0.37	1.14	1.32
	25	0.58	0.63	1.50	1.73
	50	1.30	1.42	2.72	2.90
	75	1.39	1.48	3.02	3.18
	100	1.42	1.42	3.17	3.31
	125	1.43	1.53	3.26	3.40
	150	1.43	1.52	3.31	3.46
	175	1.41	1.51	3.32	3.45
	200	1.39	1.50	3.31	3.44
	225	1.37	1.47	3.24	3.33
	250	1.34	1.44	3.16	3.25
	275	1.29	1.38	3.00	3.00†
	300	1.21	1.30	2.50	2.50†
	325	1.07	1.12	2.00	2.00†
	350	0.90	0.93	1.50	1.50†
	375	0.50	0.50†	1.50	1.50†
ATLAS [224]	20	1.4	1.5	2.1	2.4
$\sqrt{s}=$	40	1.8	1.9	2.8	3.0
13 TeV	60	1.9	2.0	2.9	3.1
	80	1.8	1.9	2.8	3.0
	100	1.7	1.8	2.5	2.5†
MoEDAL [164]	15	0.07	0.09	–	–
$\sqrt{s}=8$ TeV	20	0.12	0.16	–	–
	25	0.19	0.27	–	–

Continued on next page

Table 4.6 – continued from previous page

Experiment/ energy	Q (e)	DY γ exchange		PF	
		LO	RES	LO	RES
	50	0.56	0.62	–	–
	75	0.58	0.64	–	–
	100	0.55	0.62	–	–
	125	0.50	0.56	–	–
	130	0.49	0.56	–	–
	140	0.47	0.53	–	–
	145	0.47	0.53	–	–
	150	0.46	0.52	–	–
	175	0.40	0.46	–	–
ATLAS [236]	10	0.49	0.49*	–	–
$\sqrt{s} = 8$ TeV	20	0.78	0.81	–	–
	40	0.92	0.95	–	–
	60	0.88	0.92	–	–

Table 4.7: 95% CL experimental mass limits for spin-1/2 HECOs with (RES) and without (LO) resummation techniques to calculate production cross sections. Reported bounds are not necessarily extracted from the same dataset size.

Experimental lower limits at 95% CL on spin-1/2 HECO mass (TeV)							
Exp/energy	Q (e)	DY γ exchange		DY γ/Z^0 exchange		PF	
		LO	RES	LO	RES	LO	RES
MoEDAL [165]	10	0.29	0.29*	0.32	0.32*	0.41	0.41*
$\sqrt{s} = 13$ TeV	15	0.62	0.72	0.62	0.80	0.95	1.21
	20	0.92	1.08	0.93	1.15	1.38	1.68
	25	1.19	1.36	1.17	1.45	1.80	2.13
	50	1.85	2.02	1.84	2.10	3.00	3.27
	75	1.94	2.10	1.93	2.16	3.25	3.51
	100	1.98	2.14	1.97	2.08	3.39	3.66

*Resummation is valid for $Q \gtrsim 11e$, so there is no change in the mass limit for $Q = 10e$.
†There is no experimental sensitivity for HECO masses higher than this value.

Table 4.7: (Continued)

Experimental lower limits at 95% CL on spin-$\frac{1}{2}$ HECO mass (TeV)							
Exp/energy	Q (e)	DY γ exchange		DY γ/Z^0 exchange		PF	
		LO	RES	LO	RES	LO	RES
	125	2.00	2.15	1.99	2.10	3.48	3.72
	150	2.00	2.16	1.98	2.10	3.52	3.75
	175	1.98	2.13	1.97	2.17	3.53	3.73
	200	1.94	2.10	1.94	2.13	3.50	3.69
	225	1.90	2.03	1.90	2.08	3.44	3.60
	250	1.83	1.95	1.84	2.02	3.00	$3.00^{\dagger}$
	275	1.74	1.84	1.74	1.88	3.00	$3.00^{\dagger}$
	300	1.61	1.70	1.62	1.75	2.50	$2.50^{\dagger}$
	325	1.38	1.46	–	–	2.00	$2.00^{\dagger}$
	350	1.00	$1.00^{\dagger}$	–	–	1.50	$1.50^{\dagger}$
	375	0.20	$0.20^{\dagger}$	–	–	1.50	$1.50^{\dagger}$
	400	–	–	–	–	1.50	$1.50^{\dagger\ddagger}$
ATLAS [224, 237] $\sqrt{s} = 13$ TeV	20	1.83	2.02	1.8	1.9	2.5	2.7
	40	2.05	2.22	2.2	2.3	3.1	3.4
	60	2.00	2.18	2.2	2.4	3.1	3.4
	80	1.86	2.02	2.1	2.2	3.0	$3.0^{\dagger}$
	100	1.65	1.80	1.9	2.1	2.5	$2.5^{\dagger}$
MoEDAL [164] $\sqrt{s} = 8$ TeV	20	0.28	0.36	0.31	0.36	–	–
	25	0.44	0.55	0.44	0.53	–	–
	50	0.78	0.88	0.78	0.87	–	–
	75	0.78	0.88	0.78	0.84	–	–
	100	0.73	0.84	0.71	0.80	–	–
	125	0.66	0.75	0.64	0.72	–	–
	130	0.64	0.74	0.62	0.70	–	–
	140	0.58	0.68	0.62	0.69	–	–
	145	0.52	0.66	0.51	0.60	–	–
	150	0.50	0.63	0.58	0.66	–	–
ATLAS [236] $\sqrt{s} = 8$ TeV	10	0.78	0.78^{*}	–	–	–	–
	20	1.05	1.14	–	–	–	–
	40	1.16	1.25	–	–	–	–
	60	1.07	1.15	–	–	–	–

Table 4.7: (Continued)

Experimental lower limits at 95% CL on spin-$\frac{1}{2}$ HECO mass (TeV)							
Exp/energy	Q (e)	DY γ exchange		DY γ/Z^0 exchange		PF	
		LO	RES	LO	RES	LO	RES

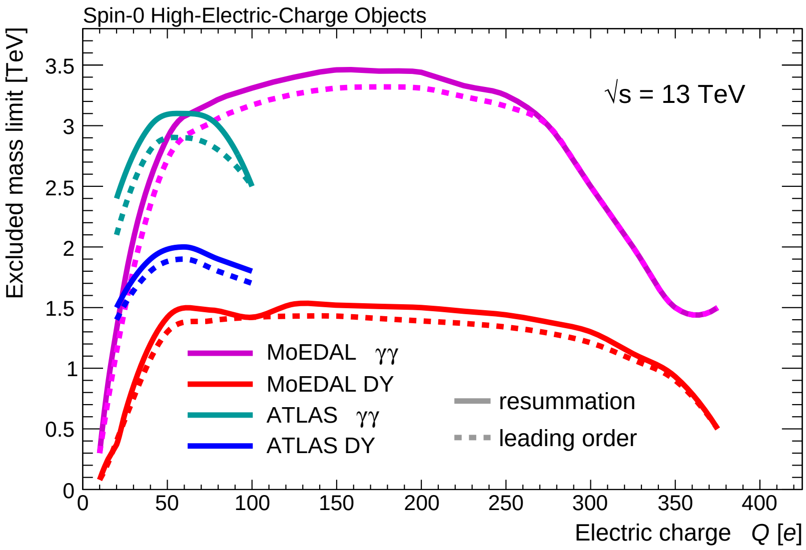

Figure 4.12: Excluded lower mass limits for spin-0 HECOs from ATLAS [224] and MoEDAL [165] at $\sqrt{s} = 13$ TeV at leading order (dashed lines) and re-calculated with resummation (solid lines). The dips around 250 GeV and 350 GeV are artifacts of the curve smoothing.

Before closing the section, it is important to stress once again that the above results were formally derived in the Feynman gauge $\lambda = 1$, which is a "preferred" (physical) gauge according to the PT framework. Nonetheless, for the sake of argument, one might consider the effects of working in a different gauge, e.g. the Landau one $\lambda \to \infty$, on the physical results. In this respect, it should be noted that the cross sections depend on the wave-function renormalization $\mathcal{Z}^\star$ at the UV fixed point, see Eq. (4.58), which, unlike the photon-wavefunction renormalization $\omega^\star$ and

*Resummation is valid for $Q \gtrsim 11e$, so there is no change in the mass limit for $Q = 10e$.
†There is no experimental sensitivity for HECO masses higher than this value.
‡The excluded mass range is 0.5–1.5 TeV.

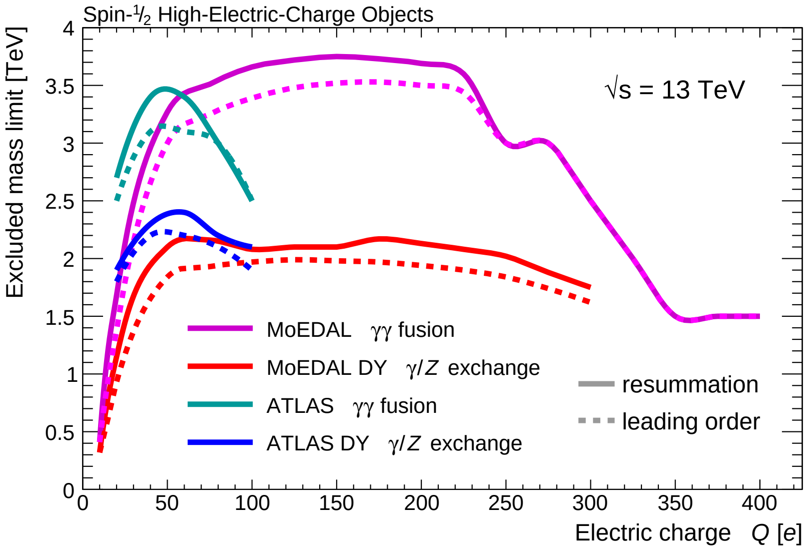

Figure 4.13: Excluded lower mass limits for spin-1/2 HECOs from ATLAS [224] and MoEDAL [165] at $\sqrt{s} = 13$ TeV at leading order (dashed lines) and re-calculated with resummation (solid lines). The dips around 250 GeV and 350 GeV are artifacts of the curve smoothing.

the renormalised scalar self-interaction coupling $H^\star$, depends on the gauge parameter to first order in the small quantity g^2/h. This would result in increased values of the DY and PF production cross sections by 20% and 44%, respectively, compared to the Feynman gauge. Given that mass bounds are extracted from the logarithms of the cross sections, the above effect would have negligible consequences for the scalar HECO bounds.

4.5 Conclusions

In this chapter, resummation techniques applicable to the study of objects with high electric charge, known as HECOs, were investigated. These hypothetical particles are actively sought in experimental searches at contemporary colliders, representing potential indicators of physics beyond the Standard Model. By employing Dyson-Schwinger resummation methods, an effective Lagrangian was developed to describe the dynamics of HECOs through appropriately dressed DY and PF processes. This approach enabled the derivation of theoretically reliable mass bounds and consistent interpretations of experimental data based on cross section upper limits. It has been demonstrated that these techniques significantly enhance the mass bounds on HECOs obtained from collider searches conducted by collaborations such as ATLAS and MoEDAL.

The resummation effects were implemented within UFO models, compatible with Monte Carlo event generators such as MADGRAPH, focusing on the DY and PF production mechanisms for spin-$1/2$ and spin-0 HECOs at the LHC. For spin-$1/2$, two UFO models were constructed: the first accounting solely for photon exchange and the second including both photon and Z^0-boson exchange, thereby providing a more comprehensive representation of the relevant physics. Similarly, for spin-0 HECOs, a UFO model was created to describe processes involving photon interactions exclusively, providing an effective framework for scalar HECO analyses. In addition, the developed UFO models, which include resummation effects, have been made publicly available for use by experimental collaborations and can be accessed at Ref. [238]. These models are compatible with Monte Carlo event generators, enabling their direct implementation in simulations and searches for HECOs. By providing these tools, this work facilitates further experimental investigations into HECOs at both current and future colliders. Collaborations such as ATLAS, MoEDAL, and others involved in the search for new physics BSM can utilise these models to enhance the accuracy and reliability of their analyses.

The application of these UFO models is not restricted to the LHC, but may also be employed for event simulation and cross section calculations at future colliders, including e^+e^- Higgs factories.

To incorporate these resummation effects, two new input parameters were introduced: the charge multiplicity n, related to the HECO charge $g = ne$, and the UV cutoff parameter Λ. These parameters influence the HECO mass and consequently affect the calculated cross sections. For spin–$1/2$ HECOs, the production via the DY process improves by a factor of approximately 2.1, while PF production experiences an enhancement by a factor of approximately 4.75. For spin-0 HECOs, the DY production improves by a factor of approximately 1.66, and PF production increases by ~ 2.76. These results demonstrate the significant impact of incorporating resummation effects on the predictive power of the UFO model.

The outcomes obtained in this chapter were employed to reinterpret results from experimental collaborations such as ATLAS and MoEDAL, which initially treated production mechanisms at the tree level. By incorporating resummation effects, more reliable and improved HECO mass bounds were derived.

Chapter 5

Constraining Magnetic Monopoles via $\gamma\gamma$ Events

5.1 Light-by-Light Scattering

Magnetic monopoles, as predicted by Dirac [177], can play a significant role in enhancing photon-photon interactions due to their large EM coupling. One of the most intriguing aspects of this interaction is their contribution to *box diagrams* in LbL scattering processes [239].

LbL scattering, a process where photons interact with one another, is a rare and subtle phenomenon in QED. The elastic scattering of two photons in vacuum, $\gamma\gamma \to \gamma\gamma$, is a purely quantum mechanical process that occurs at leading order in the fine-structure constant, $\mathcal{O}(\alpha^4)$, via virtual box diagrams involving charged particles. Within the SM, these box diagrams are mediated by loops of charged fermions (leptons and quarks) and bosons ($W^{\pm}$) [240].

Potential BSM contributions could manifest as heavy charged particles, such as monopoles, appearing in the virtual loop as depicted in Fig. 5.1, particularly at high diphoton invariant masses. High-energy regimes accessible at modern colliders, where the production of multiple photons serves as a probe of photon-photon interactions.

The experimental observation of LbL scattering has been achieved in ultra-peripheral heavy-ion collisions at the LHC by the ATLAS and

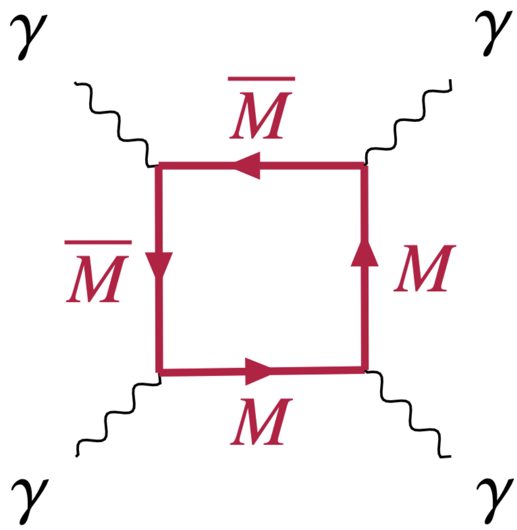

Figure 5.1: Monopole contribution to light-by-light scattering.

CMS collaborations [241, 242]. Such detectors are specifically optimised to detect such high-energy photon signatures with minimal background contamination. Consequently, the study of LbL scattering processes offers an exceptional opportunity to probe contributions from MMs, opening a window to new physics BSM.

In this thesis work, two different theoretical scenarios have been employed to constrain the mass of magnetic monopoles using diphoton events: EFT in Section 5.2 and Born-Infeld (BI) in Section 5.3.

5.1.1 Central Exclusive Processes

The final-state signature of interest arises from diphoton production via central exclusive processes (CEP):

$$A + B \xrightarrow{\gamma\gamma} A + \gamma\gamma + B,$$

where A and B represent the incoming hadrons, which may be protons (p) or lead nuclei (Pb), scattering at extremely small angles relative to the beam direction. In this topology, the final state consists of two photons, detectable in the central detector, and two intact hadrons scattered at small angles. This distinct signature ensures a clean experimental environment with minimal contamination from QCD interactions or pile-up events, making CEP an ideal channel for precision studies of LbL scattering [240].

The process is mediated by quasi-real photons emitted from the EM fields of the incoming hadrons, which interact through $\gamma\gamma$ scattering. These photons are characterised by low virtualities, $Q^2 < 1/R^2$, where R is the charge radius of the emitting hadrons. This property ensures that the photons are nearly on-shell, enabling the application of the equivalent photon approximation (EPA) [239] to describe the photon flux. In this framework, the hadrons are treated as sources of photon beams, and the elastic diphoton production cross section can be expressed as a convolution of the photon fluxes from each hadron with the elementary cross section for $\gamma\gamma \to \gamma\gamma$. Mathematically, this is given by:

$$\sigma^{\text{excl}}_{\gamma\gamma\to\gamma\gamma} = \int d\omega_1 d\omega_2 \frac{f_{\gamma/A}(\omega_1)}{\omega_1} \frac{f_{\gamma/B}(\omega_2)}{\omega_2} \sigma_{\gamma\gamma\to\gamma\gamma}(\sqrt{s_{\gamma\gamma}}), \tag{5.1}$$

where ω_1 and ω_2 are the photon energies, and $f_{\gamma/A}(\omega)$ and $f_{\gamma/B}(\omega)$ represent the photon flux distributions emitted by hadrons A and B, respectively.

CEP provides a particularly well-suited platform for exploring physics BSM. Deviations from the expected LbL scattering rates could indicate the presence of new particles, such as axion-like particles (ALPs) or exotic bound states like monopolia.

The c.o.m. energy of the diphoton system is given by $\sqrt{s_{\gamma\gamma}} = m_{\gamma\gamma} = \sqrt{4\omega_1\omega_2}$. The maximum photon energy, $\omega^{\max}$, is governed by the relation $\omega^{\max} \sim \gamma/b_{\min}$, where $b_{\min}$ represents the smallest separation between the two charged hadrons, determined by their radii $R_{A,B}$, and $\gamma = \sqrt{s_{NN}}/(2m_N)$ is the beam Lorentz factor (valid in collisions where A and B are identical hadrons). Here, $\sqrt{s_{NN}}$ and m_N denote the nucleon-nucleon c.o.m. energy and the nucleon mass, respectively [240].

Ultraperipheral collisions (UPCs), where the impact parameter of the two colliding hadrons exceeds the sum of their radii, offer a particularly clean environment for photon-photon interaction studies [243]. In UPCs, the strong interaction is suppressed, ensuring that EM interactions dominate. This suppression significantly reduces QCD backgrounds, making UPCs ideal for investigating photon-induced processes such as LbL scattering and exclusive diphoton production.

In PbPb collisions, the photon spectrum is softer than in pp collisions. At a collision energy of $\sqrt{s_{NN}} = 5.5$ TeV, the maximum photon energy is approximately 80 GeV, resulting in diphoton invariant masses of up to 160 GeV. However, the photon flux in PbPb collisions is enhanced by a factor of Z^4, where Z is the ion's atomic number. This enhancement, combined with reduced pile-up effects and lower QCD backgrounds, provides significant advantages for diphoton studies. Both ATLAS [241, 244, 245] and CMS [242, 246] have observed such processes in UPC events [243].

In contrast, pp collisions generate a harder photon spectrum, enabling access to much higher diphoton invariant masses. Proton-proton collisions also benefit from larger datasets at the LHC, enhancing statistical precision. The technique of proton tagging, where intact protons are detected in forward detectors, allows for the reconstruction of CEP events with high accuracy. Forward proton detectors, such as the ATLAS Forward Physics (AFP) detector [247] and the CT-PPS detector [248], deployed during LHC Run 2, have enabled such measurements. Searches for exclusive diphoton events using forward proton tagging have been carried out by CT-PPS [249, 250] and AFP-ATLAS [251], although no significant excess above background expectations has been observed.

The AFP-ATLAS collaboration has also searched for ALPs through resonant diphoton production, placing stringent constraints on their existence [251, 252]. LbL scattering further enables investigations into ALPs and other exotic states, such as monopolia [205, 253, 254].

Studies of LbL scattering, whether in heavy-ion or proton collisions, provide a unique avenue for testing QED, probing the SM in high-energy regimes, and searching for signatures of NP.

5.2 EFT Interpretation

In this section, the EFT framework is explored to constrain MM masses. When the mass scale of NP is significantly higher than the energy accessible in current experiments, interactions involving four photons can be effectively described using an EFT approach. This incorporates NP through higher-dimensional operators in the Lagrangian. Specifically, the photon-photon interaction within the EFT framework can be expressed using the following Lagrangian [255, 256]:

$$\mathcal{L}_{4\gamma} = \zeta_1 F_{\mu\nu} F^{\mu\nu} F_{\rho\sigma} F^{\rho\sigma} + \zeta_2 F_{\mu\nu} F^{\nu\rho} F_{\rho\lambda} F^{\lambda\mu}, \tag{5.2}$$

where $F_{\mu\nu}$ denotes the EM field strength tensor. The parameters ζ_1 and ζ_2 characterise the contributions of the dimension-8 operators that arise from BSM physics. These operators are highly suppressed in the SM due to their higher dimensional nature. Consequently, these parameters can effectively parametrise any deviations from SM predictions in the $\gamma\gamma \to \gamma\gamma$ process.

Quartic photon couplings can be modified via loops of new heavy particles or new resonances that couple to photons [256, 257]. For energies much smaller than the mass of these exotic particles, the low-energy EFT results in higher order of the Heisenberg and Euler theory [258] of LbL scattering, where $\zeta_{1,2}$ are expressed as [256]

$$\zeta_i = \alpha^2 Q^4 m^{-4} N c_i, \tag{5.3}$$

where Q and m are the charge and mass of the particle running in the loop, N counts all additional multiplicities such as colours or flavours and c_i are spin-dependent coefficients. These coefficients arise from the higher-order terms in the EFT, which result from integrating out heavy particles that couple to photons. Their values depend on the spin of the particles involved, reflecting the different contributions to the photon-photon interaction processes. Notably, the coefficients attain their maximum values for spin-1 particles and their minimum values for spin-0 configurations.

The coefficients c_i are given by:

$$c_1 = \begin{cases} \frac{1}{288}, & s = 0 \\ -\frac{1}{36}, & s = \frac{1}{2} \\ -\frac{5}{32}, & s = 1 \end{cases}, \quad c_2 = \begin{cases} \frac{1}{360}, & s = 0 \\ \frac{7}{90}, & s = \frac{1}{2} \\ \frac{27}{40}, & s = 1 \end{cases} \tag{5.4}$$

Now, in the case of MMs, the EFT Lagrangian (5.2) is written in the form [259]:

$$\mathcal{L}_{4\gamma}^{\rm MM} = \frac{1}{36}\left(\frac{g}{\sqrt{4\pi}M}\right)^4 \cdot \left[\frac{\beta_+ + \beta_-}{2}(F_{\mu\nu}F^{\mu\nu})^2 + \frac{\beta_+ - \beta_-}{2}(F_{\mu\nu}\tilde{F}^{\mu\nu})^2\right] \tag{5.5}$$

where $\tilde{F}^{\mu\nu} = \epsilon^{\mu\nu\alpha\beta}F_{\alpha\beta}/2$ is the dual field tensor of $F^{\mu\nu}$, $g = ng_D$ is the MM magnetic charge from (3.2), and the $\beta_\pm$ coefficients are:

$$\beta_+ = \begin{cases} \frac{1}{5}, & s = 0 \\ \frac{11}{10}, & s = \frac{1}{2} \\ \frac{63}{5}, & s = 1 \end{cases}, \quad \beta_- = \begin{cases} \frac{3}{20}, & s = 0 \\ -\frac{3}{10}, & s = \frac{1}{2} \\ \frac{9}{20}, & s = 1. \end{cases} \tag{5.6}$$

For convenience, we define the constant

$$A = \frac{1}{72}\left(\frac{g_D}{\sqrt{4\pi}}\right)^4 = \frac{1}{1152\alpha^2},$$

using the relation in Eq. (3.2).

For the LHC c.o.m. energies considered here, the value of α at the Z-boson mass scale is used, i.e., $\alpha = 1/127.94$, which results in $g_D = 64e$ and $A \simeq 14.21$. It is worth noting that the Dirac charge value differs from the widely considered $68.5e$ in the literature, which is derived from an α value of $1/137$.

Through the coefficients:

$$b_\pm = A\left(\frac{n}{M}\right)^4 (\beta_+ \pm \beta_-), \tag{5.7}$$

the Lagrangian (5.2) can be written in the form (5.5) with the substitutions

$$\zeta_1 = b_+ - 2b_-, \quad \zeta_2 = 4b_-. \tag{5.8}$$

The anomalous couplings $\zeta_{1,2}$ have been constrained in pp collisions of 103 fb^{-1} of integrated luminosity by the CMS-TOTEM Collaboration at a c.o.m. energy of 13 TeV [249, 260] in a search for exclusive photon production on this effective extension of the SM. The latest limits at 95% confidence level can be parameterised as [260]

$$\begin{aligned} &a_0\zeta_1^2 + a_1\zeta_1\zeta_2 + a_2\zeta_2^2 < 1, \\ &a_0 = 194.0 \text{ TeV}^8, \\ &a_1 = 161.7 \text{ TeV}^8, \\ &a_2 = 44.47 \text{ TeV}^8. \end{aligned} \tag{5.9}$$

If $\zeta_{1,2}$ are expressed in terms of (5.8) and (5.7), then the experimental constraint (5.9) is transformed into lower bounds to monopole masses:

$$\begin{aligned} \left(\frac{M}{n}\right)^8 &> A^2(a_{++}\beta_+^2 + a_{+-}\beta_+\beta_- + a_{--}\beta_-^2), \\ a_{++} &= a_0 - 4a_1 + 16a_2 = 259.0 \text{ TeV}^8, \\ a_{+-} &= -6a_0 + 16a_1 - 32a_2 = -0.32 \text{ TeV}^8, \\ a_{--} &= 9a_0 - 12a_1 + 16a_2 = 517.5 \text{ TeV}^8. \end{aligned} \tag{5.10}$$

Finally, by using the spin-specific $\beta_\pm$ values from Eq. (5.6), the constraints (5.10) lead to the following indirect limits for Dirac (i.e. point-like) monopoles of mass M, charge ng_D and spin s:

$$\frac{M}{|n|} > \begin{cases} 2.86 \text{ TeV}, & s = 0 \\ 4.05 \text{ TeV}, & s = \frac{1}{2} \\ 7.33 \text{ TeV}. & s = 1 \end{cases} \tag{5.11}$$

Exclusion limits on MM mass as a function of Q in Dirac charge g_D units are reported in Fig. 5.2 for scalar, fermionic and vector monopoles.

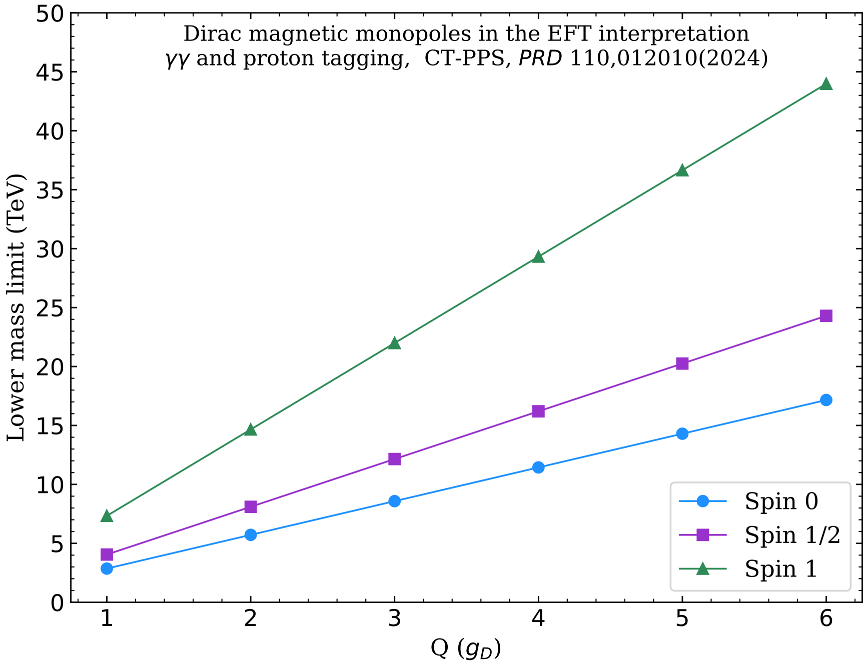

Figure 5.2: Exclusion lower mass limits for spin-0 (blue), spin-1/2 (purple) and spin-1 (green) MMs as a function of Q in Dirac charge g_D units, by using limits on EFT parameters $\zeta^{\gamma}_{1,2}$ set by CT-PPS [260].

The variation in mass constraints across different spin states results from the spin-dependent coefficients $c_{i,s}$ in Eq. 5.3. These coefficients reach their maximal values for spin-1 monopoles and minimal values for spin-0 configurations. This demonstrates the sensitivity of the constraints to the spin of the magnetic monopoles and highlights the importance of considering different spin states in the search for NP.

5.3 Born-Infeld Scenario

An alternative approach to constraining MMs involves the BI theory, which introduces nonlinear modifications to classical electrodynamics [261, 262].

Originally proposed by Born and Infeld in the 1930s to address the problem of divergent self-energy of point charges in classical electrodynamics, the BI framework imposes an upper bound on the electric field strength by modifying the standard QED Lagrangian.

Such Lagrangian, which describes the kinetic terms for the EM field, is given by:

$$\mathcal{L}_{\text{QED}} = -\frac{1}{4}F_{\mu\nu}F^{\mu\nu}, \tag{5.12}$$

where $F_{\mu\nu}$ is the EM field strength tensor, defined as $F_{\mu\nu} = \partial_\mu A_\nu - \partial_\nu A_\mu$, with A_μ being the EM four-potential.

The BI extension modifies this Lagrangian to include nonlinear terms that limit the strength of the electric field. The BI Lagrangian is expressed as:

$$\mathcal{L}_{\text{BI}} = \beta^2 \left(1 - \sqrt{1 + \frac{1}{2\beta^2}F_{\mu\nu}F^{\mu\nu} - \frac{1}{16\beta^4}(F_{\mu\nu}\tilde{F}^{\mu\nu})^2}\right), \tag{5.13}$$

where β is a free parameter with dimensions of mass squared in four-dimensional spacetime. The term $\tilde{F}^{\mu\nu}$ represents the dual field strength tensor, defined as $\tilde{F}^{\mu\nu} = \frac{1}{2}\epsilon^{\mu\nu\rho\sigma}F_{\rho\sigma}$, where $\epsilon^{\mu\nu\rho\sigma}$ is the Levi-Civita symbol.

The nonlinear terms in the BI Lagrangian introduce corrections to Maxwell's equations, which lead to modifications in EM wave propagation and other phenomena. This has implications for the interaction of MMs with EM fields. In particular, the BI framework predicts deviations from the linear Coulomb potential at high field strengths, which may be relevant for exploring the behaviour of monopoles in extreme environments such as heavy-ion collisions or near strong magnetic sources [262]. The BI theory also plays a role in cosmology and astrophysics, where it has been applied to investigate nonlinear effects in EM fields associated with compact astrophysical objects [263] and early-universe scenarios [264].

Additionally, experimental constraints on the BI parameter β have been derived from high-energy collider experiments, where precision measurements of photon-photon scattering can reveal deviations from standard QED [262]. In this context, an alternative approach to constraining MMs is provided by the BI theory via nonlinear modifications to QED.

Incorporating the BI extension into the SM via the hypercharge sector, specifically the $U(1)_Y$ gauge group, allows for the existence of finite-energy monopole solutions. These solutions, which are of Cho-Maison type [181, 182], are characterised by a monopole mass M_{CM}. The total mass is expressed as the sum of two contributions:

$$M_{\text{CM}} = E_0 + E_1, \tag{5.14}$$

where E_0 corresponds to the contribution from the BI extension of the $U(1)_Y$ hypercharge, and E_1 arises from the remaining terms in the Lagrangian. Specifically, the contribution from the BI term is related to the hypercharge mass scale $M_Y = \cos\theta_W M'$, where θ_W is the weak mixing angle and $M' = \sqrt{\beta}$ is the Born–Infeld mass scale. Recent estimates show that $E_0 \approx 72.8 M_Y$ [265] and $E_1 \approx 7.6$ TeV [266].

Expanding the BI Lagrangian in powers of β^{-2}, one can derive a connection between the anomalous gauge quartic couplings $\zeta_{1,2}$ (as defined in Eq. (5.2)) and the BI parameter β [267]. The relationship is given by:

$$\zeta_1 = -\frac{1}{32\beta^2}, \quad \zeta_2 = \frac{1}{8\beta^2}. \tag{5.15}$$

Thus, the constraints from the CT-PPS [260] experiment can be translated into a limit on β:

$$\beta = M'^2 > 0.71 \text{ TeV}^2, \tag{5.16}$$

which, in turn, provides an upper bound on the mass of the Cho-Maison monopole:

$$M_{\text{CM}} \approx 7.6 + 72.8 \cos\theta_W M' > 61 \text{ TeV}. \tag{5.17}$$

Additionally, loops of MMs would contribute to LbL scattering, as shown in Fig. 5.1. One can assume that their effects at energies much smaller than the monopole mass scale $\mathcal{M}_{MM}$ can be calculated by treating the monopoles as point-like. As is the case for many BSM scenarios, the value of $\mathcal{M}_{MM}$ lies well beyond the direct reach of current colliders.

5.4 Conclusions

Investigating the existence of magnetic monopoles is among the main open questions in particle physics today. This chapter has focused on constraining the mass of magnetic monopoles through indirect searches, particularly via diphoton events. These hypothetical particles can contribute to box-diagram processes, making them accessible through high-energy photon-photon interactions.

Light-by-light scattering, recently observed at the LHC by ATLAS and CMS, provides a unique avenue to probe physics beyond the Standard Model, including monopole-induced effects. Among the diphoton final state signatures, central exclusive $\gamma\gamma$ production stands out due to its clean experimental signature, where central photons are detected while intact outgoing hadrons are tagged using dedicated forward detectors. This approach significantly improves background suppression, and with it the sensitivity to NP contributions.

Constraints on magnetic monopoles have been derived within both the EFT framework and the BI theory. In the EFT approach, lower bounds on monopole masses were set by reinterpreting existing limits on anomalous gauge quartic couplings $\zeta_{1,2}$, previously obtained by the CMS-TOTEM collaboration in their search for central exclusive diphoton production. Experimental constraints from the CT-Precision Proton Spectrometer at the LHC provided lower bounds on monopole masses, with values ranging from $M > 2.86$ TeV for spin-0 monopoles to $M > 7.33$ TeV for spin-1 monopoles. These results highlight the potential of indirect searches to probe magnetic monopoles and emphasise the importance of precision measurements in photon-photon interactions for unveiling NP.

Incorporating the BI theory into the $U(1)_Y$ hypercharge sector of the Standard Model revealed the existence of finite-energy monopole solutions of Cho-Maison type. By relating the BI parameter β to anomalous gauge quartic couplings, constraints from collider experiments led to an estimated monopole mass of $M_{\text{CM}} > 61$ TeV.

Moving forward, further improvements in experimental precision, as well as refined theoretical frameworks, will be crucial in enhancing the sensitivity of indirect searches for magnetic monopoles. The ongoing and future collider programs, coupled with advanced data analysis techniques, may provide deeper insights into the existence and properties of these hypothetical yet theoretically well-motivated objects.

Chapter 6

Angular Correlations as Probes for New Physics

This chapter, based on [268–271], in which the PhD candidate is the first author, explores the potential of employing two-particle angular correlations as a tool for discovering NP. Angular correlations provide a complementary approach to conventional searches for NP, offering sensitivity to effects that may manifest as diffuse patterns across a large number of final-state particles.

The study focuses on a QCD-like HV model featuring new coloured states known v-quarks and v-gluons, which interact via a confining gauge group in the hidden sector. These particles communicate with the Standard Model through mediator particles, or communicators, typically with masses below 1 TeV. Such hidden sectors introduce unique experimental signatures, such as modified angular correlations, arising from the interplay between visible and invisible partonic cascades.

Future e^+e^- colliders, such as the ILC, provide an ideal environment for these studies due to their clean experimental conditions and well-defined initial states. This chapter investigates the feasibility of employing two-particle angular correlations at e^+e^- colliders for detecting signatures of HV scenarios.

6.1 Two-particle angular correlations

Two-particle angular correlations provide a crucial tool in collider physics for probing particle production dynamics and searching for deviations from the SM [272–274]. These correlations, observed in the relative angular distributions of particle pairs, reveal information about fundamental conservation laws, quantum interference effects and specific production mechanisms. By analysing patterns in the azimuthal angle difference $\Delta\phi$ and rapidity separation Δy, insights into both perturbative and non-perturbative processes can be obtained.

Unlike hadronic collisions, the clean environment of e^+e^- collisions allows for a well-defined reference frame, where the z-axis typically aligns with the direction of the back-to-back jets. Throughout this work, the *thrust* reference frame has been adopted. The rapidity y of each charged particle is computed with respect to this axis, while the azimuthal angle ϕ is defined in the plane transverse to it, event by event. The analysis focuses exclusively on angular differences between pairs of charged SM final-state particles labelled as '1' and '2', quantified as $\Delta y \equiv y_1 - y_2$ and $\Delta\phi \equiv \phi_1 - \phi_2$.

To construct the two-particle correlation functions, all distinct pairs of charged particles within an event are considered. For each pair, the angular differences Δy and $\Delta\phi$ are calculated and filled into a two-dimensional histogram, yielding the signal distribution $S(\Delta y, \Delta\phi)$. No ordering is imposed on the particles, and all combinations contribute once per event. The resulting distribution is then normalised by the total number of such pairs.

To obtain the background distribution $B(\Delta y, \Delta\phi)$ representing uncorrelated pairs, a mixed-event technique is employed. Each event i in the sample is paired with a subsequent uncorrelated event j (typically $j = i + 1$). All possible charged-particle pairs are formed between the two events, and the angular variables for these inter-event pairs are consistently computed in the thrust frame of event i. This ensures that both Δy and $\Delta\phi$ are defined with respect to a single, physically meaningful reference. The resulting histogram is normalised by the total number of mixed pairs.

Two-particle angular correlations are typically quantified using correlation functions of the form:

$$C^{(2)}(\Delta y, \Delta\phi) = \frac{S(\Delta y, \Delta\phi)}{B(\Delta y, \Delta\phi)}, \tag{6.1}$$

where $S(\Delta y, \Delta\phi)$ represents the density of particle pairs within the same event:

$$S(\Delta y, \Delta\phi) = \frac{1}{N_{\text{pairs}}} \frac{d^2 N^{\text{same}}}{d\Delta y\, d\Delta\phi}, \tag{6.2}$$

and $B(\Delta y, \Delta\phi)$ denotes the density of particle pairs from different events

$$B(\Delta y, \Delta\phi) = \frac{1}{N_{\text{mix}}} \frac{d^2 N_{\text{mix}}}{d\Delta y d\Delta\phi}. \tag{6.3}$$

Let us note that, according to the above definition, the absence of any correlation between particles corresponds to $C^{(2)}(\Delta y, \Delta\phi) = 1$. Positive (negative) correlations result in values greater (less) than unity.

Focusing on the azimuthal dependence of the correlation function, it is worth it defining the so-called *azimuthal yield*, $Y(\Delta\phi)$, by integrating over a specific Δy range:

$$Y(\Delta\phi) = \frac{\int_{y_{\text{inf}} \leq |\Delta y| \leq y_{\text{sup}}} S(\Delta y, \Delta\phi) dy}{\int_{y_{\text{inf}} \leq |\Delta y| \leq y_{\text{sup}}} B(\Delta y, \Delta\phi) dy}, \tag{6.4}$$

where $y_{\text{inf/sup}}$ defines the lower/upper integration limit for different rapidity intervals depending on the kinematic region of interest.

Angular correlations in high-energy collisions are influenced by various physical mechanisms. At hadron colliders, correlations can arise from back-to-back particle production in hard scatterings, jet fragmentation and collective effects in quark-gluon plasma [275, 276]. In e^+e^- collisions, angular correlations are primarily driven by the dynamics of parton showers and hadronisation.

Correlations play a fundamental role in the study of hadronic dynamics, dating back to the early days of cosmic ray and accelerator physics [277, 278]. More recently, the study of angular correlations has revealed new phenomena in heavy-ion collisions, later also observed in smaller systems such as proton-proton and proton-nucleus collisions [279, 280]. Of particular interest is the long-range angular correlation, characterised by a *ridge-like structure* in the final-state hadrons, emitted almost collinearly but with a significant rapidity difference. This ridge structure appears in a region where the correlation function is less affected by other known sources such as resonance decays and the fragmentation of energetic partons.

Since the LHC began operations, the CMS collaboration has observed a ridge structure on the nearside ($\Delta\phi \sim 0$) in high-multiplicity collisions [279, 281], and this observation has since been confirmed by other experiments at both the LHC and RHIC [282] in smaller collision systems, such as proton-ion collisions [276, 283, 284]. Subsequent studies have expanded to the away-side ($\Delta\phi \sim \pi$) in proton-proton, proton-ion and deuteron-ion collisions [285]. Various theoretical explanations have been proposed to understand these initially unexpected phenomena [273, 274, 286–289]. Almost all of them suggest the existence of an unconventional state of matter, such as quark-gluon plasma, at the primary interaction of the collision, ultimately yielding collective effects among final-state SM particles.

In contrast, no clear ridge-like signal has been found in e^+e^- data analysed by experiments such as ALEPH [290] and Belle [291], except for recent claims at the highest available energy and high multiplicity in [292]. The absence of ridge structures in e^+e^- collisions is consistent with the lack of gluonic fields and beam remnants, which are characteristic of hadron collisions. This cleaner environment makes e^+e^- colliders an excellent platform for studying angular correlations and searching for BSM physics.

These studies aim to provide insights into unknown stages of matter beyond the QCD parton shower. For instance, while QCD effects in hadron collisions have uncovered phenomena like the Glasma or Glass-Gluon Condensate [293], such states cannot be achieved in e^+e^- collisions due to the absence of initial gluonic fields.

In heavy-ion collisions, ridge structures are attributed to collective flow dynamics, while in e^+e^- systems, angular correlations are dominated by back-to-back dijet topologies resulting from $q\bar{q}$ pair production. These dijets fragment along characteristic $1 + \cos^2\theta$ angular distributions relative to the beam axis. Pairwise correlations of the global dijet topology vary depending on the event orientation, leading to smearing effects in the two-particle angular correlation function. Such effects reduce sensitivity to detecting collective behaviours or anomalies, which may only occur between the outgoing quarks.

The nearside peak correlation, located near $(\Delta y, \Delta\phi) = (0, 0)$, primarily arises from track pairs originating within the same jet. Conversely, the away-side correlation, elongated along $\Delta\phi \sim \pi$, reflects back-to-back momentum balancing. These features are commonly observed across various collision systems and provide valuable probes into the dynamics of particle production. Furthermore, to enhance sensitivity to specific physical processes, selection criteria such as p_T, charge, and particle type can be applied. For instance, high-p_T correlations reveal hard scattering processes, while low-p_T correlations often highlight collective or soft-QCD effects.

In summary, angular correlations provide a versatile tool for probing both perturbative and non-perturbative phenomena in high-energy collisions.

Motivated by unexpected correlation structures observed in high-energy collisions, this chapter examines potential anomalies—not limited to ridge effects—in both azimuthal and (pseudo)rapidity correlations. In this context, the clean environment of e^+e^- colliders is particularly advantageous for exploring potential NP signatures.

A detailed investigation of HV scenarios in e^+e^- collisions will be presented in the following chapter.

6.2 Hidden Valley Phenomenology

The term *Hidden Valley* encompasses a wide class of models where the SM gauge group G_{SM} is extended by a hidden non-Abelian group G_v [294]. In these models, all SM particles are neutral under G_v, while new light particles ($v-$*particles*) are introduced that carry charges under G_v and are neutral under G_{SM}. The dynamics of the HV sector are governed by the properties of the gauge group G_v, the spin and number of particles in the theory and their representations under G_v. A key feature of HV models is the ultra-weak coupling between the hidden sector and the visible SM sector. The communication between these two sectors occurs via higher-dimensional operators at the TeV scale, which may arise from a variety of mechanisms. These include the exchange of a neutral Z' boson, loops of heavy particles carrying both G_{SM} and G_v charges, heavy sterile neutrinos, or even couplings involving the Higgs boson or multiple Higgs fields.

In a confining HV scenario, $v-$particles assemble themselves into G_v-neutral composite states, referred to as "$v-$hadrons". These $v-$hadrons can then decay into SM particles through higher-dimensional operators, with lifetimes that vary based on the underlying parameters of the model, such as the $v-$quark masses. The mass spectrum, lifetimes, and multiplicities of the $v-$hadrons depend intricately on the details of the HV dynamics. For instance, a QCD-like hidden sector would involve $v-$hadrons such as $v-$pions (v-π), $v-$eta mesons (v-η), $v-$kaons (v-K), and $v-$nucleons, analogous to QCD hadronisation [294–296].

These scenarios are particularly suitable for studying radiation effects due to the significant mass disparity between communicators and $v-$particles. Typically, communicators have masses around the TeV scale, whereas $v-$particle masses can be as low as 1–10 GeV. If both communicators and $v-$particles are charged under a new gauge G_v, they will radiate gauge bosons. The larger the mass ratio between communicators and $v-$particles, the greater the available phase space for radiation, both in the visible and hidden sectors. Therefore, if observable effects are to be detected, they are likely to manifest in such scenarios.

The impact of the hidden sector on visible particle spectra depends on how the hidden sector interacts with the SM. This interaction could occur via a Higgs boson, multiple Higgs bosons, a Z' boson, heavy sterile neutrinos, or through loops involving heavy particles charged under both SM and HV gauge interactions.

6.2.1 QCD-like scenario

The scenario studied in this thesis is a *QCD-like* model [295]. In this framework, the hidden sector gauge group G_v is analogous to QCD, featuring a strong coupling constant α_v that evolves similarly to the strong coupling. This behaviour leads to the confinement of hidden sector particles at low energies, resulting in the hadronisation of v-particles into G_v-neutral composite states.

Here, a HV scenario with a non-Abelian $SU(3)$ gauge group is considered. The hidden gauge boson, denoted as g_v, is assumed to be massless for simplicity. The $SU(3)$ gauge group remains unbroken, mirroring the behaviour of the QCD sector, which governs the dynamics of the hidden valley.

The HV particle content includes F_v, which are charged under both the SM and HV $SU(3)$ gauge groups. These particles couple flavour-diagonally to their SM counterparts, sharing the same SM charge and colour while residing in the fundamental representation of the HV gauge group. Each F_v particle *promptly* decays into its corresponding SM state (f) and an invisible, massive HV particle (q_v), as described by the decay $F_v \to f q_v$. Here, q_v is charged under the $SU(3)$ HV gauge group.

In this study, F_v is assumed to be a spin-1/2 particle, while q_v is taken to have spin-0. The mass of q_v is constrained to be less than that of F_v, preventing the formation of stable F_v particles. This mass hierarchy ensures that q_v strongly influences the decay dynamics of F_v, which in turn governs the observable experimental signatures.

HV particles are required to be pair-produced, with production occurring through electroweak processes. At lepton colliders, these processes are dominated by $\ell^+\ell^- \to \gamma^*/Z^0 \to F_v\bar{F}_v$, where ℓ represents SM charged leptons. This mechanism allows for the production of F_v particles, which subsequently decay into SM particles and invisible q_v particles. The pair production cross sections for F_v states include a factor of $N_c = 3$, reflecting the fundamental representation of the $SU(3)$ HV gauge group.

The clean experimental environment of e^+e^- colliders enhances the sensitivity to HV signatures. These features make e^+e^- colliders ideal for probing BSM physics within the HV framework.

Both F_v and q_v can radiate hidden gluons (g_v) due to their charge under the HV $SU(3)$ gauge group. These radiative processes include $F_v \to F_v g_v$ and $q_v \to q_v g_v$. In addition, non-Abelian branchings such as $g_v \to g_v g_v$ are allowed, further enriching the dynamics of the hidden sector.

Parton showers play a central role in capturing the evolution of HV radiation. By modelling the sequential emission of g_v gluons, including non-Abelian branching, the parton shower provides insights into the interplay between hidden sector dynamics and observable phenomena. The radiation patterns and their impact on experimental signatures form a key focus of this thesis.

This study specifically investigates the influence of the invisible HV sector on the partonic cascade leading to final-state SM particles, which could result in potentially observable effects. These effects arise because both the visible and hidden cascades share the event's total energy, thereby modifying their respective phase spaces. For concreteness, the analysis is restricted to a QCD-like HV scenario involving q_v-quarks, g_v-gluons, and an equivalent "strong" coupling constant α_v.

6.3 Analysis at detector level

In this work, the feasibility of detecting HV signals at e^+e^- colliders has been investigated using the Pythia Monte Carlo event generator [297], a tool widely regarded for its reliability and comprehensive implementation of HV production channels. Fast detector simulations were carried out with the SGV tool [298], employing the geometry and acceptances corresponding to the large model of the International Large Detector (ILD) concept for the ILC, as detailed in [299].

Simulated events were generated in a format compatible with that used by the ILD concept group, enabling the application of tools within the ILC-Soft package for event reconstruction and analysis. The reconstruction process is based on the Particle Flow approach, which aims to identify all individual particles in the final state using advanced pattern recognition algorithms. The reconstructed candidates, referred to as Particle Flow Objects (PFOs), form the basis of the subsequent analysis.

For the study at the detector level, a c.o.m. energy of $\sqrt{s} = 250$ GeV was chosen to correspond to the suggested initial operation of the ILC as a Higgs boson factory. Additionally, exploratory analyses were extended to $\sqrt{s} = 500$ GeV and 1 TeV at the particle level. For this study, unpolarised beams were taken into account.

The HV signal arises via the process $e^+e^- \to D_v\bar{D}_v \to$ hadrons, where D_v denotes the lightest communicator particle, which is the hidden-sector analogue of the SM d-quark. For the benchmark scenarios, the coupling constant was set to $\alpha_v = 0.1$, and the communicator mass m_{D_v} was fixed at 125 GeV, with four distinct v-quark masses: $m_{q_v} = 0.1, 10, 50$ and 100 GeV. Additional configurations included $m_{D_v} = 80$ and 100 GeV with $m_{q_v} =$ 40 and 50 GeV, respectively. At higher energies ($\sqrt{s} > 250$ GeV), the pair production of heavier communicator particles, $T_v\bar{T}_v$, was also included, where T_v is the hidden-sector partner of the SM top quark.

The main background at $\sqrt{s} = 250$ GeV originates from inclusive $e^+e^- \to q\bar{q}$ production of all SM quark flavours, excluding the top quark due to the threshold constraint. Four-fermion production, primarily $e^+e^- \to WW$, was found to contribute negligibly. A previous investigation [269] examined signal and background processes at the particle level without considering Initial State Radiation (ISR), which was included in the present study, as its effect is critical to the analysis.

Cross sections for the HV and SM processes, estimated using Pythia, are summarised in Table 6.1, along with selection efficiencies, average charged-track multiplicities, and their root-mean-square (RMS) values.

To improve signal sensitivity and reduce background contamination, the following sequence of selection cuts was applied. $S1$ imposes zero displaced vertices per jet and a maximum of 15 charged and 22 neutral PFOs; $S2$ applies cuts on the reconstructed ISR photon candidate's angle and energy, requiring $|\cos\theta_{\gamma_{\text{ISR}}}| < 0.5$ and $E_{\gamma_{\text{ISR}}} < 40$ GeV; $S3$ applies jet-level constraints, with $m_{jj} < 130$ GeV and leading jet energy below 80 GeV; and $B1$ selects events with a thrust value greater than 0.95. The $S1$–$S3$

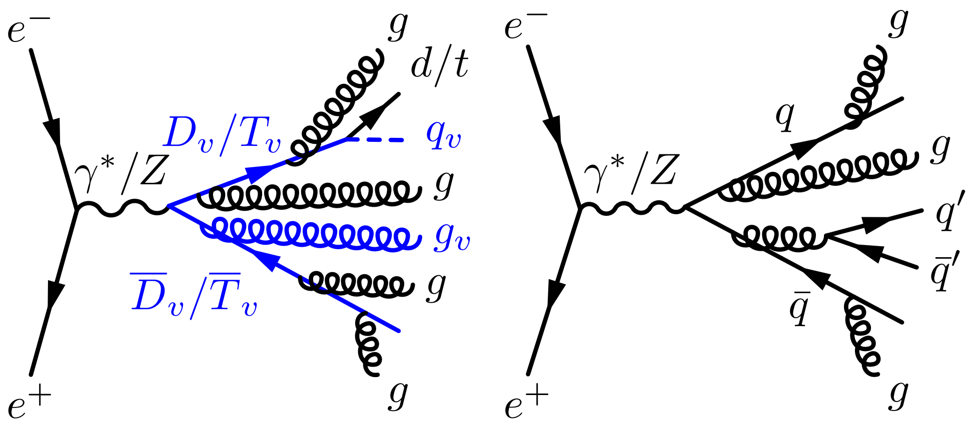

(a) Hidden valley **(b)** SM light quarks

Figure 6.1: Leading diagrams of production in e^+e^- collisions for a) HV, and b) SM light quarks including bottom.

cuts are applied when constructing the signal distribution $S(\Delta y, \Delta\phi)$, while the background distribution $B(\Delta y, \Delta\phi)$ is built using events that pass $S1$, $S2$, and $B1$. Selection efficiencies for the different processes, after applying these cuts in combination, are summarised in Table 6.2. In this table, we also distinguish between the $q\bar{q}$-RR background, dominated by radiative return events where initial-state radiation lowers the effective centre-of-mass energy, and the $q\bar{q}$-Cont. (continuum) background, which corresponds to $q\bar{q}$ production at partonic level with an invariant mass close to $\sqrt{s}$ before parton shower.

Two-particle angular correlations were evaluated in the thrust axis frame through the function $C^{(2)}(\Delta y, \Delta\phi)$, as illustrated in Fig. 6.2. Detector-level distributions were analysed both before (Fig. 6.2a) and after (Fig. 6.2b) applying selection cuts. For the *pure* HV signal, benchmark masses $m_{q_v} =$ 100 GeV, $m_{D_v} = 125$ GeV, and $\alpha_v = 0.1$ were employed, with decays of $D_v \to d + q_v$ initiating both visible and invisible partonic cascades. The near-side peak at $(\Delta y \simeq 0, \Delta\phi \simeq 0)$, dominated by intra-jet particle pairs, and the away-side ridge at $\Delta\phi \simeq \pi$, arising from back-to-back momentum conservation, were evident in both the HV and SM scenarios.

The application of selection cuts produced significant changes in the distributions. For $1.6 < |\Delta y| < 3$, a near-side ridge with two symmetric peaks at $\Delta\phi \simeq 0$ was observed in the SM case, resembling HV-like

Table 6.1: Inclusive cross sections for $e^+e^- \to D_v\bar{D}_v$, $e^+e^- \to q\bar{q}$ and $e^+e^- \to WW \to 4q$ processes at $\sqrt{s} = 250$ GeV, with different assignments for the m_{D_v} and m_{q_v} masses. Efficiencies of the selection criteria described in the main text, average charged-track multiplicities and their RMS, are shown.

Process		σ_{Pythia} [pb]	Eff. [%]	$\langle N_{\text{ch}} \rangle$
$e^+e^- \to D_v\bar{D}_v$	m_{D_v}			
$m_{q_v} = 0.1$ GeV	125 GeV	0.13	36	12.4 ± 3.7
$m_{q_v} = 10$ GeV	125 GeV	0.12	36	12.4 ± 3.7
$m_{q_v} = 50$ GeV	125 GeV	0.12	42	11.4 ± 3.5
$m_{q_v} = 100$ GeV	125 GeV	0.12	42	6.5 ± 2.1
$m_{q_v} = 50$ GeV	100 GeV	1.29	42	11.1 ± 3.4
$m_{q_v} = 40$ GeV	80 GeV	1.54	36	18.0 ± 4.9
$e^+e^- \to q\bar{q}$ w/ ISR		48	$\lesssim 0.01$	9.9 ± 3.4
$e^+e^- \to WW \to 4q$		7.4	$\lesssim 0.001$	–

signatures. This structure is attributed to ISR effects, where the effective c.o.m. energy approaches the Z-boson resonance, greatly enhancing production rates. Such ISR-induced features underscore the importance of including this effect in the analysis, as they may mimic potential HV signals.

It is worth emphasising that all angular observables are computed in the thrust reference frame. In the HV case, although each D_v decay produces an invisible v-quark, the two visible SM quarks typically emerge in opposite hemispheres and dominate the thrust reconstruction. This results in a dijet-like topology, which explains the clear away-side peak at $\Delta\phi \simeq \pi$ in the HV signal.

To study this further, the azimuthal yield $Y(\Delta\phi)$, defined in Eq. (6.4), was examined for two rapidity intervals, $0 < |\Delta y| \leq 1.6$ and $1.6 < |\Delta y| < 5$, both before and after applying selection cuts, as shown in Fig. 6.3. Note that the HV signal for various combinations of m_{Dv} and m_{qv} is analysed alongside the SM background, while a separate analysis of the SM background alone is also provided.

The distributions used in the numerator of the yield are defined as:

$$S^{\text{SM}}(\Delta y, \Delta\phi) = \frac{1}{N^{\text{SM}}_{\text{pairs}}} \frac{d^2 N^{\text{SM}}_{\text{same}}}{d\Delta y\, d\Delta\phi}, \tag{6.5}$$

Table 6.2: Breakdown of efficiencies of the selection criteria described in the main text. For simplicity, only one HV model is shown, since results are very similar for the rest: $e^+e^- \to D_v\bar{D}_v$ with $m_{D_v} = 125$ GeV and $m_{q_v} = 100$ GeV. The two SM processes described in the text and in Table 6.1 are also shown. The definition of the cuts, $S1 - S3$ and $B1$ are defined in the text. In this table we also differentiate between the $q\bar{q}$-RR (dominated by radiative return events) and the $q\bar{q}$-Cont. in the continuum (*i.e.,* with $m_{q\bar{q}}^{inv} \sim \sqrt{s}$ at partonic level and before parton shower).

	Efficiency [%]			
Cuts	HV	$q\bar{q}$-RR	$4q$	$q\bar{q}$-Cont.
$S1 =$ multiplicity cuts	89	30	64	40
$S1 + S2 = S1+$ ISR photon cuts	42	3.8	12	8.8
$S1 + S2 + S3 = S1 + S2+$ energy and inv. mass cuts	42	$\lesssim 0.01$	$\lesssim 0.001$	–
$S1 + S2 + B1 = S1 + S2+$ Thrust cut	–	–	–	5.6

$$S^{\text{SM+HV}}(\Delta y, \Delta\phi) = \frac{1}{N_{\text{pairs}}^{\text{SM}} + N_{\text{pairs}}^{\text{HV}}} \left(\frac{d^2 N_{\text{same}}^{\text{SM}}}{d\Delta y\, d\Delta\phi} + \frac{d^2 N_{\text{same}}^{\text{HV}}}{d\Delta y\, d\Delta\phi} \right). \tag{6.6}$$

A pronounced peak at $\Delta\phi \sim \pi$ is observed in the HV+SM case for $0 < |\Delta y| \leq 1.6$, clearly distinguishing it from the SM-only background. This discrepancy in shape between the HV+SM and *pure* SM distributions after selection cuts would potentially serve as a valuable signature of a hidden sector, complementing traditional BSM searches.

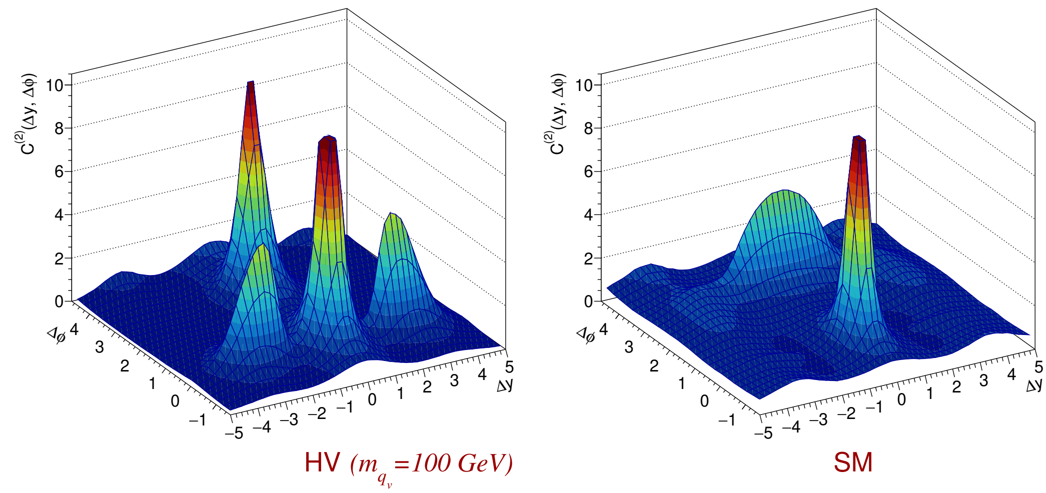

(a) Detector-level distributions for the *pure* HV signal (left) and the SM background (right) with no selection applied to the $S(\Delta y, \Delta\phi)$ reconstruction. Angular variables are defined in the thrust axis frame.

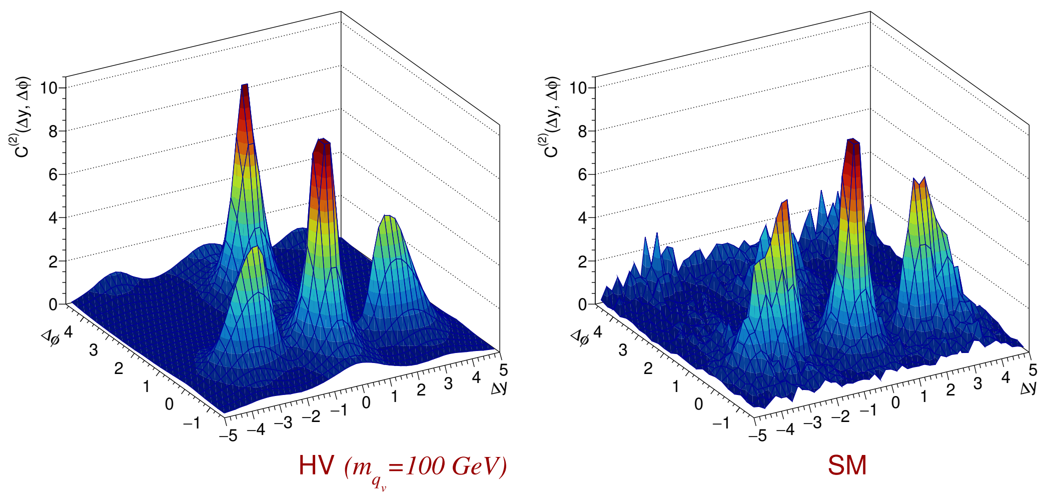

(b) Detector level distributions for the *pure* HV signal (left) and the SM background (right) after the signal enriching experimental cuts applied to the $S(\Delta y, \Delta\phi)$ reconstruction. Angular variables are defined in the thrust axis frame.

Figure 6.2: 3D plots of the two-particle angular correlation function in the thrust frame, $C^{(2)}(\Delta y, \Delta\phi)$, at detector level, separately for the pure HV signal and the SM background in e^+e^- collisions at $\sqrt{s} = 250$ GeV. In the pure HV case, $m_{q_v} = 100$ GeV, m_{D_v} =125 GeV and $\alpha_v = 0.1$ were set. For the SM case, light quarks include the bottom flavour.

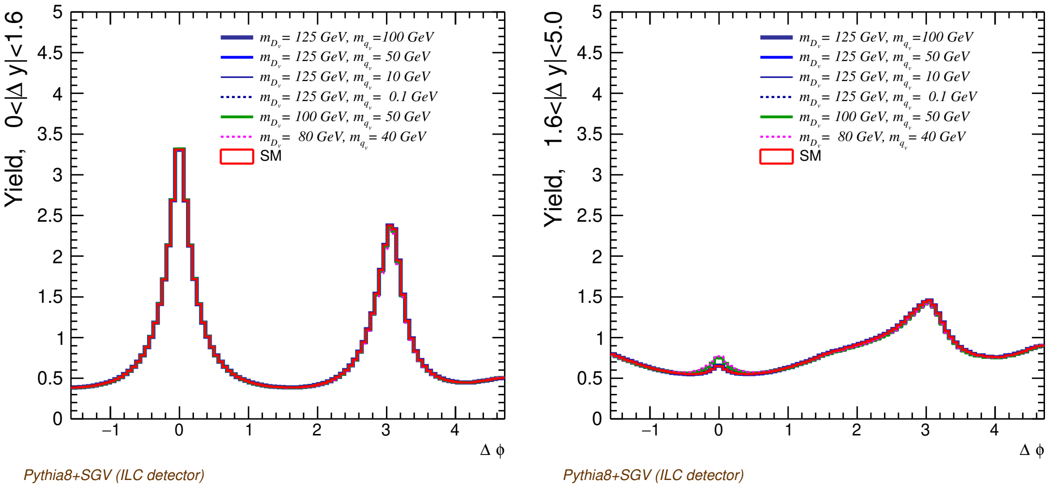

(a) Detector-level yield distributions as a function of $\Delta\Phi$ with no selection cuts applied.

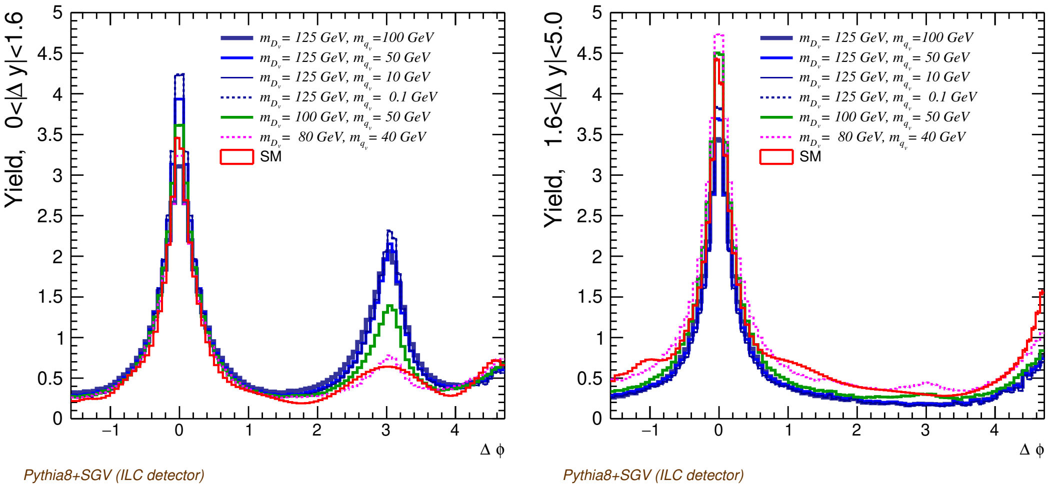

(b) Detector-level yield distributions as a function of $\Delta\Phi$ after the selection cuts were applied to enrich the $S(\Delta y, \Delta\phi)$ sample with HV signal events.

Figure 6.3: Yield $Y(\Delta\phi)$ for both HV signal *combined* with SM and for pure SM background (red line) for the $0 < |\Delta y| < 1.6$ (left) and $1.6 < |\Delta y| < 5$ (right) intervals.

6.4 Prospects on the Experimental Sensitivity

Analyses searching for BSM physics in high-energy collisions using angular correlations, as proposed in this work, offer several advantages over conventional methods, such as relying on cross section excesses or invariant mass peaks. In particular, yield distributions, as defined in Eq. (6.4), benefit from the near-complete cancellation of reconstruction efficiencies, detector acceptances, luminosity dependence, and cross section uncertainties. However, modelling uncertainties could pose a limitation for these observables. To address this, a study was performed assuming different scenarios for statistical and systematic uncertainties.

To estimate statistical uncertainties, a collected integrated luminosity of 100 fb^{-1} was assumed, corresponding approximately to one year of data collection under the H20-staged ILC scenario [119]. Systematic uncertainties were categorised into two primary sources: detector performance modelling and fragmentation uncertainties related to the final hadronisation of the partonic cascade. Both sources were estimated using educated guesses based on current knowledge.

The uncertainty arising from detector performance was evaluated through a bin-by-bin comparison of yield distributions at particle and detector levels. The absolute difference between the two levels was taken as the uncertainty, accounting for kinematic resolution effects, including angular track reconstruction and detector acceptance. This approach represents a conservative, worst-case scenario, as it overestimates experimental uncertainties.

Fragmentation uncertainty was assessed by comparing yield predictions at the particle level generated using two different fragmentation models implemented in Pythia and Herwig [300, 301]. The total uncertainty for each bin was obtained by adding the statistical uncertainty for the expected number of events to the systematic uncertainties associated with the SM yield Y_{SM}, with HV production incorporated only in Pythia.

The results of this analysis are summarised in Fig. 6.4, where σ_Y denotes the estimated uncertainty. Two scenarios were considered: one using current state-of-the-art modelling uncertainties and another assuming a one-order-of-magnitude improvement in systematic uncertainty estimation.

In the first scenario, the sensitivity of the observable was calculated by comparing the HV and SM predictions for Y with the expected uncertainties. At 100 fb^{-1}, sensitivity is primarily limited by systematic uncertainties, with detector performance uncertainties dominating over all others. Nevertheless, the discovery potential remains significant, particularly near the prominent Y peak at $\Delta\phi \sim \pi$ within $0 < |\Delta y| \leq 1.6$.

In the second scenario, the uncertainty improvements could arise from better detector performance modelling and more robust fragmentation modelling of HV processes. Under these assumptions, sensitivity would be drastically enhanced, enabling potential discovery across most of the accessible phase space. While this represents an educated estimate, it underscores the importance of pursuing optimised detector designs and advancements in Monte Carlo tools to minimise modelling uncertainties further.

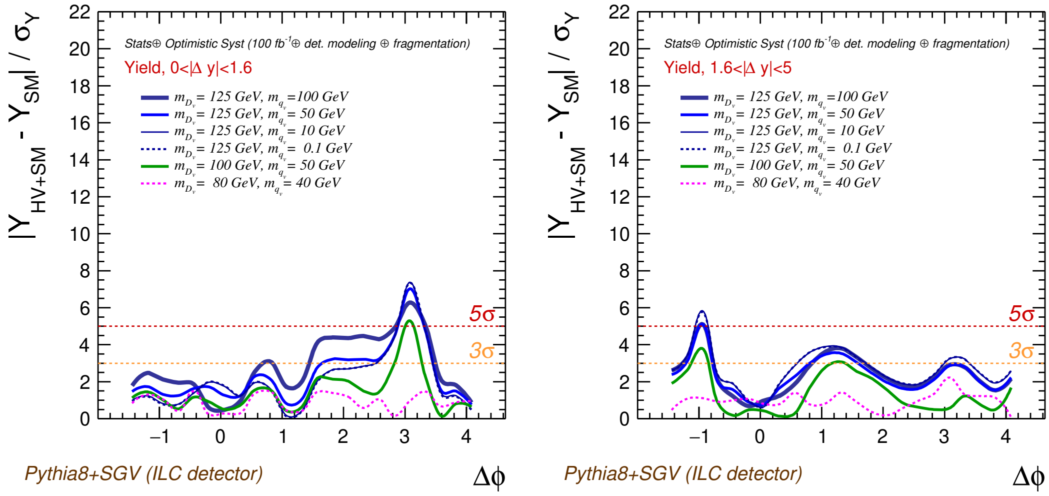

(a) Systematic uncertainties based on the current state-of-the-art knowledge.

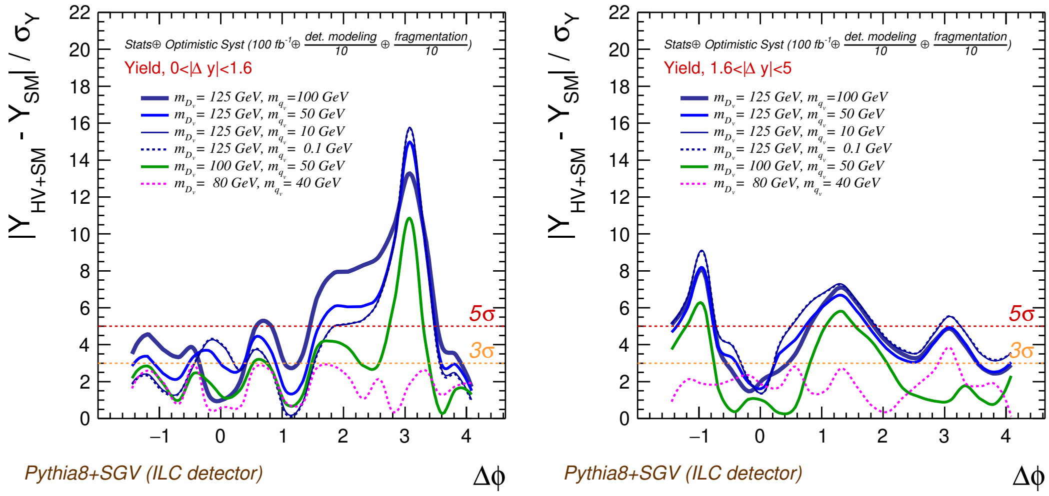

(b) Systematic uncertainties improved by one order of magnitude.

Figure 6.4: Expected experimental sensitivity for Hidden Valley models alongside the SM background after collecting 100 fb^{-1} of integrated luminosity. Yield measurements are shown for $0 < |\Delta y| < 1.6$ (left) and $1.6 < |\Delta y| < 5$ (right). The experimental sensitivity is dominated by systematic uncertainties related to detector response, parton showers, and fragmentation modelling.

6.5 Different energies and colliders

So far, the focus was on a future e^+e^- collider operating at $\sqrt{s}$ = 250 GeV, but likely those machines will later run at higher energies. Therefore the study was extended to $\sqrt{s} = 0.5$ and 1 TeV at particle level.

For the HV signal $e^+e^- \to Q_v\bar{Q}_v \to$ hadrons, we consider the two extreme cases: the lightest communicator D_v and the heaviest one T_v which decays into $q_v t$. It was confirmed that intermediate masses yield intermediate results.

Besides the $q\bar{q}$ and $WW \to 4q$ backgrounds, we also take into account the production of $t\bar{t}$, which, in fact, becomes relevant at these energies. Table 6.3 presents the cross sections obtained from PYTHIA. The mass of D_v and T_v was set equal to $\sqrt{s}/2$, and results for different m_{q_v} are shown. No large variations are obtained around this mass assignment to the communicator. According to expectations, the contribution from the SM backgrounds decreases with energy. For the HV signal, a reduction of the cross section by two orders of magnitude is obtained at $\sqrt{s} = 1$ TeV.

This study is also relevant for the e^+e^- option of the FCC operating at an energy of $\sqrt{s} = 240$ GeV, i.e. very near to the one assumed so far. The limited coverage in the forward region makes the ISR-photon detection less efficient, yet the pertinent optimisation of selection cuts recovers sensitivity to a HV signal [302]. Further investigations for the FCC case are expected to take place in the future to refine these studies.

Table 6.3: Inclusive cross sections of the HV signal and SM background at $\sqrt{s} = 500$ GeV and $\sqrt{s} = 1$ TeV. Cross section predictions do not depend on the m_{q_v} value unless it is too large to make the process kinematically inaccessible. The signal corresponds to D_v and T_v pair production with the D_v/T_v mass set equal to $\sqrt{s}/2$. Whenever kinematically allowed, $t\bar{t}$ production has been included as a SM background source in addition to lighter flavours considered at $\sqrt{s} = 250$ GeV.

Process	$\sigma_{\sqrt{s}=500\text{GeV}}$ [pb]	$\sigma_{\sqrt{s}=1\text{TeV}}$ [pb]
	$m_{D_v} = 250$ GeV	$m_{D_v} = 500$ GeV
$e^+e^- \to D_v\bar{D}_v$	2.4×10^{-2}	4.4×10^{-3}
	$m_{T_v} = 250$ GeV	$m_{T_v} = 500$ GeV
$e^+e^- \to T_v\bar{T}_v$	9.5×10^{-2}	1.8×10^{-2}
$e^+e^- \to q\bar{q}$ with ISR	11	2.9
$e^+e^- \to t\bar{t}$	0.59	0.19
$WW \to 4q$	3.4	1.3

6.6 Conclusions

The study of particle correlations in high-energy colliders provides valuable insights into matter under extreme temperature and density conditions, reminiscent of the early universe when quarks and gluons existed as free particles before hadronisation. Moreover, such analyses serve as a complementary approach to conventional methods for probing the existence of new phenomena, as proposed in previous studies [272, 303] and further investigated in this work.

Motivated by experimental observations of unexpected structures in angular correlations from hadronic collisions, this study explored the potential of detecting hidden sectors at future e^+e^- colliders using two-particle angular correlations. A QCD-like HV model was considered, involving v-quarks and v-gluons interacting with the SM through communicators of typical mass $\lesssim 1$ TeV. The analysis focused on $D_v\bar{D}_v$ pair production at $\sqrt{s} = 250$ GeV, consistent with the anticipated mass of the lightest communicator. The study was extended briefly to higher energies (up to 1 TeV) at the particle level, demonstrating promising prospects for such scenarios.

The findings suggest that two-particle azimuthal correlations at a future e^+e^- Higgs factory could serve as an effective tool for uncovering NP provided it is kinematically accessible. While the analysis employed a specific HV model, similar signatures are expected for other hidden sector scenarios. Additionally, it cannot be ruled out that collective effects from sources unrelated to BSM physics may also contribute to such correlation patterns.

These findings highlight the importance of pursuing complementary search strategies, such as angular correlation studies, in combination with conventional methods. By broadening the range of techniques employed, the discovery potential of future high-energy colliders can be significantly enhanced, offering a more comprehensive approach to exploring fundamental physics.

Chapter 7

Conclusions and Outlook

This thesis has explored various avenues to search for BSM physics, focusing on HIPs such as magnetic monopoles and HECOs, as well as hidden sector scenarios accessible at high-energy colliders. By combining analytical calculations, constraints from EFT and BI theory, advanced resummation techniques, and collider simulations, this work presents a comprehensive strategy to probe NP both at present and future experimental facilities.

The investigation of magnetic monopoles was primarily conducted through indirect searches at the LHC, using diphoton events to exploit LbL scattering processes. These processes, sensitive to NP contributions, offer a clean experimental signature where events with central photons are collected with forward proton tagging. Constraints on monopole masses were derived within both EFT and BI frameworks. The EFT approach leveraged anomalous quartic gauge coupling limits from LHC experiments, setting lower mass bounds that reached beyond 7 TeV for spin-1 monopoles. The incorporation of BI theory into the hypercharge sector of the SM further constrained the existence of Cho–Maison monopoles to masses exceeding 60 TeV. These results underscore the importance of precision measurements in photon–photon interactions as a powerful indirect probe of BSM physics.

Complementing the monopole studies, significant efforts were devoted to HECOs. These hypothetical particles, characterised by their large electric charges, have been the focus of both theoretical modelling and experimental searches. The thesis extended DS resummation techniques previously applied to spin-1/2 HECOs to the scalar (spin-0) sector. In contrast to the fermionic case, scalar HECOs require a minimal self-interaction term to ensure the existence of a non-trivial UV fixed point. These were implemented into UFO models compatible with Monte Carlo event generators such as MadGraph, enabling realistic simulations of HECO production at colliders. The resummed cross-sections demonstrated significant enhancements over tree-level estimates, with improvements up to a factor of 2.1 for Drell–Yan processes and 4.75 for photon-fusion mechanisms. Consequently, mass bounds derived from ATLAS and MoEDAL data improved by up to 30%, highlighting the importance of resummation effects in interpreting experimental constraints.

Furthermore, this dissertation explored hidden sector signatures through the analysis of two-particle angular correlations at future e^+e^- colliders. Motivated by experimental observations of unexpected structures in hadronic collisions, a QCD-like HV model was considered, featuring v-quarks and v-gluons interacting with the SM via mediators of mass typically $\lesssim$ 1 TeV. Detector-level simulations focused on $D_v\bar{D}_v$ pair production at a c.o.m. energy of 250 GeV, corresponding to the expected mass range for the lightest communicators. To assess the future collider potential, the study was extended at particle level to higher energies of 500 GeV and 1 TeV, indicating promising prospects for probing hidden sectors. The results demonstrated that two-particle azimuthal correlations at an e^+e^- Higgs factory could serve as a valuable tool for discovering NP if kinematically accessible. While the analysis centred on a specific HV model, similar signatures are expected across various hidden sector scenarios.

In conclusion, this thesis has shown how combining advanced theoretical methods, detailed simulations, and experimental data can significantly improve the search for NP. The tools and models developed here provide experimental collaborations with valuable resources to better study fundamental particles and interactions.

Chapter 8

Resum de la tesi

Aquesta tesi investiga la possibilitat d'explorar nova física a partir de dades de col·lisionadors, combinant models teòrics amb resultats experimentals. El treball cobreix diferents extensions del Model Estàndard (SM) i l'impacte que poden tindre en la cerca de partícules exòtiques, com els Monopols Magnètics (MMs) i els objectes de càrrega elèctrica elevada (HECOs). A més, s'examinen futures instal·lacions de col·lisionadors i l'impacte de correlacions angulars en la recerca de nova física.

8.1 Introducció

8.1.1 El Model Estàndard de la Física de Partícules

El SM descriu les interaccions fonamentals entre les partícules elementals a partir del grup de simetria $SU(3)_C \times SU(2)_L \times U(1)_Y$. Aquestes interaccions s'organitzen en tres forces fonamentals: la interacció forta, responsable de la cohesió nuclear mitjançant l'intercanvi de gluons; la interacció feble, que causa processos com la desintegració beta i es transmet a través dels bosons W i Z; i la interacció electromagnètica, mediada pel fotó i responsable de les forces entre partícules carregades. A més, el bosó de Higgs proporciona el mecanisme pel qual les partícules adquireixen massa mitjançant la ruptura espontània de la simetria electrodèbil.

Tot i el seu notable èxit en la predicció i confirmació experimental de partícules, com el bosó de Higgs, el SM presenta diverses limitacions. Entre aquestes, destaca la seva incapacitat per incloure la gravetat, explicar la naturalesa de la matèria fosca i l'energia fosca, així com resoldre el problema de la jerarquia de masses entre les partícules fonamentals.

8.1.2 Motivacions per a Nova Física

Les evidències d'observacions astrofísiques i cosmològiques suggereixen que el SM no és una teoria completa. La matèria fosca, que constitueix aproximadament el 27% de l'univers, no està descrita pel SM, ja que cap de les partícules conegudes té les propietats adequades per explicar les observacions experimentals. Així mateix, l'energia fosca, que representa al voltant del 68% de l'univers i és responsable de l'expansió accelerada de l'univers, també queda fora de l'abast del SM.

A banda d'aquests problemes cosmològics, el SM presenta inconsistències teòriques. Per exemple, el problema de la jerarquia fa referència a la gran diferència entre l'escala de la interacció electrodèbil (~ 100 GeV) i l'escala de Planck ($\sim 10^{19}$ GeV), on la gravetat esdevé significativa. Sense una nova física que estabilitze la massa del bosó de Higgs, les correccions quàntiques haurien de fer-la extremadament gran. Diversos models proposen solucions, com la supersimetria (SUSY), els models amb dimensions extra i els mecanismes de composició del Higgs.

També es discuteixen les possibilitats de noves partícules massives amb interacció feble (WIMPs), els axions i les teories de gran unificació (GUTs), que podrien proporcionar una descripció més completa de les interaccions fonamentals.

8.1.3 Física de Col·lisionadors

La nostra comprensió de la física subnuclear es basa, en gran mesura, en l'estudi de col·lisions d'alta energia entre partícules elementals. Els col·lisionadors són dispositius sofisticats dissenyats per a accelerar partícules carregades —com electrons, protons i les seues antipartícules— mitjançant camps elèctrics i magnètics, dirigint aquests feixos energètics a col·lisions

controlades. Aquestes màquines tenen un paper fonamental en l'exploració de les interaccions fonamentals i en la recerca de física més enllà del Model Estàndard (BSM). Els col·lisionadors acceleren dos feixos en direccions oposades per provocar col·lisions frontals, maximitzant així l'energia disponible al sistema centre de masses i millorant la capacitat per a descobrir nous fenòmens.
Els col·lisionadors moderns es classifiquen principalment en col·lisionadors d'hadrons i col·lisionadors de leptons, cadascun amb avantatges específics. Els col·lisionadors d'hadrons, com el Gran Col·lisionador d'Hadrons (LHC), aconsegueixen energies més altes, tot i que han d'afrontar entorns de col·lisió més complexos a causa de l'estructura composta dels hadrons. Per contra, els col·lisionadors de leptons —com els proposats acceleradors d'electrons i positrons— proporcionen condicions experimentals més netes, cosa que permet realitzar mesuraments d'alta precisió per posar a prova el Model Estàndard i detectar efectes subtils de nova física.
Entre els paràmetres clau de rendiment es troben la luminositat i l'energia en el centre de masses, tots dos essencials per a determinar la probabilitat de processos rars i la sensibilitat global de l'experiment. Altes lluminositats garanteixen taxes de col·lisió suficients per a estudiar esdeveniments poc freqüents, mentre que energies més altes permeten explorar nous règims cinemàtics per a la producció de partícules. Els avanços tecnològics en el disseny d'acceleradors —com els sincrotrons, acceleradors lineals i tecnologies d'imants de darrera generació— continuen ampliant aquests límits.

Els col·lisionadors han sigut crucials per a descobriments clau en física, com ara el bosó de Higgs, i han permés fer proves rigoroses del sector electrodèbil. Els projectes de col·lisionadors futurs busquen complementar les instal·lacions actuals, centrant-se tant en estudis de precisió com en l'exploració de nous límits energètics per desvelar fenòmens desconeguts.

8.1.4 Partícules Altament Ionitzants

Les Partícules Altament Ionitzants (HIPs) són entitats hipotètiques proposades en nombroses teories BSM, incloent-hi les GUTs, models

SUSY i marcs teòrics amb dimensions extra. Aquestes partícules es caracteritzen per tenir càrregues elèctriques o magnètiques elevades i, sovint, masses considerables, la qual cosa els confereix una capacitat d'ionització excepcional en travessar els materials dels detectors. Aquesta propietat les converteix en indicadors potencials de física BSM.

La detecció de les HIPs es basa en les seues interaccions amb els mitjans dels detectors, predominantment mitjançant processos d'ionització. Quan aquestes partícules travessen la matèria, perden energia interactuant amb els electrons atòmics, i aquesta pèrdua (poder de frenada) depén fonamentalment de la seua massa, càrrega i velocitat. La mitjana de pèrdua d'energia per unitat de longitud, o potència de frenada, es pot expressar com $\langle \frac{dE}{dx} \rangle \propto z^2 \cdot \frac{1}{\beta^2}$, on z és la càrrega de la partícula i β la seua velocitat relativa a la de la llum. Aquesta deposició d'energia permet la seua identificació i seguiment experimental. Per a HIPs carregades amb masses significativament superiors a la dels electrons, els models d'ionització estàndard proporcionen prediccions fiables de la pèrdua d'energia, facilitant la seua possible detecció.

Les recerques experimentals de HIPs en instal·lacions d'acceleradors, inclosos esforços dedicats al LHC, aprofiten els senyals únics d'aquestes partícules, com ara trajectòries altament ionitzants i retards en l'arribada als detectors. Malgrat les recerques exhaustives, no s'ha trobat evidència concloent de la seua existència, cosa que ha permés establir límits estrictes sobre els seus espectres de massa i càrrega. Els experiments actuals i futurs continuen perfeccionant les tècniques de detecció i ampliant l'exploració de l'espai de paràmetres de les HIPs, oferint perspectives prometedores per a la descoberta de nova física.

8.2 Objectius

Aquest treball de tesi se centra en l'aplicació de tècniques avançades per abordar fenòmens rellevants en la física de partícules, especialment aquells que requereixen tractaments no perturbatius i metodologies innovadores per incorporar contribucions d'alta complexitat. Concretament, es plantegen tres objectius interrelacionats.

- El primer objectiu consisteix en l'estudi dels HECOs. A causa dels grans acoblaments electromagnètics d'aquests objectes, la teoria de pertorbacions esdevé inaplicable, ja que la sèrie de Feynman no convergeix. Per superar aquesta limitació i obtenir resultats més fiables, es desenvolupa i s'aplica un marc de resummació basat en les equacions de Dyson–Schwinger (DS). Aquesta aproximació no pertorbativa permet incloure efectes de tots els ordres de la sèrie de Feynman, proporcionant una descripció precisa dels propagadors i dels vèrtexs d'interacció dels HECOs. Això permet millorar la predicció d'observables clau com les seccions eficaces de producció i l'evolució dels acoblaments amb la massa. A més, es busca integrar eines experimentals mitjançant el desenvolupament d'un model "Format Universal de FeynRules" (UFO) basat en aquests acoblaments efectius resumats, que permeti simular els processos de producció amb generadors d'esdeveniments com MadGraph, amb l'objectiu final d'extraure límits fiables sobre la massa dels HECOs.

- El segon objectiu se centra en constrenyer la massa dels monopols magnètics mitjançant la producció de dífotons en processos centrals exclusius (CEP), que constitueixen el mecanisme estàndard per a la dispersió llum–llum ($\gamma\gamma \to \gamma\gamma$). En aquest context, s'analitzen els diagrames de caixa, on el gran acoblament electromagnètic dels monopols, tal com va predir Dirac, intensifica significativament aquestes interaccions. Per extreure límits sobre la massa dels monopols, es consideren dues aproximacions teòriques complementàries: d'una banda, la teoria de camps efectius (EFT), adequada per descriure les interaccions a energies baixes i mitjanes; de l'altra, l'escenari de Born–Infeld (BI), que introdueix correccions no lineals a l'electrodinàmica per explorar els efectes a energies més altes. L'anàlisi conjunta d'aquests dos marcs teòrics permet obtenir límits sobre la massa dels monopols.

- El tercer objectiu consisteix en sondejar la nova física mitjançant l'estudi de correlacions angulars entre dues partícules. Es consideren models de la "Vall Oculta" (HV) on s'analitzen interaccions entre v-quarks i v-gluons, que interactuen amb el Model Estàndard a través de mediadors amb masses de l'ordre 1 TeV. L'anàlisi de les correlacions angulars permet identificar patrons subtils que poden evidenciar la presència d'interaccions o partícules exòtiques, ampliant així les possibilitats de detecció en col·lisionadors futurs, com l'ILC.

Aquestes obres es discuteixen en detall als capítols 4, 5 i 6. En conjunt, aquests treballs constitueixen una recerca capdavantera que integra tècniques teòriques avançades amb estratègies experimentals innovadores. Aquesta combinació estableix un vincle sòlid entre les prediccions teòriques i la interpretació de les dades experimentals, obrint noves vies en l'exploració de fenòmens exòtics més enllà del Model Estàndard.

8.3 Metodologias

La metodologia d'aquest treball es fonamenta en un enfocament multimètode que combina una revisió teòrica exhaustiva amb l'aplicació de tècniques computacionals avançades per al càlcul d'amplituds, la simulació de processos i l'anàlisi de dades.

8.3.1 Metodologia per a la resummació DS i la implementació en models UFO per a HECOs de spin-$\frac{1}{2}$ i spin-0

En aquest treball s'aplica una metodologia no perturbativa basada en les equacions de DS, adequada per a situacions amb acoblaments grans on la teoria de pertorbacions deixa de ser aplicable. Aquest enfocament permet obtenir paràmetres dinàmics com la massa efectiva i els factors d'acoblament, oferint una descripció coherent dels processos en règims d'acoblament fort. Aquests resultats es tradueixen en un lagrangià eficaç del qual s'extrauen les regles de Feyman resumades, que finalment s'implementen en models UFO compatibles amb generadors d'esdeveniments com MadGraph. A continuació es descriuen els passos clau per als dos casos (spin-$\frac{1}{2}$ i spin-0).

8.3.1.1 Cas Spin-$\frac{1}{2}$

Lagrangià Bàsic i Propagadors "Dressed": S'inicia amb el lagrangià bàsic de QED:

$$\mathcal{L}_{\text{bare}} = -\frac{1}{4}F_{\mu\nu}F^{\mu\nu} + \frac{\lambda}{2}(\partial_\mu A^\mu)^2 + \overline{\psi}\Big(i\partial\!\!\!/ + g\,A\!\!\!/ - m\Big)\psi, \tag{8.1}$$

on $g = ne$ ($n \in \mathbb{Z}^+$) és la càrrega nua, m el massa nua i λ el paràmetre de gauge. Es proposa l'ansatz per als propagadors i el vèrtex:

$$\begin{aligned}
G(p) &= i\,\frac{\mathcal{Z}\,p\!\!\!/ + M}{\mathcal{Z}^2\,p^2 - M^2}, \\
\Delta_{\mu\nu}(q) &= \frac{-i}{(1+\omega)q^2}\left(\eta_{\mu\nu} + \frac{1+\omega-\lambda}{\lambda}\frac{q_\mu q_\nu}{q^2}\right), \\
\Gamma_\mu &= g\,\mathcal{Z}\,\gamma_\mu.
\end{aligned} \tag{8.2}$$

Aquí, las correccions $\mathcal{Z}$, ω i M es consideren independents de l'impuls.

Equacions de Dyson–Schwinger i Regles de Feynman Resumades

Les equacions de DS permeten tractar acoblaments forts on la teoria de pertorbacions falla. Mitjançant regularització dimensional i fixant el gauge de Feynman ($\lambda = 1$), s'obté un sistema d'equacions per als factors de renormalització ($\mathcal{Z}, \omega, M$). Aquestes equacions presenten un **punt fix ultraviolat (UV)**, caracteritzat per:

$$\lim_{k\to\infty}(\mathcal{Z}, \omega, \tilde{M}) = (\mathcal{Z}^\star, \omega^\star, \tilde{M}^\star),$$

on $\mathcal{Z}^\star \simeq 1.477$, $\omega^\star \simeq 0.431$ i $\tilde{M} = M/k$ és finit. Aquest punt fix garanteix l'estabilitat i la unitarietat de la teoria a altes energies, assegurant resultats físicament consistents.

Rescalant els camps:

$$A_\mu \to \frac{A_\mu}{\sqrt{1+\omega}}, \quad \psi \to \frac{\psi}{\sqrt{\mathcal{Z}}},$$

s'obté el lagrangià eficaç:

$$\mathcal{L}_{\text{ef}} = \frac{1}{2} A_\mu \left(\eta^{\mu\nu} \Box - \frac{\omega}{1+\omega} \partial^\mu \partial^\nu \right) A_\nu + \overline{\psi} \left(i\partial\!\!\!/ + \frac{g}{\sqrt{1+\omega}} A\!\!\!/ - \frac{M}{\mathcal{Z}} \right) \psi.$$

Les regles de Feynman resumades resultants són:

$$G^{\text{ef}}(p) = i\,\frac{p\!\!\!/ + \mathcal{M}}{p^2 - \mathcal{M}^2}, \quad \Delta^{\text{ef}}_{\mu\nu}(q) = \frac{-i}{q^2} \left(\eta_{\mu\nu} + \omega^\star \frac{q_\mu q_\nu}{q^2} \right), \quad \Gamma^{\text{ef}}_\mu = g\,\mathcal{Z}^\star\,\gamma_\mu,$$

on $\mathcal{M} = M/\mathcal{Z}$ és la massa eficaç. Aquests resultats són crucials per calcular observables a altes energies, especialment en l'estudi d'HECOs, on la resummació assegura prediccions fiables més enllà del règim pertorbatiu.

Massa efectiva i regles de Feynman resumades

Aquesta secció presenta l'evolució de la massa dels HECOs amb l'escala de renormalització i les regles de Feynman efectives utilitzades per calcular observables en col·lisionadors.

Massa corrent La massa dels HECOs evoluciona amb l'escala de renormalització k com:

$$\mathcal{M}(k) = k \exp\left(-\frac{2\pi}{\alpha(k)} (\mathcal{Z}(k) - 1) \right), \tag{8.3}$$

amb la condició $\mathcal{M}(m) = m$ quan $k = m$. A l'escala UV Λ:

$$\mathcal{M}(\Lambda) = \Lambda \exp\left(-\frac{2\pi}{\alpha^\star} (\mathcal{Z}^\star - 1) \right). \tag{8.4}$$

Per a un HECO amb càrrega ne:

$$\frac{\mathcal{M}(\Lambda)}{\Lambda} \simeq \exp\left(-\frac{587}{n^2} \right). \tag{8.5}$$

Regles de Feynman resumades En el punt fix UV, les regles efectives són:

$$\begin{aligned} G^{\text{eff}}(p) &= i\frac{\not{p} + \mathcal{M}(\Lambda)}{p^2 - \mathcal{M}(\Lambda)^2}, \\ \Gamma^{\text{eff}}_{\mu} &= g\,\mathcal{Z}^{\star}\gamma_{\mu}, \\ \Delta^{\text{eff}}_{\mu\nu}(q) &= \frac{-i}{q^2}\left(\eta_{\mu\nu} + \omega^{\star}\frac{q_{\mu}q_{\nu}}{q^2}\right). \end{aligned} \tag{8.6}$$

Aquestes expressions substitueixen els vèrtexs i propagadors a nivell arbre en els processos Drell–Yan i de fusió de fotons, garantint prediccions fiables més enllà del règim perturbatiu.

Contribució del bosó Z^0

Els HECOs també interaccionen amb el bosó Z^0 mitjançant:

$$\mathcal{L}_{\text{int}} = \frac{1}{2}e|n|\tan\theta_W\,\overline{\mathcal{H}}\gamma^{\mu}Z^0_{\mu}\mathcal{H}. \tag{8.7}$$

A altes energies, el propagador del Z^0 es pot aproximar com a sense massa:

$$\Delta^{Z^0}_{\mu\nu}(p) \approx -\frac{i}{p^2}\left(\eta_{\mu\nu} - \frac{p_{\mu}p_{\nu}}{p^2}\right), \tag{8.8}$$

aporten correccions subdominants respecte a les del fotó a les energies dels col·lisionadors actuals.

8.3.1.2 Cas Spin-0

Aquesta secció estén l'aproximació de resummació mitjançant les equacions de DS als HECOs escalars (espín 0), els quals requereixen fortes auto-interaccions ($h \gg g^2$) per garantir l'existència d'un punt fix no trivial en l'UV. Aquesta resummació captura les correccions quàntiques no pertorbatives i proporciona prediccions fiables per a les masses dels HECOs escalars.

Aproximació no pertorbativa Partint del lagrangià nu:

$$\mathcal{L}_{\rm nu} = \frac{1}{2}A^\mu\left[\eta_{\mu\nu}\Box - (1-\lambda)\partial_\mu\partial_\nu\right]A^\nu + D_\mu\phi(D^\mu\phi)^* - m^2\phi\phi^* - \frac{h}{4}(\phi\phi^*)^2,$$

les correccions quàntiques condueixen al lagrangià vestit:

$$\mathcal{L}_{\rm ef} = \frac{1}{2}A^\mu\left[\eta_{\mu\nu}\Box - \frac{1-\lambda+\omega}{1+\omega}\partial_\mu\partial_\nu\right]A^\nu + (\partial_\mu\phi + i\tilde{g}A_\mu\phi)(\partial^\mu\phi^* - i\tilde{g}A^\mu\phi^*) - \tilde{M}^2\phi\phi^* - \frac{\tilde{H}}{4}(\phi\phi^*)^2,$$

amb els paràmetres efectius:

$$\tilde{g} = \frac{g}{\sqrt{1+\omega}}, \quad \tilde{M}^2 = \frac{M^2}{\mathcal{Z}^2}, \quad \tilde{H} = \frac{H}{\mathcal{Z}^4}.$$

Els propagadors i vèrtexs vestits resultants són:

$$G(p) = \frac{i}{\mathcal{Z}^2p^2 - M^2}, \quad D_{\mu\nu}(q) = \frac{-i}{(1+\omega)q^2}\left(\eta_{\mu\nu} + \frac{1+\omega-\lambda}{\lambda}\frac{q_\mu q_\nu}{q^2}\right),$$

$$\Gamma_\mu = ig\mathcal{Z}(p^1_\mu \pm p^2_\mu), \quad \Gamma_{\mu\nu} = 2ig^2\mathcal{Z}^2\eta_{\mu\nu}.$$

Punt fix i massa vestida Resolent les equacions de flux del grup de renormalització (RG) en el límit UV ($k\to\infty$), s'obté un punt fix no trivial:

$$\lim_{k\to\infty}(\mathcal{Z},\omega,H) = (\mathcal{Z}^\star,\omega^\star,H^\star),$$

amb solucions aproximades per a $g^2/h \ll 1$:

$$\omega^\star \simeq \frac{4g^2}{3h}, \quad (\mathcal{Z}^\star)^2 \simeq 1 + \frac{8g^2}{h}, \quad H^\star \simeq \frac{h}{4}.$$

Les condicions d'unitarietat i positivitat imposen:

$$h \gtrsim 12.12\,g^2, \quad 0 \le \omega^\star \lesssim 0.11.$$

La massa vestida dels HECOs escalars en el punt fix UV és:

$$\tilde{M} = \Lambda\,\exp\left(-\frac{32\pi^2}{h}\right),$$

i, en saturar el límit d'acoblament màxim:

$$\tilde{M} \simeq \Lambda \, \exp\left(-\frac{2.64\,\pi^2}{g^2}\right).$$

Elecció de gauge Seguint la Tècnica de Pinch, s'adopta la gauge de Feynman ($\lambda = 1$) per garantir observables físics independents del gauge. Aquesta elecció assegura condicions coherents amb la unitarietat i l'estabilitat.

Implementació en Models UFO i Simulació

Els resultats teòrics obtinguts en ambdós casos es tradueixen en models UFO, compatibles amb generadors d'esdeveniments com MadGraph5_aMC@NLO. Es desenvolupen almenys dos models:

- **Intercanvi de γ:** Producció només mitjançant fotons (processos DY i PF).
- **Intercanvi de γ/Z^0 (només per a spin-$1/2$):** Inclou contribucions del Z^0 en processos DY.

Ambdós models incorporen com a paràmetres d'entrada la multiplicitat de càrrega n i l'escala de tall Λ, que afecten la massa dels HECOs i les seccions eficaces. Per a les energies del LHC, s'utilitza $\alpha_{\mathrm{EM}} = 1/127.94$. La validació s'ha realitzat comparant les simulacions de Monte Carlo amb càlculs analítics efectuats amb Mathematica. Les comparacions de seccions eficaces es presenten a les Taules 4.1, 4.2, 4.3, 4.4, 4.5.

Aquests models serveixen com a eina per comparar les prediccions teòriques amb les dades experimentals, permetent establir límits fiables sobre la massa dels HECOs.

8.3.2 Restriccions per a Monopols Magnètics mitjançant Esdeveniments $\gamma\gamma$

Aquesta secció presenta el marc teòric i la metodologia emprada per estudiar MMs a través de la dispersió LbL en col·lisions a altes energies.

Dispersió Llum-per-Llum i Contribució dels Monopols La dispersió LbL és un procés quàntic rar on dos fotons interaccionen via diagrames de caixa, amb contribucions del SM i potencials extensions, com els MMs. A les energies accessibles als acceleradors actuals, els monopols poden modificar la secció eficaç d'aquest procés, especialment en col·lisions ultra-perifèriques (UPC) en pp i $PbPb$.

Modelització mitjançant EFT L'EFT descriu la interacció de quatre fotons mitjançant operadors de dimensió vuit, permetent parametritzar contribucions de nova física a energies accessibles als col·lisionadors actuals. El lagrangià efectiu pren la forma:

$$\mathcal{L}_{4\gamma} = \zeta_1 F_{\mu\nu}F^{\mu\nu}F_{\rho\sigma}F^{\rho\sigma} + \zeta_2 F_{\mu\nu}F^{\nu\rho}F_{\rho\lambda}F^{\lambda\mu}, \tag{8.9}$$

on $F_{\mu\nu}$ és el tensor de camp electromagnètic i els coeficients ζ_1, ζ_2 descriuen desviacions respecte al Model Estàndard (SM). Aquests termes poden originar-se de partícules carregades pesants que apareixen en diagrames de caixa, incloent-hi els MMs. Els coeficients ζ_1, ζ_2 són sensibles a l'espín de la partícula en el bucle, com es veu en:

$$\zeta_i \sim \frac{\alpha^2 Q^4}{M^4} N c_i, \tag{8.10}$$

on Q és la càrrega, M la massa de la partícula, N compta multiplicitats addicionals, i els coeficients c_i depenen de l'espín, amb valors màxims per a partícules de spin-1 i mínims per a spin-0.

Per als monopols magnètics, la seva contribució a ζ_1, ζ_2 es pot escriure com:

$$\mathcal{L}_{4\gamma}^{\mathrm{MM}} = \frac{1}{36}\left(\frac{g}{\sqrt{4\pi}M}\right)^4 \left[\frac{\beta_+ + \beta_-}{2}(F_{\mu\nu}F^{\mu\nu})^2 + \frac{\beta_+ - \beta_-}{2}(F_{\mu\nu}\tilde{F}^{\mu\nu})^2\right], \tag{8.11}$$

amb $\beta_\pm$ depenent de l'espín del monopole. Les restriccions experimentals a $\zeta_{1,2}$ en col·lisions pp han sigut derivades per CMS-TOTEM en la cerca de producció exclusiva de fotons, permetent imposar límits inferiors a la massa dels MMs.

Interpretació segons la Teoria de Born-Infeld La teoria de Born-Infeld modifica la QED per mitjà de termes no lineals que imposen un límit superior a la intensitat del camp elèctric. El lagrangià BI s'expressa com:

$$\mathcal{L}_{\mathrm{BI}} = \beta^2 \left(1 - \sqrt{1 + \frac{1}{2\beta^2} F_{\mu\nu} F^{\mu\nu} - \frac{1}{16\beta^4} (F_{\mu\nu} \tilde{F}^{\mu\nu})^2} \right), \tag{8.12}$$

on β és un paràmetre lliure que caracteritza la intensitat màxima del camp elèctric. En integrar aquest model dins del sector hiper-càrrega $U(1)_Y$ del Model Estàndard, es prediu l'existència de solucions finites de monopols de Cho-Maison. La relació entre β i els acoblaments anòmals és:

$$\zeta_1 = -\frac{1}{32\beta^2}, \quad \zeta_2 = \frac{1}{8\beta^2}. \tag{8.13}$$

Aquestes relacions permeten traduir les restriccions de CMS-TOTEM en un límit per a β, i per tant, en una cota inferior per a la massa del monopole de Cho-Maison.

En resum, aquesta metodologia integra l'anàlisi quàntica dels diagrames de caixa en LbL, l'aproximació del fotó equivalent per descriure els fluxos fotònics en CEP, i dos marcs teòrics (EFT i BI) que permeten traduir les desviacions observades en termes de límits en la massa dels monopols. Així, es construeix una eina potent per a la recerca de nous efectes BSM a través d'analítiques i simulacions en col·lisionadors d'alta energia.

8.3.3 Estudi de correlacions angulars i la recerca de senyals Hidden Valley

Aquest estudi explora el potencial d'utilitzar correlacions angulars entre dues partícules com a eina per descobrir nova física en el context de models de HV. La metodologia adoptada es pot descriure en els següents passos:

1. **Definició de la funció de correlació:** S'estableix la funció de

correlació de dues partícules:

$$C^{(2)}(\Delta y, \Delta\phi) = \frac{S(\Delta y, \Delta\phi)}{B(\Delta y, \Delta\phi)}, \tag{8.14}$$

on $S(\Delta y, \Delta\phi)$ és la densitat de parelles de partícules trobades en el mateix esdeveniment i $B(\Delta y, \Delta\phi)$ és la densitat de parelles obtinguda mitjançant la mescla d'esdeveniments (background).

2. Obtenció del rendiment angular:

Per estudiar la dependència en l'angle azimutal, s'integra la funció S sobre un rang definit de diferències de rapiditat, donant lloc al rendiment:

$$Y(\Delta\phi) = \frac{\int_{y_{\text{inf}}}^{y_{\text{sup}}} S(\Delta y, \Delta\phi)\, d\Delta y}{\int_{y_{\text{inf}}}^{y_{\text{sup}}} B(\Delta y, \Delta\phi)\, d\Delta y}, \tag{8.15}$$

on y_{inf} i y_{sup} defineixen els límits d'integració en rapiditat. Aquesta quantitat permet identificar patrons i anomalies en la distribució d'angles que podrien ser indicatius de senyals HV.

3. Simulació i reconstrucció d'esdeveniments:

Per avaluar les correlacions angulars, es generen esdeveniments amb simuladors de Monte Carlo (com PYTHIA), en entorns amb col·lisions e^+e^- (per exemple, a l'ILC). L'entorn net d'aquests col·lisionadors facilita la reconstrucció precisa dels esdeveniments i l'extracció dels objectes de flux de partícules (PFOs). Aquests PFOs són utilitzats per calcular les densitats $S(\Delta y, \Delta\phi)$ i $B(\Delta y, \Delta\phi)$.

4. Aplicació de talls de selecció:

Per millorar la sensibilitat als senyals de nova física, s'apliquen criteris de selecció que permeten enriquir la mostra d'esdeveniments amb possibles signatures HV.Aquests talls es defineixen considerant diverses variables cinemàtiques, amb l'objectiu de reduir la contribució del fons del Model Estàndard.

5. Interpretació dels resultats:

Els patrons obtinguts en la distribució $Y(\Delta\phi)$ es comparen amb les expectatives del Model Estàndard. Per exemple, una discrepància en el pic a $\Delta\phi \sim \pi$ o la presència d'estructures "ridge" en certes regions de diferència de rapiditat poden suggerir la presència d'interaccions entre partícules del sector ocult i les partícules SM. Així, es pot deduir si hi ha efectes addicionals, com els previsibles en un model HV, que afecten la distribució angular.

8.4 Resultats

Aquesta secció presenta els principals resultats obtinguts al llarg d'aquesta tesi, que inclouen anàlisis teòriques, càlculs numèrics i estudis de simulació.

8.4.1 Resultats per als HECOs

Es presenten els resultats obtinguts en l'estudi dels HECOs, considerant tant les partícules d'espín 0 com les d'espín 1/2. Els resultats es basen en la comparació entre les seccions eficaces calculades a nivell arbre i aquelles que incorporen els efectes de ressumació DS. Aquesta aproximació millora les prediccions per als processos de producció via Drell–Yan (DY) i fusió de fotons (PF), permetent establir límits de massa més estrictes i fiables per als HECOs.

Les Taules 4.4, 4.1, 4.5 i 4.3 proporcionen una comparació entre les seccions eficaces a nivell arbre i després d'incorporar els efectes de ressumació per als processos DY i PF en col·lisions pp a $\sqrt{s} = 13$ TeV. Per al procés DY s'ha utilitzat el PDF `NNPDF23` [229], mentre que per a la PF s'ha emprat el PDF `LUXqed17` [230]. La comparació mostra que, per a una mateixa massa — massa nua a nivell arbre i $\mathcal{M}(\Lambda)$ després de la ressumació — les seccions eficaces es mantenen del mateix ordre de magnitud, validant així els models UFO desenvolupats i els càlculs subjacents. Tanmateix, s'observa un augment significatiu en la secció eficaç després d'aplicar la ressumació, amb factors d'increment de ~ 1.66 per a DY i ~ 2.76 per a PF en el cas d'espín 0, mentre que per a l'espín 1/2 els factors són de ~ 2.1 i ~ 4.75, respectivament. Aquesta diferència s'explica per la dependència de les seccions amb la càrrega elèctrica: $\sigma_{DY} \propto n^2$ i $\sigma_{PF} \propto n^4$. En conseqüència, els valors de secció per a la PF són significativament superiors als del procés DY a les energies del LHC i per al rang de masses considerat.

A més, s'ha realitzat una comparació directa entre HECOs d'espín 0 i d'espín 1/2 per tal d'entendre millor les diferències en la producció segons l'espín. La Figura 8.1 mostra aquesta comparació per als processos DY i PF respectivament. Es pot observar que, per a la mateixa càrrega i massa, els HECOs d'espín 1/2 tenen seccions eficaces lleugerament més altes que els d'espín 0, degut a la diferent estructura dels vèrtexs i els factors d'espín involucrats.

Els efectes de ressumació s'han utilitzat per reinterpretar els resultats experimentals de les col·laboracions ATLAS [224, 237] i MoEDAL [164, 165]. Les Taules 4.6 i 4.7, així com la Figura 8.2, presenten els límits de massa a un 95% CL per a HECOs d'espín 0 i espín 1/2, mostrant com els límits obtinguts amb ressumació són més estrictes que els calculats a nivell arbre. Les millores poden arribar fins a un 30%, depenent de la càrrega i la massa del HECO. Aquesta millora en els límits de massa té implicacions directes per a les cerques de nova física als col·lisionadors actuals i futurs.

8.4.2 Exploració de Monopols amb Esdeveniments de Difotons

Aquest apartat presenta la recerca indirecta de monopols magnètics mitjançant la dispersió llum-llum en la producció CEP d'esdeveniments dífotons al LHC. S'han utilitzat dos marcs teòrics per restringir la massa dels MMs: la EFT i BI, amb alta sensibilitat a nova física.

En l'EFT, els efectes de nova física en els acoblaments quàrtics de fotons es modelitzen amb els paràmetres anòmals $\zeta_{1,2}$. Reinterpretant els límits experimentals de CT-PPS a $\sqrt{s} = 13$ TeV, s'obtenen restriccions per a monopols amb càrrega de Dirac (g_D):

$$\frac{M}{|n|} > \begin{cases} 2.86 \text{ TeV}, & s = 0, \\ 4.05 \text{ TeV}, & s = \frac{1}{2}, \\ 7.33 \text{ TeV}, & s = 1. \end{cases}$$

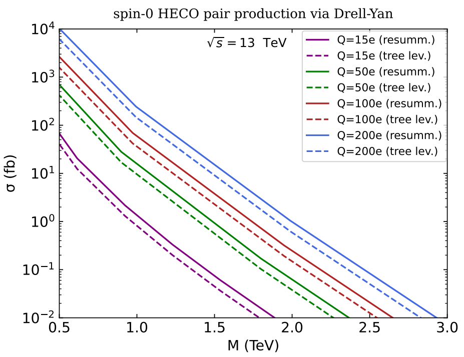

(a) DY: HECOs d'espín 0

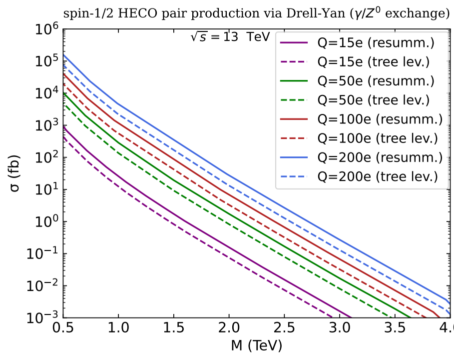

(b) DY: HECOs d'espín 1/2

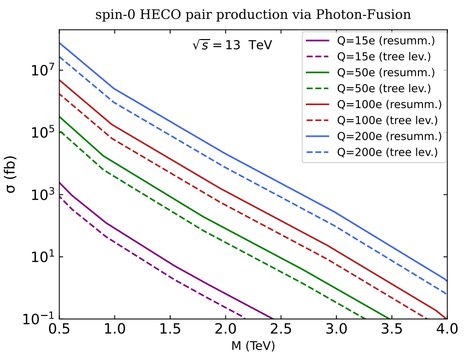

(c) PF: HECOs d'espín 0

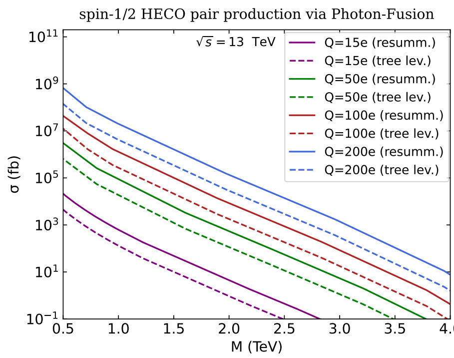

(d) PF: HECOs d'espín 1/2

Figure 8.1: Comparació entre les seccions eficaces abans i després de la ressumació per a HECOs d'espín 0 i 1/2 en els processos Drell–Yan i fusió de fotons a $\sqrt{s} = 13$ TeV.

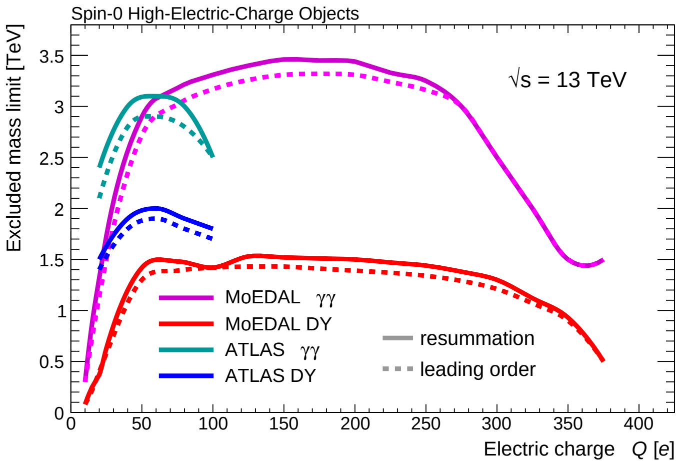

(a) Límits inferiors d'exclusió per a HECOs d'espín 0 en funció de la càrrega elèctrica, mostrant els càlculs a nivell arbre i amb ressumació per als processos DY i PF.

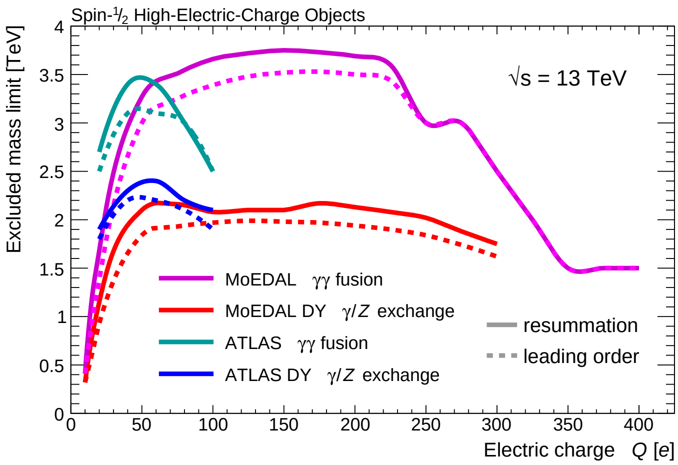

(b) Límits inferiors d'exclusió per a HECOs d'espín 1/2 en funció de la càrrega elèctrica, mostrant els càlculs a nivell arbre i amb ressumació per als processos DY i PF.

Figure 8.2: Comparació dels límits inferiors d'exclusió per a HECOs d'espín 0 i 1/2 a $\sqrt{s} = 13$ TeV, destacant els efectes de la ressumació en els processos DY i PF.

Com es veu en la Figura 8.3, els límits milloren amb l'espín, sent més restrictius per a monopols vectorials per la seua major contribució als diagrames de caixa.

En el marc BI, que introdueix correccions no lineals a l'electrodinàmica, es relaciona el paràmetre β amb $\zeta_{1,2}$ per derivar:

$$\beta > 0.71 \text{ TeV}^2, \quad M_{\text{CM}} > 61 \text{ TeV}.$$

Aquesta estimació situa la massa dels monopols Cho-Maison molt per damunt del rang accessible en acceleradors, demostrant el potencial de les mesures indirectes per explorar escales inabastables mitjançant producció directa.

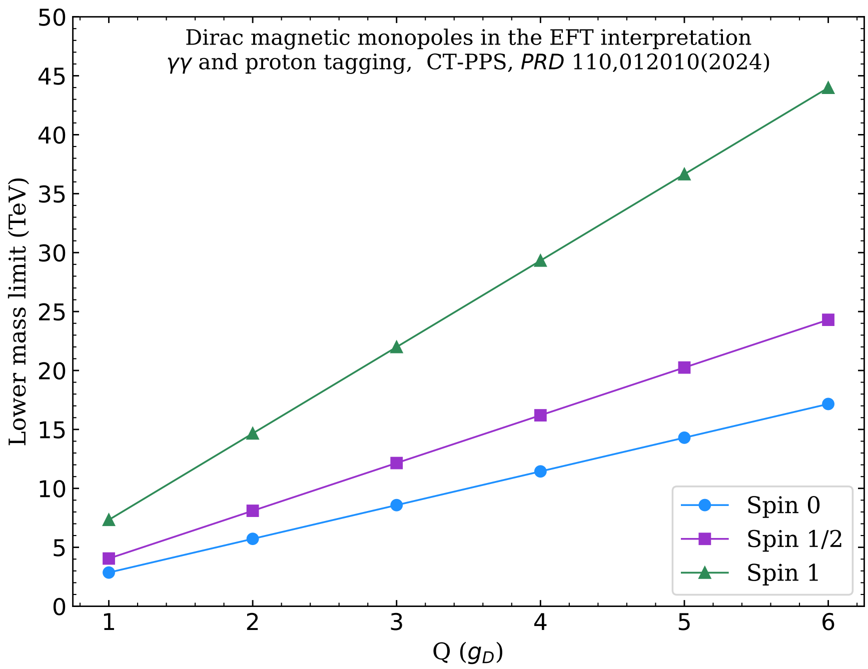

Figure 8.3: Límits inferiors d'exclusió per a la massa dels monopols magnètics en funció de la càrrega en unitats de g_D, segons CT-PPS [260].

8.4.3 Sensibilitat a sectors ocults mitjançant correlacions angulares de dues partícules

S'han avaluat les correlacions angulars a nivell de detector en un escenari HV amb comunicadors de massa $m_{D_v} = 125$ GeV i partícules ocultes q_v de massa variable, a $\sqrt{s} = 250$ GeV. Els resultats es presenten mitjançant la distribució del rendiment angular $Y(\Delta\phi)$ (Fig. 8.4), per dos intervals de pseudorapidessa: $0 < |\Delta y| \leq 1.6$ i $1.6 < |\Delta y| < 5$.

Sense talls de selecció, la distribució està dominada pel fons SM, amb un pic a $\Delta\phi \sim \pi$ per la producció de jets convencionals. Aplicant criteris d'enriquiment del senyal, el senyal HV destaca clarament en $0 < |\Delta y| \leq 1.6$, evidenciant la capacitat de les correlacions angulars per discriminar nova física. Per $1.6 < |\Delta y| < 5$, la senyal HV mostra diferències notables respecte al fons, suggerint una cascada partònica modificada per sectors ocults.

Amb una lluminositat integrada de 100 fb^{-1}, la incertesa dominant prové d'efectes sistemàtics del detector. Una millora en la modelització i el rendiment detector podria incrementar significativament la sensibilitat, consolidant les correlacions angulars com una eina prometedora per a la recerca de nova física a futurs col·lisionadors.

A més, l'anàlisi s'ha ampliat a $\sqrt{s} = 500$ GeV i 1 TeV, a nivell de partícules, per estudiar com varia el senyal HV en condicions d'energia més alta. En aquest cas, s'han considerat dos escenaris extrems: mediadors lleugers D_v i pesants T_v, amb masses iguals a $\sqrt{s}/2$. Els resultats mostren que, mentre la contribució del fons SM disminueix amb l'energia, la secció eficaç del senyal HV es redueix en dos ordres de magnitud a $\sqrt{s} = 1$ TeV. Aquest patró és esperat, ja que la producció de partícules noves esdevé menys freqüent a mesura que l'energia creix.

Aquest estudi també és rellevant per al Future Circular Collider (FCC-e^+e^-) operant a $\sqrt{s} = 240$ GeV, amb lleugeres diferències per la menor cobertura en la regió capdavantera. No obstant això, una optimització dels talls de selecció podria recuperar sensibilitat al senyal HV. Futures investigacions es duran a terme per refinar aquests estudis.

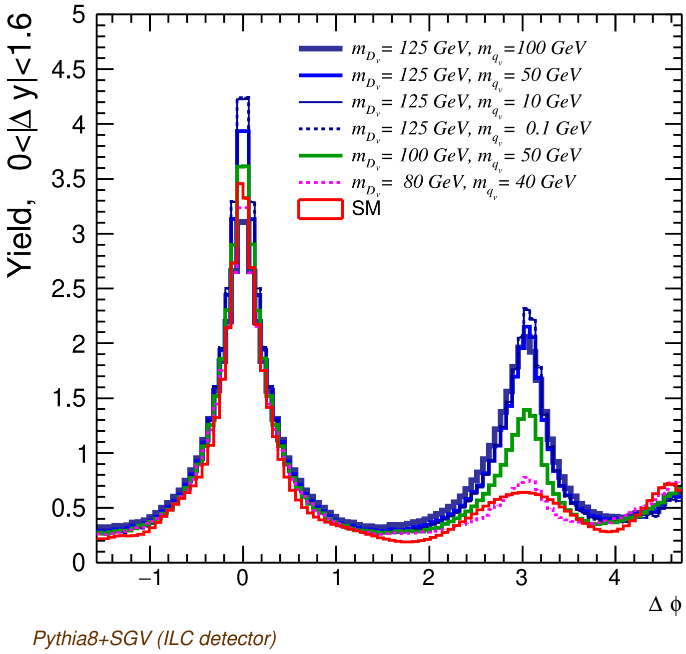

Figure 8.4: Distribució del rendiment angular $Y(\Delta\phi)$ després de talls de selecció per a $0 < |\Delta y| \leq 1.6$. El pic a $\Delta\phi \sim \pi$ suggereix la presència d'un sector ocult.

8.5 Conclusions

Aquesta tesi ha explorat diverses estratègies per a la recerca de física BSM, centrant-se en HIPs com els MMs i HECOs, així com en signatures de sectors ocults en col·lisionadors d'alta energia. Mitjançant una combinació de càlculs analítics, EFT, resumació DS i simulacions de col·lisionadors, s'han derivat límits experimentals i eines per a la recerca de nova física en experiments actuals i futurs.

Pel que fa als HECOs, s'han aplicat tècniques de ressumació DS per millorar la descripció teòrica d'aquestes partícules altament carregades, tant per a HECOs d'espín-1/2 com per a HECOs d'espín-0. Per als primers, la ressumació ha incrementat la secció eficaç en un factor de 2.1 per a la producció DY i 4.75 per a la fusió de fotons (PF), mentre que per als HECOs escalars, els increments han estat de 1.66 en DY i 2.76 en PF. Aquests efectes han permès reinterpretar els resultats experimentals d'ATLAS i MoEDAL, millorant els límits sobre la massa de fins a un 30%. Per facilitar la implementació experimental, s'han desenvolupat models UFO compatibles amb generadors d'esdeveniments Monte Carlo, ara disponibles públicament per a estudis en col·lisionadors actuals i futurs. Aquesta eina permet simulacions més precises de la producció d'HECOs i possibilita la comparació directa amb resultats experimentals, consolidant la seua cerca en experiments com ATLAS i MoEDAL.

En el cas dels MMs, s'han utilitzat cerques indirectes al LHC mitjançant processos LbL observats per ATLAS i CMS. Dins del marc EFT, s'han establert límits de massa per a MMs amb spin-1 superiors a 7 TeV, mentre que l'extensió BI a l'hipercàrrega del SM ha predit MMs Cho-Maison amb masses superiors a 60 TeV. Aquests resultats subratllen la importància d'estudis precisos d'interaccions fotó-fotó per a la recerca de nova física.

En l'estudi de sectors ocults, s'han analitzat correlacions angulars en col·lisionadors e^+e^-, considerant un model HV amb v-quarks i v-gluons acoblats al SM mitjançant mediadors lleugers. Simulacions a nivell de detector per $\sqrt{s} = 250$ GeV han confirmat la sensibilitat d'aquestes correlacions a nova física, mentre que extensions a 500 GeV i 1 TeV han mostrat perspectives prometedores. Aquestes signatures podrien ser explorades en futurs col·lisionadors com el FCC-e^+e^-, amb optimitzacions en la selecció d'esdeveniments per mantenir sensibilitat a HV. Els patrons observats podrien també indicar altres fenòmens com efectes col·lectius, ressaltant la necessitat de complementar aquesta estratègia amb altres tècniques experimentals.

Appendix A

Scalar self-energy and self-interaction

A.1 Loop integrals

Dimensional regularization is employed in $d = 4 - \epsilon$ with $\epsilon \to 0^+$, where g and h are rescaled as $g \to g k^{\epsilon/2}$ and $h \to h k^{\epsilon/2}$, respectively. This leads to the integral evaluation:

$$\int \frac{d^d p}{(2\pi)^d} \frac{1}{p^2 - A^2} = -\frac{i\pi^{d/2}}{(2\pi)^d} A^{2-\epsilon} \Gamma(-1 + \epsilon/2) = \frac{iA^{2-\epsilon}}{8\pi^2 \epsilon} + A^{2-\epsilon} f_1 \ , \tag{A.1}$$

where f_1 is a dimensionless and finite function, and Γ represents the gamma function. Consequently, the following result is obtained:

$$\int \frac{d^d p}{(2\pi)^d} \frac{1}{(p^2 - A^2)^2} = \frac{d}{d(A^2)} \int \frac{d^d p}{(2\pi)^d} \frac{1}{p^2 - A^2} = \frac{iA^{-\epsilon}}{8\pi^2 \epsilon} + A^{-\epsilon} f_2 \ , \tag{A.2}$$

where f_2 is also dimensionless and finite. Additionally, the integral

$$\int \frac{d^d p}{(2\pi)^d} \frac{1}{p^2} = \lim_{A \to 0} \int \frac{d^d p}{(2\pi)^d} \frac{1}{p^2 - A^2} = 0 \tag{A.3}$$

vanishes in the limit $A \to 0$.

Furthermore, the following integral holds:

$$\int \frac{d^d p}{(2\pi)^d} \frac{1}{p^2(p^2 - A^2)} = A^{-2} \int \frac{d^d p}{(2\pi)^d} \left(\frac{1}{p^2} - \frac{1}{p^2 - A^2} \right) = -\frac{iA^{-\epsilon}}{8\pi^2 \epsilon} + A^{-\epsilon} f_1 \ . \tag{A.4}$$

Infrared divergences are regularised in $d' = 4 + \epsilon$, where $\epsilon > 0$, such that:

$$\int \frac{d^{d'} p}{(2\pi)^{d'}} \frac{1}{p^4} = \lim_{A \to 0} \int \frac{d^{d'} p}{(2\pi)^{d'}} \frac{1}{(p^2 - A^2)^2} = \lim_{A \to 0} \left(-\frac{iA^{+\epsilon}}{8\pi^2 \epsilon} + A^{+\epsilon} f_3 \right) = 0 \ , \tag{A.5}$$

where f_3 is dimensionless and finite.

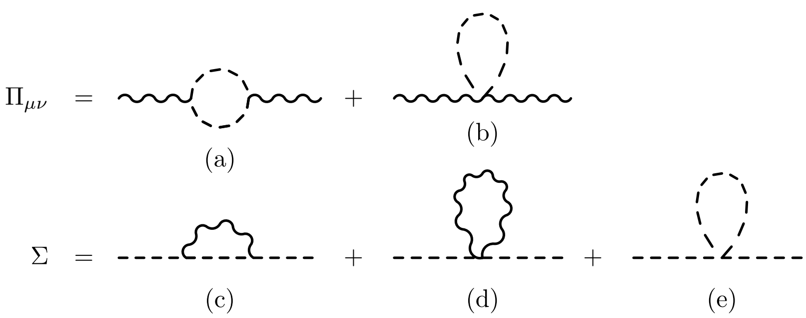

Figure A.1: One-loop self-energy diagrams for the photon (a+b) and the scalar field (c+d+e). In the proposed resummation, all vertices and internal lines are replaced by their dressed counterparts.

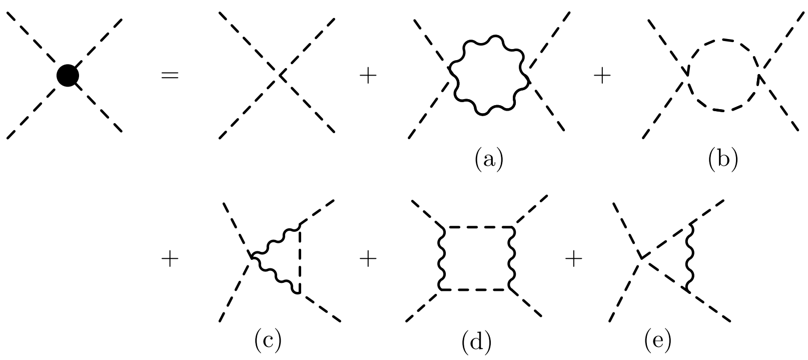

Figure A.2: One-loop corrections to the scalar self-coupling. Each diagram contributes three times due to the three possible external momentum channels. In the proposed resummation, all vertices and internal lines are replaced by the dressed ones.

A.2 Polarization tensor of gauge bosons

The polarization tensor is defined as

$$i\Pi_{\mu\nu}(q) \equiv D^{-1}_{\mu\nu}(q) - D^{-1}_{(bare)\mu\nu}(q) \ , \tag{A.6}$$

which is transverse and expressed as

$$\Pi_{\mu\nu}(q) \equiv -\omega \left(q^2\eta_{\mu\nu} - q_\mu q_\nu \right) \ . \tag{A.7}$$

At one-loop order, contributions to the polarization tensor arise solely from the gauge coupling, with no contributions from scalar self-interactions. The result is obtained from the sum of diagrams (a) and (b) in Fig. A.1, yielding [304]:

$$\omega^{(1)} = \frac{g^2}{24\pi^2}\frac{1}{\epsilon}\left(\frac{k}{m}\right)^{\epsilon} + \text{finite terms} \ . \tag{A.8}$$

In the resummation approach considered here, the bare quantities in the loop integrals are substituted with their dressed counterparts, leading to the modified expression:

$$\omega = \frac{g^2}{24\pi^2\mathcal{Z}^2}\frac{1}{\epsilon}\left(\frac{k\mathcal{Z}}{M}\right)^{\epsilon} + \text{finite terms} \ . \tag{A.9}$$

A.3 Scalar self energy

The scalar self energy is

$$i\Sigma(p) \equiv G^{-1}(p) - G^{-1}_{(bare)}(p) = (\mathcal{Z}^2 - 1)p^2 - (M^2 - m^2) \ , \tag{A.10}$$

and has contributions from three graphs, shown in Fig. A.1. The graphs (d) and (e) do not depend on the external momentum, such that they do not contribute to the correction $\mathcal{Z}$. The graph (d) does not contribute since it leads to a quadratic divergence, not seen by dimensional regularisation

$$\begin{aligned}\Sigma_{(d)} &= -2g^2\eta_{\mu\nu}\mathcal{Z}^2k^\epsilon\int\frac{d^dq}{(2\pi)^d}\frac{\eta^{\mu\nu}+\xi q^\mu q^\nu/q^2}{(1+\omega)q^2} \\ &= -2g^2\mathcal{Z}^2k^\epsilon\frac{4+\xi}{1+\omega}\int\frac{d^dq}{(2\pi)^d}\frac{1}{q^2}=0\ ,\end{aligned}\tag{A.11}$$

where $\xi\equiv(1+\omega-\lambda)/\lambda$. The contribution from the graph (e) is

$$\begin{aligned}\Sigma_{(e)}(0) &= -\frac{Hk^\epsilon}{\mathcal{Z}^2}\int\frac{d^dq}{(2\pi)^d}\frac{1}{q^2-(M/\mathcal{Z})^2} \\ &= \frac{H}{\mathcal{Z}^2}\frac{i}{8\pi^2\epsilon}\left(\frac{M}{\mathcal{Z}}\right)^2\left(\frac{k\mathcal{Z}}{M}\right)^\epsilon+\text{finite}\ .\end{aligned}\tag{A.12}$$

The contribution (c) to the scalar self energy is

$$\Sigma_{(c)}(p)=-\frac{\mathcal{Z}^2g^2k^\epsilon}{1+\omega}\int\frac{d^dq}{(2\pi)^d}\left(\eta_{\mu\nu}+\xi\frac{q_\mu q_\nu}{q^2}\right)\frac{(q+2p)^\mu(q+2p)^\nu}{q^2[\mathcal{Z}^2(p+q)^2-M^2]}\ ,\tag{A.13}$$

such that the mass correction is given by

$$\begin{aligned}\Sigma_{(c)}(0)+\Sigma_{(e)}(0) &= \frac{H}{\mathcal{Z}^2}\frac{i}{8\pi^2\epsilon}\left(\frac{M}{\mathcal{Z}}\right)^2\left(\frac{k\mathcal{Z}}{M}\right)^\epsilon \\ &\quad -ig^2\frac{1+\xi}{1+\omega}k^\epsilon\int\frac{d^dq}{(2\pi)^d}\frac{1}{q^2-M^2/\mathcal{Z}^2} \\ &= \frac{H}{\mathcal{Z}^2}\frac{i}{8\pi^2\epsilon}\left(\frac{M}{\mathcal{Z}}\right)^2\left(\frac{k\mathcal{Z}}{M}\right)^\epsilon \\ &\quad +\frac{ig^2}{8\pi^2\lambda}\left(\frac{k\mathcal{Z}}{M}\right)^\epsilon\left(\frac{M}{\mathcal{Z}}\right)^2+\text{finite}\end{aligned}\tag{A.14}$$

which leads to

$$M^2-m^2=\frac{1}{8\pi^2\epsilon}\left(\frac{g^2}{\lambda}+\frac{H}{\mathcal{Z}^2}\right)\left(\frac{M}{\mathcal{Z}}\right)^2\left(\frac{k\mathcal{Z}}{M}\right)^\epsilon+\text{finite}\ .\tag{A.15}$$

The derivative correction is given by

$$
\begin{aligned}
8(\mathcal{Z}^2-1) &= i\left.\frac{\partial^2\Sigma_3}{\partial p^\rho\partial p_\rho}\right|_{p=0} \\
&= -\frac{8g^2k^\epsilon}{1+\omega}\int\frac{d^dq}{(2\pi)^d}\left[\frac{(1+\xi)(M/\mathcal{Z})^2}{[q^2-(M/\mathcal{Z})^2]^3}\right. \\
&\quad\left.-\frac{2(1+\xi)}{[q^2-(M/\mathcal{Z})^2]^2}+\frac{4+\xi}{q^2[q^2-(M/\mathcal{Z})^2]}\right] \\
&= \frac{8g^2k^\epsilon}{1+\omega}\int\frac{d^dq}{(2\pi)^d}\left[\frac{2(1+\xi)}{[q^2-(M/\mathcal{Z})^2]^2}\right. \\
&\quad\left.-\frac{(4+\xi)(\mathcal{Z}/M)^2}{q^2-(M/\mathcal{Z})^2}\right]+\text{finite} \\
&= \frac{g^2}{\pi^2\epsilon}\left(\frac{k\mathcal{Z}}{M}\right)^\epsilon\left(\frac{3}{1+\omega}-\frac{1}{\lambda}\right)+\text{finite}\ .
\end{aligned}
\tag{A.16}
$$

A.4 Scalar self-interaction

The diagrams contributing to the scalar self-interaction are shown on Fig.A.2, and the total contribution to the scalar self-coupling is denoted

$$
H = h + H_{(a)} + H_{(b)} + H_{(c)} + H_{(d)} + H_{(e)}\ , \tag{A.17}
$$

where we will ignore finite terms. All these graphs count three times, due to the different number of channels for the incoming/outgoing momenta. The graph (a) has an infrared divergence but does not contribute, since

$$
\begin{aligned}
H_{(a)} &\propto \eta^{\mu\nu}\eta^{\rho\sigma}\int\frac{d^{d'}q}{(2\pi)^{d'}}\frac{1}{[(1+\omega)q^2]^2}\left(\eta_{\mu\rho}+\xi\frac{q_\mu q_\rho}{q^2}\right)\left(\eta_{\nu\sigma}+\xi\frac{q_\nu q_\sigma}{q^2}\right) \\
&= \frac{4+2\xi+\xi^2}{(1+\omega)^2}\int\frac{d^{d'}q}{(2\pi)^{d'}}\frac{1}{q^4}=0\ .
\end{aligned}
\tag{A.18}
$$

From a physical point of view, the cancellation of the infrared divergence is explained by soft photons emitted/absorbed by the external scalar legs.

The improved one-loop diagram from the graph (b) is given by

$$-ik^{\epsilon}H_{(b)} = 3(-ik^{\epsilon}H)^2 \int \frac{d^dq}{(2\pi)^d}\frac{i^2}{(\mathcal{Z}^2p^2 - M^2)^2} \ , \tag{A.19}$$

where no symmetry factor is present since the scalar is charged [231]. We have then

$$H_{(b)} = -\frac{3H^2}{\mathcal{Z}^4}\frac{1}{8\pi^2\epsilon}\left(\frac{k\mathcal{Z}}{M}\right)^{\epsilon} \ . \tag{A.20}$$

The graph (c) is given by

$$\begin{aligned}
-ik^{\epsilon}H_{(c)} &= 3\times 2ig^2\mathcal{Z}^2(ig\mathcal{Z})^2\eta^{\mu\nu}k^{2\epsilon}\int\frac{d^dq}{(2\pi)^d}\frac{(-i)^2q^{\rho}q^{\sigma}}{[(1+\omega)q^2]^2} \\
&\quad\times\left(\eta_{\mu\rho}+\xi\frac{q_{\mu}q_{\rho}}{q^2}\right)\left(\eta_{\nu\sigma}+\xi\frac{q_{\nu}q_{\sigma}}{q^2}\right)\frac{i}{\mathcal{Z}^2q^2-M^2} \\
&= -6g^4\mathcal{Z}^2\left(\frac{1+\xi}{1+\omega}\right)^2 k^{2\epsilon}\int\frac{d^dq}{(2\pi)^d}\frac{1}{q^2(q^2-(M/\mathcal{Z})^2)} \\
&= -\frac{6g^4\mathcal{Z}^2}{\lambda}\frac{ik^{\epsilon}}{8\pi^2\epsilon}\left(\frac{k\mathcal{Z}}{M}\right)^{\epsilon} + \text{finite} \ .
\end{aligned} \tag{A.21}$$

such that

$$H_{(c)} = \frac{3g^4\mathcal{Z}^2}{4\pi^2\lambda\epsilon}\left(\frac{k\mathcal{Z}}{M}\right)^{\epsilon} \ . \tag{A.22}$$

The graph (d) is given by

$$\begin{aligned}
-ik^{\epsilon}H_{(d)} &= 3(ig\mathcal{Z})^4k^{2\epsilon}\int\frac{d^dq}{(2\pi)^d}\frac{(-i)^2q^{\mu}q^{\nu}q^{\rho}q^{\sigma}}{[(1+\omega)q^2]^2} \\
&\quad\times\left(\eta_{\mu\nu}+\xi\frac{q_{\mu}q_{\nu}}{q^2}\right)\left(\eta_{\rho\sigma}+\xi\frac{q_{\rho}q_{\sigma}}{q^2}\right)\frac{i^2}{(\mathcal{Z}^2q^2-M^2)^2} \\
&= 3g^4\left(\frac{1+\xi}{1+\omega}\right)^2 k^{2\epsilon}\int\frac{d^dq}{(2\pi)^d}\frac{1}{[q^2-(M/\mathcal{Z})^2]^2} \\
&= \frac{3g^4}{\lambda^2}\frac{ik^{\epsilon}}{8\pi^2\epsilon}\left(\frac{k\mathcal{Z}}{M}\right)^{\epsilon} + \text{finite} \ .
\end{aligned} \tag{A.23}$$

such that

$$H_{(d)} = -\frac{3g^4}{8\pi^2\lambda^2\epsilon}\left(\frac{k\mathcal{Z}}{M}\right)^{\epsilon} \ . \tag{A.24}$$

The graph (e) is given by

$$
\begin{aligned}
-ik^\epsilon H_{(e)} &= -3iH(ig\mathcal{Z})^2 k^{2\epsilon} \int \frac{d^dq}{(2\pi)^d} \frac{i^2 q^\mu q^\nu}{(\mathcal{Z}^2 q^2 - M^2)^2} \frac{-i}{(1+\omega)q^2} \\
&\quad \times \left(\eta_{\mu\nu} + \xi \frac{q_\mu q_\nu}{q^2}\right) \\
&= -\frac{3Hg^2}{\mathcal{Z}^2\lambda} \frac{1+\xi}{1+\omega} k^{2\epsilon} \int \frac{d^dq}{(2\pi)^d} \frac{1}{[q^2 - (M/\mathcal{Z})^2]^2} \\
&= -\frac{3Hg^2}{\mathcal{Z}^2\lambda} \frac{ik^\epsilon}{8\pi^2\epsilon} \left(\frac{k\mathcal{Z}}{M}\right)^\epsilon + \text{finite} .
\end{aligned}
\tag{A.25}
$$

such that

$$
H_{(e)} = \frac{3Hg^2}{8\pi^2 \mathcal{Z}^2 \lambda \epsilon} \left(\frac{k\mathcal{Z}}{M}\right)^\epsilon \ . \tag{A.26}
$$

Appendix B

UFO model validation

The UFO models developed for HECOs, as detailed in Section 4.2.5, have been thoroughly validated to ensure their accuracy and consistency. This validation compares cross sections obtained from analytical calculations, performed using the MATHEMATICA 13.0.1 package FEYNCALC 9.3.1 [305], with results from MADGRAPH5_aMC@NLO simulations. This procedure not only verifies the precision of the implemented UFO models but also builds confidence in their predictive reliability for collider simulations.

B.1 Validation at Tree Level

For both spin-½ and spin-0 HECOs, the validation began by examining tree-level predictions. The total HECO pair-production cross section was computed for both Drell-Yan (DY) and photon-fusion (PF) processes. The MADGRAPH results were then compared to analytical calculations derived using MATHEMATICA. These comparisons were carried out for scenarios where the initial particles—up-quarks or photons—collide directly, without the inclusion of parton distribution functions (PDFs). For this purpose, the `no-PDF` option in MADGRAPH was utilised.

Tables B.1 and B.2 summarise the results for spin-½ HECOs, while Tables B.3 and B.4 present the corresponding results for spin-0 HECOs. The UFO-to-theory ratios consistently approach unity, confirming that the simulation code accurately reproduces theoretical predictions at tree level.

Table B.1: Cross section of spin-1/2 HECO production of mass $M = 1$ TeV via the DY $u\bar{u} \to \mathcal{H}\overline{\mathcal{H}}$ process at $\sqrt{s} = 13$ TeV obtained with MadGraph and with theoretical calculations at tree level. The simulation/theory ratio is also listed.

DY $u\bar{u} \to \mathcal{H}\overline{\mathcal{H}}$ tree level @ $\sqrt{s} = 13$ TeV, $M = 1$ TeV						
$Q\,(e)$	γ-only exchange			γ/Z^0 exchange		
	σ_{MadGraph} (pb)	$\sigma_{\text{Mathematica}}$ (pb)	UFO/Theory	σ_{MadGraph} (pb)	$\sigma_{\text{Mathematica}}$ (pb)	UFO/Theory
20	0.0349	0.0348	1.003	0.0315	0.0314	1.003
40	0.1395	0.1390	1.007	0.1262	0.1257	1.004
60	0.3141	0.3127	1.005	0.2845	0.2828	1.006
80	0.5579	0.5560	1.004	0.5056	0.5028	1.005
100	0.8748	0.8687	1.004	0.7903	0.7857	1.006
120	1.2589	1.2509	1.005	1.1371	1.1313	1.005
140	1.7142	1.7026	1.006	1.5482	1.5399	1.005
160	2.2332	2.2238	1.007	2.0229	2.0113	1.006
180	2.8277	2.8145	1.005	2.5620	2.5455	1.006
200	3.4926	3.4747	1.003	3.1536	3.1426	1.003

Table B.2: Cross section of spin-1/2 HECO production of mass $M = 1$ TeV via the PF $\gamma\gamma \to \mathcal{H}\overline{\mathcal{H}}$ process at $\sqrt{s} = 13$ TeV obtained with MadGraph and with theoretical calculations at tree level. The simulation/theory ratio is also listed.

PF tree level $\gamma\gamma \to \mathcal{H}\overline{\mathcal{H}}$ @ $\sqrt{s} = 13$ TeV, $M = 1$ TeV			
Q (e)	σ_{MadGraph} (pb)	$\sigma_{\text{Mathematica}}$ (pb)	UFO/Theory
20	7.438×10^{3}	7.398×10^{3}	1.005
40	7.732×10^{4}	7.692×10^{4}	1.004
60	3.539×10^{5}	3.528×10^{5}	1.003
80	1.082×10^{6}	1.076×10^{6}	1.006
100	2.596×10^{6}	2.580×10^{9}	1.006
120	5.327×10^{6}	5.300×10^{6}	1.005
140	9.814×10^{6}	9.761×10^{6}	1.005
160	1.668×10^{7}	1.659×10^{7}	1.005
180	2.663×10^{7}	2.651×10^{7}	1.004
200	4.052×10^{7}	4.033×10^{7}	1.005

Table B.3: Cross section of scalar HECO production at tree level via the DY $u\bar{u} \to \mathcal{H}\overline{\mathcal{H}}$ process at $\sqrt{s} = 13$ TeV obtained with MadGraph by importing the related UFO model and with theoretical calculations. The simulation/theory ratio is also listed.

DY at tree level $u\bar{u} \to \mathcal{H}\overline{\mathcal{H}}$ @ $\sqrt{s} = 13$ TeV, $M = 1$ TeV			
Q (e)	σ_{MadGraph} (pb)	$\sigma_{\text{Mathematica}}$ (pb)	UFO/Theory
20	8.418×10^{-3}	$8.382\ \times10^{-3}$	1.004
60	7.588×10^{-2}	$7.543\ \times10^{-2}$	1.006
100	2.107×10^{-1}	$2.095\ \times10^{-1}$	1.005
140	4.132×10^{-1}	$4.107\ \times10^{-1}$	1.006
180	6.829×10^{-1}	$6.789\ \times10^{-1}$	1.005
220	1.019	1.014	1.006

Table B.4: Cross section of spin-0 HECO production at tree level via the PF $\gamma\gamma \to \mathcal{H}\overline{\mathcal{H}}$ process at $\sqrt{s} = 13$ TeV obtained with MadGraph by importing the related UFO model and with theoretical calculations. A HECO mass $M = 1$ TeV is assumed. The simulation/theory ratio is also listed.

PF at tree level $\gamma\gamma \to \mathcal{H}\overline{\mathcal{H}}$ @ $\sqrt{s} = 13$ TeV, $M = 1$ TeV			
Q (e)	σ_{MadGraph} (pb)	$\sigma_{\text{Mathematica}}$ (pb)	UFO/Theory
20	1.263×10^2	1.255×10^2	1.006
60	1.023×10^4	1.017×10^4	1.006
100	7.897×10^4	7.845×10^4	1.005
140	3.026×10^5	3.013×10^5	1.006
180	8.279×10^5	8.235×10^5	1.006
220	1.846×10^6	1.838×10^6	1.006

B.2 Validation with Resummation Effects

The UFO models incorporating DS resummation effects were validated using the same methodology applied at tree level. The results, summarised in Tables B.5, B.6, B.7 and B.8 confirm the accuracy of these models for both DY and PF processes. The UFO-to-theory ratios remain consistent across all cases, demonstrating the reliability of the resummation effects implemented in the UFO models.

Table B.5: Cross section of spin-1/2 HECO production via the DY $u\bar{u} \to \mathcal{H}\overline{\mathcal{H}}$ process at $\sqrt{s} = 13$ TeV obtained with MadGraph by importing the relevant UFO models and with theoretical calculations. Resummation with $\Lambda = 2$ TeV is assumed. The simulation/theory ratio is also listed.

DY with resummation $u\bar{u} \to \mathcal{H}\overline{\mathcal{H}}$ @ $\sqrt{s} = 13$ TeV, $\Lambda = 2$ TeV						
Q (e)	γ-only exchange			γ/Z^0 exchange		
	σ_{MadGraph} (pb)	$\sigma_{\text{Mathematica}}$ (pb)	UFO/Theory	σ_{MadGraph} (pb)	$\sigma_{\text{Mathematica}}$ (pb)	UFO/Theory
20	0.0762	0.0758	1.005	0.0659	0.0655	1.006
40	0.3048	0.3027	1.007	0.2632	0.2616	1.006
60	0.6837	0.6807	1.004	0.5919	0.5886	1.005
80	1.2151	1.2097	1.004	1.0508	1.0462	1.004
100	1.8976	1.8898	1.004	1.6460	1.6345	1.007
120	2.7372	2.7210	1.006	2.3682	2.3537	1.006
140	3.7261	3.7032	1.006	3.2251	3.2035	1.006
160	4.8712	4.8366	1.007	4.2083	4.1843	1.005
180	6.1548	6.1210	1.006	5.3224	5.2955	1.005
200	7.5927	7.5568	1.004	6.5758	6.5379	1.006

Table B.6: Cross section of spin-1/2 HECO production via the PF $\gamma\gamma \to \mathcal{H}\overline{\mathcal{H}}$ process at $\sqrt{s} = 13$ TeV obtained with MadGraph by importing the relevant UFO models and with theoretical calculations. Resummation with $\Lambda = 2$ TeV is assumed. The simulation/theory ratio is also listed.

PF with resummation $\gamma\gamma \to \mathcal{H}\overline{\mathcal{H}}$ @ $\sqrt{s} = 13$ TeV, $\Lambda = 2$ TeV			
Q (e)	σ_{MadGraph} (pb)	$\sigma_{\text{Mathematica}}$ (pb)	UFO/Theory
20	7.438×10^{3}	7.398×10^{3}	1.005
40	7.732×10^{4}	7.692×10^{4}	1.004
60	3.539×10^{5}	3.528×10^{5}	1.003
80	1.082×10^{6}	1.076×10^{6}	1.006
100	2.596×10^{6}	2.580×10^{9}	1.006
120	5.327×10^{6}	5.300×10^{6}	1.005
140	9.814×10^{6}	9.761×10^{6}	1.005
160	1.668×10^{7}	1.659×10^{7}	1.005
180	2.663×10^{7}	2.651×10^{7}	1.004
200	4.052×10^{7}	4.033×10^{7}	1.005

Table B.7: Cross section of spin-0 HECO production via the DY $u\bar{u} \to \mathcal{H}\overline{\mathcal{H}}$ process at $\sqrt{s} = 13$ TeV obtained with MadGraph by importing the related UFO model and with theoretical calculations. Resummation with $\Lambda = 2$ TeV is assumed. The simulation/theory ratio is also listed. No PDF is considered.

DY with resummation $u\bar{u} \to \mathcal{H}\overline{\mathcal{H}}$ @ $\sqrt{s} = 13$ TeV, $\Lambda = 2$ TeV			
Q (e)	σ_{MadGraph} (pb)	$\sigma_{\text{Mathematica}}$ (pb)	UFO/Theory
20	1.396×10^{-2}	1.388×10^{-2}	1.006
60	1.149×10^{-1}	1.144×10^{-2}	1.004
100	3.149×10^{-1}	3.131×10^{-1}	1.006
140	6.151×10^{-1}	6.113×10^{-1}	1.006
180	1.015	1.009	1.006
220	1.514	1.506	1.005

Table B.8: Cross section of spin-0 HECO production via the PF $\gamma\gamma \to \mathcal{H}\overline{\mathcal{H}}$ process at $\sqrt{s}$ = 13 TeV obtained with MadGraph by importing the related UFO model and with theoretical calculations. Resummation with Λ = 2 TeV is assumed. The simulation/theory ratio is also listed. No PDF has been used.

PF with resummation $\gamma\gamma \to \mathcal{H}\overline{\mathcal{H}}$ @ $\sqrt{s} = 13$ TeV, $\Lambda = 2$ TeV			
Q (e)	σ_{MadGraph} (pb)	$\sigma_{\text{Mathematica}}$ (pb)	UFO/Theory
20	$3.458{\times}10^{2}$	$3.439{\times}10^{2}$	1.006
60	$2.320{\times}10^{4}$	$2.309{\times}10^{4}$	1.005
100	$1.750{\times}10^{5}$	$1.741{\times}10^{4}$	1.005
140	$6.677{\times}10^{5}$	$6.643{\times}10^{5}$	1.005
180	$1.820{\times}10^{6}$	$1.810{\times}10^{5}$	1.006
220	$4.058{\times}10^{6}$	$4.034{\times}10^{6}$	1.006

Acknowledgments

During this long and challenging journey called "PhD", many people have played a fundamental role in helping me reach this point. Listing each of them by name would be impossible, so I apologise in advance for not being able to thank everyone individually.

First and foremost, I would like to express my deepest gratitude to my supervisor, Vasiliki, for believing in me and in my potential. Her support made it possible for me to undertake this PhD and develop as a researcher.

I am also grateful to my research group, AITANA — especially Adrián and Marcel — with whom I have had the pleasure of collaborating.

My sincere thanks go to my collaborators Nick, Miguel Ángel and Redamy for their important input and for contributing significantly to my growth as a researcher.

I would also like to thank Oscar, my tutor, and the MoEDAL collaboration, which I am glad to be part of.

There's one person who has been by my side from the very beginning: Pierpaolo. He stood by me through the toughest times, taking care of me, supporting me with so much patience, love, and understanding. I'll always be deeply grateful for that.

I also want to thank my family, who have supported me for as long as I can remember, even when all sorts of challenges came up over the years. They never stopped believing in me, and that meant everything.

Now it's time to thank what I consider one of the most robust pillars of my life: all my friends.

The greatest thing that this PhD experience in Valencia has given me is the extraordinary people I have met here, many of whom have become like a second family to me.

A special thank you goes to Mariam. Even though we've only known each other for two years, it feels like we have been friends forever. Thank you for all our conversations over glasses of wine, for sharing both the joys and the struggles, and most of all, for always being there.

I also want to thank an amazing group of people I had the pleasure of spending time with: Adri, Ali, David, Fra, Juan, Marta, Naseem, Paolo, Pepe and Quique. Thank you for the many laughs you gave me. Those moments of joy and lightness really made a difference.

And a big thank you to the very first group I joined when I moved here: the IATA crew. In particular, Androniki, Baibhab, Chitra, Drona, Ele, Fabian, Fede, Gorka, Juli and Kostas. With some of you, I walked this path from the very beginning – so many great memories that made this experience even more special.

Of course, grazie al "Banco del Mutuo Soccorso", i.e. Gloria, Lorenzo and Tessa. Thank you for all the silly moments wandering around bars and the laughter, as well as the deep conversations we shared along the way. On this note, thanks also to the "isolani" gang (Mari, Ale, Ago and Silvia).

Grateful as well to the friends I met toward the end of this journey — among them, Kari, whose sweetness brought moments of ease.

And then there are the people who have always been part of my life. Thanks to Nancy, who's been by my side since our school days and through every chapter since, as we grew up together. A heartfelt thank you as well to all my friends in Bronte, whose support has always meant so much to me.

I also want to thank the people whose support has been constant since my undergraduate days — especially Ale, Seby, Pana and "La Compagine" guys. I'm also grateful for the wonderful people my years in Bologna brought into my life, whose friendship has remained strong over time despite the distance — in particular, Stefy, Giuly, Mati and Sara.

A special mention goes to *art*, in all its forms, which has always saved me — particularly *music*, my loyal companion through countless hours of

hard work and moments of discouragement.

To all the people I haven't named but who have been part of this journey, *thank you from the bottom of my heart.* Your presence, in whatever form it came, left a mark on this chapter of my life.

Bibliography

[1] W. N. Cottingham and D. A. Greenwood, *An Introduction to the Standard Model of Particle Physics*. Cambridge University Press, 7, 2023, 10.1017/9781009401685.

[2] S. L. Glashow, *Partial Symmetries of Weak Interactions*, *Nucl. Phys.* **22** (1961) 579.

[3] S. Weinberg, *A model of leptons*, *Phys. Rev. Lett.* **19** (1967) 1264.

[4] A. Salam, *Weak and electromagnetic interactions*, in *Elementary Particle Physics: Relativistic Groups and Analyticity*, N. Svartholm, ed., pp. 367–377, Almqvist & Wiksell, 1968.

[5] C. P. Burgess and G. D. Moore, *The standard model: A primer*. Cambridge University Press, 12, 2006.

[6] S. Weinberg, *Non-abelian gauge theories of the strong interactions*, *Phys. Rev. Lett.* **31** (1973) 494.

[7] H. Fritzsch, M. Gell-Mann and H. Leutwyler, *Advantages of the Color Octet Gluon Picture*, *Phys. Lett. B* **47** (1973) 365.

[8] F. Quevedo and A. Schachner, *Cambridge Lectures on The Standard Model*, `2409.09211`.

[9] F. Englert and R. Brout, *Broken symmetry and the mass of gauge vector mesons*, *Phys. Rev. Lett.* **13** (1964) 321.

[10] S. L. Glashow, J. Iliopoulos and L. Maiani, *Weak interactions with lepton-hadron symmetry*, *Phys. Rev. D* **2** (1970) 1285.

[11] ALEPH, DELPHI, L3, OPAL, LEP Electroweak Working Group collaboration, *A Combination of preliminary electroweak measurements and constraints on the standard model*, hep-ex/0612034.

[12] CDF collaboration, *Observation of top quark production in $\bar{p}p$ collisions with the collider detector at fermilab*, *Phys. Rev. Lett.* **74** (1995) 2626.

[13] D0 collaboration, *Observation of the top quark*, *Phys. Rev. Lett.* **74** (1995) 2632.

[14] ATLAS collaboration, *Observation of a new particle in the search for the Standard Model Higgs boson with the ATLAS detector at the LHC*, *Phys. Lett. B* **716** (2012) 1.

[15] CMS collaboration, *Observation of a New Boson at a Mass of 125 GeV with the CMS Experiment at the LHC*, *Phys. Lett. B* **716** (2012) 30.

[16] P. W. Higgs, *Broken symmetries and the masses of gauge bosons*, *Phys. Rev. Lett.* **13** (1964) 508.

[17] ATLAS collaboration, *The ATLAS Experiment at the CERN Large Hadron Collider*, *JINST* **3** (2008) S08003.

[18] CMS collaboration, *The CMS Experiment at the CERN LHC*, *JINST* **3** (2008) S08004.

[19] The Nobel Committee for Physics, *The 2013 nobel prize in physics*, 2013.

[20] Y. Fukuda, T. Hayakawa, E. Ichihara, K. Inoue, K. Ishihara, H. Ishino et al., *Evidence for oscillation of atmospheric neutrinos*, *Physical Review Letters* **81** (1998) 1562–1567.

[21] SNO collaboration, *Measurement of the rate of $\nu_e + d \to p + p + e^-$ interactions produced by ^8B solar neutrinos at the Sudbury Neutrino Observatory*, *Phys. Rev. Lett.* **87** (2001) 071301.

[22] SNO collaboration, *Direct evidence for neutrino flavor transformation from neutral-current interactions in the sudbury neutrino observatory*, *Phys. Rev. Lett.* **89** (2002) 011301.

[23] KamLAND collaboration, *First results from kamland: Evidence for reactor antineutrino disappearance*, *Phys. Rev. Lett.* **90** (2003) 021802.

[24] K2K collaboration, *Measurement of neutrino oscillation by the k2k experiment*, *Phys. Rev. D* **74** (2006) 072003.

[25] T. P. Cheng and L.-F. Li, *Neutrino Masses, Mixings and Oscillations in SU(2) x U(1) Models of Electroweak Interactions*, *Phys. Rev. D* **22** (1980) 2860.

[26] P. Minkowski, *$\mu \to e\gamma$ at a Rate of One Out of 10^9 Muon Decays?*, *Phys. Lett. B* **67** (1977) 421.

[27] M. Gell-Mann, P. Ramond and R. Slansky, *Complex Spinors and Unified Theories*, *Conf. Proc. C* **790927** (1979) 315.

[28] T. Yanagida, *Horizontal gauge symmetry and masses of neutrinos*, *Conf. Proc. C* **7902131** (1979) 95.

[29] G. Lazarides, Q. Shafi and C. Wetterich, *Proton Lifetime and Fermion Masses in an SO(10) Model*, *Nucl. Phys. B* **181** (1981) 287.

[30] R. N. Mohapatra and G. Senjanovic, *Neutrino Mass and Spontaneous Parity Nonconservation*, *Phys. Rev. Lett.* **44** (1980) 912.

[31] R. Foot, H. Lew, X. G. He and G. C. Joshi, *Seesaw Neutrino Masses Induced by a Triplet of Leptons*, *Z. Phys. C* **44** (1989) 441.

[32] A. Strumia and F. Vissani, *Neutrino masses and mixings and...*, hep-ph/0606054.

[33] G. Altarelli and F. Feruglio, *Models of neutrino masses and mixings*, *New Journal of Physics* **6** (2004) 106–106.

[34] V. C. Rubin and W. K. Ford, Jr., *Rotation of the Andromeda Nebula from a Spectroscopic Survey of Emission Regions*, *Astrophys. J.* **159** (1970) 379.

[35] J. A. Tyson, G. P. Kochanski and I. P. Dell'Antonio, *Detailed mass map of cl 0024+1654 from strong lensing*, *Astrophysical Journal* **498** (1998) L107.

[36] Planck collaboration, *Planck 2018 results. vi. cosmological parameters*, *Astronomy & Astrophysics* **641** (2020) A6.

[37] J. de Swart, G. Bertone and J. van Dongen, *How Dark Matter Came to Matter*, *Nature Astron.* **1** (2017) 0059 [1703.00013].

[38] F. Chadha-Day, J. Ellis and D. J. E. Marsh, *Axion dark matter: What is it and why now?*, *Sci. Adv.* **8** (2022) abj3618.

[39] S. Dodelson and L. M. Widrow, *Sterile neutrinos as dark matter*, *Physical Review Letters* **72** (1994) 17.

[40] P. H. Frampton, M. Kawasaki, F. Takahashi and T. T. Yanagida, *Primordial Black Holes as All Dark Matter*, *JCAP* **04** (2010) 023.

[41] B. C. Lacki and J. F. Beacom, *Primordial Black Holes as Dark Matter: Almost All or Almost Nothing*, *Astrophys. J. Lett.* **720** (2010) L67.

[42] A. Kashlinsky, *LIGO gravitational wave detection, primordial black holes and the near-IR cosmic infrared background anisotropies*, *Astrophys. J. Lett.* **823** (2016) L25.

[43] J. R. Espinosa, D. Racco and A. Riotto, *Cosmological Signature of the Standard Model Higgs Vacuum Instability: Primordial Black Holes as Dark Matter*, *Phys. Rev. Lett.* **120** (2018) 121301.

[44] S. Clesse and J. García-Bellido, *Seven Hints for Primordial Black Hole Dark Matter*, *Phys. Dark Univ.* **22** (2018) 137.

[45] V. A. Mitsou, *Shedding Light on Dark Matter at Colliders*, *Int. J. Mod. Phys. A* **28** (2013) 1330052 [1310.1072].

[46] A. G. Riess et al., *Observational evidence from supernovae for an accelerating universe and a cosmological constant*, *Astronomical Journal* **116** (1998) 1009.

[47] S. Perlmutter et al., *Measurements of ω and λ from 42 high-redshift supernovae*, *Astrophysical Journal* **517** (1999) 565.

[48] D. J. Eisenstein et al., *Detection of the baryon acoustic peak in the large-scale correlation function of sdss luminous red galaxies*, *Astrophysical Journal* **633** (2005) 560.

[49] S. Weinberg, *Cosmological constant*, *Review of Modern Physics* **61** (1989) 1.

[50] Y. Zeldovich, *The cosmological constant and the theory of elementary particles*, *Soviet Physics Uspekhi* **11** (1968) 381.

[51] R. Caldwell, R. Dave and P. Steinhardt, *Cosmological imprint of an energy component with general equation of state*, *Physical Review Letters* **80** (1998) 1582.

[52] I. Zlatev, L. Wang and P. Steinhardt, *Quintessence, cosmic coincidence, and the cosmological constant*, *Physical Review Letters* **82** (1999) 896.

[53] T. Clifton, P. G. Ferreira, A. Padilla and C. Skordis, *Modified gravity and cosmology*, *Physics Reports* **513** (2012) 1.

[54] S. Nojiri and S. D. Odintsov, *Introduction to modified gravity and gravitational alternative for dark energy*, *International Journal of Geometric Methods in Modern Physics* **4** (2007) 115.

[55] A. H. Guth, *Inflationary universe: A possible solution to the horizon and flatness problems*, *Physical Review D* **23** (1981) 347.

[56] A. D. Linde, *A new inflationary universe scenario: A possible solution to the horizon, flatness, homogeneity, isotropy, and primordial monopole problems*, *Physics Letters B* **108** (1982) 389.

[57] A. D. Linde, *Chaotic inflation*, *Physics Letters B* **129** (1983) 177.

[58] A. D. Sakharov, *Violation of CP Invariance, C asymmetry, and baryon asymmetry of the universe*, *Pisma Zh. Eksp. Teor. Fiz.* **5** (1967) 32.

[59] M. Fukugita and T. Yanagida, *Baryogenesis Without Grand Unification*, *Physics Letters B* **174** (1986) 45.

[60] E. W. Kolb and M. S. Turner, *The Early Universe*, vol. 69. Taylor and Francis, 5, 2019, 10.1201/9780429492860.

[61] L. Randall and R. Sundrum, *A large mass hierarchy from a small extra dimension*, *Phys. Rev. Lett.* **83** (1999) 3370.

[62] G. F. Giudice and R. Rattazzi, *Theories with gauge-mediated supersymmetry breaking*, *Phys. Rept.* **322** (2008) 419.

[63] Particle Data Group, *Review of Particle Physics*, *Prog. Theor. Exp. Phys.* **2022** (2022) 083C01.

[64] J. Wess and B. Zumino, *Supergauge transformations in four-dimensions*, *Nucl. Phys. B* **70** (1974) 39.

[65] H. E. Haber and L. Stephenson Haskins, *Supersymmetric theory and models.*, in *Theoretical Advanced Study Institute in Elementary Particle Physics: Anticipating the Next Discoveries in Particle Physics*, pp. 355–499, WSP, 2018, DOI [1712.05926].

[66] N. Arkani-Hamed, S. Dimopoulos and G. R. Dvali, *The hierarchy problem and new dimensions at a millimeter*, *Phys. Lett. B* **429** (1998) 263.

[67] L. Randall and R. Sundrum, *An Alternative to compactification*, *Phys. Rev. Lett.* **83** (1999) 4690 [hep-th/9906064].

[68] C. A. Baker, D. Doyle, P. Geltenbort, K. Green, M. van der Grinten, P. G. Harris et al., *An Improved experimental limit on the electric dipole moment of the neutron*, *Phys. Rev. Lett.* **97** (2006) 131801.

[69] R. D. Peccei and H. R. Quinn, *CP Conservation in the Presence of Instantons*, *Phys. Rev. Lett.* **38** (1977) 1440.

[70] R. D. Peccei and H. R. Quinn, *Constraints Imposed by CP Conservation in the Presence of Instantons*, *Phys. Rev. D* **16** (1977) 1791.

[71] S. Weinberg, *A New Light Boson?*, *Phys. Rev. Lett.* **40** (1978) 223.

[72] F. Wilczek, *Problem of Strong P and T Invariance in the Presence of Instantons*, *Phys. Rev. Lett.* **40** (1978) 279.

[73] S. M. Carroll, *The cosmological constant*, *Living Reviews in Relativity* **4** (2001) 1.

[74] T. Padmanabhan, *Cosmological constant - the weight of the vacuum*, *Physics Reports* **380** (2003) 235.

[75] L. Susskind, *The Anthropic landscape of string theory*, `hep-th/0302219`.

[76] N. Arkani-Hamed, H. Georgi and S. D. Thomas, *The sledgehammer and the scalpel: A theory of high-energy physics beyond the standard model*, *Physical Review D* **76** (2007) 056005.

[77] J. Polchinski, *String theory. Vol. 1: An introduction to the bosonic string*, Cambridge Monographs on Mathematical Physics. Cambridge University Press, 12, 2007, 10.1017/CBO9780511816079.

[78] J. Polchinski, *String theory. Vol. 2: Superstring theory and beyond*, Cambridge Monographs on Mathematical Physics. Cambridge University Press, 12, 2007, 10.1017/CBO9780511618123.

[79] C. Rovelli, *Loop quantum gravity*, *Living Rev. Rel.* **1** (1998) 1 [`gr-qc/9710008`].

[80] S. Weinberg, *Baryon and Lepton Nonconserving Processes*, *Phys. Rev. Lett.* **43** (1979) 1566.

[81] W. Buchmuller and D. Wyler, *Effective Lagrangian Analysis of New Interactions and Flavor Conservation*, *Nucl. Phys. B* **268** (1986) 621.

[82] B. Grzadkowski, M. Iskrzynski, M. Misiak and J. Rosiek, *Dimension-Six Terms in the Standard Model Lagrangian*, *JHEP* **10** (2010) 085.

[83] I. Brivio and M. Trott, *The Standard Model as an Effective Field Theory*, *Phys. Rept.* **793** (2019) 1.

[84] A. Manohar and H. Georgi, *Chiral Quarks and the Nonrelativistic Quark Model*, *Nucl. Phys. B* **234** (1984) 189.

[85] E. Fermi, *Tentativo di una teoria dell'emissione dei raggi beta*, *Z. Phys.* **88** (1934) 161.

[86] J. Wess and B. Zumino, *Supergauge transformations in four dimensions*, *Nuclear Physics B* **70** (1974) 39.

[87] E. Witten, *Dynamical breaking of supersymmetry*, *Nuclear Physics B* **188** (1981) 513.

[88] S. Dimopoulos and H. Georgi, *Softly broken supersymmetry and su(5)*, *Nuclear Physics B* **193** (1981) 150.

[89] G. Jungman, M. Kamionkowski and K. Griest, *Supersymmetric dark matter*, *Physics Reports* **267** (1996) 195.

[90] ATLAS collaboration, *Search for supersymmetry in final states with two same-sign or three leptons and jets using 36 fb^{-1} of $\sqrt{s} = 13$ TeV pp collision data with the ATLAS detector*, *JHEP* **09** (2017) 084 [1706.03731].

[91] ATLAS collaboration, *Search for supersymmetry in events with four or more charged leptons in 139 fb^{-1} of $\sqrt{s}$ = 13 TeV pp collisions with the ATLAS detector*, JHEP **07** (2021) 167 [2103.11684].

[92] ATLAS collaboration, *Search for supersymmetry in final states with missing transverse momentum and multiple b-jets in proton-proton collisions at $\sqrt{s}$ = 13 TeV with the ATLAS detector*, JHEP **03** (2020) 145.

[93] ATLAS collaboration, *Search for supersymmetry using vector boson fusion signatures and missing transverse momentum in pp collisions at $\sqrt{s}$ = 13 TeV with the ATLAS detector*, JHEP **12** (2024) 116 [2409.18762].

[94] CMS Collaboration, *Search for supersymmetry in events with a photon, a lepton, and missing transverse momentum in proton-proton collisions at 13 TeV*, Phys. Lett. B **780** (2018) 384.

[95] CMS collaboration, *Search for supersymmetry in final states with disappearing tracks in proton-proton collisions at $\sqrt{s}$ =13 TeV*, Phys. Rev. D **109** (2024) 072007 [2309.16823].

[96] CMS collaboration, *Combined search for electroweak production of winos, binos, higgsinos, and sleptons in proton-proton collisions at $\sqrt{s}$ =13 TeV*, Phys. Rev. D **109** (2024) 112001 [2402.01888].

[97] H. Georgi and S. L. Glashow, *Unity of all elementary-particle forces*, *Physical Review Letters* **32** (1974) 438.

[98] J. C. Pati and A. Salam, *Lepton number as the fourth color*, *Physical Review D* **10** (1974) 275.

[99] S. L. Glashow, *Towards a unified theory: Threads in a tapestry*, *Reviews of Modern Physics* **52** (1980) 539.

[100] P. Langacker, *Grand unification and proton decay*, *Physics Reports* **72** (1981) 185.

[101] G. 't Hooft, *Magnetic monopoles in unified gauge theories*, *Nuclear Physics B* **79** (1974) 276.

[102] A. M. Polyakov, *Particle spectrum in quantum field theory*, *JETP Letters* **20** (1974) 194.

[103] SUPER-KAMIOKANDE collaboration, *Search for proton decay via p→ e+ π0 and p→ μ+ π0 in 0.31 megaton · years exposure of the super-kamiokande water cherenkov detector*, *Physical Review D* **90** (2014) 072005.

[104] H. Fritzsch and P. Minkowski, *Unified interactions of leptons and hadrons*, *Annals of Physics* **93** (1975) 193.

[105] Y. Fukuda et al., *Evidence for oscillation of atmospheric neutrinos*, *Physical Review Letters* **81** (1998) 1562.

[106] F. Gursey, P. Ramond and P. Sikivie, *A Universal Gauge Theory Model Based on E6*, *Phys. Lett. B* **60** (1976) 177.

[107] J. L. Hewett and T. G. Rizzo, *Low-Energy Phenomenology of Superstring Inspired E(6) Models*, *Phys. Rept.* **183** (1989) 193.

[108] S. M. Barr, *A New Symmetry Breaking Pattern for SO(10) and Proton Decay*, *Phys. Lett. B* **112** (1982) 219.

[109] M. B. Green and J. H. Schwarz, *Anomaly cancellation in supersymmetric d=10 gauge theory and superstring theory*, *Physics Letters B* **149** (1987) 117.

[110] I. Antoniadis, *A Possible new dimension at a few TeV*, *Phys. Lett. B* **246** (1990) 377.

[111] S. Dimopoulos and G. Landsberg, *Black holes at high-energy colliders*, *Physical Review Letters* **87** (2001) 161602.

[112] M. Perelstein, *Introduction to Collider Physics*, in *Theoretical Advanced Study Institute in Elementary Particle Physics: Physics of the Large and the Small*, pp. 421–486, 2011, DOI [1002.0274].

[113] A. Buckley, C. White and M. White, *Practical Collider Physics*. IOP, 12, 2021, 10.1088/978-0-7503-2444-1.

[114] M. D. Schwartz, *TASI lectures on collider physics.*, in *Theoretical Advanced Study Institute in Elementary Particle Physics: Anticipating the Next Discoveries in Particle Physics*, pp. 65–100, 2018, DOI [1709.04533].

[115] H. Abramowicz and A. Caldwell, *HERA collider physics*, *Rev. Mod. Phys.* **71** (1999) 1275 [hep-ex/9903037].

[116] R. R. Wilson, *The Tevatron*, *Phys. Today* **30N10** (1977) 23.

[117] R. Assmann, M. Lamont and S. Myers, *A brief history of the LEP collider*, *Nucl. Phys. B Proc. Suppl.* **109** (2002) 17.

[118] L. Evans and P. Bryant, eds., *LHC Machine*, *JINST* **3** (2008) S08001.

[119] P. Bambade et al., *The International Linear Collider: A Global Project*, 1903.01629.

[120] L. Linssen, A. Miyamoto, M. Stanitzki and H. Weerts, eds., *Physics and Detectors at CLIC: CLIC Conceptual Design Report*, 1202.5940.

[121] M. Bai et al., *C^3: A "Cool" Route to the Higgs Boson and Beyond*, in *Snowmass 2021*, 10, 2021, 2110.15800.

[122] FCC collaboration, *FCC-ee: The Lepton Collider: Future Circular Collider Conceptual Design Report Volume 2*, *Eur. Phys. J. ST* **228** (2019) 261.

[123] B. De Raad, *The CERN SPS Proton-Antiproton Collider*, *IEEE Trans. Nucl. Sci.* **32** (1985) 1650.

[124] M. Gyulassy and L. McLerran, *New forms of qcd matter discovered at rhic*, *Nuclear Physics A* **750** (2005) 30.

[125] J. P. Delahaye, M. Diemoz, K. Long, B. Mansoulié, N. Pastrone, L. Rivkin et al., *Muon Colliders*, 1901.06150.

[126] G. Moortgat-Pick, H. Baer, M. Battaglia, G. Belanger, K. Fujii, J. Kalinowski et al., *Physics at the e+ e- Linear Collider. Physics at the e+ e- Linear Collider*, *Eur. Phys. J. C* **75** (2015) 371 [1504.01726].

[127] S. Riemann, *Physics at Future* $e^{+}e^{-}$ *Colliders*, *Acta Phys. Polon. B* **50** (2019) 1695.

[128] CEPC Study Group, *CEPC Conceptual Design Report: Volume 1 - Accelerator*, 1809.00285.

[129] ILC International Development Team, *The International Linear Collider: Report to Snowmass 2021*, 2203.07622.

[130] CLICdp, CLIC collaboration, *The Compact Linear Collider (CLIC) - 2018 Summary Report*, 1812.06018.

[131] S. Dasu, E. A. Nanni, M. E. Peskin, C. Vernieri et al., *Strategy for understanding the higgs physics: The cool copper collider*, *arXiv preprint* (2022) [2203.07646].

[132] CEPC Study Group, *CEPC Technical Design Report: Accelerator*, *Radiat. Detect. Technol. Methods* **8** (2024) 1 [2312.14363].

[133] G. Apollinari, I. Béjar Alonso, O. Brüning, P. Fessia, M. Lamont, L. Rossi et al., *High-Luminosity Large Hadron Collider (HL-LHC): Preliminary Design Report*, *CERN Yellow Report* (2015) .

[134] LHCb collaboration, *The LHCb Detector at the LHC*, *JINST* **3** (2008) S08005.

[135] ALICE collaboration, *The ALICE experiment at the CERN LHC*, *JINST* **3** (2008) S08002.

[136] TOTEM collaboration, *The TOTEM experiment at the CERN Large Hadron Collider*, *JINST* **3** (2011) S08007.

[137] LHCf collaboration, *The LHCf detector at the CERN Large Hadron Collider*, *JINST* **3** (2010) S08006.

[138] MoEDAL collaboration, *Technical Design Report of the MoEDAL Experiment*, 6, 2009, https://cds.cern.ch/record/1181486.

[139] FASER collaboration, *The FASER experiment at the CERN LHC*, *Phys. Rev. D* **99** (2019) 095011.

[140] SND@LHC collaboration, *The SND@LHC experiment*, *JINST* **15** (2020) P12004.

[141] FCC collaboration, *FCC-hh: The Hadron Collider*, *Eur. Phys. J. ST* **228** (2019) 755–1107.

[142] M. Benedikt and F. Zimmermann, *Future Circular Colliders*, in *Proceedings of the ICFA Mini-Workshop on Future Circular Colliders*, 2018, https://cds.cern.ch/record/2642471.

[143] M. L. Mangano, *Physics at the FCC-hh, a 100 TeV pp Collider*, *CERN Yellow Reports: Monographs* (2017) .

[144] M. Fairbairn, A. C. Kraan, D. Milstead, T. Sjostrand, P. Skands and T. Sloan, *Stable massive particles at colliders*, *Phys. Rept.* **438** (2007) 1.

[145] W. R. Leo, *Techniques for Nuclear and Particle Physics Experiments: A How-To Approach*. Springer-Verlag, 1987.

[146] ATLAS TRT collaboration, *The ATLAS transition radiation tracker*, in *8th International Conference on Advanced Technology and Particle Physics (ICATPP 2003): Astroparticle, Particle, Space Physics, Detectors and Medical Physics Applications*, pp. 497–501, 11, 2003, DOI [hep-ex/0311058].

[147] ATLAS TRT collaboration, *The ATLAS Transition Radiation Tracker (TRT) proportional drift tube: Design and performance*, *JINST* **3** (2008) P02013.

[148] ATLAS collaboration, *Search for heavy long-lived multi-charged particles in the full LHC Run 2 pp collision data at $\sqrt{s} = 13$ TeV using the ATLAS detector*, Phys. Lett. B **847** (2023) 138316 [2303.13613].

[149] CMS collaboration, *Search for heavy long-lived charged particles in pp collisions at $\sqrt{s} = 7$ and 8 TeV*, JHEP **1307** (2013) 122.

[150] CMS collaboration, *Search for heavy stable charged particles in proton-proton collisions at $\sqrt{s} = 13$ TeV*, Phys. Rev. D **102** (2020) 032007.

[151] MoEDAL collaboration, *The Physics Programme of the MoEDAL Experiment at the LHC*, Int. J. Mod. Phys. A **29** (2014) 1430050 [1405.7662].

[152] J. L. Pinfold, *Searching for exotic particles at the LHC with dedicated detectors*, Nucl. Phys. B Proc. Suppl. **78** (1999) 52.

[153] J. Pinfold, *MoEDAL becomes the LHC's magnificent seventh*, *CERN Cour.* **50N4** (2010) 19.

[154] N. E. Mavromatos and V. A. Mitsou, *Magnetic monopoles revisited: Models and searches at colliders and in the cosmos*, International Journal of Modern Physics A **35** (2020) 2030012.

[155] A. De Roeck, H. P. Hächler, A. M. Hirt, M. D. Joergensen, A. Katre, P. Mermod et al., *Development of a magnetometer-based search strategy for stopped monopoles at the Large Hadron Collider*, Eur. Phys. J. C **72** (2012) 2212.

[156] MoEDAL collaboration, *Timepix3 as solid-state time-projection chamber in particle and nuclear physics*, PoS **ICHEP2020** (2021) 720.

[157] MoEDAL-MAPP collaboration, *MoEDAL-MAPP, an LHC Dedicated Detector Search Facility*, in *Snowmass 2021*, 9, 2022, 2209.03988.

[158] MoEDAL collaboration, *Search for Magnetic Monopoles with the MoEDAL Prototype Trapping Detector in 8 TeV Proton-Proton Collisions at the LHC*, *JHEP* **1608** (2016) 067.

[159] V. A. Mitsou, *The MoEDAL experiment at the LHC: status and results*, *J. Phys. Conf. Ser.* **873** (2017) 012010 [1703.07141].

[160] MoEDAL collaboration, *Search for magnetic monopoles with the MoEDAL forward trapping detector in 2.11 fb^{-1} of 13 TeV proton-proton collisions at the LHC*, *Phys. Lett. B* **782** (2018) 510 [1712.09849].

[161] M. Staelens, *Recent Results and Future Plans of the MoEDAL Experiment*, in *Meeting of the Division of Particles and Fields of the American Physical Society*, 10, 2019, 1910.05772.

[162] MoEDAL collaboration, *First Search for Dyons with the Full MoEDAL Trapping Detector in 13 TeV pp Collisions*, *Phys. Rev. Lett.* **126** (2021) 071801 [2002.00861].

[163] MoEDAL collaboration, *Magnetic Monopole Search with the Full MoEDAL Trapping Detector in 13 TeV pp Collisions Interpreted in Photon-Fusion and Drell-Yan Production*, *Phys. Rev. Lett.* **123** (2019) 021802 [1903.08491].

[164] MoEDAL collaboration, *Search for highly-ionizing particles in pp collisions at the LHC's Run-1 using the prototype MoEDAL detector*, *Eur. Phys. J. C* **82** (2022) 694 [2112.05806].

[165] MoEDAL collaboration, *Search for Highly Ionizing Particles in pp Collisions during LHC Run 2 Using the Full MoEDAL Detector*, *Phys. Rev. Lett.* **134** (2025) 7 [2311.06509].

[166] MoEDAL collaboration, *MoEDAL, MAPP and future endeavours*, *PoS* **DISCRETE2020-2021** (2022) 017.

[167] K. Sakurai, D. Felea, J. Mamuzic, N. E. Mavromatos, V. A. Mitsou, J. L. Pinfold et al., *SUSY discovery prospects with MoEDAL*, *J. Phys. Conf. Ser.* **1586** (2020) 012018 [1903.11022].

[168] D. Felea, J. Mamuzic, R. Masełek, N. E. Mavromatos, V. A. Mitsou, J. L. Pinfold et al., *Prospects for discovering supersymmetric long-lived particles with MoEDAL*, *Eur. Phys. J. C* **80** (2020) 431 [2001.05980].

[169] B. S. Acharya, A. De Roeck, J. Ellis, D. K. Ghosh, R. Masełek, G. Panizzo et al., *Prospects of searches for long-lived charged particles with MoEDAL*, *Eur. Phys. J. C* **80** (2020) 572 [2004.11305].

[170] G. Shiu and L.-T. Wang, *D matter*, *Phys. Rev. D* **69** (2004) 126007 [hep-ph/0311228].

[171] J. R. Ellis, N. E. Mavromatos and D. V. Nanopoulos, *Time dependent vacuum energy induced by D particle recoil*, *Gen. Rel. Grav.* **32** (2000) 943 [gr-qc/9810086].

[172] J. R. Ellis, N. E. Mavromatos and D. V. Nanopoulos, *Derivation of a Vacuum Refractive Index in a Stringy Space-Time Foam Model*, *Phys. Lett. B* **665** (2008) 412 [0804.3566].

[173] J. R. Ellis, N. E. Mavromatos and M. Westmuckett, *A Supersymmetric D-brane model of space-time foam*, *Phys. Rev. D* **70** (2004) 044036 [gr-qc/0405066].

[174] J. R. Ellis, N. E. Mavromatos and M. Westmuckett, *Potentials between D-branes in a supersymmetric model of space-time foam*, *Phys. Rev. D* **71** (2005) 106006 [gr-qc/0501060].

[175] N. E. Mavromatos, S. Sarkar and A. Vergou, *Stringy Space-Time Foam, Finsler-like Metrics and Dark Matter Relics*, *Phys. Lett. B* **696** (2011) 300 [1009.2880].

[176] N. E. Mavromatos, V. A. Mitsou, S. Sarkar and A. Vergou, *Implications of a Stochastic Microscopic Finsler Cosmology*, *Eur. Phys. J. C* **72** (2012) 1956 [1012.4094].

[177] P. A. M. Dirac, *Quantised singularities in the electromagnetic field,*, *Proc. Roy. Soc. Lond. A* **133** (1931) 60.

[178] A. Rajantie, *Introduction to magnetic monopoles*, *Contemporary Physics* **53** (2012) 195.

[179] J. Preskill, *Magnetic Monopoles*, *Ann. Rev. Nucl. Part. Sci.* **34** (1984) 461.

[180] L. Patrizii, Z. Sahnoun and V. Togo, *Searches for cosmic magnetic monopoles: past, present and future*, *Phil. Trans. Roy. Soc. Lond. A* **377** (2019) 20180328.

[181] Y. M. Cho and D. Maison, *Monopoles in Weinberg-Salam model*, *Phys. Lett. B* **391** (1997) 360 [hep-th/9601028].

[182] J. Ellis, N. E. Mavromatos and T. You, *The Price of an Electroweak Monopole*, *Phys. Lett. B* **756** (2016) 29 [1602.01745].

[183] J. Preskill, *Cosmological Production of Superheavy Magnetic Monopoles*, *Phys. Rev. Lett.* **43** (1979) 1365.

[184] M. Barriola and A. Vilenkin, *Gravitational Field of a Global Monopole*, *Phys. Rev. Lett.* **63** (1989) 341.

[185] C. T. Hill, *Monopolonium*, *Nucl. Phys. B* **224** (1983) 469.

[186] L. N. Epele, H. Fanchiotti, C. A. Garcia Canal and V. Vento, *Monopolium: The Key to monopoles*, *Eur. Phys. J. C* **56** (2008) 87 [hep-ph/0701133].

[187] K. A. Milton, *Theoretical and Experimental Status of Magnetic Monopoles*, *Rept. Prog. Phys.* **69** (2006) 1637.

[188] CMS, TOTEM collaboration, *CMS-TOTEM Precision Proton Spectrometer*, 9, 2014, https://cds.cern.ch/record/1753795.

[189] M. M. Altakach, P. Lamba, R. Masełek, V. A. Mitsou and K. Sakurai, *Discovery prospects for long-lived multiply charged particles at the LHC*, *Eur. Phys. J. C* **82** (2022) 848 [2204.03667].

[190] V. A. Mitsou, *Looking for charged detector-stable particles at the LHC*, *PoS* **CORFU2023** (2024) 112.

[191] S. R. Coleman, *Q-balls*, *Nucl. Phys. B* **262** (1985) 263.

[192] A. Kusenko and M. Shaposhnikov, *Supersymmetric q-balls as dark matter*, *Physics Letters B* **418** (1998) 46–54.

[193] E. Farhi and R. L. Jaffe, *Strange Matter*, *Phys. Rev. D* **30** (1984) 2379.

[194] S. B. Giddings and S. Thomas, *High Energy Colliders as Black Hole Factories: The End of Short Distance Physics*, *Phys. Rev. D* **65** (2002) 056010.

[195] J. Schwinger, *A Magnetic Model of Matter*, *Science* **165** (1969) 757.

[196] J. F. Gunion, H. E. Haber, G. L. Kane and S. Dawson, *The Higgs Hunter's Guide*, *Front. Phys.* **80** (2000) 1.

[197] M. Hirsch, R. Masełek and K. Sakurai, *Detecting long-lived multi-charged particles in neutrino mass models with MoEDAL*, *Eur. Phys. J. C* **81** (2021) 697 [2103.05644].

[198] A. Zee, *A Theory of Lepton Number Violation, Neutrino Majorana Mass, and Oscillation*, *Phys. Lett. B* **93** (1980) 389.

[199] K. S. Babu, *Model of 'Calculable' Majorana Neutrino Masses*, *Phys. Lett. B* **203** (1988) 132.

[200] E. Ma, *Verifiable radiative seesaw mechanism of neutrino mass and dark matter*, *Phys. Rev. D* **73** (2006) 077301.

[201] Y. Kurochkin, I. Satsunkevich, D. Shoukavy, N. Rusakovich and Y. Kulchitsky, *On production of magnetic monopoles via gamma gamma fusion at high energy p p collisions*, *Mod. Phys. Lett. A* **21** (2006) 2873.

[202] T. Dougall and S. D. Wick, *Dirac magnetic monopole production from photon fusion in proton collisions*, *Eur. Phys. J. A* **39** (2009) 213 [0706.1042].

[203] S. Baines, N. E. Mavromatos, V. A. Mitsou, J. L. Pinfold and A. Santra, *Monopole production via photon fusion and Drell–Yan processes: MadGraph implementation and perturbativity via velocity-dependent coupling and magnetic moment as novel features*, *Eur. Phys. J. C* **78** (2018) 966 [1808.08942].

[204] W.-Y. Song and W. Taylor, *Pair production of magnetic monopoles and stable high-electric-charge objects in proton–proton and heavy-ion collisions*, *Journal of Physics G: Nuclear and Particle Physics* **49** (2022) 045002.

[205] V. Vento, *Hidden Dirac Monopoles*, *Int. J. Mod. Phys. A* **23** (2008) 4023 [0709.0470].

[206] J. Alexandre and N. E. Mavromatos, *Weak-U(1) $\times$ strong-U(1) effective gauge field theories and electron-monopole scattering*, *Phys. Rev. D* **100** (2019) 096005 [1906.08738].

[207] A. K. Drukier and S. Nussinov, *Monopole Pair Creation in Energetic Collisions: Is It Possible?*, *Phys. Rev. Lett.* **49** (1982) 102.

[208] K. Farakos, G. Koutsoumbas and N. E. Mavromatos, *Effective Abelian lattice gauge field theories for scalar-matter-monopole interactions*, *Phys. Rev. D* **109** (2024) 114512 [2401.12101].

[209] I. K. Affleck and N. S. Manton, *Monopole Pair Production in a Magnetic Field*, *Nucl. Phys. B* **194** (1982) 38.

[210] O. Gould and A. Rajantie, *Thermal Schwinger pair production at arbitrary coupling*, *Phys. Rev. D* **96** (2017) 076002 [1704.04801].

[211] O. Gould, D. L. J. Ho and A. Rajantie, *Towards Schwinger production of magnetic monopoles in heavy-ion collisions*, *Phys. Rev. D* **100** (2019) 015041 [1902.04388].

[212] J. S. Schwinger, *On gauge invariance and vacuum polarization*, *Phys. Rev.* **82** (1951) 664.

[213] MoEDAL collaboration, *Search for magnetic monopoles produced via the Schwinger mechanism*, *Nature* **602** (2022) 63 [2106.11933].

[214] ATLAS collaboration, *Search for Magnetic Monopole Pair Production in Ultraperipheral Pb+Pb Collisions at sNN=5.36 TeV with the ATLAS Detector at the LHC*, *Phys. Rev. Lett.* **134** (2025) 061803 [2408.11035].

[215] MoEDAL collaboration, *MoEDAL Search in the CMS Beam Pipe for Magnetic Monopoles Produced via the Schwinger Effect*, *Phys. Rev. Lett.* **133** (2024) 071803 [2402.15682].

[216] J. Alexandre, N. E. Mavromatos, V. A. Mitsou and E. Musumeci, *Resummation schemes for high-electric-charge objects leading to improved experimental mass limits*, *Phys. Rev. D* **109** (2024) 036026 [2310.17452].

[217] J. Alexandre, N. E. Mavromatos, V. A. Mitsou and E. Musumeci, *Impact of resummation on the production and experimental bounds of scalar high-electric-charge objects*, *Phys. Rev. D* **111** (2025) 076010 [2412.19001].

[218] E. Musumeci, J. Alexandre, N. Mavromatos and V. A. Mitsou, *Revisiting experimental mass limits on HECOs using Dyson-Schwinger resummation*, *PoS* **ICHEP2024** (2025) 278 [2410.16434].

[219] E. Musumeci, *Resummation effects in HECO pair production at the LHC: UFO implementation*, *PoS* **LHCP2023** (2024) 261.

[220] M. E. Peskin and D. V. Schroeder, *An Introduction to Quantum Field Theory*. Westview Press, 1995.

[221] D. Binosi and J. Papavassiliou, *Pinch Technique: Theory and Applications*, *Phys. Rept.* **479** (2009) 1 [0909.2536].

[222] J. M. Cornwall and J. Papavassiliou, *Gauge Invariant Three Gluon Vertex in QCD*, *Phys. Rev. D* **40** (1989) 3474.

[223] J. Alexandre, J. Polonyi and K. Sailer, *Functional Callan-Symanzik equation for QED*, *Phys. Lett. B* **531** (2002) 316 [hep-th/0111152].

[224] ATLAS collaboration, *Search for magnetic monopoles and stable particles with high electric charges in $\sqrt{s}$ = 13 TeV pp collisions with the ATLAS detector*, *JHEP* **11** (2023) 112 [2308.04835].

[225] M. L. Mangano et al., *Physics at a 100 TeV pp Collider: Standard Model Processes*, 1607.01831.

[226] C. Degrande, C. Duhr, B. Fuks, D. Grellscheid, O. Mattelaer and T. Reiter, *UFO - The Universal FeynRules Output*, *Comput. Phys. Commun.* **183** (2012) 1201 [1108.2040].

[227] L. Darmé, C. Degrande, C. Duhr, B. Fuks, M. Goodsell, G. Heinrich et al., *Ufo 2.0: the 'universal feynman output' format*, *The European Physical Journal C* **83** (2023) .

[228] J. Alwall, M. Herquet, F. Maltoni, O. Mattelaer and T. Stelzer, *MadGraph 5: going beyond*, *JHEP* **06** (2011) 128 [1106.0522].

[229] R. D. Ball et al., *Parton distributions with LHC data*, *Nucl. Phys. B* **867** (2013) 244 [1207.1303].

[230] A. V. Manohar, P. Nason, G. P. Salam and G. Zanderighi, *The Photon Content of the Proton*, *JHEP* **12** (2017) 046 [1708.01256].

[231] C. Itzykson and J. B. Zuber, *Quantum Field Theory*, International Series In Pure and Applied Physics. McGraw-Hill, New York, 1980.

[232] J. Papavassiliou, *Gauge Invariant Proper Selfenergies and Vertices in Gauge Theories with Broken Symmetry*, Phys. Rev. D **41** (1990) 3179.

[233] J. M. Cornwall, J. Papavassiliou and D. Binosi, *The Pinch Technique and its Applications to Non-Abelian Gauge Theories*, Cambridge Monographs on Particle Physics, Nuclear Physics and Cosmology. Cambridge University Press, 7, 2023, 10.1017/9781009402415.

[234] D. Binosi and J. Papavassiliou, *Pinch technique for Schwinger-Dyson equations*, JHEP **03** (2007) 041 [hep-ph/0611354].

[235] N. E. Mavromatos, *Quantum-Gravity Induced Lorentz Violation and Dynamical Mass Generation*, Phys. Rev. D **83** (2011) 025018 [1011.3528].

[236] ATLAS collaboration, *Search for magnetic monopoles and stable particles with high electric charges in 8 TeV pp collisions with the ATLAS detector*, Phys. Rev. D **93** (2016) 052009 [1509.08059].

[237] ATLAS collaboration, *Search for Magnetic Monopoles and Stable High-Electric-Charge Objects in 13 TeV Proton-Proton Collisions with the ATLAS Detector*, Phys. Rev. Lett. **124** (2020) 031802 [1905.10130].

[238] Feynrules Collaboration, "Simple extensions of the SM." https://feynrules.irmp.ucl.ac.be/wiki/SimpleExtensions.

[239] V. M. Budnev, I. F. Ginzburg, G. V. Meledin and V. G. Serbo, *The Two photon particle production mechanism. Physical problems. Applications. Equivalent photon approximation*, Phys. Rept. **15** (1975) 181.

[240] D. d'Enterria and G. G. da Silveira, *Observing light-by-light scattering at the Large Hadron Collider*, *Phys. Rev. Lett.* **111** (2013) 080405 [1305.7142].

[241] ATLAS collaboration, *Measurement of light-by-light scattering and search for axion-like particles with 2.2 nb^{-1} of Pb+Pb data with the ATLAS detector*, *JHEP* **03** (2021) 243 [2008.05355].

[242] CMS collaboration, *Evidence for light-by-light scattering and searches for axion-like particles in ultraperipheral PbPb collisions at $\sqrt{s_{\mathrm{NN}}} = 5.02$ TeV*, *Phys. Lett. B* **797** (2019) 134826 [1810.04602].

[243] A. J. Baltz, *The Physics of Ultraperipheral Collisions at the LHC*, *Phys. Rept.* **458** (2008) 1 [0706.3356].

[244] ATLAS collaboration, *Evidence for light-by-light scattering in heavy-ion collisions with the ATLAS detector at the LHC*, *Nature Phys.* **13** (2017) 852 [1702.01625].

[245] ATLAS collaboration, *Observation of light-by-light scattering in ultraperipheral Pb+Pb collisions with the ATLAS detector*, *Phys. Rev. Lett.* **123** (2019) 052001 [1904.03536].

[246] CMS collaboration, *Measurements of the light-by-light scattering and the Breit–Wheeler processes, and searches for axion-like particles in ultraperipheral PbPb collisions at 5.02 TeV*, CMS-PAS-HIN-21-015, , 4, 2024.

[247] L. Adamczyk et al., *Technical Design Report for the ATLAS Forward Proton Detector*, CERN-LHCC-2015-009, ATLAS-TDR-024, , 5, 2015.

[248] CMS, TOTEM collaboration, *CMS-TOTEM Precision Proton Spectrometer*, CERN-LHCC-2014-021, TOTEM-TDR-003, CMS-TDR-013, , 9, 2014.

[249] TOTEM, CMS collaboration, *First Search for Exclusive Diphoton Production at High Mass with Tagged Protons in Proton-Proton

Collisions at $\sqrt{s}$ = 13 TeV, Phys. Rev. Lett. **129** (2022) 011801 [2110.05916].

[250] CMS, TOTEM collaboration, *Search for high-mass exclusive diphoton production with tagged protons in proton-proton collisions at $\sqrt{s}$ = 13 TeV*, 2311.02725.

[251] ATLAS collaboration, *Search for an axion-like particle with forward proton scattering in association with photon pairs at ATLAS*, JHEP **07** (2023) 234 [2304.10953].

[252] C. Baldenegro, S. Fichet, G. von Gersdorff and C. Royon, *Searching for axion-like particles with proton tagging at the LHC*, JHEP **06** (2018) 131 [1803.10835].

[253] L. N. Epele, H. Fanchiotti, C. A. G. Canal, V. A. Mitsou and V. Vento, *Looking for magnetic monopoles at LHC with diphoton events*, Eur. Phys. J. Plus **127** (2012) 60 [1205.6120].

[254] N. D. Barrie, A. Sugamoto, M. Talia and K. Yamashita, *Searching for monopoles via monopolium multiphoton decays*, Nucl. Phys. B **972** (2021) 115564 [2104.06931].

[255] R. S. Gupta, *Probing Quartic Neutral Gauge Boson Couplings using diffractive photon fusion at the LHC*, Phys. Rev. D **85** (2012) 014006 [1111.3354].

[256] S. Fichet, G. von Gersdorff, B. Lenzi, C. Royon and M. Saimpert, *Light-by-light scattering with intact protons at the LHC: from Standard Model to New Physics*, JHEP **02** (2015) 165 [1411.6629].

[257] S. Fichet, G. von Gersdorff, O. Kepka, B. Lenzi, C. Royon and M. Saimpert, *Probing new physics in diphoton production with proton tagging at the Large Hadron Collider*, Phys. Rev. D **89** (2014) 114004 [1312.5153].

[258] W. Heisenberg and H. Euler, *Consequences of Dirac's theory of positrons*, Z. Phys. **98** (1936) 714 [physics/0605038].

[259] I. F. Ginzburg and A. Schiller, *Visible effect of a very heavy magnetic monopole at colliders*, *Phys. Rev. D* **60** (1999) 075016.

[260] TOTEM, CMS collaboration, *Search for high-mass exclusive diphoton production with tagged protons in proton-proton collisions at $\sqrt{s}$ = 13 TeV*, *Phys. Rev. D* **110** (2024) 012010 [2311.02725].

[261] M. Born and L. Infeld, *Foundations of the new field theory*, *Nature* **132** (1933) 1004.

[262] J. Ellis, N. E. Mavromatos and T. You, *Light-by-Light Scattering Constraint on Born-Infeld Theory*, *Phys. Rev. Lett.* **118** (2017) 261802 [1703.08450].

[263] G. W. Gibbons and C. A. R. Herdeiro, *Born-Infeld theory and stringy causality*, *Phys. Rev. D* **63** (2001) 064006 [hep-th/0008052].

[264] D. N. Vollick, *Homogeneous and isotropic cosmologies with nonlinear electromagnetic radiation*, *Phys. Rev. D* **78** (2008) 063524 [0807.0448].

[265] S. Arunasalam and A. Kobakhidze, *Electroweak monopoles and the electroweak phase transition*, *Eur. Phys. J. C* **77** (2017) 444 [1702.04068].

[266] N. E. Mavromatos and S. Sarkar, *Finite-energy dressed string-inspired Dirac-like monopoles*, *Universe* **5** (2018) 8 [1812.00495].

[267] J. Ellis, N. E. Mavromatos, P. Roloff and T. You, *Light-by-light scattering at future e^+e^- colliders*, *Eur. Phys. J. C* **82** (2022) 634 [2203.17111].

[268] E. Musumeci, A. Irles, R. Perez-Ramos, I. Corredoira, E. Sarkisyan-Grinbaum, V. A. Mitsou et al., *Exploring hidden sectors with two-particle angular correlations at future e^+e^- colliders*, 2312.06526.

[269] E. Musumeci, R. Perez-Ramos, A. Irles, I. Corredoira, V. A. Mitsou, E. Sarkisyan-Grinbaum et al., *Two-particle angular correlations in the search for new physics at future e^+e^- colliders*, in *International Workshop on Future Linear Colliders*, 7, 2023, 2307.14734.

[270] E. Musumeci, *Investigating hidden sectors at future e^+e^- colliders through two-particle angular correlations*, *EPJ Web Conf.* **315** (2024) 01031.

[271] E. Musumeci, *Probing New Physics at future e^+e^- colliders with two-particle angular correlations*, *PoS* **ICHEP2024** (2025) 316.

[272] M.-A. Sanchis-Lozano, *Prospects of searching for (un)particles from Hidden Sectors using rapidity correlations in multiparticle production at the LHC*, *Int. J. Mod. Phys. A* **24** (2009) 4529 [0812.2397].

[273] M.-A. Sanchis-Lozano and E. Sarkisyan-Grinbaum, *A correlated-cluster model and the ridge phenomenon in hadron–hadron collisions*, *Phys. Lett. B* **766** (2017) 170 [1610.06408].

[274] M.-A. Sanchis-Lozano and E. Sarkisyan-Grinbaum, *Ridge effect and three-particle correlations*, *Phys. Rev. D* **96** (2017) 074012 [1706.05231].

[275] J. C. Collins and D. E. Soper, *Angular Distribution of Dileptons in High-Energy Hadron Collisions*, *Phys. Rev. D* **16** (1977) 2219.

[276] ALICE collaboration, *Two-particle angular correlations in pb-pb collisions at $\sqrt{s_{NN}} = 2.76$ tev*, *Phys. Lett. B* **708** (2012) 249.

[277] W. Kittel and E. A. De Wolf, *Soft multihadron dynamics*. World Scientific, 2005, 10.1142/5805.

[278] R. Botet and M. Ploszajczak, *Universal fluctuations: The phenomenology of hadronic matter*. World Scientific, 2002, 10.1142/4916.

[279] CMS collaboration, *Measurement of long-range near-side two-particle angular correlations in pp collisions at $\sqrt{s}$ =13 TeV*, Phys. Rev. Lett. **116** (2016) 172302 [1510.03068].

[280] ALICE collaboration, *Long-range angular correlations on the near and away side in p-Pb collisions at $\sqrt{s_{NN}} = 5.02$ TeV*, Phys. Lett. B **719** (2013) 29 [1212.2001].

[281] CMS collaboration, *Observation of Long-Range Near-Side Angular Correlations in Proton-Lead Collisions at the LHC*, Phys. Lett. B **718** (2013) 795 [1210.5482].

[282] M. Harrison, T. Ludlam and S. Ozaki, *RHIC project overview*, Nucl. Instrum. Meth. A **499** (2003) 235.

[283] CMS collaboration, *Observation of long-range, near-side angular correlations in proton-proton collisions at the lhc*, JHEP **09** (2010) 091 [1009.4122].

[284] PHENIX collaboration, *Dihadron azimuthal correlations in au+au collisions at $\sqrt{s_{NN}} = 200$ GeV*, Phys. Rev. C **78** (2008) 014901 [0801.4545].

[285] STAR collaboration, *Disentangling the soft and hard components of jet-like correlations in d+au collisions at $\sqrt{s_{NN}} = 200$ GeV*, Phys. Rev. Lett. **97** (2006) 162301 [nucl-ex/0604018].

[286] E. V. Shuryak, *On the origin of the 'Ridge' phenomenon induced by jets in heavy ion collisions*, Phys. Rev. C **76** (2007) 047901 [0706.3531].

[287] A. Dumitru, F. Gelis, L. McLerran and R. Venugopalan, *Glasma flux tubes and the near side ridge phenomenon at RHIC*, Nucl. Phys. A **810** (2008) 91 [0804.3858].

[288] P. Bozek and W. Broniowski, *Collective dynamics in high-energy proton-nucleus collisions*, Phys. Rev. C **88** (2013) 014903 [1304.3044].

[289] J. Noronha, B. Schenke, C. Shen and W. Zhao, *Progress and Challenges in Small Systems*, in , vol. 33, p. 2430005, 2024, DOI [2401.09208].

[290] A. Badea, A. Baty, P. Chang, G. M. Innocenti, M. Maggi, C. Mcginn et al., *Measurements of two-particle correlations in e^+e^- collisions at 91 GeV with ALEPH archived data*, Phys. Rev. Lett. **123** (2019) 212002 [1906.00489].

[291] Belle collaboration, *Measurement of Two-Particle Correlations of Hadrons in e^+e^- Collisions at Belle*, Phys. Rev. Lett. **128** (2022) 142005 [2201.01694].

[292] Y.-C. Chen et al., *Long-range near-side correlation in e+e− collisions at 183-209 GeV with ALEPH archived data*, Phys. Lett. B **856** (2024) 138957 [2312.05084].

[293] F. Gelis, E. Iancu, J. Jalilian-Marian and R. Venugopalan, *The Color Glass Condensate*, Ann. Rev. Nucl. Part. Sci. **60** (2010) 463 [1002.0333].

[294] M. J. Strassler and K. M. Zurek, *Echoes of a hidden valley at hadron colliders*, Physics Letters B **651** (2007) 374–379.

[295] L. Carloni and T. Sjöstrand, *Visible effects of invisible hidden valley radiation*, Journal of High Energy Physics **2010** (2010) .

[296] L. Carloni, J. Rathsman and T. Sjöstrand, *Discerning secluded sector gauge structures*, Journal of High Energy Physics **2011** (2011) .

[297] T. Sjöstrand, S. Ask, J. R. Christiansen, R. Corke, N. Desai, P. Ilten et al., *An introduction to PYTHIA 8.2*, Comput. Phys. Commun. **191** (2015) 159 [1410.3012].

[298] M. Berggren, *SGV 3.0 – a fast detector simulation*, 1203.0217.

[299] ILD Concept Group, *International Large Detector: Interim Design Report*, 2003.01116.

[300] M. Bahr et al., *Herwig++ Physics and Manual*, *Eur. Phys. J. C* **58** (2008) 639 [0803.0883].

[301] J. Bellm et al., *Herwig 7.0/Herwig++ 3.0 release note*, *Eur. Phys. J. C* **76** (2016) 196 [1512.01178].

[302] E. Musumeci, A. Irles, R. Perez-Ramos, I. Corredoira, E. Sarkisyan-Grinbaum, V. A. Mitsou et al., *Hidden sectors at FCC-ee with two-particle angular correlations*, 09, 2024, DOI.

[303] M.-A. Sanchis-Lozano and E. K. Sarkisyan-Grinbaum, *Searching for new physics with three-particle correlations in pp collisions at the LHC*, *Phys. Lett. B* **781** (2018) 505 [1802.06703].

[304] M. D. Schwartz, *Quantum Field Theory and the Standard Model*. Cambridge University Press, 3, 2014.

[305] V. Shtabovenko, R. Mertig and F. Orellana, *FeynCalc 9.3: New features and improvements*, *Comput. Phys. Commun.* **256** (2020) 107478 [2001.04407].